High-precision lattice QCD

Fabian Justus Frech

PhD thesis
submitted in partial fulfillment of
the requirements to achieve the degree of
Dr. rer. nat.

Theoretical particle physics

Faculty of mathematics and natural sciences

Bergische Universität Wuppertal

PhD Advisor:
Prof. Dr. Z. Fodor

Submission date:
26st of May 2025

Date of defense:
11st of July 2025

Contents

II Application to Standard Model Tests

III Appendices

List of Figures

List of Tables

Acknowledgements

First and foremost, my sincere gratitude goes to Prof. Dr. Zoltan Fodor, who gave me the opportunity to conduct my Bachelor's, Master's and PhD theses in his group. This allowed me to explore the fascinating field of lattice gauge theory and gain a wide range of enriching scientific and personal experiences.
I am deeply thankful to Prof. Dr. Kalman Szabo and Dr. Finn Stokes for their close supervision, insightful discussions and the highly productive collaboration throughout the past four years. Their support and expertise have been invaluable.
Many thanks to Prof. Dr. Karl-Heinz Kampert and Prof. Dr. Christian Hölbling for kindly agreeing to serve on my examination committee.
Gratitude is also due to all members of the BMW collaboration for the fruitful scientific exchange and excellent teamwork. Special thanks go to Prof. Dr. Laurent Lellouch, Dr. Balint Toth, Dr. Andrey Kotov, Dr. Gen Wang, Dr. Davide Giusti, Dr. Andreas Risch and Keith Kelley for many stimulating discussions and collaborations.
Working in the Theoretical Particle Physics group at Bergische Universität Wuppertal has been a great pleasure. I appreciate the friendly and inspiring atmosphere, both professionally and personally. In particular, I would like to thank Prof. Dr. Christian Hölbling, Prof. Dr. Szabolcs Borsanyi, PD Dr. Stephan Dürr, Dr. Ludovica Pirelli, Dr. Ruben Kara, Timo Eichhorn, Alexander Adam, Piyush Kumar, Marc-André Petri, Tolga Kiel, Gianluca Fuwa, Philip Rouenhoff, and Nuha Chreim for many enjoyable conversations and shared moments.
Thanks also to those who took the time to proofread various versions of this thesis and provided valuable linguistic and content-related feedback: Stefan Kuhlmann, Dr. Maximilian Caspar, Piyush Kumar and Timo Eichhorn.
Financial and non-material support from the "Studienstiftung des deutschen Volkes is gratefully acknowledged.
I would also like to thank the Gauss Centre for Supercomputing (GCS) e.V., GENCI, and the EuroHPC Joint Undertaking for providing computing time on the GCS supercomputers SuperMUC-NG at the Leibniz Supercomputing Centre in Munich, HAWK at the High Performance Computing Center in Stuttgart, and JUWELS and JURECA at Forschungszentrum Jülich, as well as on the GENCI systems Joliot-Curie/Irène Rome at TGCC, Jean-Zay V100 at IDRIS, Adastra at CINES, and the Leonardo supercomputer hosted at CINECA.
Above all, I am deeply thankful to my family, especially my parents, and my friends for their continuous encouragement throughout this journey. Last of all, heartfelt thanks go to my wife Anita, who has always stood by my side and supported me in every possible way.

1 Preface

> Ich betrachte es aber als durchaus möglich, dass die Physik nicht auf dem Feldbegriff begründet werden kann, d.h. auf kontinuierlichen Gebilden.
>
> Albert Einstein [1]

1.1 Introduction

Modern particle physics experiments have reached an unprecedented level of precision. For example, the fine-structure constant of quantum electrodynamics (QED) has been measured through the recoil velocity of a Rubidium isotope after an atomic transition to a precision of one part in a billion [2]. Even more remarkably, the magnetic moment of the electron is known to a precision of one part in ten trillion [3]. However, the most widely discussed high-precision experiment today is the $g_\mu - 2$ experiment at Fermilab [4–9]. Such experiments are vital for testing the Standard Model of particle physics.

The Standard Model is a highly developed quantum field theory (QFT) that describes three of the four fundamental forces in nature: electromagnetic, weak, and strong interactions. Gravity remains beyond its scope. Developed during the second half of the 20th century [10], the model was solidified by the confirmation of the quark model [11] and validated through major experimental discoveries, including the top quark (1995) [12], the τ neutrino (2000) [13], and the Higgs boson (2012) [14].

Despite its many successes, the Standard Model is not believed to be a complete theory. Not only does it omit gravity, but it also contains internal inconsistencies, such as the Landau pole in QED [15], where the energy-dependent coupling constant diverges at very high energies. This indicates that the Standard Model is only an effective theory valid at low to intermediate energies.

High-precision experiments allow us to probe the limits of the Standard Model and search for signs of beyond-the-standard-model (BSM) physics. To interpret these experiments, we also need precise theoretical predictions. Calculations within the Standard Model are highly complex. While QED and weak interactions can be computed perturbatively using a series expansion in terms of a small coupling constant [16], this approach fails for low-energy strong interactions due to non-convergence.

In 1974, to address this issue, Kenneth Wilson proposed the idea of introducing a hard ultraviolet (UV) cutoff through lattice regularization [17]. This technique replaces continuous spacetime with a discrete four dimensional grid with spacing a, reducing the number of degrees of freedom and making computations tractable in the strong-coupling limit. One of the most significant advantages of lattice discretization is that it renders the theory finite in volume, making it amenable to numerical evaluation via Monte Carlo methods [18].

Today, lattice calculations are approaching the precision of experimental measurements [19, 20]. To achieve this, sophisticated computational techniques and the use of high-performance computing resources are required. Over the past decade, simulations have begun utilizing GPUs [21–23], and more recently, quantum computing [24] and machine learning approaches [25].

With these powerful methods, the lattice physics community provides increasingly accurate predictions that can be directly compared with experimental data. This thesis presents my contributions to this rapidly evolving and exciting field.

1.2 Overview of the Thesis

The **first part** of this thesis outlines the theoretical foundations underlying lattice field theory. It summarizes the pioneering work of previous generations of physicists who laid the groundwork for modern lattice formulations. The basics of quantum field theory and lattice gauge theory are discussed, along with the numerical and analytical methods used for data analysis.
The **second part** applies these methods to high-precision QCD studies relevant to tests of the Standard Model. Here, I present my own contributions to the field of lattice gauge theory. These contributions fall into three main categories:

- **Precise determination of the gradient flow scales** w_0 and t_0, employing multiple methodologies. These determinations achieve a level of precision that, to date, has not been reached in the literature. In particular, the w_0 scale plays a key role in our high-precision determination of the anomalous magnetic moment of the muon [20]:

  A. Boccaletti et al. (Budapest-Marseille-Wuppertal), *High precision calculation of the hadronic vacuum polarisation contribution to the muon anomaly*, arXiv:2407.10913.

- **High-precision determination of the ratio of kaon to pion decay constants**, f_K/f_π, which provides a sensitive test of CKM matrix unitarity. The precision achieved in this work also surpasses that of previous determinations. The results are to be published as [26]:

  Fabian J. Frech et al. (Budapest-Marseille-Wuppertal), *Determination of f_K/f_π from 2+1+1 flavor 4-stout staggered lattices.*

- **Studies of tail contributions to the muon** $g-2$, presented at the LATTICE2023 and LATTICE2024 conferences and published in the corresponding proceedings:

  Fabian J. Frech et al. (Budapest-Marseille-Wuppertal), *The mixing of two-pion and vector-meson states using staggered fermions*, PoS **LATTICE2023** (2024) 251, [arXiv:2401.00514].

  Fabian J. Frech et al. (Budapest-Marseille-Wuppertal), *Reconstruction of the vector meson propagator using a generalized eigenvalue problem*, PoS **LATTICE2024** (2025) 251, [arXiv:2501.19186].

1.3 Units and Conventions

In this thesis, flat spacetime is used, as is customary in particle physics, with the mostly negative metric signature:

$$g_{\mu\nu} = \eta_{\mu\nu} = \begin{pmatrix} 1 & & & \\ & -1 & & \\ & & -1 & \\ & & & -1 \end{pmatrix} \tag{1.1}$$

Throughout this work, natural units are employed, meaning that the speed of light c, the Boltzmann constant k_B, the vacuum permittivity ϵ_0 and the reduced Planck constant $\hbar$ are all set to unity. In principle, the gravitational constant G would also be set to one in such a system, however, it does not appear in this thesis. In some sections, lattice units are used, where the lattice spacing a is set to 1.

Part I

Theoretical Foundations

2 Discretization of Quantum Field Theories

Quantum Field Theory (QFT) is the standard framework for describing modern particle physics. Compared to ordinary quantum mechanics, where operators and states depend only on time, in QFT they depend on all spacetime coordinates. In this sense, quantum mechanics can be interpreted as a $(0+1)$ dimensional QFT. Unlike classical field theory, which deals with real- or complex-valued fields, QFT involves operator-valued fields. Most QFTs require Lorentz invariance, which is especially necessary when describing particles whose momenta are large compared to their masses [27–29].

2.1 Classical Scalar and Vector Fields

Classical fields $\varphi(\vec{x}, t)$ are typically real or complex-valued functions defined over spacetime, with wide-ranging applications in cosmology [30], classical electrodynamics [31], and continuum mechanics [32]. The most fundamental classical field theories are often used in their quantized form in modern particle physics [16, 33, 34].

2.1.1 Action and Lagrangian

The Hamiltonian principle states that a classical field φ^j extremizes the action $S[\varphi^j(x), \partial_\mu \varphi^j(x)]$. The index j denotes different field components, such as spin, flavor, or vector direction, and x represents the spacetime coordinates. The action is a functional given by the integral of the Lagrangian density $\mathcal{L}(\varphi^j, \partial_\mu \varphi^j)$ over all spacetime. A necessary condition for minimizing the action is:

$$\frac{\delta S[\varphi^j, \partial_\mu \varphi^j]}{\delta \varphi^i(x)} = 0, \tag{2.1}$$

where $\delta/\delta\varphi(x)$ denotes the functional derivative. Assuming that φ vanishes at the boundary of $\mathbb{R}^{3+1}$, one can derive the Euler-Lagrange equations:

$$\partial_\mu \frac{\partial \mathcal{L}}{\partial(\partial_\mu \varphi^j)} - \frac{\partial \mathcal{L}}{\partial \varphi^j} = 0. \tag{2.2}$$

Noether's Theorem

Noether's theorem describes the relationship between a symmetry transformation and a conservation law [16, 29]. The infinitesimal version of a continuous transformation is given by

$$\varphi \to \varphi' = \varphi + \varepsilon \delta\varphi, \tag{2.3}$$

where ϵ is infinitesimal and $\delta\varphi$ is some deformation of the field. This transformation leaves a theory invariant whenever the corresponding Lagrange density only changes by the four gradient of some current J^μ. The corresponding conservation law states that the vector current is conserved:

$$\partial_\mu j^\mu = 0 \quad \text{with} \quad j^\mu = \frac{\partial \mathcal{L}}{\partial(\partial_\mu \varphi)} \delta\varphi - J^\mu. \tag{2.4}$$

2.1.2 The Klein-Gordon theory

The simplest scalar field theory that is consistent with special relativity is the Klein-Gordon theory [16, 28, 29]. It is motivated by the relativistic energy-momentum-mass relation:

$$E^2 = \vec{p}^2 + m^2 \tag{2.5}$$

Using the well-known quantum mechanics substitutions

$$E \to i\partial_t, \tag{2.6}$$

$$\vec{p} \to -i\vec{\nabla}, \tag{2.7}$$

and the application on a real- or complex-valued wave function $\phi(t, \vec{x})$ we get the Lorentz-covariant wave-equation

$$\left(\partial_\mu \partial^\mu + m^2\right) \phi(x^\mu) = 0. \tag{2.8}$$

Elementary solutions of this equation are given by

$$\phi^\pm_{\vec{k}}(x^\mu) = A^\pm_{\vec{k}} e^{\pm i k_\mu x^\mu}\Big|_{k_0 = \sqrt{\vec{k}^2 + m^2}}, \tag{2.9}$$

and using Fourier transformation the most-general solution can be represented in the following way:

$$\phi(x^\mu) = \sum_{\sigma \in \{+,-\}} \int \mathrm{d}^4 k \, A^\sigma_{\vec{k}} e^{\mathrm{i}\sigma k_\mu x^\mu} \delta\left(k_0 + \sigma\sqrt{m^2 + \vec{k}^2}\right) \tag{2.10}$$

2.1.3 The Dirac theory

While the Klein-Gordon theory uses a second order differential equation to describe fields that fulfill the relativistic energy-momentum relation, the Dirac theory is a first order differential equation to describe fields that fulfill the relativistic energy-momentum relation [16, 27]. The Dirac equation is given by

$$\left(\mathrm{i}\not{\partial} - m\right) \psi = 0, \tag{2.11}$$

where we use the Feynman-slash notation

$$\not{q} = \gamma^\mu q_\mu \tag{2.12}$$

and γ^μ represents a set of matrices fulfilling the condition

$$\{\gamma^\mu, \gamma^\nu\} = 2\eta^{\mu\nu}, \tag{2.13}$$

with the metric tensor $\eta^{\mu\nu} = \mathrm{diag}\{1, -1, -1, -1\}^\mu{}_\nu$. It can be shown that these γ-matrices are at least four dimensional [29]. The Dirac equation is often called the root of the Klein-Gordon equation due to the identity

$$(-\mathrm{i}\not{\partial} - m)(\mathrm{i}\not{\partial} + m) = -(\partial_\mu \partial^\mu + m^2). \tag{2.14}$$

From this, it can be concluded that each component of every solution of the Dirac equation is a solution of the Klein-Gordon equation. It can be shown that real- or complex-valued Dirac fields ψ and $\bar{\psi}$ can lead to contradictions like the issue that the Hamiltonian is not bound from below [29]. This can be solved by taking

Grassmann-valued fields instead [35] (see Appendix 12.4).

2.2 Path Integral Quantization

There are several ways to quantize field theories but Path Integral Quantization is particularly suited for quantizing fields on the lattice.

2.2.1 Hamiltonian version of the path integral

To perform the Path Integral Quantization we start with the canonical commutation relations that are known from quantum mechanics [36]:

$$[Q_a, P_b] = \mathrm{i}\delta_{ab}, \quad [Q_a, Q_b] = [P_a, P_b] = 0 \tag{2.15}$$

for a set of operators $\{Q_a\}_a$ with the corresponding conjugate momentum operators $\{P_a\}_a$. Here, the index a describes the position[1] and internal (spinor-, flavor-, color- etc.) degrees of freedom of the quantum field [34]. As the spatial degrees of freedom are continuous and integrated instead of summed over, the Kronecker delta in Equation (2.15) has to be replaced by the Dirac distribution.
All operators Q_a commute with each other so there has to be a system of common eigenstates $|q\rangle$ with the corresponding eigenvalues q_a. The eigenvectors can be chosen orthogonally and normalized, such that they fulfill the conditions

$$\langle q'|q\rangle = \delta(q' - q), \quad \mathbb{1} = \int\!\!\!\!\!\!\int \mathrm{d}q_a \, |q\rangle \langle q| \tag{2.16}$$

where $\int\!\!\!\!\!\!\int$ denotes integration over spatial coordinates and summation over discrete indices. The same construction can be done for the canonical momenta. The scalar product of the eigenstates can be computed similar to how it is done in quantum mechanics as

$$\langle q|p\rangle = \prod_a \frac{\exp(\mathrm{i}p_a q_a)}{\sqrt{2\pi}}. \tag{2.17}$$

Up to this point we worked at a fixed time-slice. Next we want to describe the time-evolution of the operators in the Heisenberg picture:

$$Q_a(t) = \exp(\mathrm{i}Ht) Q_a \exp(-\mathrm{i}Ht) \tag{2.18}$$

$$P_a(t) = \exp(\mathrm{i}Ht) P_a \exp(-\mathrm{i}Ht) \tag{2.19}$$

Here, H is the Hamilton operator of the system. The new operators $Q_a(t)$ and $P_a(t)$ have the eigenvectors $|q,t\rangle$ resp. $|p,t\rangle$ with the eigenvalues q_a and p_a. These eigenstates are related to the eigenstates of Q_a and P_a by

$$|q,t\rangle = \exp(\mathrm{i}Ht)\,|q\rangle \;\text{ and }\; |p,t\rangle = \exp(\mathrm{i}Ht)\,|p\rangle\,. \tag{2.20}$$

These time-dependent states are not the time-evolution of the eigenstates $|q\rangle$ and $|p\rangle$ (in this case there would be a minus-sign in the exponent of the time-evolution operator), but the eigenvectors of the time-evolved operators. At a given time-slice t, these states fulfill the relations from Equation (2.16) and Equation (2.17). The expression $\langle q', t'|q, t\rangle$ describes the probability amplitude of the process going from state $|q\rangle$ to state $|q'\rangle$ in the time from t to t'. To compute this expression we start by assuming that the time difference of t and t'

[1] Since we work in the Schrödinger picture, there is no time-dependence in the operators.

is infinitesimal:

$$\begin{aligned}
\langle q', t + \mathrm{d}t | q, t\rangle &= \langle q', t | \exp(-\mathrm{i}H\mathrm{d}t) \, | q, t\rangle \\
&= \int \left(\prod_a \mathrm{d}p_a\right) \langle q', t | \exp(-\mathrm{i}H(Q(t), P(t))\mathrm{d}t) \, | p, t\rangle \, \langle p, t | q, t\rangle \\
&= \int \left(\prod_a \mathrm{d}p_a\right) \langle q', t | \exp(-\mathrm{i}H(q(t), p(t))\mathrm{d}t) \, | p, t\rangle \, \langle p, t | q, t\rangle \\
&= \int \left(\prod_a \mathrm{d}p_a\right) \exp\left[-\mathrm{i}H(q', p)\mathrm{d}t + \mathrm{i}\sum_a (q'_a - q_a)p_a\right].
\end{aligned} \tag{2.21}$$

In the third step it is assumed that all momentum operators are moved to the right and all Q-operators are moved to the left[2]. The momenta in the above equation are integrated over the whole range $(-\infty, \infty)$. Now let us split up the interval (t, t') into $N+1$ sub-intervals $[t, t_1]$, $[t_1, t_2]$, ..., $[t_n, t']$ of length $\mathrm{d}t$. Now at each t_k $(k = 1, ..., N)$ a complete set of states $|q, t_k\rangle$ is included.

$$\begin{aligned}
\langle q', t' | q, t\rangle &= \int \left(\prod_{k=1}^{N} \mathrm{d}q_k\right) \langle q', t' | q_N, t_N\rangle \, ... \, \langle q_1, t_1 | q, t\rangle \\
&= \int \left(\prod_{k=1}^{N} \frac{\mathrm{d}q_k \, \mathrm{d}p_k}{2\pi}\right) \exp\left[\mathrm{i}\sum_{k=1}^{N} \left((q_k - q_{k-1}) \cdot p_{k-1} - H(q_k, p_{k-1})\right) \mathrm{d}t\right]
\end{aligned} \tag{2.22}$$

Equation (2.22) is called the *Path Integral Quantization* of the transition amplitude. Here the indices a are included implicitly. That means in particular that in the scalar products spatial variables are integrated out. Not only transition amplitudes can be computed using the path integral but also matrix elements of generalized operators $F(P, Q)$ at times τ in the time-interval (t, t'):

$$\langle q', t' | \, F(Q(\tau), P(\tau)) \, | q, t\rangle = \int \left(\prod_{k=1}^{N} \frac{\mathrm{d}q_k \, \mathrm{d}p_k}{2\pi}\right) F(q(\tau), p(\tau)) \exp\left[\mathrm{i}\sum_{k=1}^{N} \left((q_k - q_{k-1}) \cdot p_{k-1} - H(q_k, p_{k-1})\right) \mathrm{d}t\right], \tag{2.23}$$

which results in the limit $N \to \infty$ in

$$\int \left(\prod_{k=1}^{N} \frac{\mathrm{d}q_k \, \mathrm{d}p_k}{2\pi}\right) F(q(\tau), p(\tau)) \exp\left[\mathrm{i}\int_t^{t'} \mathrm{d}\tilde{t} \left(\dot{q}(\tilde{t}) \cdot p_(\tilde{t}) - H(q(\tilde{t}), p(\tilde{t}))\right)\right]. \tag{2.24}$$

Finally we got an general expression for matrix elements in QFTs where we got rid of all operators [34].

2.2.2 Lagrangian version of the path integral

Since most commonly field theories are defined using their Lagrangian density, one wants to replace the Hamilton function in Equation (2.23) by the corresponding Lagrange function. The following derivation is similar to the one given in Section 9.3 of the QFT book by Weinberg [34].
In general, it can be assumed that the Hamilton function is polynomial of order two in the momenta and can therefore be written as

$$H[Q, P] = \frac{1}{2} A^{ab}[Q] P_a P_b + B^a[Q] P_a + C[Q]. \tag{2.25}$$

[2]This argument is taken from [34], nonetheless it is not taken care of the fact that exponentiating a sorted operator can destroy the ordering. Luckily it can be derived from Trotter's formula that unordered terms are of order $\mathrm{d}t^2$ [37]. In fact, this is the reason why infinitesimal time intervals are considered.

So the exponent from Equation (2.24) is transformed to

$$-\frac{1}{2}\int \mathrm{d}\tau\,\mathrm{d}\tau'\,\mathcal{A}^{ab}_{\tau\tau'}[q]\,p_a(\tau)p_b(\tau') - \int \mathrm{d}\tau\,\mathcal{B}^a_\tau\,p_a[\tau] - \mathcal{C}[q], \tag{2.26}$$

$$\mathcal{A}^{ab}_{\tau\tau'}[q] = A^{ab}[q(\tau)]\delta(\tau-\tau'), \tag{2.27}$$

$$\mathcal{B}^a_\tau[q] = B^a[q(\tau)] - \dot{q}^a[\tau], \tag{2.28}$$

$$\mathcal{C}[q] = \int \mathrm{d}\tau\, C[q(\tau)]. \tag{2.29}$$

With the assumption that the operators whose matrix elements we want to compute do not depend on the canonical momenta (which has shown to be the case in general), the momentum integration for the path integral can be solved with common techniques to get the result

$$\left(\det\frac{\mathrm{i}\mathcal{A}}{2\pi}\right)^{-1/2}\exp\left[-\frac{\mathrm{i}}{2}\mathcal{A}^{ab}\xi_a\xi_b - \mathrm{i}\mathcal{B}^a\xi_a - \mathrm{i}\mathcal{C}\right], \tag{2.30}$$

where the ξ denote the stationary point of the exponent. This is given by the condition

$$\dot{q} = \left.\frac{\delta H}{\delta p}\right|_{p=\xi}, \tag{2.31}$$

that is known for being one of the Hamilton equations of motion. This can be used to interpret the integrand in the exponent as a Legendre transformation to write the matrix elements in terms of the Lagrange function

$$\langle q',t'|\,F(Q(\tau),P(\tau))\,|q'',t''\rangle = \int\left(\prod_{k=1}^{N}\mathrm{d}q_k\right)\Bigg|_{q(t''=q''),\,q(t')=q'} F(q(\tau),p(\tau))\exp\left[\mathrm{i}\int \mathrm{d}t\,L[q(t),\dot{q}(t)]\right]. \tag{2.32}$$

The integral over the Lagrange function is called the action of the theory [34].

2.3 Quantum electrodynamics

Quantum electrodynamics (QED) is one of the most common QFTs. The fields that occur in this equation are $2\times N_f$ sets of Dirac spinor fields $\bar{\psi}_f$ and ψ_f and a vector potential A_μ. N_f denotes the number of flavors used in this theory, whose masses are given by m_f. If one wants to describe only photons and electrons, N_f can be set to one. Usually, it is defined via its Lagrange density

$$\mathcal{L}^{\mathrm{QED}} = -\frac{1}{4}F_{\mu\nu}F^{\mu\nu} + \sum_{f=1}^{N_f}\bar{\psi}_f(\mathrm{i}\not{D} - m_f)\psi_f, \tag{2.33}$$

$$F_{\mu\nu} = \partial_\mu A_\nu - \partial_\nu A_\mu, \tag{2.34}$$

$$D_\mu = \partial_\mu - ieA_\mu, \tag{2.35}$$

where e denotes the coupling constant of this theory. The first term in this expression describes the propagation of photons while the second term describes the propagation of fermions (zeroth order in e) and the electron photon interaction. These are the three fundamental building blocks of QED, their respective Feynman diagrams are shown in Figure 2.1. Setting up the Euler-Lagrange equations for the photon field A_μ, one immediately gets the inhomogeneous Maxwell equation, while the equations of motion of the fermion fields lead to the Dirac equation from Section 2.1.3.

Furthermore, QED is one of the most fundamental gauge theories. A gauge theory has a local symmetry transformation $\Omega(x)$ that leaves the Lagrangian invariant. The co-domain of the gauge transformations is a Lie group, called the gauge group. In QED, the gauge group is the one dimensional compact Lie group $U(1)$.

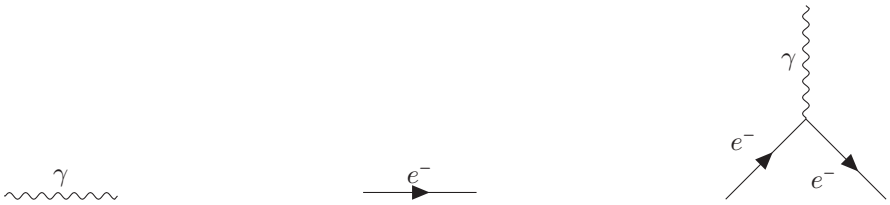

Figure 2.1 The fundamental diagrams, which can be used to construct every interaction of QED. The photon propagator is on the left, the fermion propagator is in the middle and on the right there is the only interaction vertex of QED.

The fields are transformed according to

$$\psi(x) \to \psi'(x) = e^{-\mathrm{ie}\alpha(\mathrm{x})}\psi(x), \tag{2.36}$$

$$\bar{\psi}(x) \to \bar{\psi}'(x) = \bar{\psi}(x)e^{\mathrm{ie}\alpha(x)}, \tag{2.37}$$

$$A_\mu(x) \to A'_\mu(x) = A_\mu(x) + e\partial_\mu\alpha(x). \tag{2.38}$$

where $\alpha(x)$ is a real-valued function that is at least C^1 (differentiable). As for most functions in physics, it is often assumed to be C^∞ (infinitely many times differentiable).

2.4 Quantum chromodynamics

Quantum chromodynamics (QCD) is the standard theory used to describe the strong interaction within the framework of the Standard Model, although other theoretical approaches to strong processes also exist, especially in contexts beyond or effective to QCD [38]. Its overall structure is very similar to the one of QED, but there are some crucial difficulties. First the fermion fields (called quark fields in this context) have an additional color-index that can take values from one to three. The term "color" in this context does not denote actual visual color, but is instead a conventional quantum label — introduced by analogy with "flavor" — to distinguish between different types of fermions. The three components of the quark field are related to the symmetry group, which has to be a subgroup of $U(3)$ in order to leave the mass term invariant. From experimental observations, it can be concluded that the subgroup in question must be $SU(3)$ [39]. The transformation of the vector potential A_μ takes care of the invariance of the dynamical part of the quarks under $SU(3)$-transformations. Every gauge-transformation Ω can be written as the exponential of an anti-Hermitian 3×3-matrix:

$$\Omega(x) = \exp\left(-\mathrm{i}\alpha^a(x)\frac{\lambda_a}{2}\right). \tag{2.39}$$

The index a takes values from 1 to 8 and $\frac{\lambda_a}{2}$ is a normalized orthogonal basis of the vector space of Hermitian and trace-less 3×3-matrices $\mathfrak{su}(3)$. λ_a are the Gell-Mann-matrices [40]. The gauge transformations for all the fields appearing in QCD are given by

$$\psi(x) \to \psi'(x) = \Omega(x)\psi(x), \tag{2.40}$$

$$\bar{\psi}(x) \to \bar{\psi}'(x) = \bar{\psi}(x)\Omega^\dagger(x), \tag{2.41}$$

$$A_\mu(x) \to A'_\mu(x) = \Omega(x)A_\mu(x)\Omega^\dagger(x) + \left(\partial_\mu\Omega(x)\right)\Omega^\dagger(x). \tag{2.42}$$

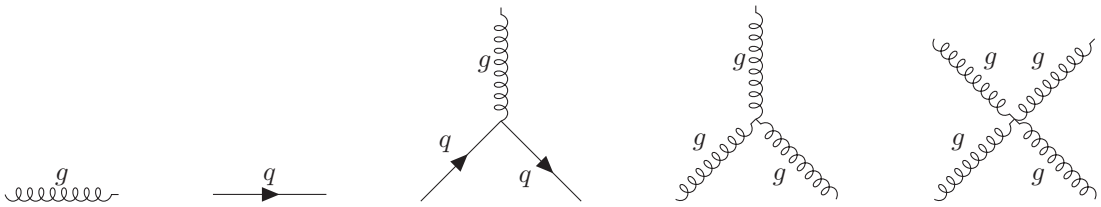

Figure 2.2 The fundamental diagrams, which can be used to construct every interaction of QCD. Compared to QED, photons are replaced by gluons and the fermions are limited to quarks. In addition, there are self-interactions of three or four gluons.

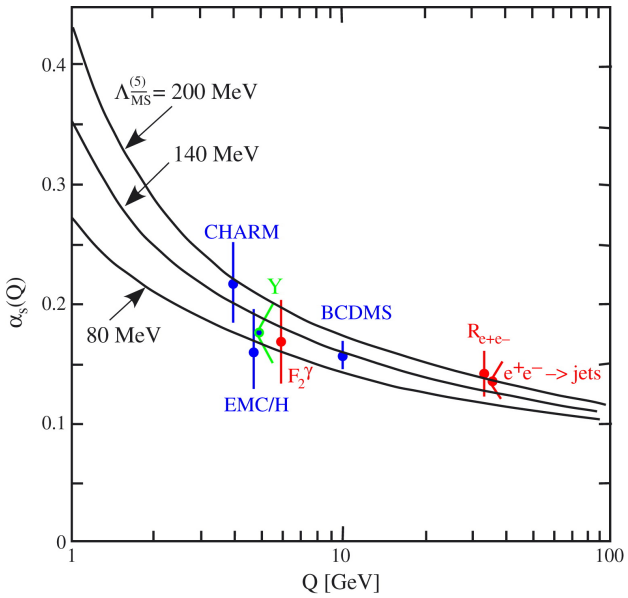

Figure 2.3 Experimental confirmation of the running of the strong coupling with respect to the energy scale [42]. The black lines are theoretical predictions for different values of the QCD energy scale $\Lambda^{(5)}_{\overline{\text{MS}}}$. This scale parameter, defined within the modified minimal subtraction scheme ($\overline{\text{MS}}$), sets the reference point at which the strong coupling constant α_s is matched to experimental data. Typical values lie in the range of a few hundred MeV [43, 44].

So there are three components of the quarks and an eight dimensional symmetry group. The boson fields (that are called gluons in QCD). The Lagrangian of QCD is defined via

$$\mathcal{L}^{\text{QCD}} = -\frac{1}{4}F^a_{\mu\nu}F^{\mu\nu}_a + \sum_{f=1}^{N_f}\bar{\psi}^c_f(\mathrm{i}\not{D}_{cd} - m_f\delta_{cd})\psi^d_f, \tag{2.43}$$

$$F^a_{\mu\nu} = \partial_\mu A^a_\nu - \partial_\nu A^a_\mu + g\sqrt{2}f^{abc}A^b_\mu A^c_\nu, \tag{2.44}$$

$$D^{cd}_\mu = \partial_\mu\delta^{cd} - \frac{\mathrm{i}e}{2}A^a_\mu\lambda^{cd}_a, \tag{2.45}$$

One of the most fundamental differences of the QCD and QED Lagrangian is the non linear term in the field strength tensor $F_{\mu\nu}$. It has to be included to take care of terms arising from the non-abelian structure of $SU(3)$. This quadratic term generates contributions of third and fourth powers of the gauge field A in the Lagrangian which can be translated directly into gluon-gluon-interactions as shown in Figure 2.2 [41].
The general approach for computing matrix elements and transition amplitudes in most QFTs and especially QED is perturbation theory. The general idea behind perturbation theory (in the context of QED) is that each of the fundamental vertices (see Figure 2.1) corresponds to a mathematical expression. Each vertex includes another factor of $\sqrt{\alpha}$ ($\sim e$) in the transition amplitude. Summing up all diagrams describing the process will give an asymptotic series in powers of e that converges to the correct QED result.
The self-interaction of the gluons on the other hand leads to an interesting feature, called asymptotic freedom,

that is shown in Figure 2.3. The coupling strength α_s of QCD increases at low energies, or equivalently, at large distances [45, 46]. Therefore the perturbative series only converges at sufficient high energy scales. So another method has to be used to compute the matrix element in QCD at low energies. In 1974, Kenneth Wilson introduced the idea of regularizing QFTs by a spacetime lattice for non-perturbative studies, such as gauge theories with confinement [17].

2.5 Wick rotation

The exponent in the path integral in Equation (2.32) is given by $\mathrm{i}S$, where S is the action of the corresponding theory in Minkowski spacetime. The action is a real quantity, so the exponential has an absolute value of one along all the field configurations. However, there are exceptions to this rule, e.g. when a finite chemical potential is introduced. So when considering the transition amplitude ($F = 1$) of the process, one finds an integral that is not convergent in a classical sense, because the domain is unbound and the absolute value of the integrand is bound from below. Of course, at configurations with large action, the fluctuation of the exponential is huge and therefore destructive interference suppresses the contribution in these action regimes, but a mathematical well-defined solution of this problem is needed.
In Minkowski spacetime, the action is defined with an integration of the Lagrange-function with respect to the time along the real axis. Now the time can be re-interpreted as a complex quantity. So we integrate along a path in the complex plane, and this path is given by the real axis. Now this path can be modified. If the integrand is a holomorphic function (which can be assumed if the action is analytic on the real axis) and the path does not cross any poles during the modification, the result of the integral remains unchanged. We only have to accept the assumption that the integrand converges to zero fast enough if $|t| \to \infty$. In case of the Wick rotation, the modification of the path is given by

$$\gamma_\alpha(t) = \exp(\mathrm{i}\alpha)t \quad (t \in \mathbb{R},\, \alpha \in [0, \pi/2]). \tag{2.46}$$

For $\alpha = 0$ we have the integration along the real axis and for $\alpha = \frac{\pi}{2}$ it is along the imaginary axis. Now we can replace the time in the action according to

$$t \to t_E = \mathrm{i}t. \tag{2.47}$$

This affects the Lagrangian and the action such that they are replaced in the following way by their Euclidean counterparts:

$$L \to -L_E \tag{2.48}$$

$$S \to \mathrm{i}S_E \tag{2.49}$$

The metric tensor $\eta^{\mu\nu}$ of the Lorentz covariant theories is also replaced:

$$\eta^{\mu\nu} \to \delta^{\mu\nu}. \tag{2.50}$$

Usually, the index zero is used for Minkowski time, while Euclidean time is denoted with the index 4. With the aforementioned substitutions, the exponential in the path integral has the form $\exp(-S_E)$ with S_E bounded from below, so the integrals converge properly [47]. The Euclidean actions for the Klein-Gordon and the

Dirac theory are

$$S_E^{\mathrm{KG}}[\phi] = \frac{1}{2}\int \mathrm{d}^4x\,\left[(\partial_t\phi)^2 + (\partial_x\phi)^2 + (\partial_y\phi)^2 + (\partial_z\phi)^2 + m^2\phi^2\right] =: \frac{1}{2}\int \mathrm{d}^4x\,\left(\partial_\mu\psi\partial_\mu\phi + m^2\phi^2\right) \tag{2.51}$$

$$S_E^{\mathrm{D}}[\bar\psi,\psi] = \int \mathrm{d}^4x\,\bar\psi(\gamma_E^4\partial_t + \gamma_E^1\partial_x + \gamma_2^E\partial_y + \gamma_E^3\partial_z + m)\psi =: \int \mathrm{d}^4x\,\bar\psi\left(\not{\partial}^E + m\right)\psi, \tag{2.52}$$

where the γ^E matrices are defined according to

$$\gamma_E^4 = \gamma^0, \quad \gamma_E^i = \mathrm{i}\gamma_E^i. \tag{2.53}$$

It follows that the Euclidean γ-matrices are Hermitian. The Yang-Mills action for photons and gluons changes to [35, 37]

$$S_E^{\mathrm{YM}} = \frac{1}{4}F_{\mu\nu}F_{\mu\nu}. \tag{2.54}$$

2.6 Lattice discretization

To compute observables in a QFT in a mathematically correct way one has to introduce an ultraviolet regulator. In case of lattice gauge theory a hard momentum cutoff is used. This is done by discretizing spacetime and only considering field values on a lattice. The spacetime variable x^μ is replaced by $a\cdot n^\mu$ with $n\in\mathbb{Z}^4$ and a being the lattice spacing. In principle it is possible to use anisotropic lattice spacings, but in the studies that are discussed here, a globally fixed spacing is used. Of course the definition of operations like derivatives and integrals (which are fundamental objects in the formulation of field theories) require a continuous spacetime. So they have to be replaced by discrete operators that reproduce them in the limit $a\to 0$. A possible (but not unique) discretization of these operators could be

$$\partial_\mu\phi(x) \to \frac{\phi(a(n+\hat\mu)) - \phi(a(n-\hat\mu))}{2a}, \tag{2.55}$$

$$\int \mathrm{d}^4x\,\phi(x) \to a^4\sum_{n\in\mathbb{Z}^4}\phi(an), \tag{2.56}$$

where $\hat\mu$ is a short notation for the unit vector in μ-direction. Applying this discretization on the free Dirac action for fermions that is given in Equation (2.52) yields

$$S_F^0[\psi,\bar\psi] = a^4\sum_n \bar\psi(an)\left(\sum_\mu\gamma_\mu\frac{\psi(a(n+\hat\mu)) - \psi(a(n-\hat\mu))}{2a} + m\psi(an)\right). \tag{2.57}$$

The lattice spacing a is set to one (lattice units) often. As it was discussed before there are gauge transformations that can act on the quark fields, on the lattice they are given by $\Omega(an)$. So if the transformation of the quark fields is given by

$$\psi(n) \to \Omega(n)\psi(n), \tag{2.58}$$

$$\bar\psi(n) \to \bar\psi(n)\Omega^\dagger(n), \tag{2.59}$$

the product of quark fields at neighboring lattice sites transforms as

$$\bar\psi(n)\psi(n+\hat\mu) \to \bar\psi(n)\Omega^\dagger(n)\Omega(n+\hat\mu)\psi(n+\hat\mu). \tag{2.60}$$

So the discretized version of the fermion action is not gauge invariant anymore, which is a necessary condition for the regularization. To restore gauge invariance, the gauge links $U_\mu(n)\in SU(3)$ are included. They are

given by $N_c \times N_c$-matrices (N_c is the number of colors in the corresponding theory, three in case of QCD and 1 in case of QED). They are located on the links between the lattices sites n and $n + \hat{\mu}$ as it is shown in Figure 2.4. Whenever two quark fields $\bar{\psi}(m)$ and $\psi(n)$ are multiplied, one has to include the product of the gauge links along a path that connects the sites m and n between them. The gauge links transform according to

$$U_\mu(n) \to \Omega(n) U_\mu(n) \Omega^\dagger(n + \mu), \tag{2.61}$$

which guarantees that the product

$$\bar{\psi}(n) U_\mu(n) \psi(n + \mu) \tag{2.62}$$

is gauge invariant. A gauge link connecting the sites n and $n - \hat{\mu}$ is given by $U_\mu^\dagger(n - \mu)$. There is another way to construct gauge invariant quantities on the lattice and that is to take the trace of the product of gauge links along a closed path on the lattice. The most fundamental object is the plaquette

$$P_{\mu\nu}(n) = \mathrm{Tr}\big\{U_\mu(n) U_\mu(n + \hat{\mu}) U_\mu^\dagger(n + \hat{\nu}) U_\nu^\dagger(n)\big\}, \tag{2.63}$$

which is a closed loop along the smallest possible square in the $\mu\nu$-plane starting at n[17, 35, 37]. An example is shown in Figure 2.5.

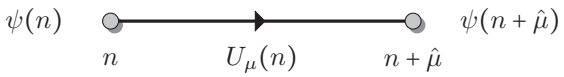

Figure 2.4 The quark fields are located at the sites on the lattice, while the gauge fields is at the links that connect adjacent lattice sites. This picture is taken from the Master Thesis of Timo Eichhorn [48].

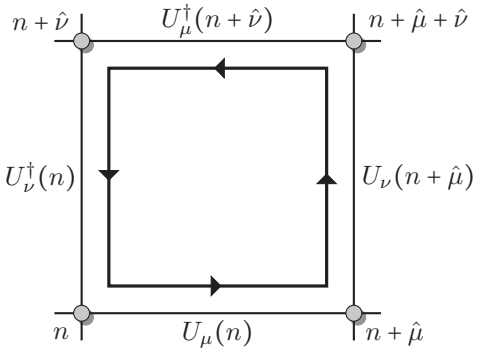

Figure 2.5 The plaquette is in general the most simple observable that can be constructed from gauge links only. It is the smallest contractible loop. This picture is taken from the Master Thesis of Timo Eichhorn [48].

2.7 The Wilson gauge action and improvements

It is evident how the lattice fermion action is related to the continuum one. The relation between gauge links on the lattice and the gauge fields in the continuum theory is a bit more involved. The gauge links are group-valued while the gauge fields takes values in the corresponding algebra. So they might be related by an exponential function. This is indeed true, but the gauge field is defined at a single point, while the gauge links are obviously not, so the gauge field is integrated along the link before the exponentiation:

$$U_\mu(an) = \exp\left(ig \int_{an}^{a(n+\hat{\mu})} A^\nu \mathrm{d}s^\nu\right) =: \exp\left(\mathrm{i}ag\tilde{A}_\mu(n)\right). \tag{2.64}$$

Here we introduced an algebra valued lattice quantity $\tilde{A}_\mu(n)$ that differs to the gauge links by terms of $\mathcal{O}(a)$. To get a lattice version of the Yang-Mills-Lagrangian, let us consider again the most simple gauge-invariant quantity on the lattice, the plaquette (see Figure 2.5 and Equation (2.63)). If we use the exponential representation in Equation (2.64) and apply a Taylor expansion of the continuous gauge fields

$$A_\nu(an + a\hat{\mu}) = A_\nu(an) + a\partial_\mu A_\nu(n) + \mathcal{O}(a^2), \tag{2.65}$$

we find that

$$P_{\mu\nu}(an) = \exp\left(\mathrm{i}a^2 g^2 F_{\mu\nu}(an) + \mathcal{O}(a^3)\right), \tag{2.66}$$

which can be expanded and reformulated to

$$S_G[U] = \underbrace{\frac{2N_c}{g^2}}_{\beta} \sum_n \sum_{\mu<\nu} \mathrm{Re}\left(1 - \frac{1}{N_c}\,\mathrm{Tr}\,P_{\mu\nu}(an)\right) = \frac{a^4}{2g^2} \sum_n \sum_{\mu,\nu} \mathrm{Tr}\left(F_{\mu\nu}^2\right) + \mathcal{O}(a^2). \tag{2.67}$$

So we got a lattice version of the gauge action that matches with the continuum up to terms proportional to a^2. However, it is possible to remove some of those artifacts [49]. By including loops of size 2×1, the action is modified to

$$S_G^{rect}[U] = \frac{\beta}{\mathrm{N_c}} \sum_{n\in\Lambda}\Big(\sum_{\mu<\nu} c_0\big(\mathrm{N_c} - \mathrm{Re\,tr}[P_{\mu\nu}(n)]\big) + \sum_{\mu\neq\nu} c_1\big(\mathrm{N_c} - \mathrm{Re\,tr}[P_{\mu,2\nu}(n)]\big)\Big), \tag{2.68}$$

where $P_{\mu,2\nu}$ is the 1×2 closed loop in the $\mu\nu$-plane. The coefficients have to be chosen according to

$$c_0 + 8c_1 = 1, \quad c_0 > 0. \tag{2.69}$$

The condition ensures that the continuum limit is correct and the tuning of the parameters can exclude higher-order contributions. For example, the Lüscher-Weisz (tree-level) action uses $c_0 = \frac{5}{3}$ and $c_1 = -\frac{1}{12}$ and has classically leading discretization effects of $\mathcal{O}(a^4)$ [50]. Other commonly used improved actions are the DBW2 and the Iwasaki action [51, 52].

3 Fermions on the lattice

Formulating fermion discretizations is a challenging, but interesting aspect of lattice QCD. In this chapter, we focus on naive and staggered fermions [53], exploring how they relate to each other, where they differ, and what mathematical challenges they pose.
From this chapter on, I will drop the subscript E from the Euclidean γ-matrices. Whenever it will be referred to the γ-matrices, the Euclidean ones are meant implicitly.

3.1 Naive Fermions

As discussed before the dynamics of the quarks, which are the fermionic fundamental particles of QCD, is described by the Euclidean Dirac equation

$$(\not{\partial} + m)\psi = 0, \tag{3.1}$$

which is the equation of motion of the Dirac action

$$S = \int d^4x \, \mathcal{L}, \tag{3.2}$$

$$\mathcal{L} = \bar{\psi}(\not{\partial} + m)\psi. \tag{3.3}$$

As mentioned before (Section 2.6) this action can be put on the lattice. If we ignore gauge field contribution, we can use a straightforward discretization scheme by replacing derivatives by symmetric finite differences and integrals by sums. The naive action for free quarks in QCD with all indices written explicitly is given by

$$S^{\text{naive}} = \sum_{n\in\Lambda} \sum_{a,b=1}^{3} \sum_{\alpha\beta=1}^{4} \bar{\psi}^a_\alpha(n) \left(\sum_{\mu=1}^{4} \gamma_\mu^{\alpha\beta} \frac{\delta_{ab}\psi^b_\beta(n+\hat{\mu}) - \delta_{ab}\psi^b_\beta(n-\hat{\mu})}{2} + \delta^{\alpha\beta}\delta_{ab} m \psi^b_\beta(n) \right), \tag{3.4}$$

which is often written as a bilinear form

$$S^{\text{naive}} = \sum_{n,m} \bar{\psi}(n) M^{\text{naive}}_{nm} \psi(m) \tag{3.5}$$

$$M^{\text{naive}}_{nm} = \frac{1}{2} \sum_{\mu=1}^{4} \gamma_\mu \left(\delta_{n+\hat{\mu},m} - \delta_{n-\hat{\mu},m} \right) + m\delta_{nm} \tag{3.6}$$

with implicit Dirac and color indices [54]. In this discretization the fermion action provides a lot of interesting symmetries [55].

3.1.1 Symmetries of the naive action

The homogeneous lattice structure of free Dirac fermions ensures that there are a lot of geometrical symmetry transformations that leave the action invariant.

Rotations and Inversions

We start with the rotational symmetry whose symmetry group is often called *special Würfel group* or SW_4, which consists of rotations of $\frac{\pi}{2}$ of all six coordinate planes. If one also allows spatial inversions, this group is extended by a factor of 2 and is called *Würfel group* or W_4. In odd dimension a spatial inversion can be represented as a global sign in the defining representation, while in even dimensions a spatial inversion can be defined by an additional sign for only one axis. The concept of the Würfel group can be generalized to arbitrary dimensions similar to the generalization of continuous rotations to $O(n)$ [56, 57]. In the Dirac representation the elementary rotations can be represented as

$$R^{\mu\nu} : \psi(n) \to \psi'(n') = \exp\left\{ i\frac{\pi}{4}\sigma_{\mu\nu} \right\} \psi(n'), \tag{3.7}$$

$$(R^{\mu\nu})^\dagger : \bar{\psi}(n) \to \bar{\psi}'(n') = \bar{\psi}(n') \exp\left\{ -i\frac{\pi}{4}\sigma_{\mu\nu} \right\}, \tag{3.8}$$

where n' is the lattice point that is received by rotating n in the $\mu\nu$-plane by an angle of $\frac{\pi}{2}$. The transformation $\exp\left\{ i\frac{\pi}{4}\sigma_{\mu\nu} \right\}$ rotates the γ-matrices in the same way [58]. Note, that these matrices only build a projective representation (see Section 12.1 of the symmetry group of a four dimensional hypercube, because of the identity

$$\left(\exp\left\{ i\frac{\pi}{4}\sigma_{\mu\nu} \right\} \right)^4 = -1 \neq 1. \tag{3.9}$$

This is related to the fact that the lattice fermions have a spin of $\frac{1}{2}$ like their continuum counterparts [29]. The inversion on the other hand is represented with

$$I_s : \psi(n) \to \psi'(n') = \gamma_4 \psi(n'), \tag{3.10}$$

$$I_s^\dagger : \bar{\psi}(n) \to \bar{\psi}'(n') = \bar{\psi}(n')\gamma_4. \tag{3.11}$$

Shift symmetry

The homogeneous structure of the free naive action provides a wide spectrum of shift symmetries. Let S_μ be the shift operator that is in the defining representation given by

$$S_\mu : \psi(n) \to \psi'(n') = \psi(n + \hat{\mu}), \tag{3.12}$$

$$S_\mu^\dagger : \bar{\psi}(n) \to \bar{\psi}'(n') = \bar{\psi}(n - \hat{\mu}), \tag{3.13}$$

from which can be concluded that the spinor structure is not affected by the shift symmetry transformations in contrast to the W_4-symmetry transformations. Now it is trivial to prove that the naive action is an invariant quantity with respect to this transformation.
Furthermore, there are power series of this shift that do not affect the action, to construct them we consider the bilinear $A(m) = \sum_n \bar{\psi}(n)\psi(n+m)$ whose invariance for $m = \pm\hat{\mu}$ and $m = 0$ implies invariance of the action. Now consider power series of the shift operator (that are not canonically symmetry transformations):

$$P(\alpha, S_\mu)\psi = \sum_{i=-\infty}^{\infty} \alpha_i S_\mu^i \psi(n) = \sum_{i=-\infty}^{\infty} \alpha_i \psi(n + i\hat{\mu}) \tag{3.14}$$

This transforms the term $A(y)$ according to

$$A(m) = \sum_n \bar{\psi}(n)\psi(n+m) \to \sum_n \sum_{ij} \alpha_i^* \alpha_j \bar{\psi}(n + i\hat{\mu})\psi(n + m + j\hat{\mu}), \tag{3.15}$$

which makes it an invariant condition if

$$\sum_{a\in\mathbb{Z}} \alpha^*_{a+i}\alpha_a = \delta_{i0}. \tag{3.16}$$

Using the Fourier convolution theorem one can conclude that the elements of α are Fourier coefficients of a $U(1)$-valued functions on a compact interval:

$$\alpha_m = \frac{1}{2\pi}\int_0^{2\pi} dp\, e^{imp}\tilde{\alpha}(p) \tag{3.17}$$

$$\tilde{\alpha}(p) \in \mathcal{L}([0,2\pi], U(1)). \tag{3.18}$$

There is a variety of function that fulfill this condition. For example, choosing $\tilde{\alpha}$ as a constant, this results in the global $U(1)$ symmetry of the action. It is somewhat more interesting to choose

$$\tilde{\alpha}(p) = \exp\{i\gamma p\}. \tag{3.19}$$

Then α_m takes the form $\mathrm{sinc}(\gamma - m)$, which is equal to $\delta_{\gamma,m}$ if γ is an integer. So for $\gamma \in \mathbb{Z}$ this is the symmetry due to the shift S^γ_μ. If m is chosen not to be an integer we can use it as a generalization of discrete shifts to arbitrary (continuous) shifts gamma. In general, these types of symmetry transformations can be interpreted as diagonal unitary operators on the momentum modes [59]:

$$|p\rangle \to \tilde{\alpha}(p)\,|p\rangle\,. \tag{3.20}$$

Taste symmetry

Apart from this geometrical symmetries, there are symmetry transformations that cannot be derived from a defining representation of a transformation in $\mathbb{R}^4$. For $\xi \in \mathbb{Z}_2^4$, consider the transformation

$$B_\xi\psi(x) = (-)^{x\cdot\xi}\prod_{\rho=1}^{4}(\gamma_5\gamma_\rho)^{\xi_\rho}\psi(x), \tag{3.21}$$

that is a symmetry of the naive action [60]. All of the B_ξ transformations are unitary, but not all of them are Hermitian. In order to do this, one defines

$$\tilde{B}_\xi = \begin{cases} iB_\xi & \text{if } B_\xi \text{ anti-Hermitian,} \\ B_\xi & \text{if } B_\xi \text{ Hermitian,} \end{cases} \tag{3.22}$$

which are all Hermitian. It is very straightforward to prove that the set of $\tilde{B}_\xi$ transformation forms a projective representation (see Section 12.1) of $\mathbb{Z}_2^4$. Using a central extension of this group (see Section 12.2) one can consider

$$\{\pm\tilde{B}_\xi | \xi \in \mathbb{Z}_2^4\}, \tag{3.23}$$

which is indeed a group that is isomorphic to $\Gamma_{0,4}$.
Since all of the group elements are Hermitian, the group elements can be used as generators of a continuous 16 dimensional symmetry group:

$$\{\exp\left(i\alpha_\xi\tilde{B}_\xi\right)|\alpha_\xi \in \mathbb{R}\}. \tag{3.24}$$

Furthermore, there are chiral symmetry transformations that do not affect the Dirac-part of the operator but generate a sign on the mass term:

$$A_\xi = i^{\|\xi\|_1} B_\xi \gamma_5 = i^{\Sigma_\mu |\xi_\mu|} B_\xi \gamma_5. \tag{3.25}$$

It can be seen very easily that we have

$$A_{\bar{\xi}} = \pm B_\xi \epsilon(n). \tag{3.26}$$

Thus, they have the same structure constants. We now can define the generators of left- and right-handed transformations by

$$B^R_\xi = \frac{1+\epsilon(n)}{2}\tilde{B}_\xi, \tag{3.27}$$

$$B^L_\xi = \frac{1-\epsilon(n)}{2}\tilde{B}_\xi. \tag{3.28}$$

We have commutation relations

$$[B^R_\xi, B^R_\zeta] = \frac{1+\epsilon(n)}{2} C^\rho_{\xi\zeta}\tilde{B}_\rho = C^\rho_{\xi\zeta} B^R_\rho, \tag{3.29}$$

$$[B^L_\xi, B^L_\zeta] = \frac{1-\epsilon(n)}{2} C^\rho_{\xi\zeta}\tilde{B}_\rho = C^\rho_{\xi\zeta} B^L_\rho, \tag{3.30}$$

$$[B^L_\xi, B^R_\zeta] = \frac{1+\epsilon(n)}{2}\frac{1-\epsilon(n)}{2} C^\rho_{\xi\zeta}\tilde{B}_\rho = 0, \tag{3.31}$$

with $C^\rho_{\xi\zeta} \in \mathbb{R}$ being the structure constants of the $\tilde{B}_\xi$. The continuous transformations generated by the right- and left-handed generators are

$$\begin{aligned} U^R &= \exp\left(\sum_\xi \alpha_\xi \frac{1+\epsilon(n)}{2}\tilde{B}_\xi\right) = \exp\left(\frac{1+\epsilon(n)}{2}\sum_\xi \alpha_\xi \tilde{B}_\xi\right) = \sum_{k\geq 0} \frac{\left(\frac{1+\epsilon(n)}{2}\sum_\xi \alpha_\xi \tilde{B}_\xi\right)^k}{k!} \\ &= 1 + \frac{1+\epsilon(n)}{2}\sum_{k\geq 1}\frac{\left(\sum_\xi \alpha_\xi \tilde{B}_\xi\right)^k}{k!} = 1 + \frac{1+\epsilon(n)}{2}\left(\exp\left(\sum_\xi \alpha_\xi \tilde{B}_\xi\right) - 1\right) \\ &= \frac{1-\epsilon(n)}{2} + \frac{1+\epsilon(n)}{2}\exp\left(\sum_\xi \alpha_\xi \tilde{B}_\xi\right) \end{aligned} \tag{3.32}$$

and

$$U^L = \frac{1+\epsilon(n)}{2} + \frac{1-\epsilon(n)}{2}\exp\left(\sum_\xi \alpha_\xi \tilde{B}_\xi\right). \tag{3.33}$$

3.1.2 The doubling problem

It is very straightforward to diagonalize the naive action matrix M^{naive}_{mn}. The Lagrange density of the action is homogeneous in space and therefore should conserve the conjugate momenta, which translates in the fact that M^{naive} is diagonal in momentum space. The Fourier transformation of equation (3.4) is given by:

$$\int \frac{dp}{2\pi}\int \frac{dq}{2\pi}\sum_{a,b=1}^{3}\sum_{\alpha,\beta=1}^{4} \bar{\psi}^a_\alpha(p)\tilde{M}\psi^b_\beta(q) = \tag{3.34}$$

$$\int \frac{dp}{2\pi}\int \frac{dq}{2\pi}\sum_{a,b=1}^{3}\sum_{\alpha,\beta=1}^{4} \bar{\psi}^a_\alpha(p)\left(i\sum_{\mu=1}^{4}\gamma^{\alpha\beta}_\mu \sin p_\mu + m\delta_{\alpha\beta}\right)\delta_{ab}\delta(p-q)\psi^b_\beta(q), \tag{3.35}$$

The Matrix $\tilde{M}$ can be inverted easily:

$$\tilde{M}^{-1} = \frac{m\delta^{\alpha\beta} - i\sum_\mu \gamma_\mu^{\alpha\beta} \sin p_\mu}{m^2 + \sum_\mu \sin^2 p_\mu} \delta_{ab}\delta(p-q). \tag{3.36}$$

The free propagator for naive quarks is then given by the backwards transformation of the inverse Matrix in momentum representation. It is common knowledge that poles in the massless propagator correspond to physical states. Since the lattice momenta p_μ are taken from the interval $[0, 2\pi)$, there are 16 momenta corresponding to a physical state:

$$(0,0,0,0),\ (0,0,0,\pi),\ ,\ldots(\pi,\pi,\pi,\pi). \tag{3.37}$$

Therefore, 15 modes correspond to unphysical states, called the *doublers* [35]. The doublers are directly related to the symmetry transformations given in Section 3.1.1. Let $p = (p_1, p_2, p_3, p_4)$ with $p_i \in \{0, 1\}$ be one of the momenta from Equation (3.37) in units of π and B_ξ with $\xi \in \mathbb{Z}_2^4$ one of the taste transformations. Then this transformation acts in the following way:

$$B_\xi p \equiv p + \xi \mod 2. \tag{3.38}$$

So the physical interpretation of this observation is the following: The naive action describes 16 quarks of the same mass instead of one. Therefore the action is symmetric when interchanging the quarks. The corresponding symmetry transformations are the B_ξ that are discussed before.

The No-go theorem

One might think that there is a way to get rid of the doublers without any disadvantages, but this is not the case:
If D be a massless discrete Dirac operator, then at least one of the following statements is not true [61]:

1. D has only one zero-mode. This is equivalent to the statement that D has no doublers.
2. D is *local*, which means that there are constants $C, c > 0$ such that

$$|D_{mn}| < C\exp\left(-c|n-m|\right). \tag{3.39}$$

   One has to note that the constant c should not depend on the lattice spacing.

3. D has the correct continuum limit, i.e

$$\lim_{a\to 0} D = \not{\partial}. \tag{3.40}$$

4. D respects chiral symmetry, i.e.,

$$\{D, \gamma_5\} = 0. \tag{3.41}$$

3.2 Staggered fermions

Staggered fermions can be introduced to reduce the number of doublers by a factor of four. This is still not consistent with the theory we want to describe, but will allow us to save a lot of simulation time by not computing 12 out of 16 identical fermions. The remaining three unwanted fermions can be removed by a technique called rooting that will be mentioned later on.

3.2.1 The staggered transformation

In order to construct staggered fermions from naive fermions, the unitary basis transformation

$$\Gamma(x) = \prod_{i=1}^{4} \gamma_i^{x_i} \quad \Gamma^\dagger(x) = \prod_{i=4}^{1} \gamma_i^{x_i} \tag{3.42}$$

is defined. The basis transformation is used to defined the staggered fields χ and $\bar{\chi}$ as:

$$\psi^\alpha(x) = \Gamma^{\alpha\beta}(x)\chi_\beta(x) \tag{3.43}$$

$$\bar{\psi}^\alpha(x) = \bar{\chi}_\beta(x)\left(\Gamma^\dagger\right)^{\beta\alpha}(x) \tag{3.44}$$

With this redefinition the free naive action in equation (3.4) becomes:

$$S = \sum_{x\mu} \bar{\chi}_\alpha(x)\left(\eta_\mu(x)\delta^{\alpha\beta}\frac{\chi_\beta(x+\hat{\mu}) - \chi_\beta(x-\hat{\mu})}{2} + m\delta^{\alpha\beta}\chi_\beta(x)\right) \tag{3.45}$$

$$\eta_\mu(x) = (-)^{\sum_{\nu<\mu} x_\nu} \tag{3.46}$$

By inspecting this expression one will notice that there is no mixing between the spinor components. It is therefore sufficient to work with only one of those which reduces the degrees of freedom and therefore the number of doublers by a factor of four. This feature is useful in the physical interpretation of the lattice fermions (because we got rid of 12 unphysical modes) as well as in terms of computational effort [62–64]. So the staggered action (which is one fourth of the naive action) is given by

$$S^{st} = \bar{\chi}M^{st}\chi, \tag{3.47}$$

$$M^{st} = \eta_\mu(x)\frac{U_{x,\mu}\delta_{x+\hat{\mu},y} - U^\dagger_{x-\mu,\mu}\delta_{x-\hat{\mu},y}}{2} + m\delta_{x,y}, \tag{3.48}$$

where the gauge links are already included, such that the action is gauge invariant.

3.2.2 Symmetry properties of staggered fermions

The (free) staggered action comes along with multiple symmetries. Averaged over all gauge field configurations, these symmetries also holds for the interacting case [59]. Before listing the most important symmetries, a few definitions have to be done:

$$\zeta_\mu(x) = (-)^{\sum_{\nu>\mu} x_\nu} \tag{3.49}$$

$$\epsilon(x) = (-)^{\sum_\mu x_\mu} \tag{3.50}$$

$$S_R(x) = \frac{1 + \zeta_\mu(x)\zeta_\nu(x) - \eta_\mu(x)\eta_\nu(x) + \zeta_\mu(x)\zeta_\nu(x)\eta_\mu(x)\eta_\nu(x)}{2}, \tag{3.51}$$

with R being a rotation in the $\mu\nu$-plane.

1. The first symmetry is the symmetry of the staggered action under rotations of $\pi/2$ in the $\mu\nu$-plane. It is similar to the corresponding symmetry transformation for naive fermions, but the pre-factor that mixes the spinor-components is replaced by a location-dependent pre-factor:

$$R^{\mu\nu} : \chi(n) \to \chi'(n') = S_R(n')\chi(n') \tag{3.52}$$

2. Of course staggered fermions also have a shift symmetry, but since the staggered action comes along with a position-dependent pre-factor, this has to be respected in the transformation rules:

$$S^{\mu} : \chi(n) \to \chi'(n') = \zeta_{\mu}(n)\psi(n') \tag{3.53}$$

3. The staggered phase $\eta_\mu(x)$ takes somehow the place of the γ-matrices, when transforming the naive action to the staggered one. This also happens when considering the spatial inversion symmetry:

$$I_s : \chi(n) \to \chi'(n') = \eta_4(n)\psi(n') \tag{3.54}$$

4. Next there is the charge conjugation symmetry that has a local pre-factor in the staggered formulation and interchanged particles and antiparticles:

$$C_0 : \chi(n) \to \epsilon(n)\bar{\chi}(n) \tag{3.55}$$

$$\bar{\chi}(n) \to -\epsilon(n)\chi(n) \tag{3.56}$$

5. The Baryon number is the only global symmetry in this list. It multiplies the quarks with a $U(1)_V$-phase factor:

$$B : \chi(n) \to g\chi(n) \quad g \in U(1) \tag{3.57}$$

6. The axial hyper-charge is explicitly broken for $m \neq 0$. The quarks are multiplied by an $U(1)_A$-phase factor.

$$H : \chi(n) \to g^{\epsilon}(n) \quad g \in U(1) \tag{3.58}$$

It has to be noted that all of the symmetries with local pre-factors are involutions expected for the shifts. If the shift operator is squared, the pre-factors cancel and what remains is the shift by two lattice units. Therefore, in momentum space, this operator $S_\mu^2 =: T_\mu$ can be represented as

$$T_\mu |p\rangle = \exp(2ip_\mu) |p\rangle . \tag{3.59}$$

Next we want to take the square root of this operator which leaves two choices for each eigenvalue. We decide to take the one with the with positive real part which ensures that the momenta are in the first Brillouin zone:

$$T_\mu^{1/2} |p\rangle = \exp(ip_\mu) |p\rangle \quad p_\mu \in \left(-\frac{\pi}{2}, \frac{\pi}{2}\right] \tag{3.60}$$

Using this definition, we can disentangle shift and taste from the symmetry operators by defining

$$\Xi_\mu = T_\mu^{-1/2} S_\mu . \tag{3.61}$$

In the defining representation the Ξ_μ operators fulfill the anticommutation relations of the euclidean γ-matrices, thus generating the 32-element group $\Gamma_{4,0}$ [59]. Also, the taste transformations anticommute with shifts in perpendicular directions and they are related to rotations via

$$R_{\mu\nu}\Xi_\nu R_{\mu\nu}^{-1}\Xi_\nu = 1. \tag{3.62}$$

This means that a rotation of the taste operators by an angular of π will not bring in a sign as it would for vectors like the shift operator.
The total symmetry group of staggered fermions[1] is then given as

$$\mathcal{G} = \{R_{\mu\nu}, I_s, C_0, \Xi_\mu, T_\mu^{1/2}\}. \tag{3.63}$$

If we consider only particles at rest, $T_\mu^{1/2}$ can be ignored (or represented trivially) and in combination with our knowledge on how the Würfel group acts on taste and charge transformations, the symmetry group at rest can be written as the semi-direct product of two groups:

$$\mathcal{G}_0 = \{C_0, \Xi_\mu\} \rtimes \{R_{\mu\nu}, I_s\} = \Gamma_{4,1} \rtimes W_4. \tag{3.64}$$

$\Gamma_{4,1}$ is the extension of $\Gamma_{4,0}$ by the generating element C_0 that anticommutes with the other generators Ξ_μ and has the property $C_0^2 = -1$. If we want to consider particles that are not at rest, we have to add back the translation group. For simplicity, we use a finite lattice N lattice site in each direction and periodic boundary conditions. Then the total symmetry group is given by [59]

$$\mathcal{G} = \{\mathbb{Z}_N^4\} \rtimes \mathcal{G}_0. \tag{3.65}$$

In the application in Chapter 10 we will consider the symmetry group at a fixed time-slice,which changed the group to

$$\mathcal{H} = \{\mathbb{Z}_N^3\} \rtimes \Gamma_{4,1} \rtimes W_3 = \{\mathbb{Z}_N^3\} \rtimes [SW_4 \times \Gamma_{2,2}]/\mathbb{Z}_2. \tag{3.66}$$

3.2.3 Momentum, spin and taste operators for staggered fermions

In the studies in the second part of this work, not only resting scalar fields are considered, but also a large variety of operators. Thus, I want to recap shortly how one can implement the different types of operators. Firstly, the are non-zero momenta. Let us consider a resting staggered field $\chi(x)$ that is put into a functional:

$$F[\chi, p = 0] = \sum_x \mathcal{A}_x \chi_x. \tag{3.67}$$

If we want to align a momentum q to the staggered field, we include a complex phase depending on the position x of the quark field:

$$F[\chi, p = q] = \sum_x \mathcal{A}_x \chi_x e^{\mathrm{i}q\cdot x}. \tag{3.68}$$

It is important that the components of p, i.e., p_μ, are a multiple of $\frac{2\pi}{L_\mu}$ if the lattice has finite extension L_μ in μ-direction. From the construction it can be seen directly that $p_\mu \equiv p_\mu + 2\pi$ and thus, the momentum is chosen from the interval $(-\pi, \pi]$. In the case of naive fermions (Section 3.1) it was shown that momenta that are multiples of π can be interpreted as different tastes and not as higher momenta. During the staggered construction we could get rid of some of those unwanted tastes. However, three unphysical tastes remain [35].

[1] We ignore the baryon number symmetry because its trivial and the axial symmetry because it is not exact.

The construction of taste and spin structure for free quarks is explained in some detail in the appendix of [60], but what is more interesting here is the taste and spin structure of mesons. A meson is a bound state consisting of a quark χ and an antiquark $\bar{\chi}$. Each of them has four spin and four taste components that are decomposed in the following way:

$$\bar{\mathbf{4}}_s \otimes \mathbf{4}_s = \mathbf{1}_s \oplus \mathbf{4}_s \oplus \mathbf{6}_s \oplus \mathbf{4}_s \oplus \mathbf{1}_s \tag{3.69}$$

$$\bar{\mathbf{4}}_t \otimes \mathbf{4}_t = \mathbf{1}_t \oplus \mathbf{4}_t \oplus \mathbf{6}_t \oplus \mathbf{4}_t \oplus \mathbf{1}_t \tag{3.70}$$

This decomposition is exactly the number of choices there are to pick out i out of 4 elements, what is exactly how meson in the continuum are defined. There, one puts i distinct γ-matrices between the quark fields, i.e., $\bar{\psi}\left(\prod_\mu \gamma_\mu^{n_\mu}\right)\psi$ with in $n \in \mathbb{Z}_2^4$. However, due to the staggered construction we have no γ-matrices acting on spinor components but there is implicit spin and taste. A staggered meson with a spinor structure of $n \in \mathbb{Z}_2^4$ and with a taste structure of $s \in \mathbb{Z}_2^4$ is given by

$$j_n^s(x) = \beta_n^s(x)\bar{\chi}(x)\chi(x + \delta x_{sn}), \tag{3.71}$$

with $\delta x_{sn} \equiv (s+n) \mod 2$ and

$$\beta_n^s(x) = (-)^{x\cdot(s^<+n^>)+n\cdot(s+n)^<}, \tag{3.72}$$

where the superscript $<$ denotes that the components of the vector are the cumulative sums of the elements with a smaller index (modulo 2) and the superscript $>$ denotes that the components of the vector are the cumulative sums of the elements with a larger index (modulo 2) [60, 65] .

4 Simulation of lattice gauge theories

The regularization with a hard cutoff is not the only advantage of discretization of spacetime. In combination with finite volume and finite time-extension, the lattice theory has a finite number of degrees of freedom in contrast to an uncountable infinite number as it is in the continuum theory. Therefore, the path-integral can be solved with a combination of analytical and numerical computations.

4.1 Wick's theorem

One of the most important statements of the spin-statistics theorem is that it is not possible to have two fermions in the same state. Therefore fermions are described by Grassmann-valued fields $\{\psi^\dagger\}$ and $\{\psi\}$ (see Section 12.4), that go in the fermion bilinear (see previous chapter 3). The total path-integral that has to be evaluated in order to get the expectation value of an observable has the form

$$\langle O \rangle = \frac{1}{Z} \int [\mathcal{D}U][\mathcal{D}\chi][\mathcal{D}\bar{\chi}]\, O[U,\chi,\bar{\chi}] \exp\left(-S_g[U] - \bar{\chi} M \chi\right), \tag{4.1}$$

$$Z = \int [\mathcal{D}U][\mathcal{D}\chi][\mathcal{D}\bar{\chi}] \exp\left(-S_g[U] - \bar{\chi} M \chi\right). \tag{4.2}$$

While the gauge fields U consists of (at most) nine complex numbers for every link on the lattice, the Grassmann field $\bar{\chi}$ and χ are harder to deal with. In principle a set of N Grassmann numbers can be represented using matrices of size $2^N \times 2^N$. Since $N \gg 1000$ usually it is not possible to store this representations. Luckily, the Grassmann integration can be done analytically, if a moment of a Gaussian integral has to be computed [35]:

$$\int [\mathcal{D}\chi][\mathcal{D}\bar{\chi}]\, \chi_{i_1}\chi_{i_2}\cdots\chi_{i_k}\bar{\chi}_{j_1}\bar{\chi}_{j_2}\cdots\bar{\chi}_{j_k} \exp\{-\bar{\chi} M \chi\} = \delta_{kl} \times f(M,\{i\},\{j\}) \tag{4.3}$$

$$f(M,\{i\},\{j\}) = (-)^k \sum_{\sigma \in S_K} \operatorname{sign}(\sigma) \left[\prod_{r=1}^{k} \left(M^{-1}\right)_{i_r, j_{\sigma(r)}}\right] \times \det M \tag{4.4}$$

This is called *Wick's theorem*. What finally remains is an integral with respect to the gauge links:

$$\langle O \rangle = \frac{1}{Z} \int [\mathcal{D}U]\, \tilde{O}[U] \exp\left(-S_g[U] + \log\det M[U]\right), \tag{4.5}$$

$$Z = \int [\mathcal{D}U] \exp\left(-S_g[U] + \log\det M[U]\right), \tag{4.6}$$

where $\tilde{O}[U]$ is $O[U,\chi,\bar{\chi}]$ after expanding in powers of χ and $\bar{\chi}$ and applying Wick's theorem [16, 35].

4.2 MCMC/Sampling of Monte-Carlo data

The dimension d of an integral like the one from Equation (4.5) can easily exceed 10^6. The computational cost when approximating such integrals with standard methods like numerical Riemann-Integration increases exponentially with d. In addition, the bulk of the phase space is suppressed by the exponential, so a huge amount of the computational time would be wasted (if it were even possible to perform this kind of integrations). Instead one can choose choose N representative configurations U_i from the distribution

$$p[U] = \frac{1}{Z} \exp\left(-S_g[U] + \log\det M[U]\right) \tag{4.7}$$

and compute the observables

$$O_i = \tilde{O}[U_i] \tag{4.8}$$

on these representatives. The mean value of this measurements can be used as an estimator for the expectation value of the observable with an uncertainty proportional to the inverse square root of the number of configurations [35, 66]:

$$\langle O \rangle = \frac{1}{N} \sum_{i=1}^{N} O_i + \mathcal{O}\left(\frac{1}{\sqrt{N}}\right) \tag{4.9}$$

This approach to integration is known as Monte Carlo (MC) integration. It relies on the random sampling of configurations, much like drawing numbers from a lottery, which is where the method gets its name. The hard task is of course to find a method that generates configurations according to a given and highly non-trivial distribution. For some simpler models than QCD there are methods for a direct sampling of configurations [67], but in QCD Markow-Chain-Monte-Carlo (MCMC) methods have to be used. These kinds of algorithms generate the configurations U_i using the set $\{U_0, ..., U_{i-1}\}$ in combination with some (pseudo-)random input. This of course leads to a certain amount of correlation between the configurations U_i (and the respective observables O_i) that has to be taken into account. But this issue is explained in more detail in Section 5.1. The chain of the configurations U_i is called a Markow-chain and has to fulfill the following four properties [37]:

1. The probability from that the system evolves from a state U to a state U' ($W(U, U')$) within one update is in the interval $[0, 1]$. This statement sounds trivial but is an important aspect of the mathematical formulation.

$$0 \leq W(U, U') \leq 1 \tag{4.10}$$

2. The sum of all probabilities to evolution with the same initial configuration is one:

$$\int [\mathcal{D}U]\, W(U, U') = 1 \tag{4.11}$$

3. There is a finite probability for the system to evolve from a given configuration U to any other given configuration U' after a certain amount of steps k.

$$W^k(U, U') > 0 \tag{4.12}$$

4. The transition probability $W(U, U')$ respects the desired distribution $p[U]$.

$$W(U, U')p[U] = W(U', U)p[U'] \tag{4.13}$$

The first two conditions ensure that $W(U, U')$ is a probability density function for a given U. The third condition is called ergodicity and makes sure, that all configurations can be sampled after a finite time and the last condition (detailed balance) takes care that the configurations U_i from the Markow-Chain are samples according to the desired probability distribution $p[U]$.
To start a Markow-chain, one needs an initial configurations. For this one can choose one of two methods: a cold start or a hot start. For a cold start, the initial gauge field configuration is trivial, a common choice is $U_\mu(x) = \mathbb{1}$ for all μ and x. For a hot start, one can either use an already existing gauge configuration from the equilibrium of the algorithm or randomly chosen gauge links. If the initial configuration is outside of the equilibrium a thermalization is needed, which means that a certain amount of updates is performed before the measurement of the observables[1] can be started. To find out when the system has arrived in the equilibrium one can have look at certain observables and see at which point in the chain they start to build a plateau.

[1] that go in the final analysis of the data

In the following two sections, two examples of MCMC-algorithms will be discussed: The Metropolis algorithm, which is comparatively simple to understand and implement and the Hybrid-Monte-Carlo algorithm, that is most commonly used in lattice gauge theories. Nevertheless, there are more algorithms like heat bath [18, 68–70], overrelaxation [71–73] and instanton [74–76] updates and modifications like Metadynamics [75–80] and Density of States [81, 82]. Comparative studies can be found in [75, 76].

4.2.1 Metropolis algorithm

The Metropolis algorithm was invented by Metropolis *et al.* in 1953 [83]. I will skip a general description of the algorithm and focus on the application to lattice gauge theories. Let U_{i-1} by a given configuration with the action $S_{\text{old}} = S_g[U_{i-1}] - \log\det M[U]$. Then one link $U_\nu(y)$ of the configuration U_{i-1} is chosen in addition to a random element of the gauge group V that is close to the unity matrix. A proposal for a new gauge configuration U' is made by

$$U'_\mu(x) = U_\mu(x) \cdot V \qquad \text{if } x = y \text{ and } \mu = \nu, \tag{4.14}$$

$$U'_\mu(x) = U_\mu(x) \qquad \text{else.} \tag{4.15}$$

On the configuration U' the new action $S_{\text{new}} = S_g[U'] - \log\det M[U']$ is measured. The configuration U' is chosen to be the new configuration U_i with the probability $\min\{1, e^{-(S_{\text{new}} - S_{\text{old}})}\}$. Otherwise, U_i is set again to be U_{i-1}. This is called the Metropolis step. The acceptance rate of the new configuration can be tuned by choosing the width of the distribution of V around the unity. Commonly this algorithm is only used if no quarks are considered, i.e., $M = 0$, because the computation of the local changes is too expensive, especially because the change of the gauge field in every step is very small, so a lot of determinants have to be computed to get new independent gauge configurations.

4.2.2 Hybrid-Monte-Carlo algorithm

To solve issue with the high cost of the simulation of quarks, Duane *et al.* came up with another approach [84], called Hybrid-Monte-Carlo (HMC) algorithm. If all of the links are changed by a bit in a way that does not have a huge effect on the action, a larger change of the gauge configuration can be performed before the Metropolis step and all-in-all less determinants have to be computed. The construction of the algorithm starts by bringing to mind the path-integral expectation value

$$\langle O \rangle = \frac{\int [\mathcal{D}U]\, O[U] \exp\left(-S[U]\right)}{\int [\mathcal{D}U] \exp\left(-S[U]\right)}. \tag{4.16}$$

Now the set of canonical momenta Π of the gauge field U can be included by expanding the fraction by $\int [\mathrm{D}\Pi] \exp\left(-\frac{1}{2}\Pi^2\right)$:

$$\langle O \rangle = \frac{\int [\mathcal{D}U]\, O[U] \exp\left(-S[U]\right) \int [\mathcal{D}\Pi] \exp\left(-\frac{1}{2}\Pi^2\right)}{\int [\mathcal{D}U] \exp\left(-S[U]\right) \int [\mathcal{D}\Pi] \exp\left(-\frac{1}{2}\Pi^2\right)} \tag{4.17}$$

$$= \frac{\int [\mathrm{D}U][\mathrm{D}\Pi]\, O[U] \exp\left(-S[U] - \frac{1}{2}\Pi^2\right)}{\int [\mathcal{D}U][\mathcal{D}\Pi] \exp\left(-S[U] - \frac{1}{2}\Pi^2\right)} \tag{4.18}$$

Next, the gauge fields are distributed according to a Hamiltonian $\mathcal{H} = S[U] + \frac{1}{2}\Pi^2$ that describes a system with fields U of mass 1 in a potential $S[U]$. Therefore new gauge configurations can be can be generated by solving the Hamiltonian equations of motion

$$\frac{\mathrm{d}U}{\mathrm{d}\tau} = \frac{\partial \mathcal{H}}{\partial \Pi}, \quad \frac{\mathrm{d}\Pi}{\mathrm{d}\tau} = -\frac{\partial \mathcal{H}}{\partial U}, \tag{4.19}$$

with an additional simulation time τ, which has to be strictly distinguished from the Euclidean time t_E (or t) that is used as a coordinate on the lattice. The procedure of an update step using the HMC algorithm is as follows: First, for each lattice link $U_\mu(x)$ a corresponding conjugate momentum $\Pi_\mu(x)$ is chosen randomly from the distribution $\exp\left(-\frac{1}{2}\Pi^2\right)$. Then the Hamiltonian equations of motion (Equation (4.19)) are solved using a numerical integration scheme, because this highly coupled system of partial differential equations cannot be solved analytically. To preserve detailed balance, one uses symmetric symplectic integrators, which guarantee reversibility and volume-preservation [85]. The simplest example is the leap-frog method, where the updates are performed in the following way:

1. $U_0 = \{U_\mu(x)\}$ and $\Pi_{\frac{1}{2}} = \{\Pi_\mu(x)\} - \frac{\epsilon}{2}\frac{\partial \mathcal{H}}{\partial U}|_{\tau=0}$
2. $U_i = U_{i-1} + \epsilon \frac{\partial H}{\partial \Pi}|_{\tau=i-\frac{1}{2}}$ and $\Pi_{i+\frac{1}{2}} = U_i - \epsilon \frac{\partial H}{\partial \Pi}|_{\tau=i-\frac{1}{2}}$ (for $i = 1, ..., n-1$)
3. $U_n = U_{n-1} + \epsilon \Pi_{n-\frac{1}{2}}$

This way of alternately updating the gauge fields and the canonical momenta is superior to a standard Euler-integration scheme, which has errors of $\mathcal{O}(\epsilon)$ while the leap-frog method has errors of $\mathcal{O}(\epsilon^2)$ [35]. Also, methods up to fourth order [86] are used to further reduce numerical deviations. Of course one can never get rid of all deviations caused by the numerical integration, so after a trajectory with N steps and a step size of $\epsilon = \frac{1}{N}$ the Hamiltonian has changed by $\Delta\mathcal{H}$. Since configurations should be sampled according to $\exp(-\mathcal{H})$, a Metropolis step can be included to set the new configuration either to U_n or back to U [35, 72].
There is one further difficulty that has to be discussed. When including fermions the overall action is given by

$$S = S_g[U] - \log\det M[U], \tag{4.20}$$

where $S_g[U]$ is a local and computational cheap function but $\det M[U]$ is not. So computing the force $\frac{\partial \mathcal{H}}{\partial U}$ in every step is still an extremely costly procedure. So one uses a trick called pseudo-fermions. As one might remember the determinant originates from a Gaussian integral of Grassmann variables

$$\det M = \int [\mathcal{D}\chi][\mathcal{D}\bar{\chi}] \exp\left(-\bar{\chi} M \chi\right). \tag{4.21}$$

A similar expression can be given by using complex numbers (if the matrix is Hermitian and positive definite):

$$\det M = \frac{1}{(2\pi)^n} \int [\mathcal{D}\psi][\mathcal{D}\psi^\dagger] \exp\left(-\psi^\dagger M^{-1} \psi\right). \tag{4.22}$$

Especially for small changes in the Matrix M, it could be shown that with a random vector $\psi = M\phi$ where ϕ is chosen from the distribution $\exp\left(-\bar{\phi}\phi\right)$

$$\frac{\det M[U]}{\det M[U']} = \exp\left(-\psi^\dagger (M[U] - M[U'])\psi\right) \tag{4.23}$$

is a very good estimator, whose uncertainties do not produce a significant systematical deviation in the distribution of the measurements. So before each trajectory, the ψs are drawn properly and the Hamiltonian is replaced by

$$\mathcal{H}^{pseudo} = \frac{1}{2}\Pi^2 + S_g[U] + \psi^\dagger M^{-1} \psi. \tag{4.24}$$

Of course there is still some effort necessary to compute the expression $\psi^\dagger M^{-1}\psi$ and it derivative with respect to the gauge fields in each step but this can be done using a conjugate gradient algorithm [87] which bounds the computational costs compared to a Gaussian solver.

The HMC algorithm is also useful to be applied in pure gauge theory, whenever the action is modified in a way that local changes of the link variables produce global changes of the action [77].

4.3 Rooting

We still have to clarify the issue that the staggered Dirac operator has three unphysical zero modes. In principle they can be interpreted as flavors, but in this case all flavors need to have the same mass, and since $m_c \approx 580 \times m_u$ one might be convinced that this is no proper assumption to simulate QCD. To gain a better understanding of this let us add another set of four quarks to the theory:

$$S = S_g[U] + \bar{\chi}_1 M \chi + \bar{\chi}_2 M \chi. \tag{4.25}$$

After integration of the Grassmann-fields, this will change the partition function to

$$Z^{8 \text{ quarks}} = \int [\mathcal{D}U] \exp\left(-S_g[U]\right) \times \left(\det M\right)^2. \tag{4.26}$$

It can be concluded that doubling the number of quarks of the same kind, will square the determinant in the partition function. In the same way the number of quarks can be reduced by a factor of four by using the fourth root of the determinant:

$$Z^{1 \text{ quark}} = \int [\mathcal{D}U] \exp\left(-S_g[U]\right) \times \left(\det M\right)^{1/4}. \tag{4.27}$$

This procedure was established in [88], highly criticized in [89], discussed in [90] and used in many cases [19, 20].
Now the problem appears that there occur powers of M unequal to one in the Hamiltonian:

$$\mathcal{H}^{\text{pseudo, rooted}} = \frac{1}{2}\Pi^2 + S_g[U] + \psi^\dagger M^{-\alpha} \psi, \tag{4.28}$$

with α being e.g. $\frac{1}{4}$. There are several ideas to deal with this issue. First is to use the R-algorithm, which rewrites the determinant as an effective action

$$\det M^\alpha = \exp\left(\alpha \operatorname{tr} \log M\right) = \exp\left(-S_{\mathit{eff}}\right), \tag{4.29}$$

where the parameter $\alpha \in \mathbb{R}$ can be chosen without any constraints. The problem with this algorithm is the computation of the force especially the gradient of the effective action, that is proportional to $\operatorname{tr} M^{-1} \frac{\partial M}{\partial U}$ and thus requires a full inversion of the matrix M. This is nearly impossible due to the enourmous size of the matrices in lattice QCD. Therefore, estimations are needed that include an additional $\mathcal{O}(\epsilon)$ contributions to the Hamiltonian. Through non area-preserving integrators, this error can be reduced to $\mathcal{O}(\epsilon^2)$. In this case the detailed-balance condition is not fulfilled, so the Metropolis step is not allowed. Therefore, the measurement will have $\mathcal{O}(\epsilon)$ corrections that have to be extrapolated to 0, which is not done usually.
Another choice is the Polynomial HMC (PHMC)-algorithm which tries to approximate M^α by a polynomial p in M:

$$\det M^\alpha = \int [\mathcal{D}\psi][\mathcal{D}\psi^\dagger] \exp\left(-\psi^\dagger\, p(M)\, \psi\right). \tag{4.30}$$

This algorithm does not have the problem of the R-algorithm but the degree n of the polynomial has to be chosen at $\mathcal{O}(100 - 1000)$ as one needs to save at least $n/2$ vectors at once, which increases the memory cost. In addition, comparatively large rounding errors can appear.
The current state-of-the-art choice is the rational HMC (RHMC)-algorithm which approximates M^α using a

rational function

$$r(M) = \sum_{i=1}^{n} \alpha_i (M + \beta_i)^{-1} \tag{4.31}$$

An advantage is that the inversions for all β_i can be done simultaneously so that no extra inversion time is required for the molecular dynamics evaluation [91]. In addition, n is roughly of order 20, which is much less than what is needed for polynomials [92].

4.4 Smoothing techniques

Plain gauge configurations usually provide a lot of ultra-violet noise. This means there are local fluctuations in the gauge links that can affect the condition number of the fermion matrices, the scaling of the observables at different lattice spacings, chiral symmetry- and taste-breaking effects. To reduce this noisy contributions, one can *smear* the gauge fields such that the high-energy modes are reduced.
In addition, also the sources for fermionic observables can be smeared to change the contribution of different modes in the correlation function [20].

4.4.1 Gradient flow

Gradient flow was used first in 2009 in the context of trivializing maps [93] and applied one year later in the context of scale setting [94]. The main idea is the local minimization of the gauge action density including the flow time t (not to be confused with the Euclidean time t_E or the Monte-Carlo time τ) as a fifth dimension and solving the partial differential equation

$$\frac{\mathrm{d}V}{\mathrm{d}t} = -g_0^2 \frac{\partial S}{\partial V} V \tag{4.32}$$

$$V(t=0) = U, \tag{4.33}$$

where $\frac{\partial S}{\partial V}$ is the $\mathfrak{su}(3)$-valued derivative of the action with respect to the gauge links [94]. The energy density measured on the configurations V can be computed using perturbation theory:

$$\langle E \rangle = \frac{3(N_c^2 - 1) g^2}{128\pi^2 t^2} \left(1 + \bar{c}_1 g^2 + \mathcal{O}(g^4)\right) \tag{4.34}$$

$$\bar{c}_1 = \frac{N_c(\frac{11}{3}L + \frac{52}{9} - 3\log 3) - N_f(\frac{2}{3}L + \frac{4}{9} - \frac{4}{3}\log 2)}{16\pi^2} \tag{4.35}$$

g is the renormalized coupling and $L = \log\left(8\mu^2 t\right) + \gamma_E$. μ is the energy scale with γ_E being the Euler-Mascheroni constant. Here, the energy density E is defined using the clover definition of the field strength tensor [35, 93]:

$$\begin{aligned} E &= \frac{1}{V \cdot T} \sum_x F_{\mu\nu} F_{\mu\nu} \\ F_{\mu\nu} &= \frac{-\mathrm{i}}{8} (Q_{\mu\nu} - Q_{\nu\mu}) \\ Q_{\mu\nu} &= P_{\mu,\nu} + P_{\mu,-\nu} + P_{-\mu,\nu} + P_{-\mu,-\nu} \end{aligned} \tag{4.36}$$

A visualization of the clover is given in Figure 4.1. From this it could be derived that $\langle t^2 E \rangle$ is independent of the gauge coupling at leading order. At higher order this invariance is broken, but the violation vanishes in the $t \to \infty$ limit. LÜscher suggested to consider the flow time t_0 defined as

$$\langle t^2 E \rangle|_{t=t_0} = 0.3 \tag{4.37}$$

to define a quantity that proportional to a^2 in order to define the spacing of a lattice in dependence of another gauge field.
This procedure is called Gradient Flow. If we choose $S[U]$ in the flow equation (4.32) to be the Wilson gauge action (as it was done by Lüscher), it is called Wilson flow.
In case of the Wilson flow (which is a very common choice) the following equation is solved:

$$\frac{\mathrm{d}V_\mu(n)}{\mathrm{d}t} = -g_0^2 \left(\mathcal{P}_{\mathfrak{su}(3)}(\mathcal{S}_\mu(n)V_\mu^\dagger(n))\right) V_\mu(n) \tag{4.38}$$

$$V_\nu(m)|_{t=0} = U_\nu(m) \quad \forall \nu, m. \tag{4.39}$$

Here, $\mathcal{S}_\mu(n)$ is the sum of the staples surrounding the link $V_\mu(n)$ at the same flow time as the link $V_\mu(n)$. $\mathcal{P}_{\mathfrak{su}(3)}$ denotes the projection operator on the Lie algebra $\mathfrak{su}(3)$ of anti-Hermitian traceless 3×3 matrices and is defined via [35, 48]

$$\mathcal{P}_{\mathfrak{su}(3)}(A) = \frac{A - A^\dagger}{2} - \frac{1}{6}\operatorname{Tr}\{A - A^\dagger\}. \tag{4.40}$$

This formulation comes along with $\mathcal{O}(a^2)$ discretization effects that are caused by cut-off effects of the same size in the definition of the Wilson gauge action. However, in Section 2.7 it was already mentioned that the gauge action can be modified by including larger loops. This was done first by Sint and Ramos, who called this modified flow the "Zeuthen flow" [95, 96]. In the studies done in this work we use three different versions of the Zeuthen flow. All of them are based on the flow equation

$$\frac{\mathrm{d}V_\mu(n)}{\mathrm{d}t} = -g_0^2 \left(1 + \frac{1}{12}\nabla_\mu^*\nabla_\mu\right) \frac{\partial S_{\mathrm{LW}}[V]}{\partial V_\mu(n)} V_\mu(n) \tag{4.41}$$

$$V_\nu(m)|_{t=0} = U_\nu(m) \quad \forall \nu, m \tag{4.42}$$

Here ∇_μ and ∇_μ^* denote the gauge covariant forward and backward derivatives on the lattice, respectively. These operators are defined as

$$\nabla_\mu\phi(n) = U_\mu(n)\phi(n+\hat{\mu}) - \phi(n), \tag{4.43}$$

$$\nabla_\mu^*\phi(n) = \phi(n) - U_\mu^\dagger(n-\hat{\mu})\phi(n-\hat{\mu}). \tag{4.44}$$

The three types that we call *unimproved clover (uc)*, *improved clover (ic)* and *Symanzik (sy)* differ by their definition of the energy density. The *uc* uses the clover based energy density from Equation (4.36) that is also used for the Wilson flow. For the *ic*, clover and plaquette field strength tensor are added in a way that removes all of the $\mathcal{O}(a^2)$ artifacts. The third type *sy* is defined with the Lüscher-Weisz improved energy density [50], thus, it also got rid of all $\mathcal{O}(a^2)$ contribution. However, it has different $\mathcal{O}(a^4)$ contributions than the improved clover type.

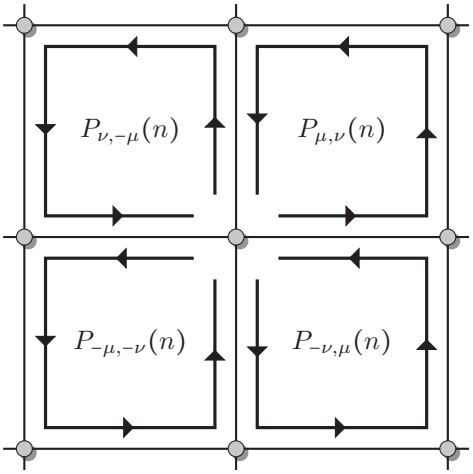

Figure 4.1 Illustration of the clover term used to define the field strength tensor on the lattice [97].

4.4.2 Smearing of the gauge field

There are different approved methods for gauge smearing like APE[2] [98], HYP[3] [99], HEX[4] [100] and stout[5] [101]. In this thesis I will only consider the latter one, which is nothing more than a gradient flow on the Wilson action using a simple Euler integration scheme. Usually a few steps of stout smearing n_{smear} is applied and for each step of stout-smearing the following procedure is done: For each link the weighted sum of all staples [37] surrounding the link is computed:

$$C_\mu(x) = \sum_{\nu \neq \mu} \rho_{\mu\nu} \left(U_\nu(x) U_\mu(x+\hat{\nu}) U_\nu^\dagger(x+\hat{\mu}) - U_\nu^\dagger(x-\hat{\nu}) U_\mu(x-\hat{\nu}) U_\nu(x-\hat{\nu}+\hat{\mu}) \right). \tag{4.45}$$

In principle $\rho_{\mu\nu}$ can be chosen arbitrary but in practice it is often set constant as [19, 102]

$$\rho_{\mu\nu} = \rho \sim 0.1. \tag{4.46}$$

These weighted staples are multiplied on the adjoint of the gauge links

$$\Omega_\mu(x) = C_\mu(x) U_\mu^\dagger(x) \tag{4.47}$$

and projected on the Lie algebra of the gauge group:

$$Q_\mu(x) = \frac{\mathrm{i}}{2} \left(\Omega_\mu^\dagger(x) - \Omega_\mu(x) \right) - \frac{\mathrm{i}}{2N_c} \operatorname{Tr} \left(\Omega_\mu^\dagger(x) - \Omega_\mu(x) \right). \tag{4.48}$$

If now $U_\mu^{(n)}(x)$ is the gauge field after n applications of stout smearing and $Q_\mu^{(n)}(x)$ is the algebra-element $Q_\mu(x)$ computed using $U_\mu^{(n)}(x)$, then

$$U_\mu^{(n+1)}(x) = \exp\left(\mathrm{i} Q_\mu^{(n)}(x) \right) U_\mu^{(n)}(x). \tag{4.49}$$

In the limit $\rho \to 0$, $n_{\text{smear}} \to \infty$ and $\rho n_{\text{smear}} = t$ the Wilson flow at flow time t is restored [103, 104].
Usually a few steps of smearing are applied to the gauge field before computing fermion matrices to reduce taste-breaking effects (staggered fermions [19]) or chiral symmetry breaking effects (Wilson fermions [105]).

[2] Named after the APE (Array Processor Experiment) collaboration
[3] Named after the hypercubic structure of this method
[4] Short for hypercubic exponential
[5] "Refers to their thick-bodied nature from the large brew of paths used in their formation (coined in a Dublin public house)." [101]

Also smearing (or the gradient flow) can be applied before measuring the topological charge

$$Q = \frac{1}{32\pi^2} \sum_x \epsilon_{\alpha\beta\gamma\delta} F^{\alpha\beta}(x) F^{\gamma\delta}(x) \tag{4.50}$$

which reduces UV-fluctuations that dominate the result [77, 106].

4.4.3 Smearing of the fermions sources

Not only the gauge fields can be smeared but also the fermion sources. According to Equation (4.3), fermionic operators are linear combinations and product of elements of the inverse fermion matrix. Usually it is not feasible to compute M^{-1} directly but what is done is to compute the matrix elements by solving the linear system

$$\xi = M\eta \tag{4.51}$$

for some random sources ξ_r $(r = 1, ..., N_{source})$ that fulfill the condition [35]

$$\langle \xi_r^T \xi_s \rangle = \delta_{rs}. \tag{4.52}$$

For example, wall sources, $\xi_{t_0}(x,t) = \frac{1}{N_x N_y N_z} \delta_{t,t_0} (-)^{r(x)}$ with $r(x)$ being either 0 or 1 randomly for each lattice site, but also point sources $\xi_{t_0,x_0}(x,t) \delta_{t_0,t} \delta_{x_0,x}$ can be taken into account. To change the contributions of different excitation to the measurement of the correlation function, the point source can be smeared using a three dimensional Laplace operator [107], thus the point source is replaced by

$$S(x) = (D^2 + m_{sc}^2)^{-1} \delta_{x,x_0} \delta_{t,t_0}, \tag{4.53}$$

where D^2 is the three dimensional gauge-covariant Laplace operator on the lattice and m_{sc} is a parameter that can be tuned. In the first publication [107] this parameter is set such that the smearing radius is about three lattice spacings. According to the affiliation of most of the authors of the paper that introduced this smearing method, it is called Wuppertal-smearing. A definition of Wuppertal smearing that is more suitable for practical applications was given, for example, in [20]. For a given pseudo-fermion field ψ the Wuppertal-smearing operator $\hat{W}$ can be applied, which is defined via:

$$[\hat{W}\psi](x) = (1-\sigma)\psi(x) + \frac{\sigma}{6} \sum_{\mu=1,2,3} \left(U_\mu^{3\mathrm{d}}(x) U_\mu^{3\mathrm{d}}(x+\hat{\mu}) \psi(x+2\hat{\mu}) + U_\mu^{3\mathrm{d},\dagger}(x-\hat{\mu}) U_\mu^{3\mathrm{d},\dagger}(x-2\hat{\mu}) \psi(x-2\mu) \right) \tag{4.54}$$

Here U^{3d} is the gauge field U after applying a few steps of three dimensional stout-smearing, i.e., $\rho_{4\mu} = \rho_{\mu 4} = 0$ in Equation (4.45). σ is a parameter that modifies the strength of the smearing procedure and similar to stout-smearing, Wuppertal-smearing can be applied a few times on the same source. In Equation (4.54), it can be seen that only sites that differ by an even number of spacings in all directions are included. This is done in order to not mixing contributions from different tastes.

5 Data analysis

In lattice QCD, a large amount of data generated by Markow-chain-Monte-Carlo algorithms has to be analyzed. Statistical and systematic effects play a major role here and have to be considered appropriately. Fortunately, a broad range of mathematical concepts and methods exist that can be adopted for use in lattice QCD. A small fraction of these methods will be explained in the following chapter.

5.1 Treating of statistical uncertainties

We analyze data from a N-element Markow chain that samples the distribution that is given by the path integral. Due to the fact that only a finite subspace of the phase space is sampled, a statistical uncertainty is introduced, which can be estimated in several ways.
The elements of the Markow chain, which are gauge configurations U_i in the context of lattice gauge theory, are used to measure observables $O[U_i]$. The expectation value of the observable is given by the mean value along the Markow chain:

$$\overline{O} = \frac{1}{N}\sum_{i=1}^{N} O[U_i]. \tag{5.1}$$

Of course, the distribution of the measurements has a width (standard deviation), which is given by the square root of the variance of the distribution. The variance is given by the mean value of the squared difference of the expectation value and the measurements, but the normalization is changed $\frac{1}{N-1}$ because the number of degrees of freedom is already reduced by one when computing the mean value. So the variance is given by

$$\sigma_O^2 = \frac{1}{N-1}\sum_{i=1}^{N}\left(O[U_i] - \overline{O}\right)^2. \tag{5.2}$$

On a finite Markow chain, it is only possible to compute estimators for expectation value and variance. Of course the true value is only reached in the case of $N \to \infty$. But in most cases it can be assumed that N is large enough to give a realistic value for those quantities.
In a Markow chain it is unavoidable that consecutive elements are dependent in some way. This effect is called autocorrelation and is a huge issue in simulation of lattice gauge theory. For example topological observables are plagued by large autocorrelation effects near the continuum limit [77]. This affects the estimation of expectation values and errors. The effect of autocorrelation can be quantified using the autocorrelation function (ACF) that gives (up to a normalization of σ_O^2) the correlation (statistical relationship) of two measurements on the Markow chain that are separated by t steps:

$$\Gamma_O(t) = \lim_{K\to\infty}\frac{1}{K}\sum_{i=1}^{K}\left(O[U_{i+t}] - \overline{O}\right)\left(O[U_i] - \overline{O}\right) \tag{5.3}$$

There is some circumstantial evidence that the autocorrelation is given by a sum of decaying exponential functions $A_i \exp\left\{\frac{t}{\tau_i}\right\}$ $(\tau_i > \tau_{i+1})$ [108]. The most relevant contribution to the autocorrelation effects originates from the case $i = 0$ and we can assume that the other contributions are suppressed exponentially. It follows that the autocorrelation time (i.e., the time until the autocorrelation reaches $1/e$) can be estimated by the integral of the ACF. Since we only have access to the ACF for integers t, the integral is replaced by a sum. This quantity is called *integrated autocorrelation time* and can be written as

$$\tau_{int}(O) = \frac{1}{2} + \sum_{t=1}^{\infty}\frac{\Gamma_O(t)}{\Gamma_O(0)} = \frac{1}{2}\sum_{t=1}^{\infty}\rho_O(t), \tag{5.4}$$

with $\rho_O(t) = \frac{\Gamma_O(t)}{\Gamma_O(0)}$ being the normalized autocorrelation function. In general, one has $N < \infty$, thus it is not possible to compute the whole series, but from some point the ACF is dominated by noise. A simple In this case, it is usual practice to stop the summation as soon as $\Gamma_O(t) < 0$.
The error of the normalized autocorrelation function can be computed via

$$\delta\rho_O(t) = \sqrt{\frac{1}{N}\sum_{m=1}^{W}\left(\rho(m+t)+\rho(m-t)-2\rho(m)\rho(t)\right)^2} \tag{5.5}$$

using the convention $\rho(-t) = \rho(t)$[109, 110].
With this proper estimation of autocorrelation effects it is finally possible to estimate the error on the mean value:

$$\delta O = \sqrt{\frac{2\sigma_O^2\tau_{int}(O)}{N}}. \tag{5.6}$$

For fully uncorrelated measurements equation (5.4) will give an integrated autocorrelation time of $\frac{1}{2}$. Therefore, the naive error on the mean values is given by

$$(\delta O)_{\text{naive}} = \frac{\sigma_O}{\sqrt{N}} \tag{5.7}$$

and can serve as a lower bound for the error on the primary observable [108–111].

5.1.1 Blocking

If a set of data has to be analyzed, blocking is a common strategy. It is done via replacing a subset of the data whose constitutions are similar in some parameters by their mean value [112]. This helps to estimate the statistical uncertainties properly. In the context of Markow chains one often blocks data that are related by autocorrelation effects. This is done by choosing $b \approx 2\tau$ and making blocks of length b in the Markow chain, where τ is the autocorrelation time of the observable. The length of the chain then reduces from N to N/b, so one has to take care that b is a divisor of N. If this is not the cases, one can discard some on the measurements. Afterwards the blocks can be treated as independent measurements and the error can be computed naively (compare equation (5.7)). The blocking procedure is sketched in Figure 5.1.

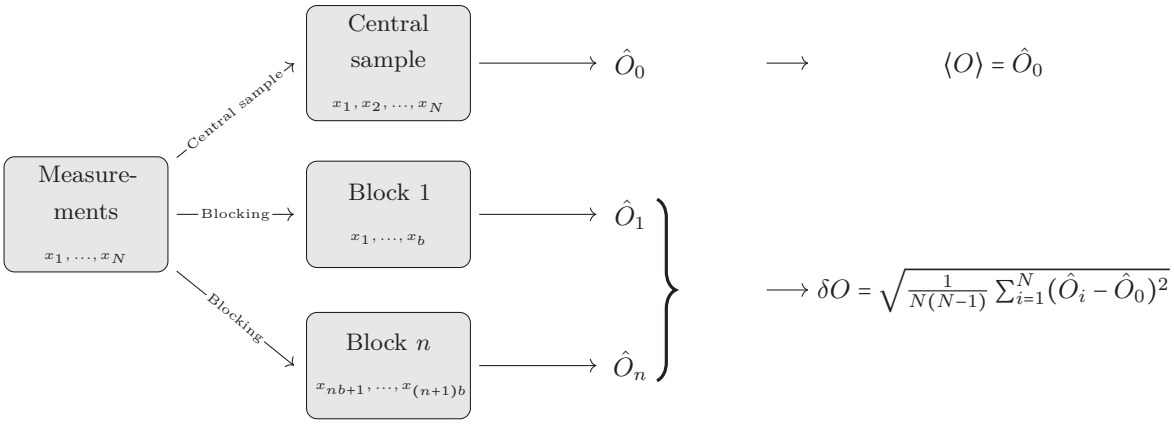

Figure 5.1 Visualization of blocking procedure.

Of course the choice of τ is not unambiguous. Typically, one chooses τ such that it is larger than the integrated autocorrelation time of a quantity with large autocorrelation effects [19], for example the topological charge, which has shown to have dominating autocorrelation times [75–78, 113].

Another way to estimate a proper value for b is measuring the variance σ^2 of certain observables in dependence of b. If one finds a region where $\sigma^2 \propto \frac{1}{b}$ one can choose a b from this region for an appropriate block size [35]. A disadvantage is that a pure blocking procedure is unpractical when computing the error of secondary observables, i.e., $f(O)$. In this case methods like Gaussian error propagation or automatic differentiation [114, 115] have to be applied, which cannot be generalized easily to arbitrary secondary observables [35]. Therefore, one can use one of two other methods: Bootstrap and Jackknife.

5.1.2 Bootstrap resampling

The method of bootstrapping uses the assumption that the sample of measurements, that we have access to, is representative for the whole set of possible measurements. So one draws (with replacement) set with N elements (the same number as there are measurements in total) out of the sample and computes the corresponding mean value. This procedure is done B times. These B mean values can be either used to compute the error on the primary observable by calculating the standard deviation of the bootstrap samples or they can be used to compute secondary observables by evaluating $f(\hat{O}_i)$ as shown in Figure 5.2. The error on the secondary observable can again be computed with the standard deviation.
To suppress autocorrelation effects one can also use a blocked bootstrapping. This means that a blocking procedure is applied to the data. The resulting mean values of the blocks are than sampled using the bootstrapping procedure [116].

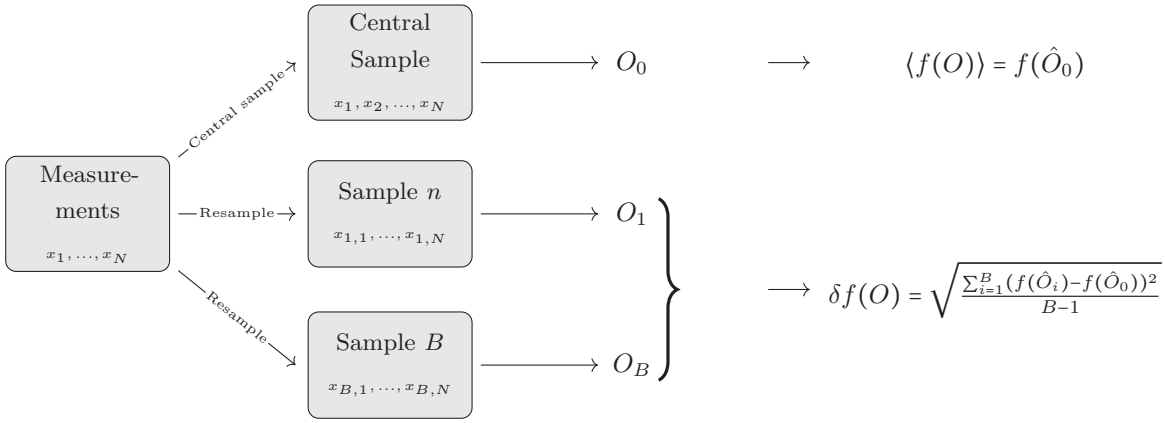

Figure 5.2 Visualization of bootstrap resampling.

5.1.3 Jackknife resampling

An alternative to the bootstrapping method is the Jackknife resampling, which is often referred to as "linearized bootstrapping". The Jackknife samples are constructed in the following way: To construct the first sample all measurements except for the first one are averaged, for the second sample all measurements except for the second are averaged and so on. Again on each Jackknife sample (and of course on the central sample), one can evaluate secondary observables $f(O)$. The value of the central sample can again be taken as the central value of the observable while the error can be computed from the standard deviation of the J Jackknife samples according to Figure 5.3 [117, 118].
Similar to the Bootstrapping procedure one can include a blocking procedure before computing the Jackknife samples to handle autocorrelation effects. This also the method that is used in the papers the second part of this thesis is based on [20, 26, 119, 120].

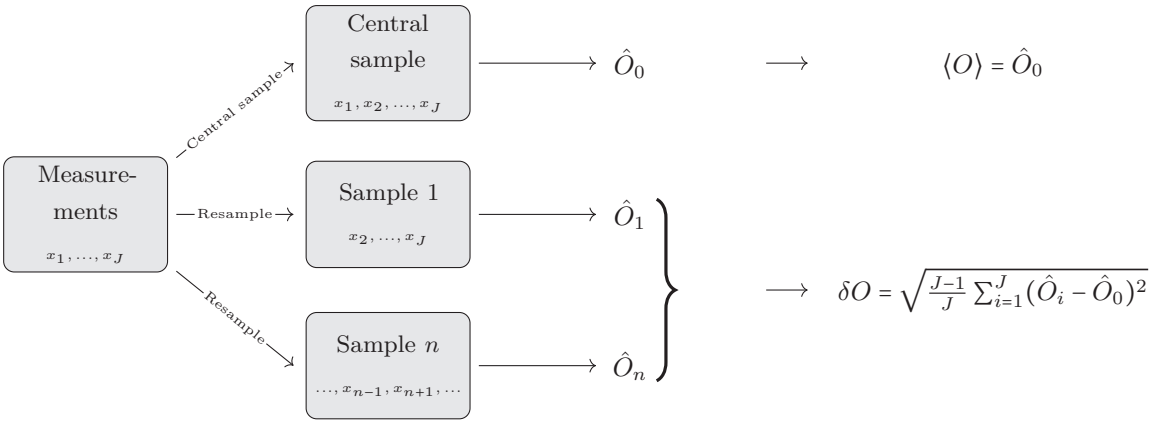

Figure 5.3 Visualization of Jackknife resampling.

5.2 Treating of systematic uncertainties

In the context of lattice gauge theory systematic errors are the uncertainties that do not originate form the Monte-Carlo evaluation of the path integral. Typically they are of the same order of magnitude than the statistical error [19, 20, 26]. Systematic errors can have different origins. Typically one of most dominant error sources is the choice of different fitting methods and models. Fits are used to extrapolate the data to the continuum and the physical point (at which the simulation parameters take the physical values), but they also can be used to estimate the energies from correlation functions. In general, one does not know the correct model or method so a variety of different forms is used and the corresponding systematic error is estimated from the width of the resulting distribution.
Another dominant source of systematic errors is the setting of the scale and the physical point. Typically, a set of physical observables is computed in the lattice simulation and then fitted to the experimental (or physical) value of the corresponding observable. Of course every uncertainty in the physical value translates in an uncertainty in the final result. So what one typically does it to perform the analysis not using the exact physical value, but with the upper and lower 1σ-deviations. From the spread of the two results, the corresponding systematic error can be estimated [19].
Lattice computations are always done in a finite volume, so there are finite volume effects that have to be accounted for. Fortunately, the finite volume effects are often small enough that a conservative estimation of the error associated to the finite volume correction does not dominate the overall error of the analysis. Of course, there are even more sources of systematic uncertainties like the strong-isospin breaking effect, or effects from other interactions like QED.

5.3 Fitting procedure

A fit is a method to tune the parameters of a mathematical model in such a way that it aligns with the data from an experiment or a simulation. Usually fitting is done by minimizing some quantity for example the likelihood or the χ^2.
Independent variables, for example lattice spacing a (in case of continuum extrapolations) or Euclidean time t (in case of mass/energy plateaus) will be labeled by x_i within this section. Dependent variables (observables such as masses or decay constants) are labeled by y_i. The fit models are given by function f_i (mostly polynomials or exponential functions in x) and the corresponding parameters that have to be tuned are called c_i.

5.3.1 χ^2

The standard way to fit a model to a set of measurements is the minimization of the χ^2. For a proper definition we need to generalize the concept of the variance mentioned in equation (5.2): The covariance matrix of a set of statistical data y_i is given by

$$\mathrm{Cov}_{ij} = \frac{N}{N-1} \sum_{i=1}^{N} \overline{(y_i - \overline{y_i})\,(y_j - \overline{y_j})}. \tag{5.8}$$

The ith diagonal element is given by variance of the quantity y_i. The off-diagonal element (ij) of Cov describes how the statistical fluctuation of y_i affect the statistical fluctuation of y_j. In some contexts it might be also useful to remove the statistical fluctuation from this expression and only to look at the statistical correlations of certain observables. Therefore, one can define correlation matrix [116, 121]

$$\mathrm{Cor}_{jk} = \frac{\mathrm{Cov}_{jk}}{\sigma_i \sigma_j} \tag{5.9}$$

by normalizing the covariance matrix with the standard deviation of the corresponding line and column. If one explicitly wants to ignore all effects originating of correlation effects, one can set all off-diagonal elements to 0 and receives

$$\Sigma_{ij} = \sigma_i^2 \delta_{ij}. \tag{5.10}$$

In this case, the correlation matrix will given by $\mathrm{Cor}_{ij} = \delta_{ij}$. To fit a model f depending on parameters $c = (c_i)_i$ and independent variables $x = (x_i)_i$ to a set of dependent variables $y = (y_i)_i$, one minimizes the χ^2 of the model and the data set. Generally spoken, the χ^2 is the relative squared difference of the model and the dependent variables. Mathematically spoken, the correlated χ^2 is given by [116, 121]

$$\chi^2_{\mathrm{corr}}(c) = \sum_i (y_i - f(x_i, c))\mathrm{Cor}^{-1}_{ij}(y_j - f(x_j, c)). \tag{5.11}$$

Furthermore, the uncorrelated χ^2 can be defined by letting out the off-diagonal elements in the covariance matrix [121]:

$$\chi^2_{\mathrm{uncorr}} = (y_i - f(x_i))\Sigma^{-1}_{ij}(y_j - f(x_j)) \tag{5.12}$$

Using standard optimizers one can tune the parameters c_i such that the corresponding χ^2 is minimized. Assuming y_i is chosen from the distribution $\mathcal{N}(f(x_i, c), \sigma_{y_i})$ the χ^2 is distributed as the sum of squares of standard normal distributed random variables. The resulting distribution is therefore called the χ^2-distribution, which is given by

$$p_n^{\chi^2}(x) = \frac{2^{-\frac{n}{2}}}{\Gamma\left(\frac{n}{2}\right)} x^{\frac{n}{2}-1} \exp\left(-\frac{x}{2}\right). \tag{5.13}$$

Here, Γ denotes the Gamma function that generalizes the factorial to the complex plane. Within this context n is often referred to the reduced number of degrees of freedom, which is given by the difference of the number independent variables n_{fit} and the number of parameters n_{param}. Also the expectation value of $p_n^{\chi^2}$ is given by n. Therefore, often the reduced chi-squared $\frac{\chi^2}{n}$ is used, whose expectation value is one. This can be used for a quick check if the fitting procedure is properly or if the model or the set of variables have to be adjusted. When dealing with correlated fits another issue occurs: The covariance matrix is made from a (comparatively small) set of Jackknife samples and therefore might be ill-conditioned, which means that condition number,

i.e., the ratio of smallest and largest eigenvalue of the covariance matrix is large in some sense. So there might be small modes, that are nothing but noise, which dominate the χ^2 due to the inversion of the covariance matrix. Usually there are two simple ways to deal with this problem: First, one can reduce n_{fit}. Since the covariance matrix is a $n_{\text{fit}} \times n_{\text{fit}}$ matrix, there are less modes and the covariance matrix can be estimated properly even with a small set of samples. Of course, the removal of some of the data points has to be justified in some way. For example in a plateau fit (which can be used to measure mass states) the points that go in to the fit should be equally distributed along the fitting window.
Furthermore, one can also perform a regularization on the covariance matrix. Basically, this is nothing else than moving the smallest eigenvalues up to a certain bound. In detail, one has to compute the singular value decomposition (SVD) of the covariance matrix

$$\text{Cov} = U\alpha V \tag{5.14}$$

where U and V are unitary matrices and α is a real diagonal matrix, whose diagonal elements are called $(\alpha_i)_{i=1,\ldots,n_{\text{fit}}}$ with $\alpha_i > \alpha_{i+1}$. A minimal value for the singular values $\alpha_{\min}$ is set, for example $\alpha_{\min} = 10^{-8}\alpha_1$. Whenever a singular value α_i is smaller than $\alpha_{\min}$ or smaller than twice its statistical error it is replaced by α_{i-1}, otherwise it is simply replaced by $|\alpha_i|$. Note, that it is important to proceed in increasing order in i to get fully correct results. Finally, the tweaked singular values are inverted and the singular value decomposition is inverted. Since the smallest modes are removed, noise will not dominate the χ^2 of the correlated fits. A big advantage compared to the first method is that none of the data points has to be removed, which will give a more reliable result [122, 123].

5.3.2 Evidence for the quality of fits

Of course, fits can have different qualities. A set of data points with a strong curvature cannot be described properly with a straight line. On the other hand, fitting data that are within errors on a straight line with a high-order polynomial can introduce unwanted high deviations in the extrapolation regime (over-fitting). Thus, there are indeed fits with different qualities. However, some methods are needed to quantify the quality of a fit. As mentioned before the expectation value of the χ^2-distribution is expected to be equal to the number of degrees of freedom, but the quantity χ^2/n is not a good parameter to describe the quality. For example this quantity tends to overvalue fits with too many parameters. But fortunately there are better alternatives.

Kolmogorow-Smirnow test

The Kolmogorow-Smirnow (KS) test is a parameter free check to test if a cumulative probability density function F_0 is consistent with a discrete test sample $\{X_i\}_{i=1..n}$. To perform a KS test, an empirical distribution function

$$\tilde{F}_n(x) = \frac{1}{n}\sum_{i=1}^{n}\theta(X_i - x) \tag{5.15}$$

is defined. The null-hypothesis states that F_0 is the correct function to describe the distribution of the X_i. The supremum of the differences of F_0 and the empirical distribution function

$$D_n = \sup_{x\in\mathbb{R}} |\tilde{F}_n(x) - F_0(x)| \tag{5.16}$$

is called the KS-statistic. For a given significancy value α, the hypothesis is accepted if the KS-statistic is smaller than

$$d_\alpha = \sqrt{\frac{-\frac{1}{2}\log\frac{\alpha}{2}}{n}}, \tag{5.17}$$

which is a useful approximation of the cumulated Kolmogorow distribution.
d_α also serves as the probability density function of the empirical distribution function. Also, one-sided KS-tests can be defined in order to test if the empirical distribution function is above

$$D_n^u = \sup_{x\in\mathbb{R}} |\tilde{F}_n(x) - F_0(x)| \times \theta(\tilde{F}_n(x) - F_0(x)) \tag{5.18}$$

or below

$$D_n^l = \sup_{x\in\mathbb{R}} |\tilde{F}_n(x) - F_0(x)| \times \theta(F_0(x) - \tilde{F}_n(x)) \tag{5.19}$$

the distributions function from the null-hypothesis.

P-value

The P-value is a measure used in statistics to quantify the strength of evidence against a null hypothesis. It indicates how likely it is that the observed data (or even more extreme data) occurs given the null hypothesis. A low P-value means that the observed data is unlikely under the null hypothesis, which calls the null hypothesis into question. The P-value is a number between zero and one. Typically one chooses a lower bound from which the fits are trusted [124, 125].
The most common example is the P-value according to the χ^2-distribution of a fit. It tells how likely it is that another fit with the same degrees of freedom is worse than the fit from the null-hypothesis. In practice this means that one has to compute the value of the cumulative distribution function of the $p_n^{\chi^2}$ probability density at the χ^2 of the null-hypothesis. So the P-value (for the χ^2-distribution) can be computed by dividing the incomplete Γ-function with argument $\frac{n}{2}$ and $\frac{\chi^2}{2}$ divided by $\Gamma\left(\frac{n}{2}\right)$:

$$P(n,\chi^2) = \frac{\Gamma\left(\frac{n}{2},\frac{\chi^2}{2}\right)}{\Gamma\left(\frac{n}{2}\right)} = \frac{\int_{\chi^2/2}^{\infty} \mathrm{d}t\, t^{\frac{n}{2}-1}e^{-t}}{\int_0^{\infty} \mathrm{d}t\, t^{\frac{n}{2}-1}e^{-t}} \tag{5.20}$$

Q-value

Bruno and Sommer suggested not to use the P-value to estimate the quality of a fit but to replace Equation (5.20) by another one [121]. Usually the name Q-value is also used for what I call the P-value. Within in this thesis, I will use the Bruno/Sommer definition

$$Q(\nu,\chi^2) = \int \mathrm{d}^{n_{\text{data}}} y\, p(y)\theta\left(\chi^2(y) - \chi^2\right), \tag{5.21}$$

$$p(y) = \frac{\exp\left(-\frac{1}{2}\chi^2(y)\right)}{\sqrt{(2\pi)^{n_{\text{data}}}\det C}}, \tag{5.22}$$

where $\chi^2(y)$ is the (not optimized) χ^2 for the data y compared to the optimized fit and C is the covariance matrix of the given data. Using substitutions this can be reformulated to

$$Q = \int \mathrm{d}^{n_{\text{data}}} z\, (2\pi)^{-\frac{n_{\text{data}}}{2}} \exp\left(-\frac{1}{2}\|z\|^2\right) \times \theta\left(z^T\cdot\nu\cdot z - \chi^2\right), \tag{5.23}$$

where ν is a symmetric positive definite matrix, that is defined by

$$\nu = C^{1/2} W (1 - \mathcal{P}) W C^{1/2}, \tag{5.24}$$

with W^2 being either the covariance matrix (in case of correlated fits) or the matrix with the inverse squared errors on the diagonal (in case of uncorrelated fits). $\mathcal{P}$ is the projection on the n_{fit} dimensional subspace that is spanned by the image of W. It was mentioned before that non-positive eigenvalues of the (measured) correlation matrix can appear, due to noise in the Jackknife estimation. So if λ_i $(i = 1...n_\nu \leq n = n_{\text{data}} - n_{\text{fit}})$ are the positive eigenvalues of ν the Q-value can be given as [121]

$$Q(\chi^2, \nu) = \int \left(\prod_{i=1}^{n_\nu} \frac{\mathrm{d}z_i \, e^{-\frac{1}{2} z_i^2}}{\sqrt{2\pi}} \right) \times \theta \left(\sum_{j=1}^{n_\nu} \lambda_j z_j^2 - \chi^2 \right). \tag{5.25}$$

In general it is not possible to compute the Q-value analytically but a Monte-Carlo evaluation of the integral with $\mathcal{O}(10^5)$ evaluation is precise enough to give a good estimator for the Q-value.

Akaike-Information criterion (AIC)

Usually, a lot of different fit models is used to describe the data from the simulation. Of course one could use the model with the best P/Q-value for the final result. But it is still possible that the best model is wrong. So a better approach is to sample a lot of different function and compute their mean value using weights that respect the quality of the fit in some way. Akaike came up with the following approach [126]: A fit through n_{data} data points with n_{fit} fit parameters and an optimized χ^2, has a weight of

$$w = \mathcal{N} \exp\left(-\frac{\chi^2}{2} - n_{\text{fit}} + n_{\text{data}} \right). \tag{5.26}$$

The normalization factor $\mathcal{N}$ is chosen such that the sum of all weights is equal to one. In [19] it was suggested to modify this weight by replacing n_{fit} by $\frac{n_{\text{fit}}}{2}$ so that the overall weight is given by

$$w = \mathcal{N} \exp\left(-\frac{\chi^2 + n_{\text{fits}} - 2n_{\text{data}}}{2} \right). \tag{5.27}$$

With this approach, fit models with many parameters are suppressed. This prevents from including models that suffer from over-fitting.

5.4 Statistical and systematic covariances

It is not trivial to compute systematic and statistical errors (and covariances) from the data. As mentioned in the previous sections, N_s different systematics are assigned to the corresponding weights and the statistical effects are considered using N_J blocked Jackknife samples and the central sample. To compute the total error and in addition separate it into its statistical and systematic contribution, the following approach was suggested in [19]: For each systematic $s = 1...N_s$, the statistical contribution is approximated by a Gaussian function with the mean value μ_s taken from the central sample and the width σ_s calculated from the Jackknife samples. All of these Gaussian functions are added using their respective weights. Since this might be impractical for a large amount of systematics, the Gaussian functions are put in a histogram. This new total histogram again has a mean μ_{tot} and a width σ_{tot}. The variance σ_{tot}^2 is the sum of the variance of the systematics σ_{sys}^2 and the statistical variance σ_{stat}^2. To figure out how the total variance is divided into these two values, the procedure is repeated by using $\sqrt{\lambda}\sigma_s$ as the width for the different systematics. The

resulting width of the histogram is called $\sigma^2_{\text{tot},\lambda}$. Then, the following system of linear equations can be solved:

$$\begin{aligned} \sigma^2_{\text{sys}} + \sigma^2_{\text{stat}} &= \sigma^2_{\text{tot}} \\ \sigma^2_{\text{sys}} + \lambda\sigma^2_{\text{stat}} &= \sigma^2_{\text{tot},\lambda} \end{aligned}, \tag{5.28}$$

The total variances and λ are known so the system can be solved for the statistical and systematic variances [19]. It is also interesting to compute statistical and systematic covariances of two observables. Of course one could fill a two dimensional histogram instead of a one dimensional one, but from experience one can know that this gets expensive in terms of computation effort because the overall number of bins can easily exceed a million if for the one dimensional case a few thousands are used. But luckily there is an easy formula to compute the covariance of two observables

$$\text{cov}(Y_1, Y_2) = \frac{1}{2}\left(\sigma^2_{Y_1+Y_2} - \sigma^2_{Y_1} - \sigma^2_{Y_2}\right). \tag{5.29}$$

Thus, if the variances of Y_1 and Y_2 are already known the covariance can be calculated with the same computational costs as the variances [127]. The remaining problem is the computation of the variance of $Y_1 + Y_2$. If both of the quantities come from the same fit and therefore are associated to the same weights, it is very easy. For each systematic s, one chooses $(Y_1 + Y_2)_s = Y_{1\,s} + Y_{2\,s}$ for all statistical samples and the weights w_s. But if both quantities have completely unrelated systematics, a different approach is needed. For example, one can draw a systematic s_1 for Y_1 according to the weights $\{w^1_s\}$ of the systematics of Y_1. The same is done for Y_2 and then $Y_{1\,s_1} + Y_{2\,s_2}$ is included in the histogram with the weight one. This procedure has to be repeated a certain amount of times D. D can be estimated by setting $Y_2 = Y_1$. Then it can be checked for which value of D the desired precision is reached, i.e., if the result is compatible with the variance from the standard procedure. If the two observables share some (flat-weighted) systematics that are aligned to an external input like different choices of a scale setting variable one can respect this correlation in the following way: Let us call these systematics s' and the remaining s''_1 resp. s''_2 . Due to the flat-weighting, all systematics s' have the same weight. Then it is looped over s' for both observables parallel and from the other observables s''_1 and s''_2 it is chosen according to the weight. Th Gaussian functions in the histogram are weighted with one.

5.5 Generalized Eigenvalue problems

In lattice QCD, a correlation function of an operator O takes the form

$$C_O(t) = \sum_i |a^O_i|^2 \exp\left(-E^O_i t\right), \tag{5.30}$$

where $E^O_0 < E^O_1 < E^O_2 ...$ are the different energies contributing the operator [35, 37]. In many cases all states above the ground state[1] are exponentially suppressed after a certain time t_{min} so that for $t > t_{\text{min}}$ it can be assumed that the correlation function only consists of the ground state's exponential function. But this is not always the case and the following problem can appear: The coefficients of the lowest energy states can be very small which will lead to the problem that t_{min} is very large. Therefore, it might already be in a region where the signal-to-noise ratio is too bad to get the desired precision. This can be the case if the vector-correlator, which has small contributions from some two-pion systems that can have lower energies than the mass of the vector correlator [119, 128] is considered.
Luckily, there is a general strategy to solve this problem. To resolve N_E different energy states, one needs N_E operators with this energy states but contributions of different strengths. Basically this means that we look for

[1] The ground state is the state with the lowest energy, i.e., $i = 0$.

a set of operators $\{O_j\}_{j=1\ldots N_E}$ that have the same quantum numbers. Now, not only the correlation functions $C_j(t) = \langle O_j^\dagger(t) O_j(0)\rangle$ have to be measured but also the cross-correlation functions $C_{jk}(t) = \langle O_j^\dagger(t) O_k(0)\rangle$ [129]. Thus, the correlation function $C = \{C^{jk}\}_{j,k=1\ldots N_E}$ with

$$C^{jk}(t) = \sum_i (a_i^j)^* a_i^k \exp(-E_i t) \tag{5.31}$$

can be used to extract the modes $\exp(-E_i t)$ using a Generalized Eigenvalue Problem (GEVP). Now a parameter t_0 is fixed in order to have

$$C^{jk}(t) = \sum_i \underbrace{\left[(a_i^j)^* a_i^k \exp(-E_i t_0)\right]}_{B_i = \{b_i^{jk}\}_{jk}} \times \exp(-E_i(t - t_0)). \tag{5.32}$$

Each matrix B_l is constructed to be the outer product of a vector a_l with itself. Therefore, it is Hermitian with rank one, and thus it has only one eigenvector v_l with a non-zero eigenvalue. This eigenvector is given by $(v_l)^m = a_l^m$. It cannot be assumed that the vectors $\{v_l\}$ build an orthogonal system, but we can generally expect that $v_l^\dagger v_k$ is small compared to $v_l^\dagger v_l$ if $k \neq l$. Thus, the multiplication of $C(t)$ with v_l can be approximated in the following way [130, 131]:

$$C(t) \cdot v_l \approx B_l \cdot v_l \times \exp(-E_l(t - t_0)), \tag{5.33}$$

or, as it is written usually:

$$C(t) v_l \approx \lambda_l(t, t_0) C(t_0) v_l, \tag{5.34}$$

$$\lambda(t, t_0) = \exp(-E_l(t - t_0)). \tag{5.35}$$

A GEVP can be solved by computing the eigenvalues and eigenvectors of $C(t_0)^{-1} \cdot C(t)$. To extract the functions $\lambda_l(t, t_0)$ for a fixed t_0 one could solve the GEVP for all t. However, the apparent order of the eigenvalues λ_l may differ from the true order due to statistical fluctuations and systematic errors (from the approximation in Equation (5.33)). Therefore, it is better to extract the eigenvectors v_l for one specific choice of t_0 and t, and then compute the eigenvalues via

$$\lambda_l(t, t_0) = v_l^\dagger \cdot C(t) \cdot v_l. \tag{5.36}$$

Part II

Application to Standard Model Tests

6 Lattice techniques

In this chapter, I provide an overview of the lattice methods and techniques employed throughout this thesis. Particular attention is given to the basic properties of our newly generated finest ensembles. In addition, the extraction of energies and decay constants from correlation functions is explained. Furthermore, I present an overview of finite-volume effects, QED corrections, and strong isospin-breaking contributions.

6.1 Action and ensembles

Gauge configurations are generated using a Symanzik improved [50] `4stout` [101] one-link staggered action. In total, there are 31 different isospin-symmetric ensembles at eight different lattice spacings. The masses are scattered around the physical point, as shown in Figure 6.1. For the sea quark contributions, an additional ensemble generated with the `4HEX` staggered action [100] and the DBW2 gauge action [51] is used. A big advantage of the `4HEX` action compared to the `4stout` action is that the taste breaking is much smaller, which also reduces the associated discretization effects. However, simulations with the `4HEX` action are more likely to suffer from topological freezing at fine lattice spacings [77]. In Table 6.1 all of the isospin symmetric `4stout` ensembles are listed. The lattice spacing a and the geometric extension given by L and T are chosen such that the physical extension of the lattice is $\sim (6^3 \times 9)\,\mathrm{fm}^4$ for all of the ensembles. The charm quark mass is not given in this table, however, it is set to 11.85 times the mass of the strange quark [19, 20, 133, 134]. Statistical errors are estimated with a blocked Jackknife procedure [112] with 48 bins (see Section 5.1.3). Of course, it has to be checked that the autocorrelation of the observables is small enough, such that the corresponding autocorrelation time is smaller than the block size. Otherwise the bins might be correlated and the overall error will be underestimated. One expects autocorrelation to be stronger on finer lattices [77], so it is sufficient to check the autocorrelation time on the finest ensemble ($\beta = 4.3032$). The time series of the topological charge is shown in Figure 6.2 while the autocorrelation function and time of the pion and kaon decay constants, the squared topological charge and the Wilson-flow based w_0 and t_0 scales can be seen in Figure 6.3. The worst autocorrelation, that is observed, is the one from the squared topological charge, the decay constants have a significant smaller autocorrelation time. Thus, it is only necessary to check whether the autocorrelation time of the squared topological charge is smaller than the block size on the finest ensemble. This condition is satisfied for all ensembles except one at $\beta = 4.3032$, which has a relatively small number of trajectories, as shown in Table 6.1. Nevertheless, the autocorrelation time of the observables of interest (decay constants and gradient-flow based scales) is significant smaller. Thus, we do not have to take care of autocorrelation effects after the blocking procedure. The scaling of the autocorrelation time of w_0 is also considered, and it is shown that the critical scaling is proportional to a^2 (see Figure 6.4). The topological susceptibility approaches, in the continuum limit, the value reported in [135]. As already mentioned in Chapter 3 different tastes come along with different hadron masses, so the pions get heavier the more the locality of the spin-taste operator is violated. In the $SU(4)$-taste-symmetry group the tastes can be labeled according $\{P, A, T, V, S\}$, which are the abbreviations for pseudo-scalar, axial-vector, tensor, vector and scalar. In combination with the pseudo-scalar spin-structure this refers to a non-locality of the spin-taste operator by 0,1,2,3 or 4 dimensions. The local operator (pseudo-scalar spin and taste structure) is the lightest and called the Goldstone taste. The mass parameters are chosen such that the masses of these mesons bracket the physical point in Figure 6.1. The taste breaking effects are quantified by

$$\begin{aligned} \Delta_{KS}(\xi) &= M_\pi^2(\xi) - M_\pi^2(P), \\ \delta_{KS}(\xi) &= 2\left(M_\eta^2 - M_\pi^2 - \Delta_{KS}(\xi)\right). \end{aligned} \tag{6.1}$$

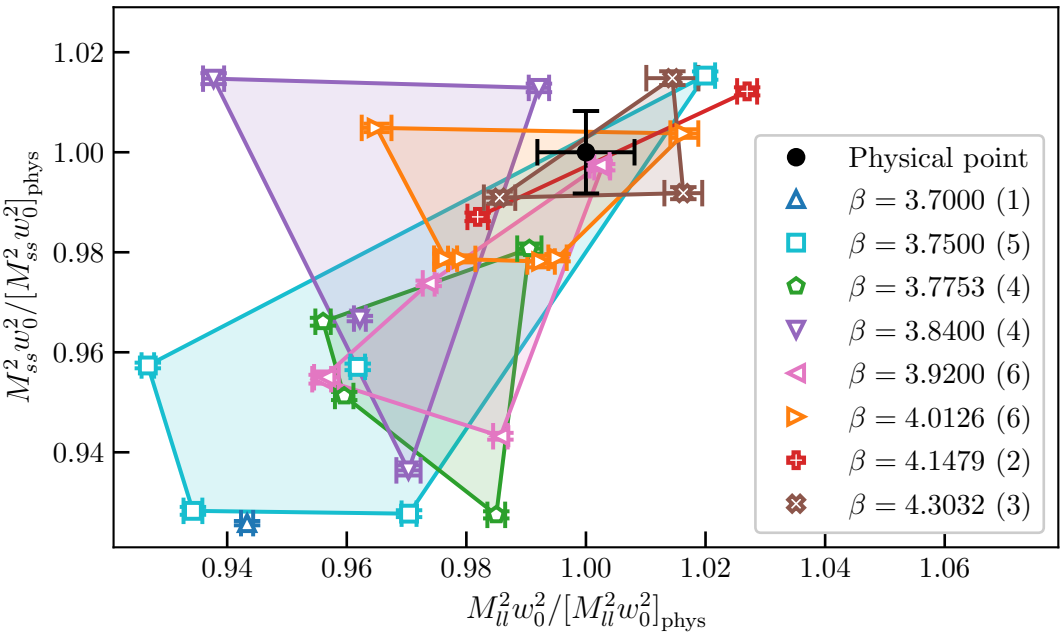

Figure 6.1 Landscape plots of the ensembles used in this study. The pseudo-scalar masses M_{ll} and M_{ss} are given in units of the w_0-scale normalized to their physical value. Each lattice spacing is aligned with a different color and the black point marks the physical point in the isospin-symmetric limit. The errorbars on the physical point originate from uncertainties on the physical values of the pseudo-scalar masses and the w_0-scale. Similar figures are shown in [20, 132].

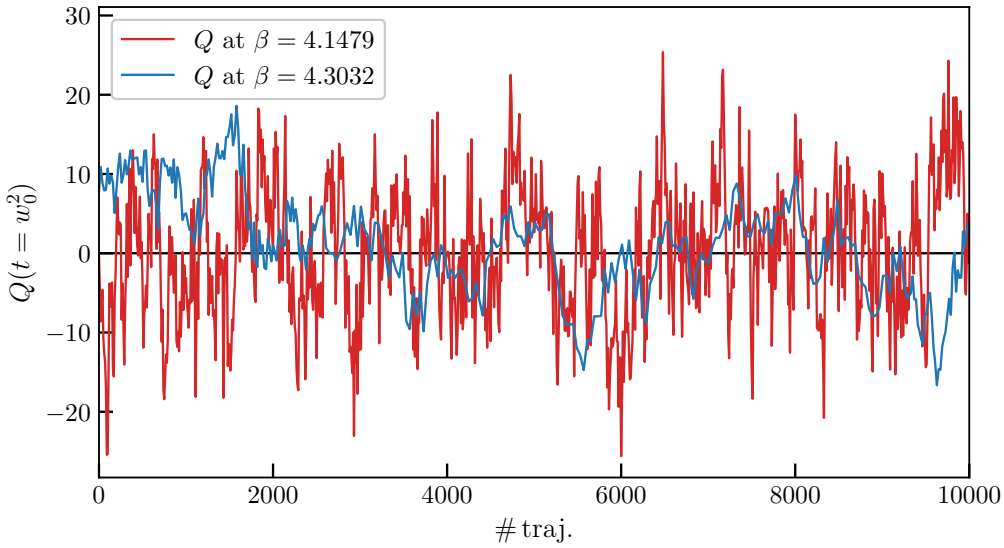

Figure 6.2 Time series of the topological charge for ensembles with the finest and second finest lattice spacings. The latter ("Monster") is discussed in detail in our recent publication [20], while the (new) finest ensemble first appears in [26]. Therefore, some details are investigated in this work.

β	a [fm]	$L \times T$	am_s	m_s/m_l	#confs	SIB
3.7000	0.1315	48×64	0.057291	27.899	904	$\surd$
3.7500	0.1191	56×96	0.049593	28.038	315	
			0.049593	26.939	516	$\surd$
			0.051617	29.183	504	$\surd$
			0.051617	28.038	522	
			0.055666	28.083	215	
3.7753	0.1116	56×84	0.047615	27.843	510	$\surd$
			0.048567	28.400	505	
			0.046186	26.469	507	$\surd$
			0.049520	27.852	385	
3.8400	0.0952	64×96	0.043194	28.500	510	$\surd$
			0.043194	30.205	436	
			0.040750	28.007	1503	
			0.049520	27.852	500	$\surd$
3.9200	0.0787	80×128	0.032440	27.679	506	
			0.034240	27.502	512	$\surd$
			0.032000	26.512	1001	
			0.032440	27.679	327	
			0.033286	27.738	1450	$\surd$
			0.034240	27.502	500	
4.0126	0.0640	96×144	0.026500	27.634	446	
			0.026500	27.124	551	$\surd$
			0.026500	27.634	2248	
			0.026500	27.124	1000	
			0.027318	27.263	985	
			0.027318	28.695	1750	
4.1479	0.0483	128×192	0.019370	27.630	1155	
			0.019951	27.104	1605	
4.3032	0.036	176×264	0.013751	27.630	857	
			0.014026	27.362	267	
			0.013751	26.825	841	

Table 6.1 Ensembles used in this study. We also give the spacing, volume and mass parameters according to the ensembles. Ensembles that are also used for strong-isospin-breaking (SIB) simulations are marked with a tick($\surd$). Further explanations on the SIB are given in Section 6.5.

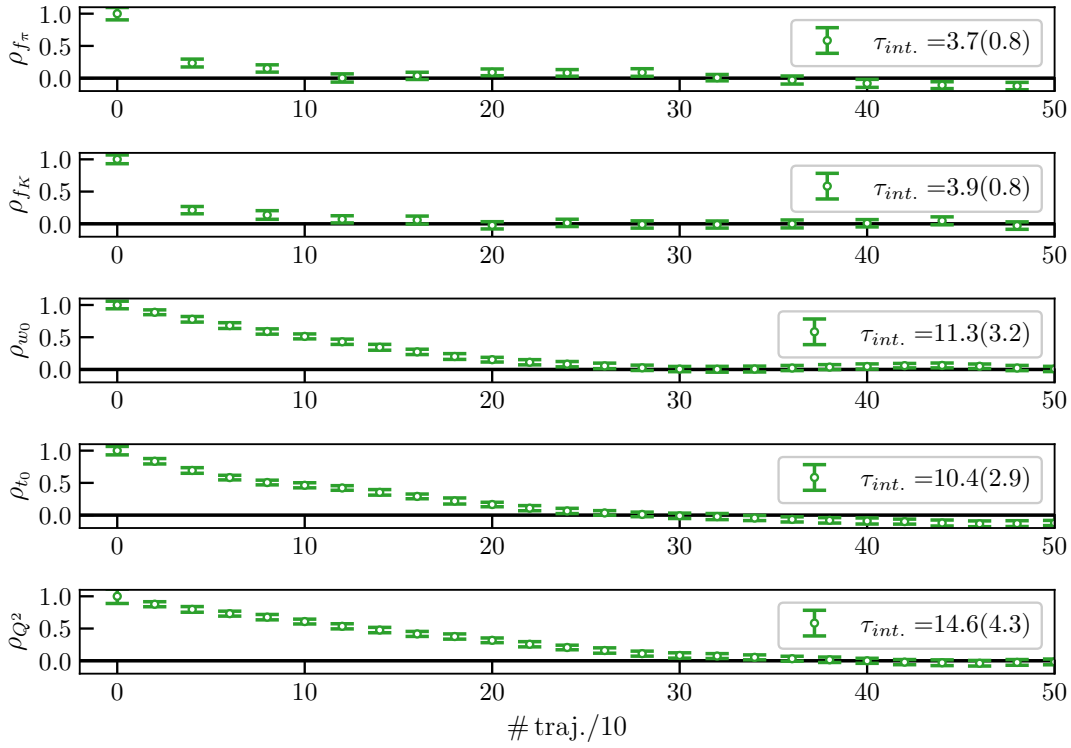

Figure 6.3 Autocorrelation functions of the kaon and pion decay constant and of the squared topological charge. The autocorrelation function and time are estimated with methods explained in [109, 110]. Even though the x-axis is given in units of trajectories of the HMC-algorithm, the ACT is given in units of measurements which is one twentieth of ACT in units of trajectories.

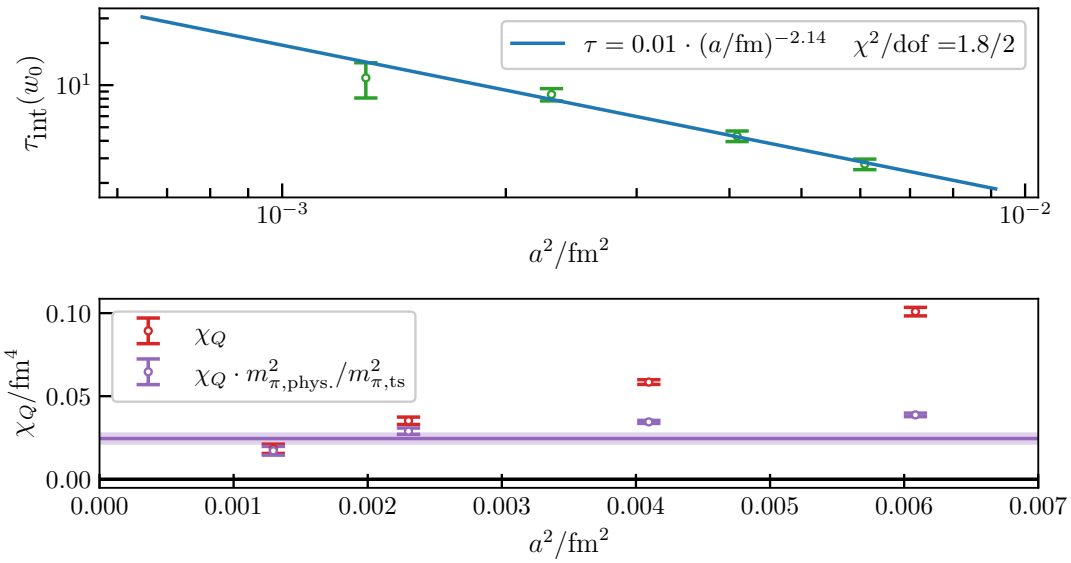

Figure 6.4 Lattice spacing dependency of the w_0-scale autocorrelation time and the topological susceptibility. The autocorrelation time of w_0 scales approximately with $1/a^2$, while the topological susceptibility approaches the limit that was estimated in [135]. After dividing out the taste-splitting of the taste-singlet pion mass [136] the topological susceptibility is very flat in terms of the lattice spacing.

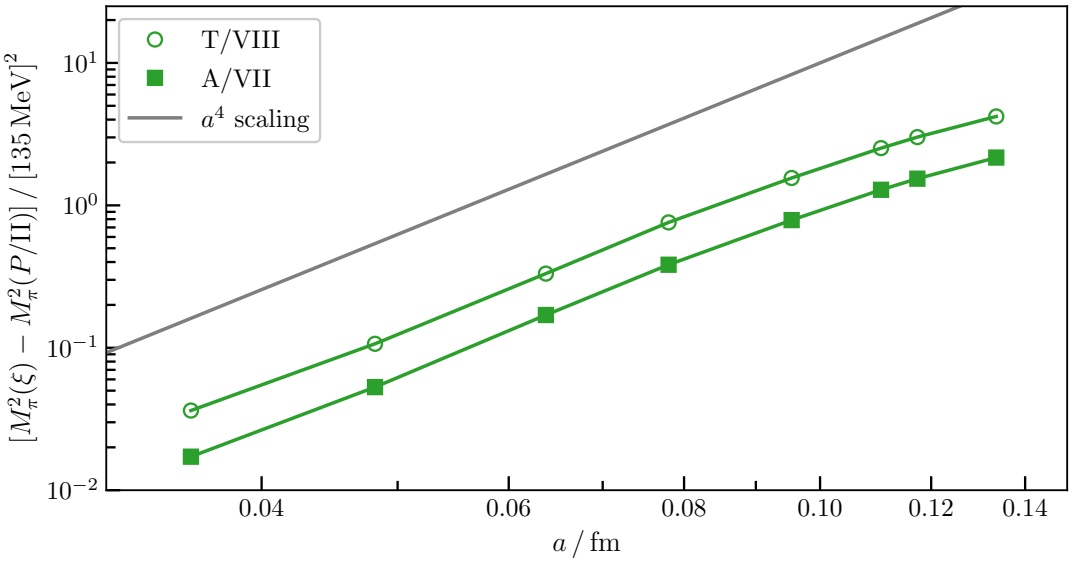

Figure 6.5 The taste-violation Δ_{KS} of two different tastes, the line shows an exact a^4 scaling. The Roman number labeling is done according to [137].

Here ξ denotes the different tastes (P,A,T,V or S), the η-meson is the meson corresponding to the λ_8-element of the eight dimensional irrep of the $SU(3)_F$, i.e.,

$$\eta = \frac{u\bar{u} + d\bar{d} - 2s\bar{s}}{\sqrt{6}}. \tag{6.2}$$

The taste splitting Δ_{KS} is expected to scale proportional to $a^2\alpha_s(1/a)^3$ as already discussed in [20]. In this study it is also shown that this behavior is somewhat similar to an a^4 scaling, which is also true for the (new) finest ensemble as it can be seen in Figure 6.5.

6.2 Gradient flow based scale setting

In Section 4.4.1 I already mentioned the scale t_0 that is defined using the gradient flow, more specific the Wilson flow, by figuring out the flow-time zero at which the equation $T(t_0) = 0.3$ with $T(t) = t^2E(t)$ holds [93, 94]. t_0 has a mass dimension of -1 and can be used to set the lattice spacing (the scale) according to

$$a = \sqrt{\frac{t_0^{\mathrm{phys}}}{t_0}} \tag{6.3}$$

with t_0^{phys} being $0.14292(104)\,\mathrm{fm}$ for $N_f = 2+1+1$ and $0.14474(57)\,\mathrm{fm}$ for $N_f = 2+1$. The values are averages from estimations of different collaborations. The averaging procedure was performed by the Flavor Lattice Averaging Group (FLAG) [138]. In 2012 the BMW collaboration suggested to use an alternative to t_0 which they called the w_0 scale. It is defined similarly to the t_0 scale, but this uses the value of $T(t)$ with t being the flow time, the w_0 scale is defined as [139].

$$\left\langle t\frac{\mathrm{d}}{\mathrm{d}t}\left[t^2E(t)\right]|_{t=w_0^2}\right\rangle = 0.3. \tag{6.4}$$

In the original publication, the following reason for this proposal was given: The old function $t^2E(t)$ depends only on energy scales larger than $\frac{1}{\sqrt{t}}$, i.e., if effects from small values of t appear that affect $T(t)$, one

will find this affects all larger values of t. The w_0 scale does not have this problem because it is defined locally. By including the derivative of the defining function $T(t)$, only effects around the energy scale $\frac{1}{\sqrt{t}}$ are considered [139]. In the first publication an $N_f = 2+1$ value for the w_0 scale was computed:

$$w_0^{\text{phys}} = 0.1755(18)(04)\,\text{fm} \tag{6.5}$$

Thus, the scale setting variable had an uncertainty of roughly one percent of its value. Current state-of-the art lattice computations on the other hand aim for even more precise results, so more accurate estimations for the scale setting variable are required.
Unfortunately, it is not that simple to compute a new physical value of w_0. Since it is a quantity with mass dimension -1 the continuum limit cannot be taken (in the limit $a \to 0$ the lattice quantity w_0 diverges). Before taking the continuum limit we need to construct a dimensionless quantity. Usually, this is done by multiplying w_0 by a quantity of mass dimension one, whose physical value can be measured from experiments. A good idea is to use a hadronic observable O where the non-QCD contributions are under control. The quantity then Ow_0 has a well-defined continuum limit, and w_0 can be determined by dividing by the physical value of O, with potential additional adjustments to account for QED effects or similar corrections, if necessary.
In general. two methods with different advantages are used. First, there is the mass of the Ω^--baryon that is known to a very high precision from experiments ($M_{\Omega^-} = 1672.45(29)\,\text{MeV}$ [43]). The downside is that the mass extraction of the Ω-baryon on the lattice is a demanding task. Second, there is the pion decay constant, f_π, that can be computed relatively easily from the pion correlator on the lattice. However, the physical value of the pion decay constant is somewhat problematic. While the pion decay width is known up to a very high precision ($2.5281(5) \times 10^{-14}\,\text{MeV}$ [140]), the radiative corrections play a significant role in the overall uncertainty. Additionally, there is the still unsolved puzzle of the CKM unitarity that might be related to a wrong estimation of $|V_{ud}|$, which is also a quantity that enters our w_0 computation if the pion decay constant is used.

6.3 Meson mass and decay constant on the lattice

The pseudo-scalar mesons on the lattice are already widely discussed in Chapter 3 and Section 6.1. In order not to have to deal with taste-breaking effects, we use Goldstone or pseudo-scalar taste for the meson operators.

$$P_{ab}(\vec{x},t) = \bar{\psi}_a(\vec{x},t)\,(\gamma_5 \otimes \xi_5)\,\psi_b(\vec{x},t) \tag{6.6}$$

Here a and b denote the flavor content of the quarks. They are either *light* (l) or *strange* (s) in most of the sections. Whenever strong-isospin-breaking is mentioned a and b refer to *up* (u), *down* (d) or *strange*. The correlator of the pseudo scalar is given by

$$G_{ab}(t) = \frac{a^3}{L^3} \sum_{\vec{x}} \langle P_{ab}(\vec{x},t) P^\dagger_{ab}(\vec{0},0)\rangle, \tag{6.7}$$

which can also be written as

$$G_{ab}(t) = \sum_{i=0}^{\infty} \left(a_i e^{-M_i t} + b_i (-)^t e^{-M_i' t} \right). \tag{6.8}$$

The second summand is called *parity partner oscillation* [62] and is only non-vanishing if the two quarks have a different mass. Thus, in our case the oscillation appears for the kaon but not for the pion. Since in the time direction periodic boundary conditions are employed one gets propagation in backwards time direction and

additionally contributions from the exponential modes that wind around the time interval N times:

$$G_{ab}(t) = \sum_{i=0}^{\infty}\sum_{N=0}^{\infty}\left[a_i\left(e^{-M_i(t+NT)} + e^{-M_i(T-t+NT)}\right) + b_i(-)^t\left(e^{-M_i'(t+NT)} + e^{-M_i'(T-t+NT)}\right)\right] \tag{6.9}$$

Here T is the time-extend of the lattice. One usually assumes that $M_i \gg M_0$ for $i \neq 0$, therefore, all those cases are exponentially suppressed and can be ignored, since their contribution is much smaller than the statistical noise from the evaluation of the path integral. Using the closed expression for the geometric series yields

$$G_{ab}(t) = a_0\frac{e^{-M_0 t} + e^{-M_0(T-t)}}{1-e^{-M_0 T}} + b_0(-)^t\frac{e^{-M_0' t} + e^{-M_0'(T-t)}}{1-e^{-M_0' T}} \tag{6.10}$$

$$= 2a_0\frac{\cosh(M_0(T/2-t))}{e^{M_0 T/2}(1-e^{-M_0 T})} + 2b_0(-)^t\frac{\cosh(M_0'(T/2-t))}{e^{M_0' T/2}(1-e^{-M_0' T})}. \tag{6.11}$$

Even for the kaon no parity partner oscillation could be observed in our data. It can be assumed that $M_0' - M_0$ is sufficiently large such that the parity partner oscillation is suppressed at the time windows considered in this study. The coefficient a_0 is related to the pseudo-scalar decay constant by

$$f_{ab} = 2(m_a + m_b)\sqrt{\frac{a_0}{M_0^3}} \Leftrightarrow a_0 = \frac{f_{ab}^2 M_0^3}{4(m_a+m_b)^2}. \tag{6.12}$$

Putting this into Equation (6.11) yields

$$G_{ab}(t) = \frac{f_{ab}^2 M_0^3}{2(m_a+m_b)^2}\frac{\cosh(M_0(T/2-t))}{e^{M_0 T/2}(1-e^{-M_0 T})}. \tag{6.13}$$

Here m_a and m_b are the quark mass parameters of the flavors a and b. It has to be noted that the definition of the decay constant is not unique but differs according to certain conventions. The prefactor 2 in Equation (6.12) can be replaced by factor of 1 or $\sqrt{2}$ depending on the physicist's choice. Nevertheless, this will not affect the ratio of kaon and pion decay constants as long as it is done consistently.
The pseudo-scalar correlator is measured using our standard random source technique (a further explanation is given in Section 10.2.2). From the correlator we extract the effective mass M_0 and the effective decay constant f_{ab} by using the following procedure: The mass is the curvature of the time dependence of the correlation function. It can be computed using the local mass extraction formula:

$$M^{\text{eff, loc}}(t) = \frac{1}{\Delta}\cosh^{-1}\frac{G(t+\Delta)+G(t-\Delta)}{2G(t)}, \tag{6.14}$$

where Δ is some quantity that is fixed in physical units. In this study we use two different values $\Delta \approx 0.2\,\text{fm}$ and $\Delta \approx 0.4\,\text{fm}$ to estimate the systematic errors from this discretization. Additionally, Δ is always chosen to be a multiple of $2a$ in order not to include artifacts from staggered oscillation.
Since it is also possible that our choice of the mass extraction formula includes a systematic bias, we also include another one, the midpoint mass extraction formula

$$M^{\text{eff, mid}}(t) = -\frac{1}{2\Delta}\left[\cosh^{-1}\frac{G(t+\Delta)}{G(T/2)} - \cosh^{-1}\frac{G(t-\Delta)}{G(T/2)}\right]. \tag{6.15}$$

An example of the effective mass according to the midpoint formula from Equation (6.15) can be seen in Figure 6.6 in the left panel. In this figure the effective mass is only shown for $1.2\,\text{fm} \leq t \leq 4.0\,\text{fm}$. In general, it can be expected that for smaller times the higher excited states from Equation (6.8) can be seen, therefore the effective mass does not build a plateau (within errorbars) for smaller t. For larger t the signal-to-noise

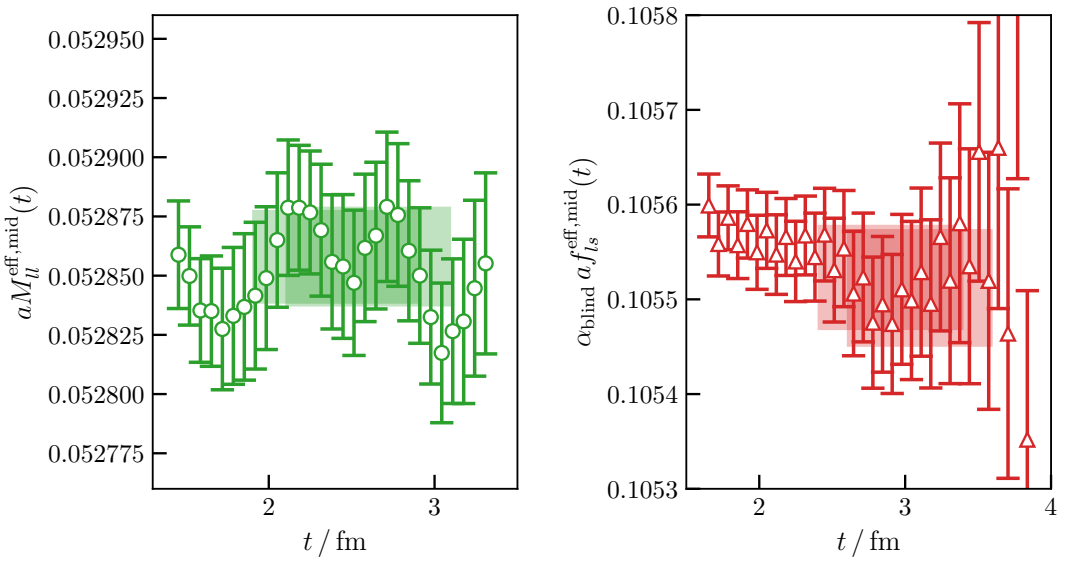

Figure 6.6 *Left panel:* Midpoint effective mass of the pion. The shaded regions denote the plateau windows that are chosen according to Figure 6.9. *Right panel:* effective decay constant of the kaon, the plateau windows are shifted by 0.5 fm according to the study in Figure 6.9. The correlation functions that belong to this data are measured on one of the ensembles with $\beta = 3.9200$.

ratio of the effective mass can decrease [141], Nevertheless, for the pion this problem is not as bad [142] as e.g. for the vector correlator [120] (see Chapter 10).
To get an expression for the effective decay constant we plug the effective mass into Equation (6.13) and solve for f to get

$$f_{ab}^{\text{eff}}(t) = \sqrt{\frac{2G_{ab}(t)(m_a+m_b)^2}{M_{ab}^{\text{eff}}(t)^3}\frac{e^{M_{ab}^{\text{eff}}(t)\frac{T}{2}}\left(1-e^{-M_{ab}^{\text{eff}}(t)T}\right)}{\cosh\left(M_{ab}^{\text{eff}}(t-\frac{T}{2})\right)}}. \tag{6.16}$$

An example for the effective decay constant of the kaon can be seen in the right panel of Figure 6.6. To extract a single value for the mass and decay constant respectively, one fits a plateau to the effective (time-dependent quantity) by minimizing either the uncorrelated or the correlated χ^2:

$$\chi^2_{\text{uncorr.}}(m) = \sum_{t=t_{\min}}^{t_{\max}} \left(\frac{m-y(t)}{\delta y(t)}\right)^2 \tag{6.17}$$

$$\chi^2_{\text{corr.}}(m) = \sum_{t^a=t_{\min}}^{t_{\max}} \sum_{t^b=t_{\min}}^{t_{\max}} (m-y(t_a))C^{-1}\left(y(t_a),y(t_b)\right)(m-y(t_b)) \tag{6.18}$$

Here $\delta y(t)$ is the standard error (Jackknife error in this study) of $y(t)$ and $C^{-1}\left(y(t_a),y(t_b)\right)$ is the inverse covariance matrix of y evaluated at $y(t_a)$ and $y(t_b)$. Usually, the correlated χ^2 is the more trustworthy quantity, because it respects the correlation of the effective mass/decay constant values at different time-slices. Nevertheless, there is a problem that was also found in lattice data by Ammer and Dürr in [143] and in experimental data [144]: The value for m from the minimization of the correlated χ^2 is outside the range of values it is fit to. This is most probably an effect of the covariance matrix estimation, because it is very sensitive to the noise of the Jackknife estimator for a large amount of time-slices included (see Figure 6.8 and Section 5.3). An example of this effect for our data can be seen in Figure 6.7, further plots on this topic can be found in [143]. From this observation the decision was made to use only uncorrelated fits for the plateaus of effective masses and decay constants. While the effective mass seems to increase for small times and to

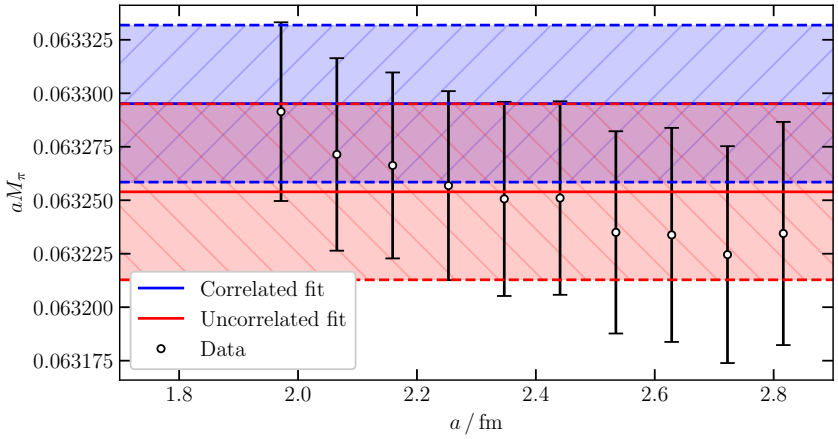

Figure 6.7 Uncorrelated and correlated plateau fit for the midpoint effective mass on one of the ensembles with $\beta = 3.8400$. Δ is set to 0.4 fm and the fit range is chosen to be $[1.9\,\text{fm}, 2.9\,\text{fm}]$. It can be seen that the mean value of the correlated fit is above all the mean values of the data points, whereas the uncorrelated mean value is in the middle of all the data.

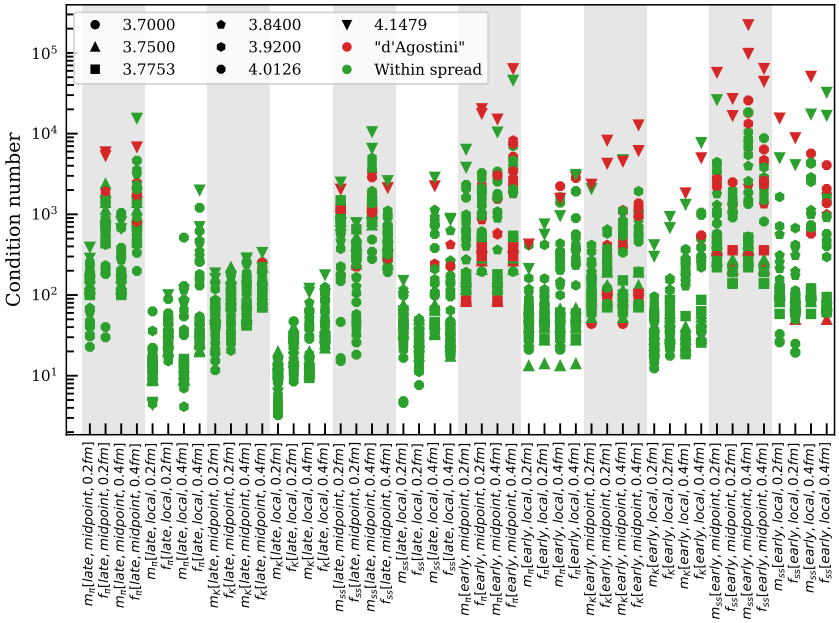

Figure 6.8 The condition number of the correlation matrix of the plateau fits. One the x-axis we show different observables with different systematics. Red points denote fits whose mean values are outside of the spread of the mean values of the data points. Especially in the upper-right corner one can notice a correlation between large condition numbers and the "d'Agostini" effect for the finer ensembles. This plot is provided courtesy of Finn Stokes, the plot was created for an internal meeting in 2022 [145].

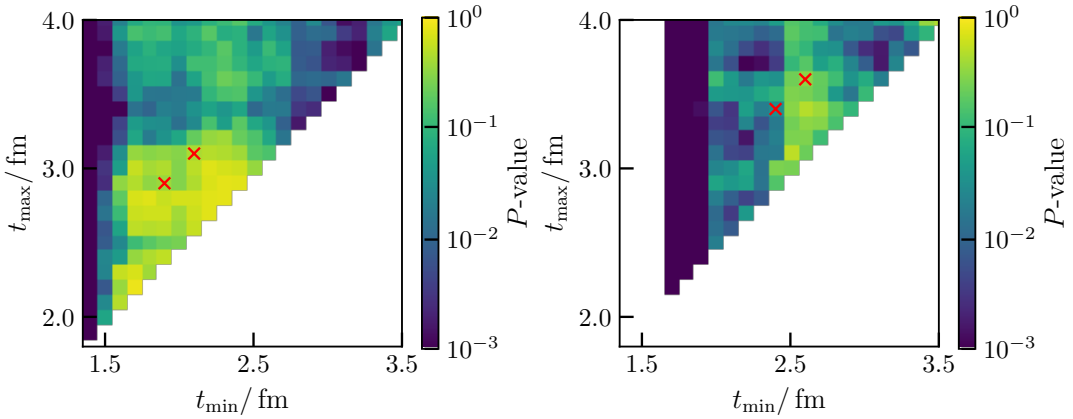

Figure 6.9 Heatmaps that describe the quality of the plateau fits in terms of the the range $[t_{\min}, t_{\max}]$. For each interval the Q-value (Section 5.3.2) is measured, the color is aligned to the P-value of the one-sided KS-test along all ensembles. Left-hand side: Plateau fits of the pion mass. Right-hand side: Plateau fits of the kaon mass.

be stable for larger times, the effective decay constant seems to decrease for both small and large times. Therefore, the total result will most probably depend significantly on the choice of the range. A good strategy to pick the correct choice is needed. Here, a strategy similar the one that was established in [20] is used. A fit range $[t_{\min}, t_{\max}]$ is picked and then the Q-value (established in [121]) according to the uncorrelated plateau fit on this range is computed for all of the ensembles (see Table 6.1). Since the Q-value is expected to follow a uniform distribution, we want to look for fit ranges at which this value is distributed uniformly or shifted towards higher Q-values. We can quantify this strategy by performing a one-sided Kolmogorov-Smirnov (KS) test [146, 147], where we compare the distribution of the Q-values for a given range along all ensembles to the identity function. An example of this type of test applied to the Ω^- baryon mass is shown in Figure 6.14. The P-value of this KS-test is shown in the heat maps in Figure 6.9 for the pseudo-scalar mesons with light-light and light-strange quark content in dependence of start and end point of the fit range. According to this test we picked two ranges of length 1.0 fm for each meson, respectively. This is done to estimate the systematic error originating from the choice of the fit range due to contamination from excited states. For the light-light mesons we pick

$$[t^1_{\min}, t^1_{\max}] = [1.9\,\text{fm}, 2.9\,\text{fm}], \tag{6.19}$$
$$[t^2_{\min}, t^2_{\max}] = [2.1\,\text{fm}, 3.1\,\text{fm}] \tag{6.20}$$

and for the light-strange quark content we decided to use

$$[t^1_{\min}, t^1_{\max}] = [2.4\,\text{fm}, 3.4\,\text{fm}], \tag{6.21}$$
$$[t^2_{\min}, t^2_{\max}] = [2.6\,\text{fm}, 3.6\,\text{fm}]. \tag{6.22}$$

An example of the plateau fits including statistical errors is shown in Figure 6.6.

6.4 Finite volume effects of pseudo-scalar masses and decay constants

The ensembles that are given in Table 6.1 have a spatial extension of around 6 fm and a temporal extension of around 9 fm. Therefore, the measurements on our ensembles differ from the infinite volume quantity by an amount that is not known exactly, but is expected to be at the order of magnitude of our target precision (see Figure 6.10). This problem is similar to the UV cut-off through the finite lattice spacing, but while discretization artifacts have to be removed with a continuum extrapolation, finite-volume (FV) effects are easier to deal with. The main idea in this study is to estimate the difference of the finite volume and the infinite volume quantity with chiral perturbation theory (χPT) and add this to the data, so that the global fit procedure is done using infinite volume observables. This also has the advantage that fluctuations that are aligned with variations in the volumes of the different ensembles are removed completely.
In the literature one can find FV corrections for the pseudo-scalar masses and decay constants up to two loops or next-to-next-to leading order (NNLO): The one loop corrections (next-to leading order) can be found in a work done by Gasser and Leutwyler [148], while Colangelo, Dürr and Hafaeli combined an existing NNLO computation of the pion scattering, that uses Lüscher's approach, to compute NNLO finite size effects of the pseudo-scalar observables [149]. Bijnens and Rössler made a full calculation of the NNLO FV effects for the desired quantities [150] and provided a software framework **CHIRON** [151] to compute the effects depending on the volume and the low-energy constants [38] that are taken directly from our simulation combined with the w_0 scale from [19, 20, 152]. Including only NLO effects the FV pion decay constant is smaller than the infinite volume quantity by about 0.11%, whereas, the difference is 0.12% if also NNLO effects are included. Therefore, the decision was made to use NLO finite volume corrections and add the difference of NNLO and NLO as a systematic error source. The resulting systematic error is much smaller than our target precision of $\sim 0.1\%$.
Unfortunately, staggered fermions come along with several tastes of pion that are heavier than in the continuum [62] as it can be seen in Equation (6.1), which results in a reduction of finite volume effects. However, the spectrum of the η-meson is distorted in another way (also Equation (6.1)), such that some of the tastes become lighter than in the continuum. This can affect the finite volume effects in an opposite way. In the next-to leading order case these effects are already computed for the Goldstone taste by Aubin and Bernard [153, 154] and for the remaining tastes by Bailey et al. [155, 156]. The formulas in the papers mentioned above depend on the taste-violation parameters $\Delta_{KS}(\xi)$ and $\delta_{KS}(\xi)$ from Equation (6.1). The values for these quantities can be measured on our ensembles and are translated into the hairpin parameters

$$\delta_A = \frac{\delta_{KS}(A)}{\Delta_{KS}(A)}, \tag{6.23}$$

$$\delta_V = \frac{\delta_{KS}(V)}{\Delta_{KS}(V)}. \tag{6.24}$$

The Fermilab-MILC collaboration [157] provides values of

$$\delta_A^{\mathrm{MILC}} = \left.\frac{\left(r_1^2 a^2 \delta_A\right)^{\mathrm{MILC}}}{\left(r_1^2 a^2 \Delta_A\right)^{\mathrm{MILC}}}\right|_{a=0.12\,\mathrm{fm}} = \frac{-0.0958(93)}{0.053983} = -1.77(17), \tag{6.25}$$

$$\delta_V^{\mathrm{MILC}} = \left.\frac{\left(r_1^2 a^2 \delta_V\right)^{\mathrm{MILC}}}{\left(r_1^2 a^2 \Delta_V\right)^{\mathrm{MILC}}}\right|_{a=0.12\,\mathrm{fm}} = \frac{0.050(24)}{0.167563} = 0.30(14). \tag{6.26}$$

From our fits (Figure 6.10) we obtain the value

$$\delta_A = -1.80 \tag{6.27}$$

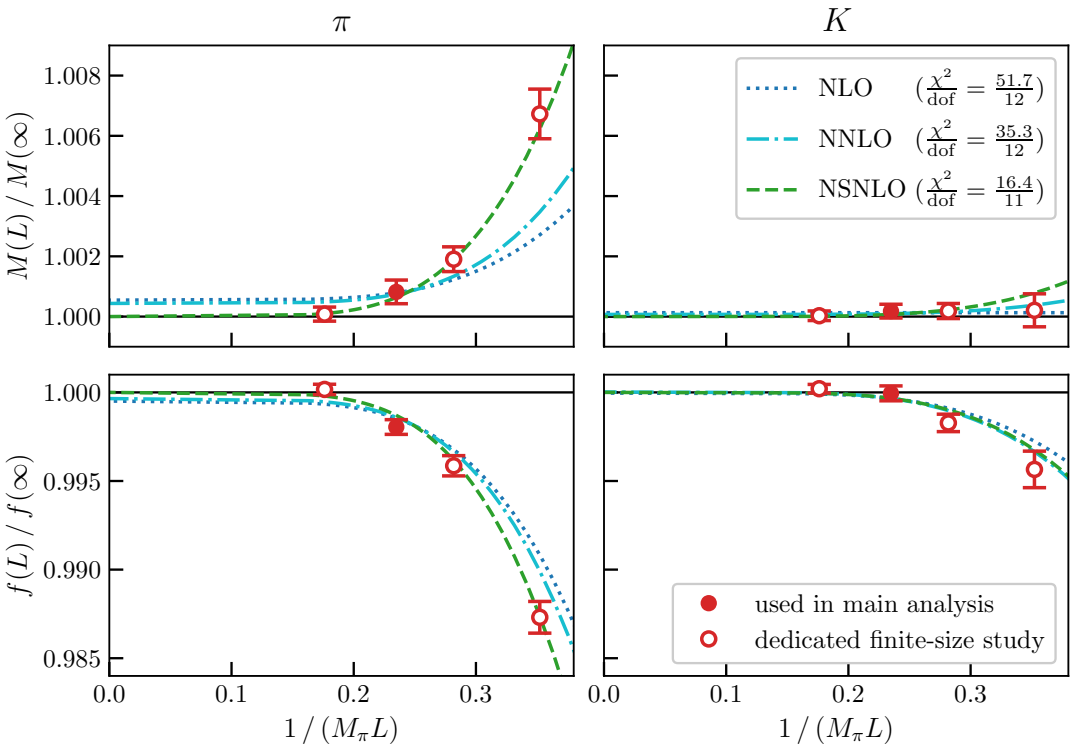

Figure 6.10 Finite volume effects of the pion and kaon (left column and right column) mass and decay constant (top row and bottom row). The points denote the values of simulations on different volumes. They can be compared to the predictions of NLO, NNLO and NSNLO that are given by the lines.

β	a [fm]	$L \times T$	am_s	m_s/m_l	#conf
3.7000	0.1315	32×64	0.057291	27.899	938
		40×64	0.057291	27.899	840
		48×64	0.057291	27.899	904
		64×64	0.057291	27.899	521

Table 6.2 Ensembles that are used in the FV study. The third ensemble corresponds to the $(6^3 \times 9)\,\mathrm{fm}^4$ extension from the ensembles in Table 6.1 and can also be found there.)

in combination with the observation that δ_V has no significant contribution and can there be neglected ($\delta_V = 0$). For NNLO no staggered χPT computations are available, therefore the continuum results from Bijnens [150, 151] are used from the difference of NNLO and NLO contributions. As mentioned before, we have a very conservative approach to estimating the systematic error for the finite volume contributions, therefore we can expect this simplification to be covered.

The data for pion and kaon mass and decay constant measured on the ensembles in Table 6.2 are shown in Figure 6.10 together with three different approaches to describe the finite-volume effects, i.e., NLO, NNLO and NSNLO (NNLO with NLO contributions from staggered χPT). The four panels are combined in a single total fit with four constraints being the infinite volume results. The NSNLO also uses δ_A as a fit parameter (see Equation (6.27)), while δ_V is set to zero. It is evident that including staggered effects is necessary for an appropriate description of the finite volume behavior. So it is decided to use the staggered NLO to correct for finite volume effects, while the difference of usual NLO and NNLO is used to estimate the systematic error of

this approach. Additionally, we use to sets of hairpin parameters

$$(\delta_A, \delta_V)^1 = (-1.76, 0.92) \tag{6.28}$$

$$(\delta_A, \delta_V)^2 = (-1.87, 0.00) \tag{6.29}$$

to account for the different values of these values by BMW and MILC collaboration.

6.5 Strong isospin-breaking and QED contributions

Up to this point it has been assumed that $m_u = m_d = m_l$, i.e., the up- and down quarks have the same mass, which results in an exact $SU(2)$-isospin-symmetry of QCD. Of course, this is not correct in reality, but since in this limit the simulations are much cheaper, this approximation is used for the main contribution of the results. Nevertheless, the result of an isospin-symmetric analysis differs from the physical value by the isospin-breaking contributions. For these isospin-breaking contributions new measurements are performed using the ensembles that are marked with a tick in Table 6.1. All the parameters are the same as in the isospin-symmetric ensembles but the two light quark flavors are replaced by up- and down-type quarks with the masses set according to

$$m_u/m_d = 0.485, \tag{6.30}$$

$$\frac{m_u + m_d}{2} = m_l. \tag{6.31}$$

To quantify the IB contributions we expand the QCD value of our target observable f_K/f_π up to first order in $\delta m = m_d - m_u$:

$$[f_{K^\pm}/f_{\pi^\pm}]^{\mathrm{QCD}} = [f_{ls}/f_{ll}]^{\mathrm{ISO}} + \frac{\partial}{\partial \delta m}[f_{K^\pm}/f_{\pi^\pm}]^{\mathrm{QCD}}\Big|_{\delta m=0} \times \delta m^{\mathrm{phys}} + \mathcal{O}\left(\delta m^{\mathrm{phys}\,2}\right) \tag{6.32}$$

Since δm is not an observable but a scheme-dependent quantity, it is more useful to replace it by a dimensionless observable that scales proportional to the isospin-breaking, $\frac{M_{dd}^2 - M_{uu}^2}{f_\pi^2} =: \frac{\Delta M^2}{f_\pi^2}$. The difference of the squares of the pseudo-scalar masses ΔM^2 is proportional to the isospin-breaking [38], while f_π^2 has no LO contributions in the isospin-breaking. The expansion of Equation (6.32) then becomes

$$[f_{K^\pm}/f_{\pi^\pm}]^{\mathrm{QCD}} = [f_{ls}/f_{ll}]^{\mathrm{ISO}} + \frac{(f_{ds} - f_{us})f_{ll}}{2\Delta M^2} \times \left[\frac{\Delta M^2}{f_\pi^2}\right]^{\mathrm{phys}} + \mathcal{O}\left(\left[\frac{\Delta M^4}{f_\pi^4}\right]^{\mathrm{phys}}\right) \tag{6.33}$$

with $\left[\frac{\Delta M^2}{f_\pi^2}\right]^{\mathrm{phys}} = 0.34850927$ [133]. This value does not have an error even if it is a physical value, because the scheme is set in a way that f_π and ΔM^2 are fixed. More on this topic can be found in Section 7.1.
The quantity $\frac{(f_{ds} - f_{us})f_{ll}}{2\Delta M^2}$ is now measured on the IB ensembles, except for f_{ll} which is taken from the corresponding isospin-symmetric ensemble due to the fact that is has higher statistics.
As it will be discussed in Section 7.1 also sea-sea contributions of can be measured, according to

$$G = \left[\frac{\mathcal{F}_K}{\mathcal{F}_\pi} - B\left[\frac{M_\pi^2}{\mathcal{F}_\pi^2}\right] - C\left[\frac{2M_K^2 - M_\pi^2}{\mathcal{F}_\pi^2}\right]\right]''_{02}, \tag{6.34}$$

where B and C describe the quark mass dependence of the target observable. Further explanations are given in Section 7.1. Here, $\mathcal{F}_H$ denotes the QED+QCD decay constant of the hadron H which is equal to f_H in the limit $e \to 0$. For simplicity, here we work in the QCD isospin symmetric limit. The notation in Equation (6.34) is a short cut for the second order contribution in the charge of the sea quarks. To derive an expression for

β	a [fm]	$L \times T$	am_s	m_s/m_l	#conf
3.7000	0.1315	24×48	0.057291	27.899	726
		48×64	0.057291	27.899	300
3.7753	0.1116	28×56	0.047615	27.843	887
3.8400	0.0952	32×64	0.043194	28.500	1110
			0.043194	30.205	1072
			0.040750	28.007	1036
			0.039139	26.893	1035
0.7300	0.1120	56×84	0.06061	33.7280	1305

Table 6.3 Ensembles that are used in the QED+QCD study. Here, dynamical QED and QCD simulations are combined, so that sea quark effects can be considered. The first eight ensembles are generated using the `4stout` action while the last one is based on the `4HEX` action.

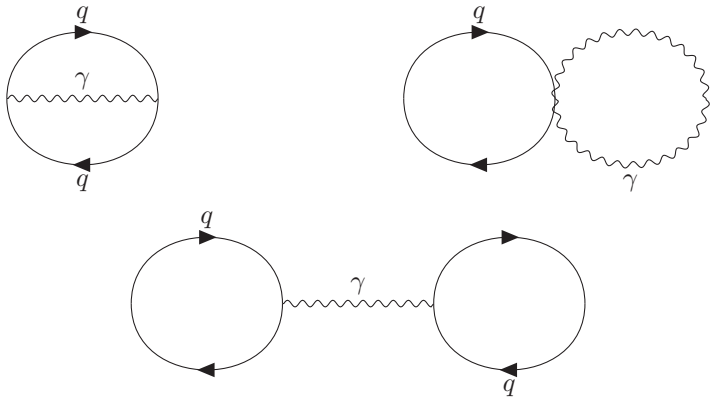

Figure 6.11 Sea quark diagrams of $\mathcal{O}(e^2)$ that are included in the study.

the latter equation the second order expansions in the sea quark charge have to be included:

$$\begin{aligned} G &= \left[\frac{\mathcal{F}_K + e_s^2\mathcal{F}_K''}{\mathcal{F}_\pi + e_s^2\mathcal{F}_\pi''} - B\left[\frac{(M_\pi + e_s^2 M_\pi'')^2}{(\mathcal{F}_\pi + e_s^2\mathcal{F}_\pi'')^2}\right] - C\left[\frac{2(M_K + e_s^2 M_K'')^2 - (M_\pi + e_s^2 M_\pi'')^2}{(\mathcal{F}_\pi + e_s^2\mathcal{F}_\pi'')^2}\right]\right]_{02}'' \\ &= \frac{\mathcal{F}_K}{\mathcal{F}_\pi}\left[\frac{\mathcal{F}_K''}{\mathcal{F}_K} - \frac{\mathcal{F}_\pi''}{\mathcal{F}_\pi}\right] - B\left[\frac{2M_\pi^2}{\mathcal{F}_\pi^2}\left[\frac{M_\pi''}{M_\pi} - \frac{\mathcal{F}_\pi''}{\mathcal{F}_\pi}\right]\right] - C\left[\frac{4M_K^2}{\mathcal{F}_\pi^2}\left[\frac{M_K''}{M_K} - \frac{\mathcal{F}_\pi''}{\mathcal{F}_\pi}\right] - \frac{2M_\pi^2}{\mathcal{F}_\pi^2}\left[\frac{M_\pi''}{M_\pi} - \frac{\mathcal{F}_\pi''}{\mathcal{F}_\pi}\right]\right] \end{aligned} \tag{6.35}$$

The corresponding quantities $\mathcal{F}_H^{(\prime\prime)}$ and $M_H^{(\prime\prime)}$ can be measured on the QCD+QED ensembles that are given in Table 6.3. The second derivative with respect to the sea quarks charge is given by the expression

$$\langle O\rangle_{02}'' = \left\langle O_0 \frac{\det s_2''}{\det s_0}\right\rangle_0 - \langle O_0\rangle_0 \left\langle \frac{\det s_2''}{\det s_0}\right\rangle_0 \tag{6.36}$$

where the subscript 0 denotes the order of QED effects of the respective quantity or the expectation value. s is the fermion matrix $\prod_f (\not{D}_{\text{stagg}} - m_f)^{1/4}$. Within the derivation the assumption was made that

$$\left\langle \frac{\det s_1'}{\det s_0}\right\rangle_0 = 0. \tag{6.37}$$

The latter notations and calculations were published first in [19]. The diagrams entering these computations are shown in Figure 6.11. The diagram on the right has a vertex with two quarks and two photons, which is a forbidden diagram in usual QED. However, at finite lattice spacing vertices with an arbitrary number of photons can occur. This can be derived easily by expanding one of the terms appearing in the discretized

fermion action:

$$\psi(x)D_\mu\psi(x) = \frac{1}{2a}\left(\psi(x)U_\mu(x)\psi(x+a\hat{\mu}) - \psi(x)U_\mu^\dagger(x-a\hat{\mu})\psi(x-a\hat{\mu})\right) \tag{6.38}$$

$$= \frac{1}{2a}\left(\psi(x)e^{\mathrm{i}aeA_\mu(x)}\psi(x+a\hat{\mu}) - \psi(x)e^{-\mathrm{i}aeA_\mu(x-a\hat{\mu})}\psi(x-a\hat{\mu})\right) \tag{6.39}$$

When expanding the latter expression in powers of the lattice spacing it is evident that the a^{-1} contributions vanish, the constant expressions reproduce the vertex from continuum QED and there are higher contributions in $(ae)^n$ that describe a vertex with n photons. This also explains why there are no diagrams with more n-photon vertices: They are not of $\mathcal{O}(e^2)$.
In addition to the `4stout` ensembles, we add some of the (more precise) `4HEX` data (see Table 6.3) in order to achieve a reduction of statistical noise and finite volume effects of the sea-quark contributions.
To compute the sea-quark effects of $\mathcal{F}_H w_0$ only sea modification to Equation (6.34) are necessary. In this case these effects are described by

$$G = \left[\mathcal{F}_H w_0 - B\left[\frac{M_\pi^2}{\mathcal{F}_\pi^2}\right] - C\left[\frac{2M_K^2 - M_\pi^2}{\mathcal{F}_\pi^2}\right]\right]''_{02}. \tag{6.40}$$

6.6 Ω operators and correlation functions

There are many different operators for the positive-parity, ground-state Ω^- baryon [137, 158, 159], but in this study we will focus on three specific operators. To be able to concisely express these operators, we define the spatial covariant shift

$$S_i\chi_a(x) = U_i(x)\chi_a(x+\hat{i}) \quad (i=1,2,3), \tag{6.41}$$

with χ_a being the quark field with flavor content a. Two sequential shifts are then written as $S_{\mu\nu} = S_\mu S_\nu$. If necessary, we also use an additional "flavor" index α, β or γ that is defined and further explained in [159]. With these definitions we can define the operators:

$$\Omega_{\mathrm{VI}}(t) = \sum_{x_k\%2=0} \epsilon_{abc}\left(S_1\chi_a S_{12}\chi_b S_{13}\chi_c - S_2\chi_a S_{21}\chi_b S_{23}\chi_c + S_3\chi_a S_{31}\chi_b S_{32}\chi_c\right) \tag{6.42}$$

$$\Omega_{\mathrm{XI}}(t) = \sum_{x_k\%2=0} \epsilon_{abc}\left(S_1\chi_a S_2\chi_b S_3\chi_c\right) \tag{6.43}$$

$$\Omega_{\mathrm{Ba}}(t) = \left[2\delta_{\alpha1}\delta_{\beta2}\delta_{\gamma3} - \delta_{\alpha3}\delta_{\beta1}\delta_{\gamma2} - \delta_{\alpha2}\delta_{\beta3}\delta_{\gamma1} + 2\delta_{\alpha1}\delta_{\gamma2}\delta_{\beta3} - \delta_{\alpha3}\delta_{\gamma1}\delta_{\beta2} - \delta_{\alpha2}\delta_{\gamma3}\delta_{\beta1}\right] \tag{6.44}$$
$$\sum_{x_k\%2=0} \epsilon_{abc}\left(S_1\chi_{a\alpha}S_{12}\chi_{b\beta}S_{13}\chi_{c\gamma} - S_2\chi_{a\alpha}S_{21}\chi_{b\beta}S_{23}\chi_{c\gamma} + S_3\chi_{a\alpha}S_{31}\chi_{b\beta}S_{32}\chi_{c\gamma}\right)$$

These three operators differ in the tastes they couple to, which means that their ground-state masses at finite a might slightly differ. Nevertheless, in the continuum the masses of these three states should be degenerate. However, we use all three of these operators to estimate the systematic uncertainty originating from the choice of the operator. To modify the contributions of the excited states, which will yield a different operator for the GEVP, we apply Wuppertal smearing (see Section 4.4.3) to either none, one, or two of the point sources. The Wuppertal smearing parameter σ is set to 0.5 and the gauge fields in the Laplacian are smeared with stout smearing and a parameter of $\rho = 0.125$. The number of smearing steps for the Wuppertal and stout smearing, respectively, can be found in Table 6.4. These numbers are tuned in a way that the smearing radius (in physical units) is roughly constant along all ensembles. The number of point and smeared sources can also be found in Table 6.4. Since smearing reduces the signal-to-noise ratio, the number of smeared sources is greater by $\mathcal{O}(10)$. The point sources are located on a random time-slice on the corners of a cube of size

$(L/2)^3$. For each of those eight points a random (canonical) unit vector in color space is chosen.

β	N_{Wptl}	N_{3d}	t_p	t_a	t_b	range #1	range #2	# pt, sm sources
3.7000	24	32	1	4	7	7…15	8…15	28928, 229376
3.7500	30	40	1	4	7	8…18	9…18	66208, 530176
3.7553	34	46	1	4	7	9…19	10…19	61024, 488192
3.8400	46	62	2	4	9	10…20	11…20	125440, 2807552
3.9200	67	90	2	6	9	12…25	13…25	137472, 3038720
4.0126	101	135	3	6	9	15…30	16…30	223360, 4235520
4.1479	178	238	5	6	11	19…40	21…40	160544, 2068736

Table 6.4 The parameters for the Ω-analysis are chosen different for each β. We give the number of smearing applications for the Wuppertal smearing (N_{Wptl}) and the three dimensional stout smearing (N_{3d}). t_p denotes the additional shift for point sources in the GEVP, t_a and t_b are the time slices chosen to estimate the Eigenvector in the GEVP. To fit the correlators we use two different fit ranges range#1 and range#2. The smearing radii as well as the ranges are kept constant in physical units along all ensembles. This table is previously published in [20].

6.7 Extraction of the Ω-baryon mass

To ensure that the forward and backward-propagating states have a consistent parity we apply the folding transformation

$$H_t \to \begin{cases} \frac{1}{2}\left(H_t + (-)^{t+1} H_{T-t}\right) & \text{if } 0 < t < \frac{T}{2} \\ H_t & t = 0 \text{ or } t = \frac{T}{2} \end{cases} \tag{6.45}$$

to the Ω^--propagator H_t.

As mentioned before, the three Baryon-operators Ω_{VI}, Ω_{XI} and Ω_{Ba} couple to different excitations. Even though the ground state dominates beyond a certain time separation, contributions from higher excitations will contaminate the signal and increase overall uncertainties. Therefore, we use a GEVP (Section 5.5) to extract the different mass excitations, similar to the reconstruction of the vector correlator in Chapter 10. This method was proposed in [130]. In this study, we use a six dimensional GEVP that includes point sources and smeared sources due to different contributions of excited states from the smearing procedure. Additionally, certain shifts of the propagator are included; this method is called pencil-of-functions and uses shifts of the correlation function to define different operators [160] according to

$$\hat{O}_i(t) = \hat{O}(t+i), \tag{6.46}$$

$$\hat{O}_i^\dagger(t) = \hat{O}^\dagger(t-i). \tag{6.47}$$

For the point sources, an additional shift t_p is introduced. In this way, the amplitude of all states entering the GEVP is of the same order of magnitude. Additionally, we can reduce the contamination from excited states that play a dominant role for early time slices in combination with point sources. In total, we use different shifts of the point and four different shifts of the smeared operator. The correlation matrix from the GEVP is given by

$$\mathbf{H}_t = \left(\begin{array}{cc|cccc} H^{pp}_{t+2t_p+0} & H^{pp}_{t+2t_p+1} & H^{ps}_{t+t_p+0} & H^{ps}_{t+t_p+1} & H^{ps}_{t+t_p+2} & H^{ps}_{t+t_p+3} \\ H^{pp}_{t+2t_p+1} & H^{pp}_{t+2t_p+2} & H^{ps}_{t+t_p+1} & H^{ps}_{t+t_p+2} & H^{ps}_{t+t_p+3} & H^{ps}_{t+t_p+4} \\ \hline H^{sp}_{t+t_p+0} & H^{sp}_{t+t_p+1} & H^{ss}_{t+0} & H^{ss}_{t+1} & H^{ss}_{t+2} & H^{ss}_{t+3} \\ H^{sp}_{t+t_p+1} & H^{sp}_{t+t_p+2} & H^{ss}_{t+1} & H^{ss}_{t+2} & H^{ss}_{t+3} & H^{ss}_{t+4} \\ H^{sp}_{t+t_p+2} & H^{sp}_{t+t_p+3} & H^{ss}_{t+2} & H^{ss}_{t+3} & H^{ss}_{t+4} & H^{ss}_{t+5} \\ H^{sp}_{t+t_p+3} & H^{sp}_{t+t_p+4} & H^{ss}_{t+3} & H^{ss}_{t+4} & H^{ss}_{t+5} & H^{ss}_{t+6} \end{array}\right), \tag{6.48}$$

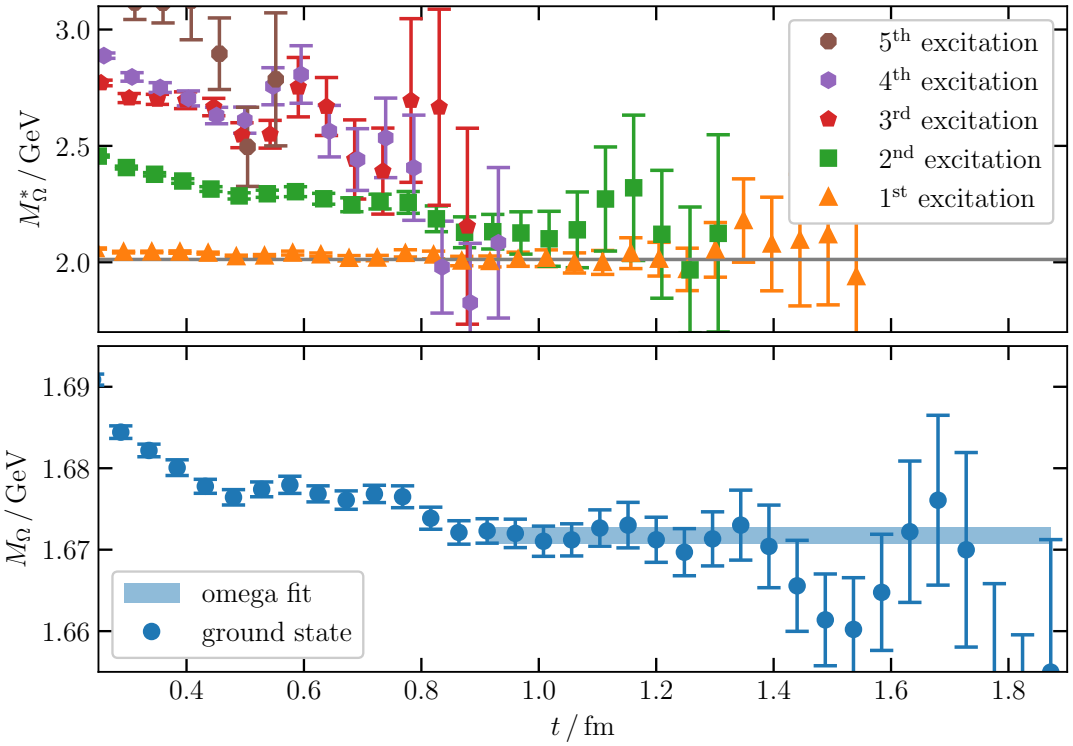

Figure 6.12 Effective mass from the Ω-propagator eigenstates on the finest ensemble with $\beta = 4.1479$. The numbers are converted to physical units by choosing $a = 0.0483\,\text{fm}$. *Upper panel:* Excitations of the Ω baryon extracted with the GEVP. The gray horizontal line corresponds to a measurement of the Belle collaboration [161]. *Lower panel:* Ground state effective mass from the GEVP. The blue band corresponds to a single exponential fit to the ground state propagator. Figure is previously published in [20].

where the superscripts denote the respective choice of smeared (s) and unsmeared (p) source and sink. For fixed t_a and t_b we solve the GEVP

$$\mathbf{H}_{t_a} \cdot v(t_a, t_b) = \lambda(t_a, t_b)\mathbf{H}_{t_b} \cdot v(t_a, t_b). \tag{6.49}$$

The parameters t_a and t_b are chosen differently for the respective ensembles. The explicit values can be found in Table 6.4. To reconstruct the function $\lambda(t_a - t_b) = \lambda(t_a, t_b)$ the vector-matrix-vector product

$$P(t; t_a, t_b) = v^\dagger(t_a, t_b) \cdot \mathbf{H}_t \cdot v(t_a, t_b) \approx \lambda(t) \tag{6.50}$$

is computed. This way we can make sure that always the correct state is chosen, especially in the long-distance regime with large statistical noise. Further explanations are given in Section 5.5.
We decided to fit single-state exponential functions to the propagators instead of using plateau fits to the effective mass. However, for better visualization, we still show the effective masses for one of the finest ensembles in Figure 6.12 along with the result of our ground state fit and an experimental value [161] for the first excitation that is compatible with our data. We fit the data to the model

$$Y(t) = A\exp(-Mt) \tag{6.51}$$

by minimizing the correlated χ^2. The optimization with respect to the coefficient A can be done analytically,

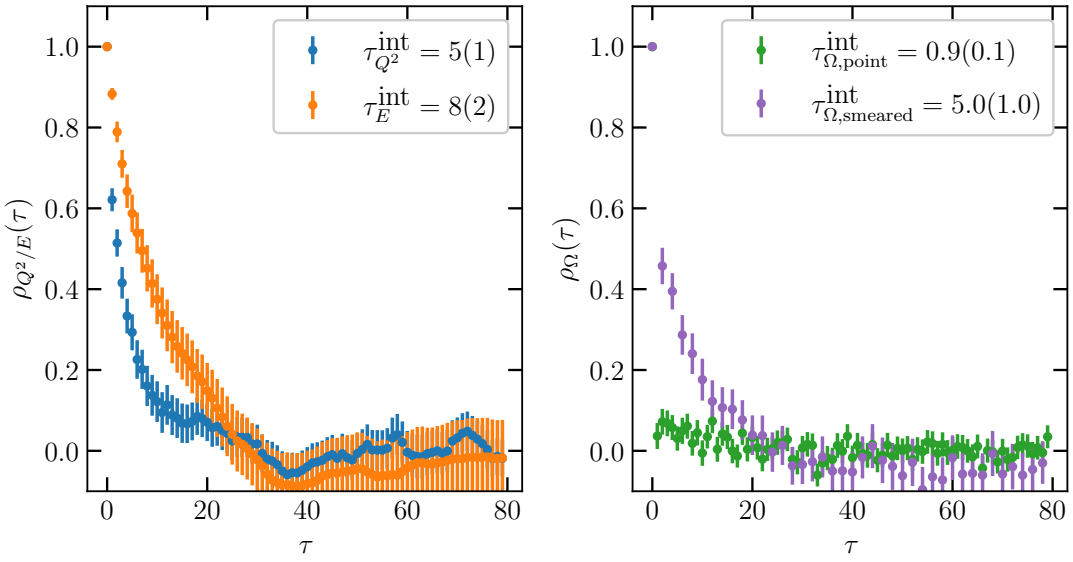

Figure 6.13 Autocorrelation functions on the $\beta = 4.1479$ ensemble. *Left panel*: Autocorrelation functions of the squared topological charge and the energy density, both at flow time w_0^2. *Right panel*: Autocorrelation function of the Ω_{VI}-operator with two point sources and two smeared sources, respectively. Figure is previously published in [20].

so we end up with a one-parameter fit

$$\tilde{Y}(t) = \frac{\sum_{t_0,t_1} \lambda(t_0) C^{-1}(t_0,t_1) \exp(-Mt_1)}{\sum_{t_0,t_1} \exp(-Mt_0) C^{-1}(t_0,t_1) \exp(-Mt_1)} \exp(-Mt), \tag{6.52}$$

where $C^{-1}(t_0,t_1)$ is the inverse covariance matrix of y, evaluated at $y(t_0)$ and $y(t_1)$. Usually, we use 48 Jackknife samples to estimate the uncertainty. However, for the stability of the covariance matrix, it is useful to use a larger amount of samples. Here, we use 200 Jackknife samples, which still ensures that the blocks are large enough to handle autocorrelation effects. The autocorrelation function of the Ω propagator can be found in Figure 6.13. The covariance matrix is inverted using an SVD-cut of 10^{-8}, as explained in Section 5.3.1, to prevent the overall result from being dominated by statistical noise [162].
Usually, it is a non-trivial task to find the optimal region in which the exponential function is fitted to the correlator. Here, we decide to use a method very similar to the one used in Section 6.3. For each ensemble, we compute the (correlated) Q-value (Section 5.3.2) [121] for a given range $[t_{\text{min}}, t_{\text{max}}]$. Then, we perform a one-sided KS-test across the ensembles, where we allow the Q-values to be tilted towards 1. The P-values of this KS-tests are shown in the right panel of Figure 6.14. Based on this figure, the decision was made to use the fit ranges $[0.9\text{ fm}, 2.0\text{ fm}]$ and $[1.0\text{ fm}, 2.0\text{ fm}]$. We use two different ranges to account for the systematic uncertainty associated with different excitations. The KS-tests for both of the chosen ranges are shown in the left panel of Figure 6.14. All in all we are able to measure the mass of the Ω-baryon on our lattices with permille precision as it can be seen in Figure 6.15.

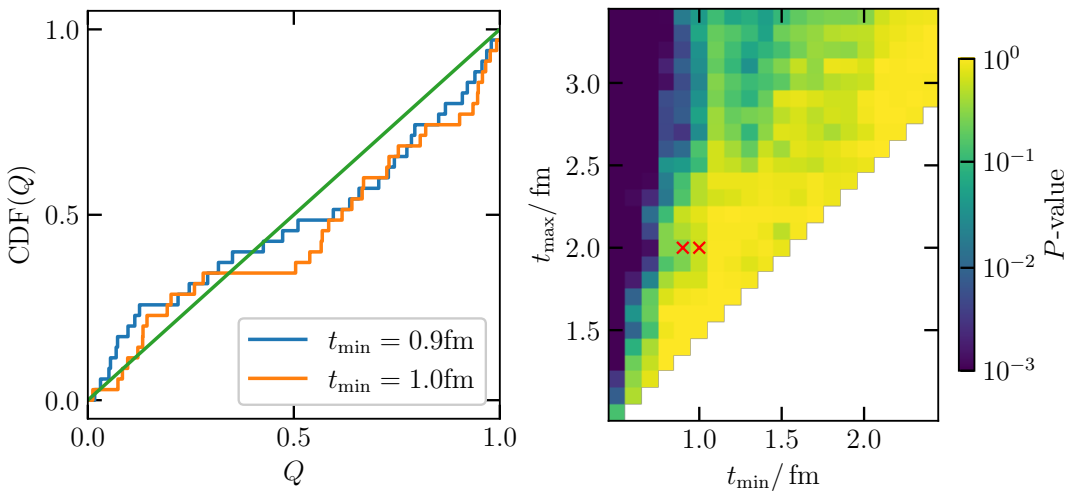

Figure 6.14 *Left panel:* KS-test of the Q-values along all ensembles for the ranges [0.9 fm, 2.0 fm] and [1.0 fm, 2.0 fm]. *Right panel:* Heatmap of the P-values of all KS-tests. The red crosses mark the fit ranges that are used within the final analysis. Figure is previously published in [20].

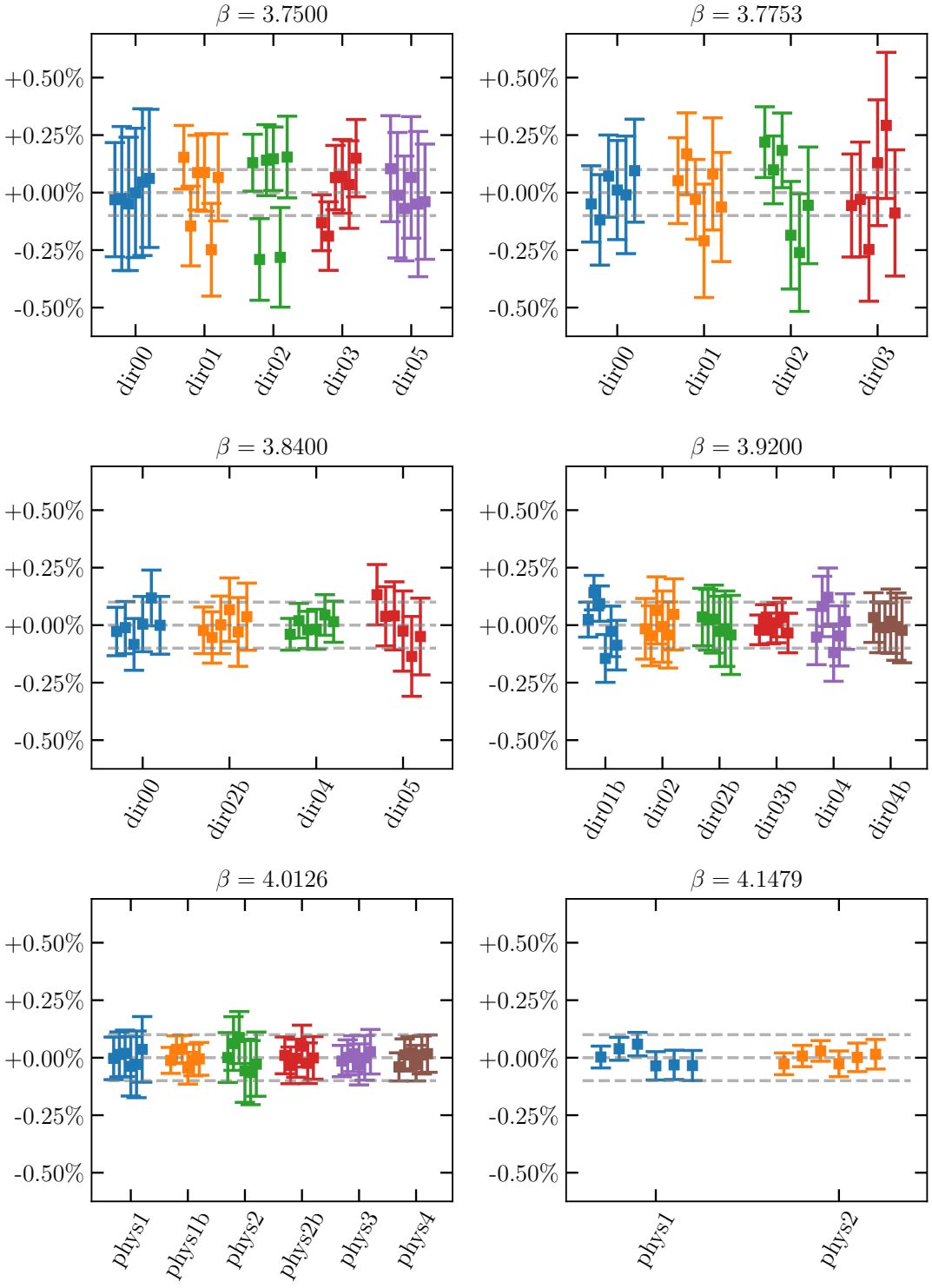

Figure 6.15 Ground state Ω baryon mass for different ensembles. For each β different colors denote different ensembles. The six data points per ensemble correspond to two different fit ranges times three different operators. Figure is previously published in [20].

7 Global analysis

In the following chapter, the choice of the scheme, i.e., our way to set the scale and the physical point, and our global fit procedure are described.

7.1 Schemes, transformations and global fit functions

The pseudo-scalar decay constant can be decomposed in the QCD and QED contributions according to

$$\mathcal{F}_H^2 = f_H^2(1+\delta_H) \quad (H=\pi,K). \tag{7.1}$$

af_H is a quantity that can be measured fairly easy using lattice QCD as it is shown in Section 6.3. Thus, it is a useful (and common [139, 163, 164]) strategy to set the lattice spacing a with this quantity. The problem arises that a proper physical (i.e., scheme independent) value does not exist for f_H and δ_H, respectively. Basically, one is free to choose how to split up the QCD and QED contributions. However, the total QCD+QED decay constant is a physical quantity that is related to the decay width by some kinematical factors. The lattice spacing in this study is set according to

$$a = \frac{af_\pi}{f_\pi^{\text{phys}}} \quad \text{with } f_\pi^{\text{phys}} = 130.5\,\text{MeV}. \tag{7.2}$$

Here, f_π^{phys} is taken from the FLAG report 2024 [138]. It should be mentioned that in the pure QCD limit $e \to 0$, $\mathcal{F}_H$ and f_H are the same quantity and can therefore be used analogously.
$\mathcal{F}_\pi$ can be determined experimentally with high precision [43, 133]. In [163] the radiative corrections are then determined using lattice simulations and the pion decay constant can thus be corrected for electromagnetic contributions. In this way, an independent value of the pure QCD pion decay constant is obtained, which is given by

$$f_\pi^{\text{GRS}} = 130.65(12)\,\text{MeV}. \tag{7.3}$$

This quantity has a one-permille uncertainty that is highly dominated by the lattice estimation of the radiative corrections. The ratio of the full QCD+QED pseudo-scalar decay constant can be expanded around the physical point with our "master equation":

$$\begin{aligned}\frac{\mathcal{F}_K}{\mathcal{F}_\pi} = A + B\left[\frac{M_\pi^2}{\mathcal{F}_\pi^2} - \text{const.}\right] + C\left[\frac{M_{ds}^2 + M_{us}^2 - M_\pi^2}{\mathcal{F}_\pi^2} - \text{const.}'\right] \\ + D\left[\frac{M_{ds}^2 - M_{us}^2}{\mathcal{F}_\pi^2} - \text{const.}''\right] + Ee_v^2 + Fe_ve_s + Ge_s^2.\end{aligned} \tag{7.4}$$

Here e_v denotes the charge of a valence quark and e_s is the charge of a sea quark. The constants are defined by the scheme. Here, we use the FLAG scheme [138] since the quantities are defined without any uncertainty. However, other groups [163] might use another scheme like the GRS, but we are able to transform our results into any scheme afterwards. The FLAG scheme is defined by

$$f_\pi^{\text{FLAG}} = 130.5\,\text{MeV}, \tag{7.5}$$
$$M_\pi^{\text{FLAG}} = 135.0\,\text{MeV}, \tag{7.6}$$
$$M_{K^+}^{\text{FLAG}} = 491.6\,\text{MeV}, \tag{7.7}$$
$$M_{K^0}^{\text{FLAG}} = 497.6\,\text{MeV}. \tag{7.8}$$

The constants A, B and C can be determined from fits to isospin-symmetric data in pure QCD

$$\left[\frac{f_K}{f_\pi}\right]^{\text{isoQCD}} = A + B\left[\frac{M_{ll}^2}{f_{ll}^2} - \text{const.}\right] + C\left[\frac{2M_{ls}^2 - M_{ll}^2}{f_{ll}^2} - \text{const.}'\right] \tag{7.9}$$

with the constants set to the according physical values in the FLAG scheme. Since these terms are symmetric with respect to the interchange of up- and down quark we can compute the antisymmetric derivative with respect to their difference and find an expression for D:

$$D = \frac{(f_{ds} - f_{us})f_{ud}}{2(M_{ds}^2 - M_{us}^2)}. \tag{7.10}$$

This expression can be rescaled by $\left[\frac{M_K^{0\,2} - M_K^{+\,2}}{2f_\pi^2}\right]^{\text{FLAG}}$ to get the isospin-breaking contributions to the ratio of the decay constants. The value of E can be taken from [163]; however, care must be taken regarding the scheme, as the GRS scheme is used there instead of the FLAG scheme. However, we can compute the transformation and the difference will be small. The F term has a flavor $SU(3)$ suppression since $\sum_{s=u,d,s} e_s = 0$ and therefore is neglected within this study. Using the notation of [19] the contribution of two sea quarks can be computed via

$$G = \left[\frac{\mathcal{F}_K}{\mathcal{F}\pi} - B\left[\frac{M_\pi^2}{\mathcal{F}_\pi^2} - \text{const.}\right] - C\left[\frac{M_{ds}^2 + M_{us}^2 - M_\pi^2}{\mathcal{F}_\pi^2}\right]\right]''_{02}. \tag{7.11}$$

Here, the parameters B and C can be taken from the isospin-symmetric fits in Equation (7.9). Using the parameters it is easy to transform to a given scheme by adjusting the constants to the desired quantities. For example, the PDG values can be used to obtain the physical result. The study in [163] from which we take the value of E uses the GRS scheme [165]. In this scheme the pseudo-scalar masses are split up into their QCD and QED contributions. In these meson matching computations they neglected the sea quark effect, thus, the QED part of their calculation only consists of valence-valence effects and thus the QCD part of the scheme-defining quantities also contains sea-sea and sea-valence effects.
The "master equations" for the observable $f_\pi w_0$ and $f_\pi\sqrt{t_0}$ can be constructed in the same way. However, Equation (7.4) includes strong-isospin breaking effects which can be neglected here.

7.2 Global fit procedure

At this point, we have data for the isospin-symmetric and the isospin-breaking (IB) parts of f_K/f_π at infinite volume, finite lattice spacing and quark masses scattering around the physical point. Next we want to extrapolate the data to the physical point[1] as well as the continuum $a = 0$. We perform three different global fits according to

$$Y = A + BX_l + CX_s, \tag{7.12}$$

$$D = A_{\text{IB}} + B_{\text{IB}}X_l + C_{\text{IB}}X_s, \tag{7.13}$$

$$G = A_{\text{sea}}. \tag{7.14}$$

The quantities A, B and C are computed using fits to our isospin-symmetric data, while the isospin-breaking data are fitted to D. The sea-quark contributions G are taken from fits the QCD+QED data. X_l is a quantity proportional to the light quark mass deviation from the physical point and X_s is proportional to the strange quark mass deviation. In Equation (7.13) also the X_l (and no X_u or X_d) is used because this would make up

[1] This is the point at which the expectation values of certain observables (e.g. pseudo-scalar masses, ...) match their physical counterparts

second order effects in the isospin-breaking which are ignored in this study. X_l and X_s are used to interpolate the data to the physical point. This can be done very precisely, because the ensembles are defined in a way that they scatter closely around the physical point (see Section 6.1) [19, 20]. The sea quark effects are not interpolated to the physical point, since the meson masses do not scatter aroung the physical value due to large finite volume effects. However, an additional finite volume scaling is included in A_{sea}. The quantities A, B and C (and their isospin-breaking counterparts) are function depending on the lattice spacing that can be used to extrapolate the data to the continuum. In this study we choose this three functions to be polynomials in a^2 respectively Δ_{KS}. The quantity a^2 is set using the ratio $\left(\frac{af_\pi}{f_\pi^{\text{phys}}}\right)^2$, where the numerator can be measured on each ensemble and the denominator can be taken from [133]. Alternatively, one could use the w_0-scale [139, 152] that is used e.g. in the $g-2$ studies [19, 20] and is further explained in Section 9. Δ_{KS} is used as another parameter to quantify the discretization effects. It is much more sensitive to the lattice spacing than a^2, in fact it is $a^2\alpha_s(1/a)^3$, where α_s is the strong coupling at the energy scale $1/a$. In Section 6.1 it could be shown that at small lattice spacing this is close to an a^4 scaling. Of course, on the lattice only $a^2\Delta_{KS}$ could be measured so the definition of a^2 that was mentioned before is used to remove the a^2 prefactor.

7.2.1 Isospin symmetric

For the isospin symmetric fit the quantity for the light quark mass deviation is set as

$$X_l = \frac{M_{ll}^2}{f_{ll}^2} - \left[\frac{\left(M_{\pi^\pm}^{\text{phys}}\right)^2}{\left(f_{\pi^\pm}^{\text{phys}}\right)^2}\right] \tag{7.15}$$

and the strange quark mass deviation is given as

$$X_s = \frac{M_{ls}^2 - \frac{1}{2}M_{ll}^2}{f_{ll}^2} - \left[\frac{\left(M_{K^\pm}^{\text{phys}}\right)^2 - \frac{1}{2}\left(M_{\pi^\pm}^{\text{phys}}\right)^2}{\left(f_{\pi^\pm}^{\text{phys}}\right)^2}\right]. \tag{7.16}$$

The function A is a polynomial in a^2 and Δ_{KS} with the constraint that the sum of the maximum degrees in a^2 and Δ_{KS} is larger than zero and smaller than four. The function B and C are constructed in a similar way, but the maximum total degree is one, whereas B and C are also allowed to be lattice spacing independent. Since continuum extrapolation is a feature of Symanzik effective theory, which states that a lattice discretization is an asymptotic expansion in the lattice spacing around the continuum, it is possible to have a finite radius of convergence [49, 166, 167]. Therefore, it is possible that some of the ensembles with larger lattice spacings should not be included in the continuum extrapolation. In order to deal with this issue we decide to skip up to four of the largest lattice spacings. Of course, we make sure to reduce the degree of the $A/B/C$-polynomials so that over-fitting is avoided, e.g. if we remove the four largest spacing, only four spacings remain, therefore A should not have more than three free parameters ($\deg(A) \leq 2$). We use the same argument for the B and C polynomial, but only the five spacing with more than two ensembles are counted.
There is one further exception for the polynomial allowed within the analysis:

$$A(a^2, \Delta_{KS}) = A_0 + A_1 a^2 + A_2 a^4 + A_1' \Delta_{KS} \tag{7.17}$$

This polynomial has a^4 and Δ_{KS} contributions. From Figure 6.5 it is known that both terms are very similar. In this type of fits a significant instability could be observed. So we decided to skip this function. It can be

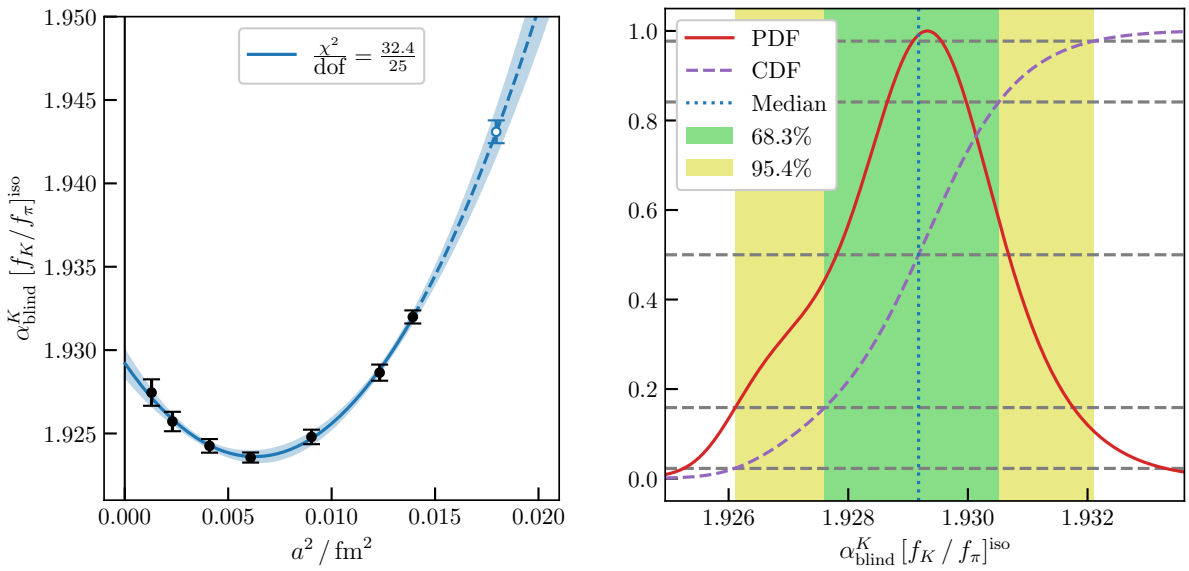

Figure 7.1 *Left panel:* Continuum extrapolation of the decay constant ratio of kaon and pion in the isospin-symmetric limit. The shown fit is linear in a^2, Δ_{KS}, X_l and X_s. The points are shifted to the physical point and are averaged if they correspond to the same lattice spacing, open points are not included in the fits. Solid lines denote the fit range, dashed lines denote regions outside of the fit range. The light blue gives the statistical deviation estimated by Jackknife resampling. *Right panel:* Histogram and cumulative distribution function of the continuum extrapolated results of the pseudo-scalar decay constant ratio. The green and yellow bands give the one and two σ neighborhoods, respectively.

assumed that the contributions from this polynomial to the overall result are covered by the polynomials

$$A(a^2, \Delta_{KS}) = A_0 + A_1 a^2 + A_1' \Delta_{KS}, \tag{7.18}$$

$$A(a^2, \Delta_{KS}) = A_0 + A_1 a^2 + A_2 a^4. \tag{7.19}$$

An example of one of the best isospin-symmetric fits to f_K/f_π is shown in the right panel of Figure 7.1. It includes taste-breaking effects proportional to D_{KS} as well as usual a^2 discretization effects. The shift to the physical point has no lattice spacing dependence in the example and the coarsest ensemble is excluded from the fit. However, the fit aligns well with the excluded data point.

7.2.2 isospin-breaking

For the strong-isospin-breaking contributions (D) only six lattice spacings, with at most two ensembles each, are available (Table 6.1. The light quark mass deviation is given by

$$X_l = \frac{M_{ud}^2}{f_{ud}^2} - \left[\frac{\left(M_{\pi^\pm}^{\mathrm{phys}}\right)^2}{\left(f_{\pi^\pm}^{\mathrm{phys}}\right)^2}\right] = \frac{M_{ll}^2}{f_{ll}^2} - \left[\frac{\left(M_{\pi^\pm}^{\mathrm{phys}}\right)^2}{\left(f_{\pi^\pm}^{\mathrm{phys}}\right)^2}\right] + \mathcal{O}(\delta m^2), \tag{7.20}$$

which is the same expression as for the isospin-symmetric fit up to contributions in δm^2. For the strange quark mass deviation the expression is changed a little bit to

$$X_s = \frac{M_{us}^2 + M_{ds}^2 - M_{ll}^2}{2 f_{ll}^2} - \left[\frac{\left(M_{K^\pm}^{\mathrm{phys}}\right)^2 + \left(M_{K^0}^{\mathrm{phys}}\right)^2 - \left(M_{\pi^\pm}^{\mathrm{phys}}\right)^2}{2\left(f_{\pi^\pm}^{\mathrm{phys}}\right)^2}\right] + \mathcal{O}(\delta m^2). \tag{7.21}$$

Since the overall number of ensembles is much smaller in this case also the number of available functions has to be reduced. The maximum total degree of of the A_{IB} polynomial is reduced from three to two compared to the isospin-symmetric fits. B_{IB} and C_{IB} are numbers in this case with the additional constraint that at least one of them is fixed to zero. A representative fit of the isospin-breaking continuum extrapolation is shown in Figure 7.2.
Of course, all of these reductions compared to to the isospin-symmetric case will lead to a larger relative spread of mean value but since isospin-breaking effects are expected to be sub-percent, this will not affect the overall precision significantly.

7.2.3 Sea quark contributions

The quantity G (defined in Equation (6.35)) that describes the sea quark contributions to f_k/f_π is measured on the ensembles in Table 6.3. Since there are only three lattice spacings available and the data have a relatively large statistical uncertainty it was made the decision to include only constant and linear functions in a^2 for the continuum extrapolation. Due to large finite volume effects (most of the ensembles have a box size of $\sim 3\,\mathrm{fm}$) the pion and kaon masses are not scattered around the physical point. The extrapolation of X_l and X_s to zero can provide large fit instabilities. Therefore, X_l and X_s are not considered in this study ($B = C = 0$) and we assume that the deviation of the result by shifting the physical point is covered by the large statistical errors. Since there are two 6 fm boxes available on the coarsest lattice spacing also a finite size scaling of $\frac{1}{L^2}$ is included in the analysis. Of course, usually one does not fit an explicit dependence with two independent variables (reduced number of degrees of freedom should be at least one) but we decided to include it to somehow deal with the finite volume effects. Examples of the continuum and infinite volume extrapolations can be seen in Figure 7.2. The `4HEX` ensemble is expected to have smaller discretization artifacts than the other ones. Therefore, when we include it in the fit its lattice artifacts are overestimated. By repeating the analysis with the assumption that the lattice spacing of this specific ensemble is exactly zero, we also include an underestimation of the discretization effects. Thus, we include a conservative estimation of the uncertainty originating from the lattice actions.

7.3 Further aspects of the analysis

In this section we want to highlight some methods and ideas that are important for this study but do not fit really into one of the other sections.

7.3.1 Weighting of the systematics

Within the previous sections a lot of different systematics were mentioned. Basically, there are three kinds of systematics:

1. Systematics related to the extraction of mass and decay constants from the propagator:
   - Local vs. midpoint effective mass
   - Size of the time steps in the effective mass formula $\mathrm{d}t \in \{0.2\,\mathrm{fm}, 0.4\,\mathrm{fm}\}$
   - Early vs. late fit range of the mass and decay constant plateaus
2. Systematics related to the NSNLO finite volume corrections
   - Choice of the Hairpin parameters: $(\delta_A, \delta_V) \in \{(-1, 76, 0.92), (-1.87, 0.00)\}$
   - NSNLO finite volume corrections: NSNLO = SNLO + $\{0, 2\} \times (\mathrm{NNLO} - \mathrm{NLO})^2$

[2] For the isospin-breaking analysis we do not compute NNLO correction but use directly $\{0, 2\} \times$ SNLO.

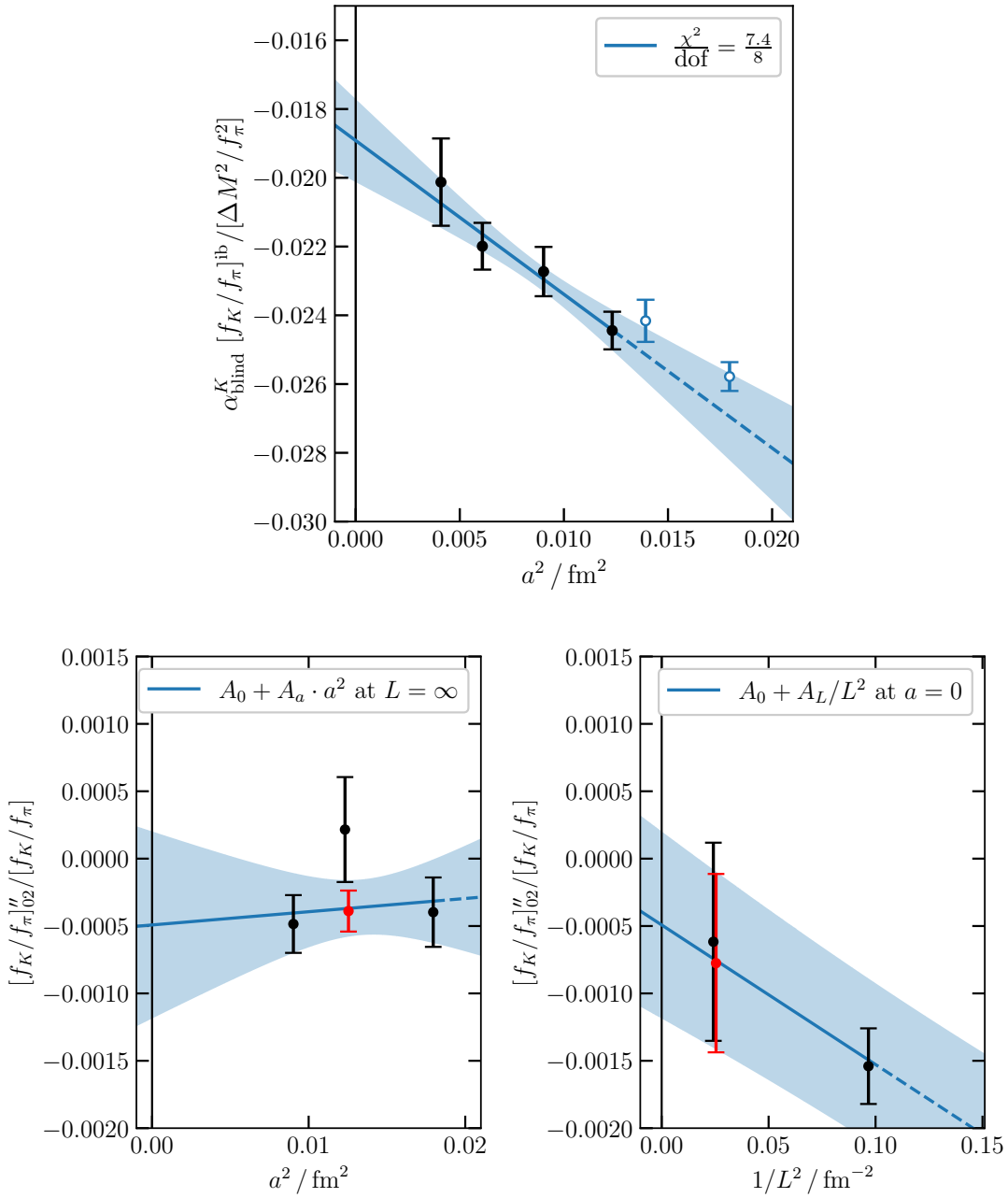

Figure 7.2 *Upper panel*: Continuum extrapolation of the strong-isospin breaking contributions to f_K/f_π. The fit form is a linear function in a^2. All points that correspond to the same lattice spacing are averaged since no quark mass dependence is considered in this fit form. The open points denote points that are not included in the overall fit. *Lower panels:* Relative sea quark contributions to f_K/f_π. The data are fitted to zero lattice spacing and infinite volume simultaneously. We present the continuum extrapolation and infinite volume and the infinite volume extrapolation at zero lattice spacing. In order to do so, the QED+QCD ensembles from Table 6.3 are used. The red points denote the `4HEX` ensemble that is not included in the averaging procedure of measurements at same a or L, respectively. The results corresponding to this fits are given in Table 8.1.

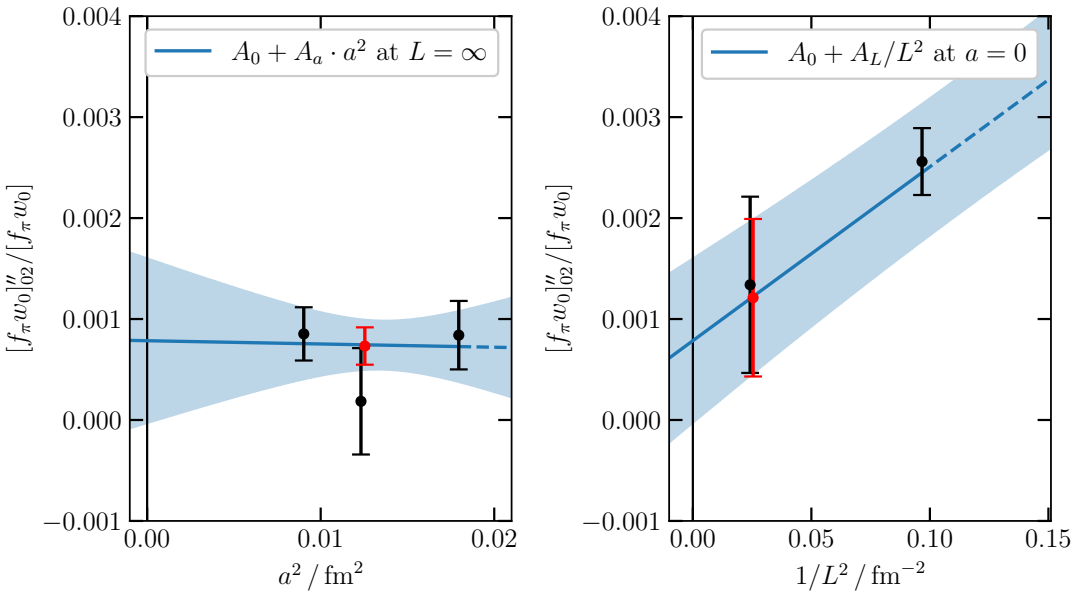

Figure 7.3 Sea quark effects contributing to $f_\pi w_0$. On the left plot the continuum extrapolation at infinite volume is given while on the right plot the infinite volume extrapolation at zero lattice spacing is shown. The strategy is the same as used for the sea quark contributions to f_K/f_π (see Section 6.5 and 7.2). The results corresponding to this fits are given in Table 8.3.

3. Systematics related to the global fit procedure

- Cutting out up to four[3] of the smallest β-values
- a^2 contributions up to third[4] order
- Δ_{KS} contributions up to third[5] order
- Nine[6] total combinations of B and C functions

As it is in done in [19] and in [20] the systematics related to the global fit procedure are weighted according to a modified version of the Akaike-Information-Criterion (AIC) [19, 126]:

$$p = \mathcal{N} \exp\left(-\frac{1}{2}\left(\chi^2_{\text{fit}} + 2n_{\text{fit}} - n_{\text{data}}\right)\right). \tag{7.22}$$

Here χ^2 denotes the total χ^2 of the global fit as described in Section 7.2, n_{fit} is the number of parameters that are used in this specific fit and n_{data} is the number of data points (ensembles) incorporated in this fit. $\mathcal{N}$ is a properly chosen normalization factor. The remaining systematics are "flat-"weighted, which means that for a fixed fit procedure all fit have the same weight. For example if we fit the data to

$$Z = A_0 + a^2 A_1 + B_0 X_l + C_0 X_s \tag{7.23}$$

[3]Three for isospin-breaking
[4]Second for IB
[5]Second for IB
[6]Three for IB

with no β cuts and label all systematics related the mass/decay constant extraction or FV effects by i, j, we get a weight for each continuum limit of

$$w_j^Z = \frac{p_Z^j}{\sum_Z p_Z^j \sum_i 1} \tag{7.24}$$

$$p_Z^j = \exp\left(-\frac{1}{2}\left(\chi^2_{\mathrm{Z,j}} - 21\right)\right), \tag{7.25}$$

where $\chi^2_{\mathrm{Z,j}}$ is the χ^2 of the data to the fit model Z using remaining systematics j.

7.3.2 Blinding and cross checks

To be unbiased during the process of analyzing the data, the kaon decay constant, w_0 and $\sqrt{t_0}$ are multiplied with different unknown blinding factors $\alpha^{\pi}_{\mathrm{blind}}$, $\alpha^{w_0}_{\mathrm{blind}}$ and $\alpha^{t_0}_{\mathrm{blind}}$ respectively. The value of the blinding factors is not known by any of the people involved in this project. The advantage of a multiplicative blinding factor is that our relative precision is unchanged by the blinding procedure, so it can be compared to precisions of other collaboration during the process.
Each step of the whole analysis was performed by at least two people from the group consisting of Fabian Frech, Keith Kelley, Finn Stokes, Gen Wang and Kalman Szabo. This rigorous crosscheck procedure helps ensure the absence of inadvertent errors.

8 Lattice results

In this chapter the total results of the lattice studies are given. Especially, the lattice results to f_K/f_π and their IB and QED (sea quark) contributions are given. Furthermore, the lattice estimates of the dimensionless quantities $M_\Omega w_0$, $f_\pi w_0$ and $f_\pi\sqrt{t_0}$ and the sea quark contributions to $\mathcal{F}_\pi w_0$ are given.

8.1 Computation of the pseudo-scalar decay constant ratio

Our final results of the fits that were performed during the analysis of f_K/f_π are given in Table 8.1. In the upper plots one can see different continuum extrapolations of $[f_K/f_\pi]_{\text{iso}}$ as functions of a^2 and Δ_{KS}, respectively. The colors denote the different weights of the corresponding fits. In the histogram the overall distribution of the isospin symmetric data is shown. The table next to it shows the error budget of this particular analysis from which it can be concluded that the continuum extrapolation (β but, A and A' fit form) is the dominant source of systematic errors. In the table below you can find all of the results of this analysis. On the diagonal there are the results of the isospin-symmetric analysis (A) and its derivatives with respect to X_l (B) and X_s (C). D represents the strong-isospin breaking contributions and G are the sea quark effects. A computation of the valence quark effects can be found in [163].

8.2 Computation of $M_\Omega w_0$

As mentioned before, the physical value of w_0 can be obtained by extrapolating the dimensionless product of w_0 with either M_Ω or f_π, and then dividing by the corresponding physical value. The global fit of the combination

$$w_0 = \frac{(w_0 M_\Omega)^{\text{lat}}}{M_\Omega^{\text{phys}}}, \tag{8.1}$$

where M_Ω^{phys} is the experimentally measured mass of the Ω baryon, can be seen in Figure 8.2. The continuum extrapolation is done using polynomials in either $a^2 = \frac{\left[(aM_\Omega)^{\text{lat}}\right]^2}{\left[M_\Omega^{\text{phys}}\right]^2}$ or $\frac{a^2\Delta_{KS}}{[(aM_\Omega)^{\text{lat}}]^2}$ up to degrees of order three. Similarly to the f_K/f_π global fit in Section 7.2 the coarsest three lattice spacings can be excluded, and the physical point is reached via interpolations in X_l and X_s. The histogram of all the fits can be seen in Figure 8.2. The left-hand side of the histogram has a Gaussian shape, while the right-hand side has a longer tail. This can be explained by the curvature of the data in combination with the third-order polynomial in a^2 that shift the continuum limit towards higher values, as evident in the continuum extrapolation above. The error budget is given in Table 8.2. The most dominant systematic error source is the choice of the continuum parameter, which makes sense because Δ_{KS} provides a much smaller extrapolation range than the usual a^2 fits. The next largest error source (even larger than the statistical error) is the choice of the fit range for the Ω propagator. Thus, we can see how important proper analysis of the Ω baryon mass is in this context. For example, in the global fits for the decay constant the choice of the fit ranges only contributed sub-leading to the total error.

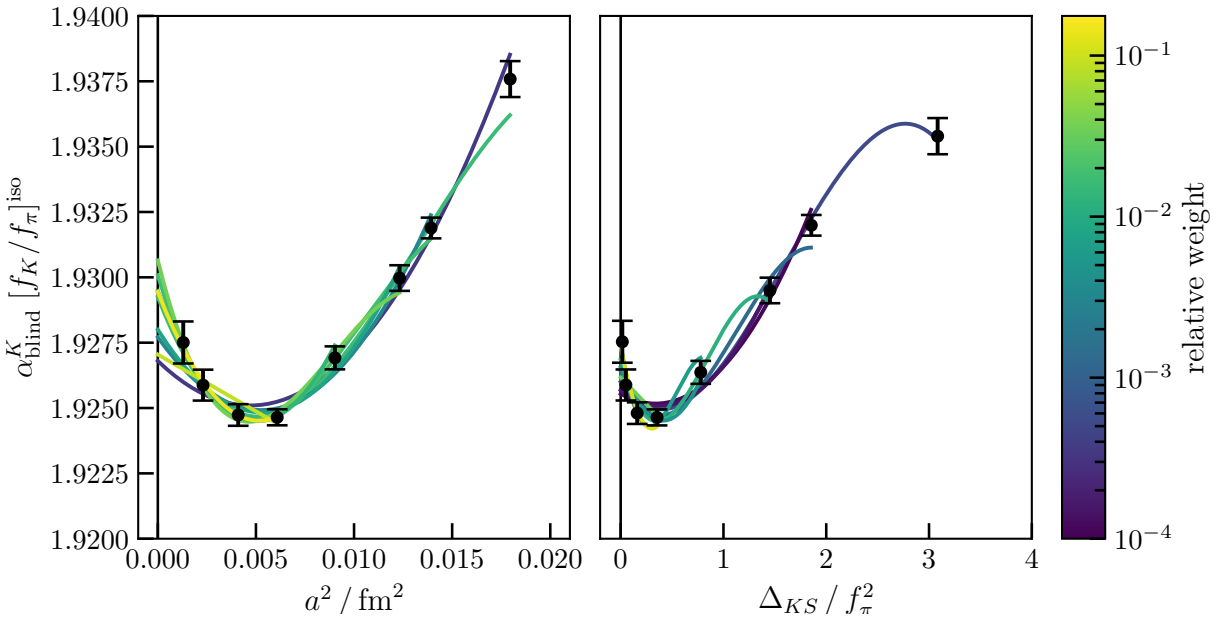

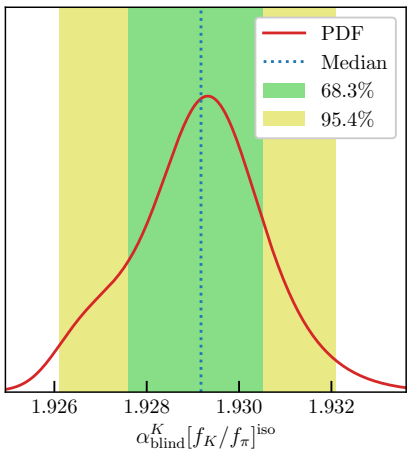

median	1.9292	
statistical error	0.0011	0.058 %
full systematic error	0.0010	0.053 %
Plateau region	0.000018	0.00095 %
Effective mass dt	0.00013	0.0070 %
Effective mass form	0.00016	0.0081 %
Hairpin parameters	0.0000032	0.00017 %
NNLO XPT FV	0.0000022	0.00011 %
Beta cut	0.00017	0.0088 %
A	0.00062	0.032 %
A' fit form	0.00037	0.019 %
B fit form	0.000046	0.0024 %
C fit form	0.000030	0.0016 %

	A	*B*	*C*	*D*	*G*
A	$1.9292(12)(^{+8}_{-12})[^{+14}_{-17}]$	0.06(0.06)(0.06)	0.22(0.1)(0.39)	0.08(0.05)(0.11)	–
B		$-0.030(18)(^{+11}_{-8})[^{+21}_{-20}]$	−0.22(−0.34)(−0.02)	0.07(−0.01)(0.17)	–
C			$0.0157(17)(^{+7}_{-13})[^{+18}_{-21}]$	0.21(0.19)(0.23)	–
D				$-0.0186(33)(^{+29}_{-16})[^{+44}_{-37}]$	–
G					$-0.0005(7)(^{+12}_{-4})[^{+14}_{-8}]$

Table 8.1 Blinded lattice results of the f_K/f_π-study. *Upper left panel:* Different continuum extrapolations in a^2, the points are shifted to physical masses and are averaged if they correspond to the same lattice spacing. The colors denote relative weights of the corresponding fits. *Upper-right panel:* Different continuum extrapolations in Δ_{KS}. *Center left panel:* Total histogram of the isospin-symmetric f_K/f_π continuum extrapolation. *Center right panel:* Error budget of the f_K/f_π continuum extrapolation. *Lower panel*: Continuum results (diagonal) and their correlation coefficients with the corresponding statistical and systematic contributions (off-diagonal). The medians from the tables and the histograms differ slightly. This is an artifact of the binning of the histogram. However, for the final results the values from the tables are taken, which use the methods from [19, 20].

8.3 Computation of $f_\pi w_0$

For the computation of $f_\pi w_0$ we add another systematic ingredient by computing the gradient flow based scale w_0 with either the Wilson or the Symanzik improved Zeuthen-flow (see Section 4.4). This systematic is chosen to be a flat-weighted ingredient within the analysis. Furthermore, we skip the finest ensembles ($\beta = 4.3032$) since they were not available when the paper was originally published [20]. A comparison of pure a^2 and pure Δ_{KS} fit forms can be seen in Figure 8.3. Here, the relative weight of the corresponding fit is marked with an associated color. Below that, the total histogram of the distributions of the continuum values of $f_\pi w_0$ and the error budget are given. The error budget is dominated the choice of the gradient flow (Wilson flow vs. Symanzik improved Zeuthen flow). At the bottom, the results of the constituents of the analysis are given. On the diagonal, the FLAG scheme continuum result (A) and its derivatives with respect to X_l and X_s (B and C) are given. The G-coefficient describes the sea quark contributions to the total result. For these quantities, the first error is statistical, the second is systematic and the third (in squared brackets) is the total error. On the off-diagonals of the table, you can find the correlation coefficients of the respective quantities split up into their statistical and systematic contributions.

8.4 Computation of $f_\pi \sqrt{t_0}$

The computation of $f_\pi \sqrt{t_0}$ largely follows the same procedure as the computation of $f_\pi w_0$, with only a few differences. Obviously, the target observable is replaced by $f_\pi \sqrt{t_0}$, and we only compute the pure QCD value of $\sqrt{t_0}$ in the FLAG scheme, as we do not have access to data for the sea quark contributions.
A comparison of different fit forms depending on only a^2 or Δ_{KS} is shown in Figure 8.4. Continuum extrapolations only depending on Δ_{KS} do not seem to describe the data properly, while combinations of a^2 and Δ_{KS} contributions are suitable to describe the data. It can also be seen that the overall error is dominated by the continuum extrapolation followed by the choice of the gradient flow.

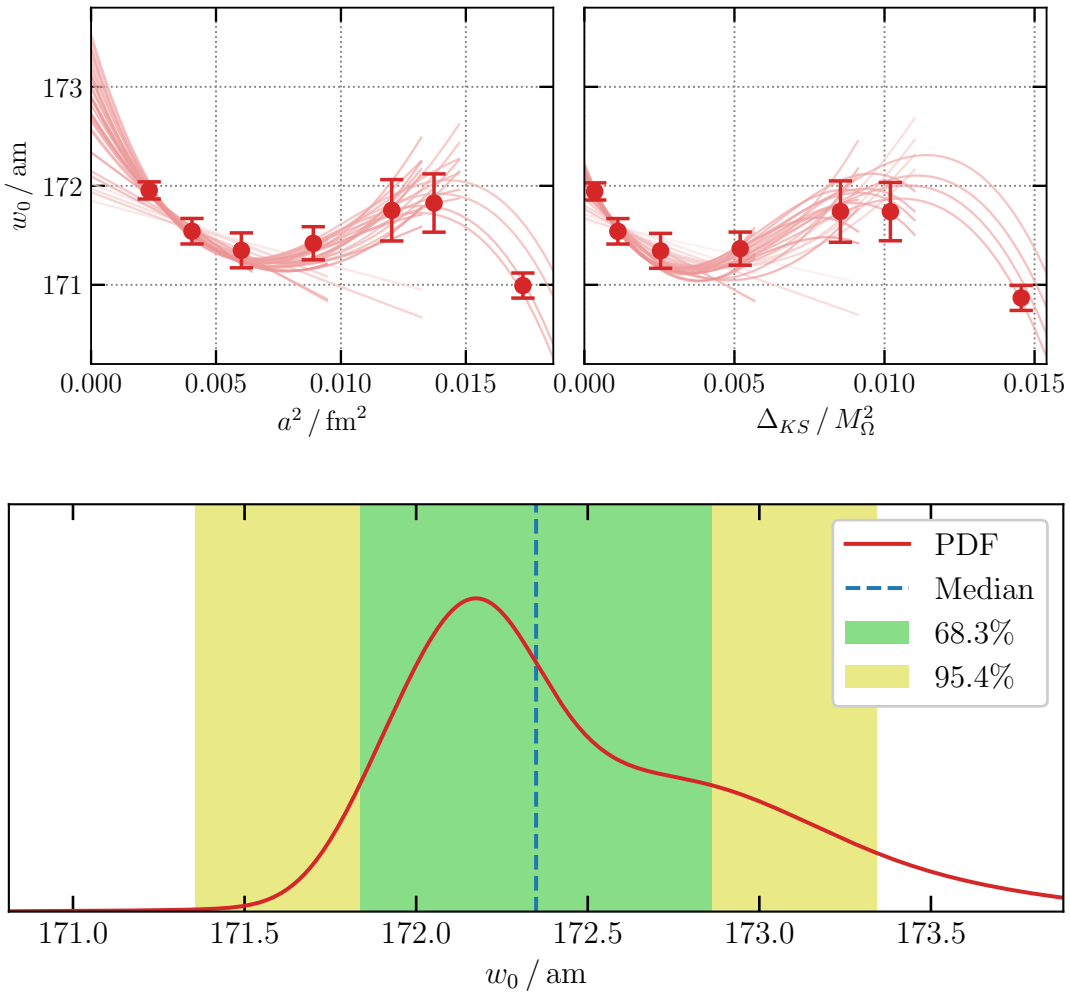

Median	172.35 am	
Total error	0.51 am	0.30 %
Statistical error	0.22 am	0.13 %
Systematic error	0.46 am	0.27 %
Pseudo-scalar fit range	0.01 am	< 0.01 %
Omega baryon fit range	0.24 am	0.14 %
Physical value of M_Ω	0.06 am	0.03 %
Lattice spacing cuts	0.09 am	0.05 %
Order of fit polynomials	0.17 am	0.10 %
Continuum parameter (Δ_{KS} or a^2)	0.30 am	0.17 %

Table 8.2 *Upper left panel:* Continuum extrapolation of the w_0 scale, estimated with the Ω baryon mass, in terms of a^2. *Upper right panel:* Continuum extrapolation of the same quantity in terms of Δ_{KS}. *Center panel:* Total histogram of w_0 with the one- and two-sigma bands *Lower panel:* Error budget of w_0 computed with the mass of the Ω baryon. Previously published in [20].

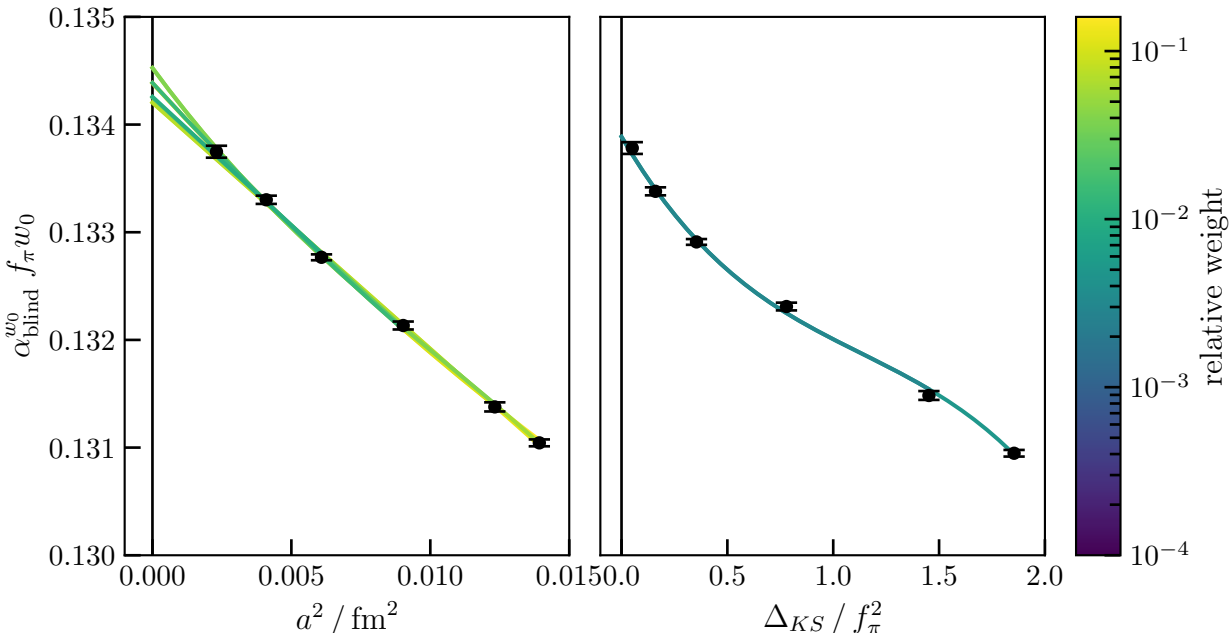

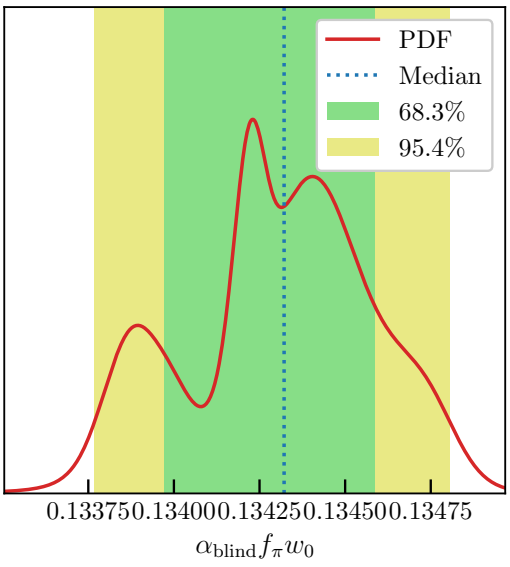

median	0.13455	
statistical error	0.00015	0.11 %
full systematic error	0.00027	0.20 %
Wilson/Zeuthen(sy)	0.00017	0.12 %
Plateau region	0.000016	0.012 %
Effective mass dt	0.00000075	0.00056 %
Effective mass form	0.000025	0.019 %
Hairpin parameters	0.0000017	0.0013 %
NNLO XPT FV	0.000014	0.010 %
Beta cut	0.000063	0.047 %
A	0.00011	0.085 %
A' fit form	0.000057	0.042 %
B fit form	0.0000059	0.0044 %
C fit form	0.0000048	0.0036 %

	A	B	C	G
A	$0.1346(1)(^{+2}_{-3})[^{+2}_{-4}]$	$-0.09(0.02)(-0.22)$	$-0.03(0.42)(-0.52)$	–
B		$0.0069(21)(^{+13}_{-0})[^{+25}_{-21}]$	$-0.19(-0.17)(-0.24)$	–
C			$-3(15)(^{+4}_{-9})[^{+16}_{-8}] \times 10^{-5}$	–
G				$9(9)(^{+2}_{-9})[^{+10}_{-13}] \times 10^{-5}$

Table 8.3 Blinded lattice results of the $f_\pi w_0$-study. *Upper left panel:* Different continuum extrapolations in a^2, the points are shifted to physical masses and are averaged if they correspond to the same lattice spacing. The colors denote relative weights of the corresponding fits. *Upper right panel:* Different continuum extrapolations in Δ_{KS}. *Center left panel:* Total histogram of the isospin-symmetric $f_\pi w_0$ continuum extrapolation. *Center right panel:* Error budget of the $f_\pi w_0$ continuum extrapolation. *Lower panel*: Continuum results (diagonal) and their correlation coefficients (off-diagonal).

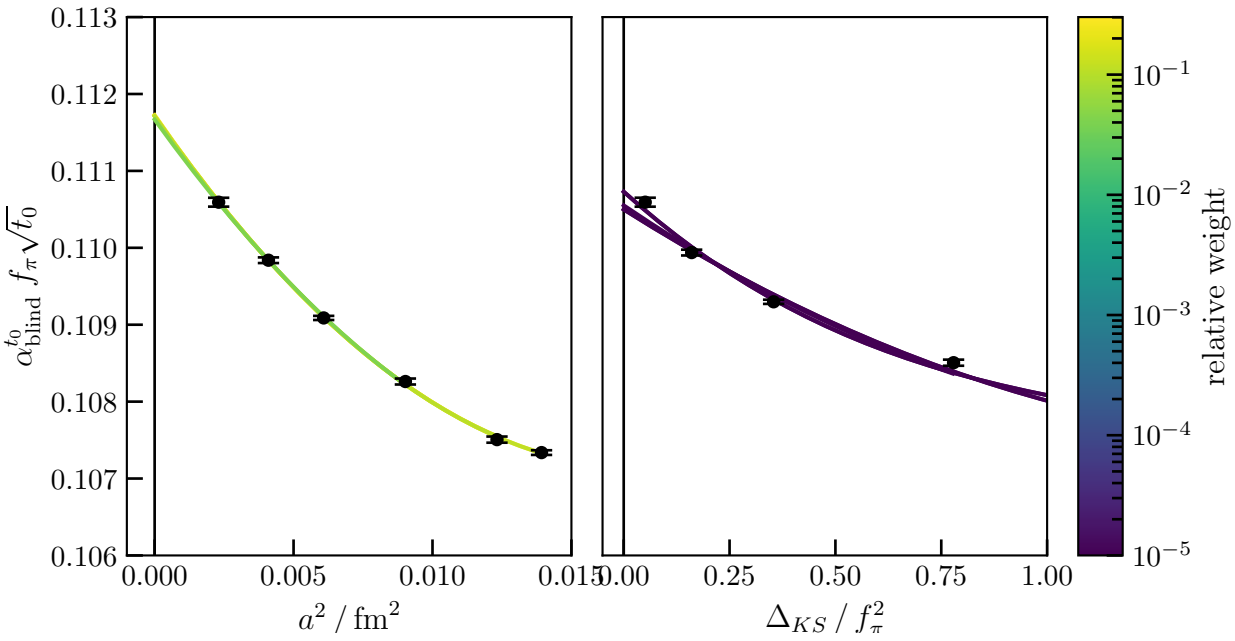

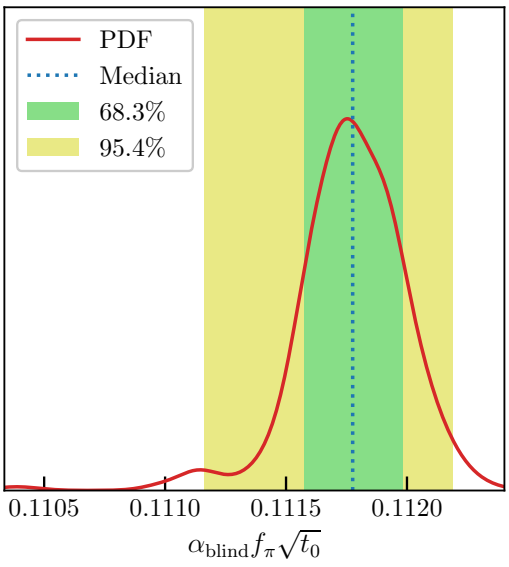

median	0.11184	
statistical error	0.00018	0.16 %
full systematic error	0.00020	0.18 %
Wilson/Zeuthen(sy)	0.000096	0.085 %
Plateau region	0.000030	0.027 %
Effective mass dt	0.0000100	0.0089 %
Effective mass form	0.000015	0.014 %
Hairpin parameters	0.0000053	0.0048 %
NNLO XPT FV	0.000018	0.016 %
Beta cut	0.000067	0.060 %
A	0.00012	0.11 %
A' fit form	0.000047	0.042 %
B fit form	0.0000059	0.0053 %
C fit form	0.000025	0.022 %

	A	B	C	G
A	$0.1118(2)(^{+2}_{-3})[^{+3}_{-4}]$	$0.03(0.01)(0.07)$	$0.10(-0.05)(0.31)$	–
B		$0.0069(22)(^{+13}_{-5})[^{+25}_{-24}]$	$-0.20(-0.12)(-0.36)$	–
C			$3(2)(^{+0}_{-2})[^{+2}_{-3}] \times 10^{-4}$	–
G				–

Table 8.4 Blinded lattice results of the $f_\pi\sqrt{t_0}$-study. *Upper left panel:* Different continuum extrapolations in a^2, the points are shifted to physical masses and are averaged if they correspond to the same lattice spacing. The colors denote relative weights of the corresponding fits. *Upper right panel:* Different continuum extrapolations in Δ_{KS}. *Center left panel:* Total histogram of the isospin-symmetric $f_\pi\sqrt{t_0}$ continuum extrapolation. *Center right panel:* Error budget of the $f_\pi\sqrt{t_0}$ continuum extrapolation. *Lower panel*: Continuum results (diagonal) and their correlation coefficients (off-diagonal).

9 Phenomenology

The lattice simulations discussed in the previous chapters aim to address tensions between experimental results and theoretical predictions. Beyond this, lattice QCD offers powerful tools to investigate fundamental aspects of the standard model such as the unitarity of the CKM matrix and the anomalous magnetic moment of the muon. Additionally, scale setting - that is, the determination of the lattice spacing - remains a crucial and ongoing challenge in lattice QCD, often leading to discrepancies and debates within the lattice community.

9.1 The anomalous magnetic moment of the muon

The anomalous magnetic moment of the muon $a_\mu = \frac{g_\mu - 2}{2}$ is currently one of the most important test parameters for the standard model of particle physics. In experiments, it has been measured up to a precision of 0.2 ppm [8], with the current experimental average being

$$a_\mu = 116,592,055(25) \times 10^{-11}. \tag{9.1}$$

From the theory point of view its value is dominated by electromagnetic contributions that can be computed using perturbation theory. In addition, there are small contributions from electroweak and hadronic light-by-light effects [168–174]. Also, hadronic vacuum polarization (HVP) effects contribute to a_μ by a small amount, which is called $a_\mu^{\text{LO-HVP}}$. Although the absolute contribution is very small compared to the QED contribution, the error is dominated by the HVP part [168]. Currently, there are two methods that are used to obtain a value for $a_\mu^{\text{LO-HVP}}$: A lattice computation from first principles, and the data-driven approach. With lattice QCD, $a_\mu^{\text{LO-HVP}}$ can be computed from the vector correlation function via

$$a_\mu^{\text{LO-HVP}} = \alpha^2 \int_0^\infty \mathrm{d}t\, K(t)\, C_{1\gamma I}(t), \tag{9.2}$$

$$K(t) = \int_0^\infty \frac{\mathrm{d}Q^2}{m_\mu^2} \omega\left(\frac{Q^2}{m_\mu^2}\right)\left(t^2 - \frac{4}{Q^2}\sin^2\left(\frac{tQ}{2}\right)\right), \tag{9.3}$$

$$\omega(x) = \frac{\left[x + 2 - \sqrt{x(x+4)}\right]^2}{\sqrt{x(x+4)}}, \tag{9.4}$$

where $C_{1\gamma I}(t)$ is the one-photon irreducible part of the vector propagator, m_μ the mass of the muon and α the electromagnetic fine-structure constant. Using the R-ratio the HVP-contributions to a_μ can be computed using [127]

$$a_\mu^{\text{LO-HVP}} = \left(\frac{\alpha m_\mu}{2\pi}\right)^2 \int_0^\infty \frac{\mathrm{d}s}{s^2}\, \hat{K}(s) R(s), \tag{9.5}$$

$$\hat{K}(s) = \frac{3s^{5/2}}{8m_\mu^4} \int_0^\infty \mathrm{d}t\, e^{-t\sqrt{s}} K(t). \tag{9.6}$$

Commonly, the time interval $[0, \infty)$ is split into several windows. This is done because different length scales on the lattice come along with different statistical and systematic subtleties that can be considered separately with this approach. Whenever an integration with respect to the Euclidean time is performed on the lattice,

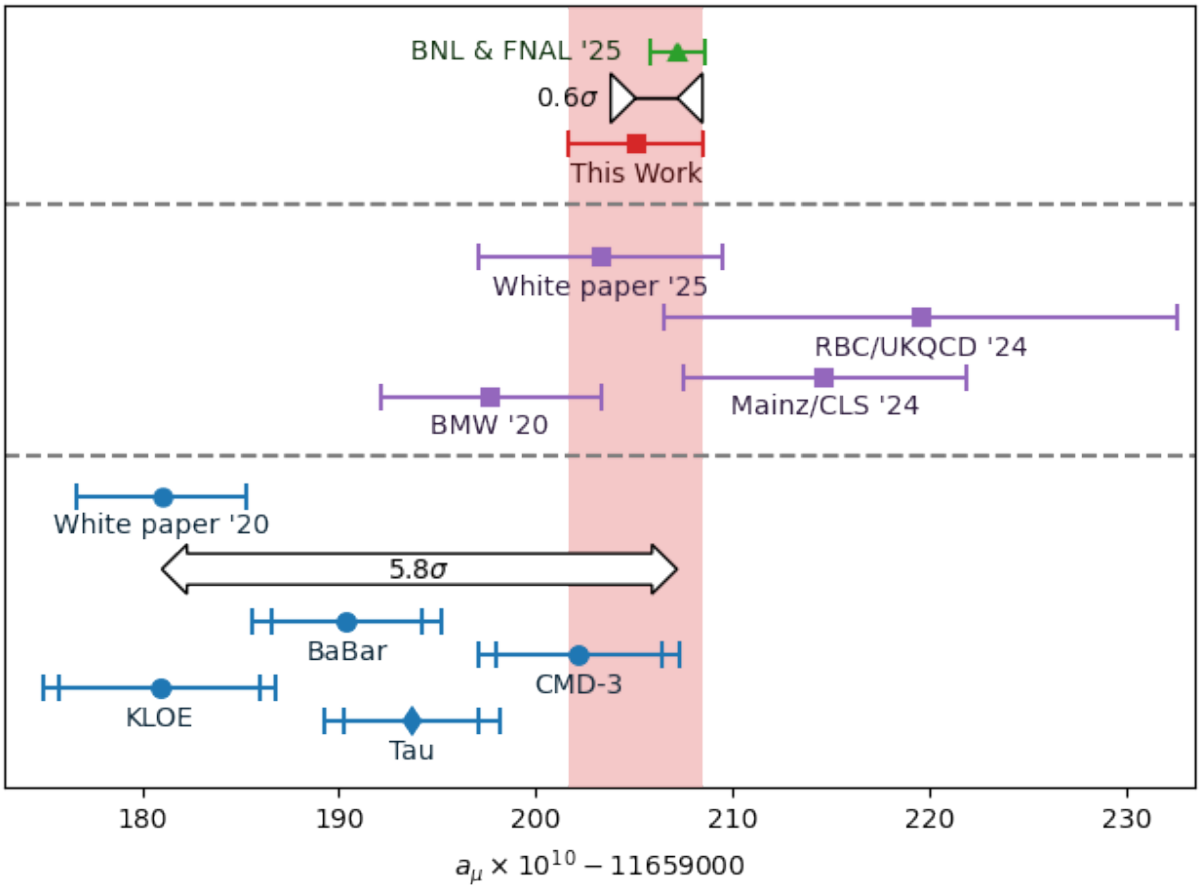

Figure 9.1 Comparison of experimental measurements and theoretical predictions (with or without data-driven inputs). The green data point represents the mean value of experimental measurements of a_μ [8, 175–177] while the other data are theoretical predictions that estimate the HVP contributions in different ways: The purple data points show pure lattice calculations [19, 178–180] while the blue ones use different data-driven approaches [181–190]. The best theoretical prediction (red), that is available at the moment uses data-driven approaches for the small tail contributions of the HVP. Figure is taken from [20].

we can pick out a time interval (t_i, t_f) with the (smooth) window function

$$W(t; t_i, t_f, \Delta) = \begin{cases} 1, & \text{if } t_i = 0 \text{ and } t_f = \infty \\ 1 - \theta(t - t_f, \Delta), & \text{if } 0 = t_i < t_f < \infty \\ \theta(t - t_i, \Delta) - \theta(t - t_f, \Delta), & \text{if } 0 < t_i < t_f < \infty \\ \theta(t - t_i, \Delta), & \text{if } 0 < t_i < t_f = \infty \end{cases} \tag{9.7}$$

$$\theta(t, \Delta) = \frac{1 + \tanh\left(\frac{t}{\Delta}\right)}{2}, \tag{9.8}$$

where usually $\Delta = 0.15\,\text{fm}$ and the three windows $[0.0\,\text{fm}, 0.4\,\text{fm}]$ (short distance), $[0.4\,\text{fm}, 1.0\,\text{fm}]$ (intermediate distance) and $[1.0\,\text{fm}, \infty\,\text{fm})$ (long distance) are chosen [127, 168, 191].

The first theoretical computation of $a_\mu^{\text{LO-HVP}}$ that reaches the precision of the experiments was done by the BMW collaboration in 2020 (see Figure 9.1). At the same time another group of theoretical physicists published a value of $a_\mu^{\text{LO-HVP}}$ that showed a 5σ-disagreement with the experimental results [168]. In this paper the HVP effects were estimated using a data-driven approach that uses the R-ratio of electron-positron scattering for the HVP. Due to the fact that at the current level of precision there are a lot of contradicting predictions for $a_\mu^{\text{LO-HVP}}$ this is a very interesting topic for physicists that look for Beyond-Standard-Model

(BSM) effects. In order to resolve this problem experimentalists and theorist aim to increase the precision of their respective results.
After the first experimental values of $g-2$ from Fermilab were published in 2021 [192], the update came out in 2023 with the precision given in Equation (9.1) [8]. The final results with the best precision are expected to be published in 2025. Also, a lot of lattice calculations were published during the last years [179, 180, 193–199].
An important aspect of a high-precision computation of $a_\mu^{\text{LO-HVP}}$ is the setting of the lattice spacing. This is often done using the gradient-flow based observable w_0 that has to be determined beforehand up to a very high precision. In the previous chapters the computations of different dimensionless quantities with the w_0 were discussed. From this we can extract this quantity in different ways:
Using the mass of the Ω-baryon we get a total results of

$$w_0 = 0.17245(22)(46)[51]\,\text{fm} \tag{9.9}$$

where the first error is statistical and the second is systematic. Here, strong-isospin breaking contributions of $\sim 0.0001\,\text{fm}$ are added to the lattice results [19, 20] of $M_\Omega w_0$ after dividing by the physical mass of the Ω^- baryon [43].
To extract w_0 from the $f_\pi w_0$-combination we have to bring the pion decay rate

$$\Gamma(\pi^+ \to \ell\bar{\nu}_\ell) = \frac{G_F^2}{8\pi} m_\ell^2 M_\pi \left(1 - \frac{m_\ell^2}{M_\pi^2}\right)^2 \times |V_{u\bar{d}}|^2 \times f_\pi^2 \times (1+\delta_\pi) \tag{9.10}$$

to mind. The experimentally estimated value of this quantity is [140]

$$\Gamma^{\text{exp}}(\pi^+ \to \ell\bar{\nu}_\ell) = 3.8408(7) \times 10^{-7}\,\text{s}^{-1}. \tag{9.11}$$

The pure QCD decay constant is defined by dividing out the kinematical factors as well as the first CKM element $|V_{ud}| = 0.97373(31)$ [200] and radiative corrections [163]:

$$f_\pi^{\text{GRS}} = 130.65(12)\,\text{MeV} \tag{9.12}$$

Thus, we can compute w_0 by transforming $f_\pi w_0$ into the GRS-scheme (with the coefficients from Table 8.3), adding the sea quark effects and dividing out f_π^{GRS}

$$\alpha_{\text{blind}}^{w_0} w_0 = \frac{1}{f_\pi^{\text{GRS}}} \left(A + B(X_l^{\text{GRS}} - X_l^{\text{FLAG}}) + C(X_s^{\text{GRS}} - X_s^{\text{FLAG}}) + G(B,C)\right), \tag{9.13}$$

which results in a total value of

$$w_0 = 0.17270(21)_{\text{stat.}}(34)_{\text{QCD}}(19)_{\text{valence \& exp}}(9)_{\text{sea}}[45]_{\text{tot.}}\,\text{fm} \tag{9.14}$$

In Figure 9.2, it can be seen that the overall distribution of w_0 exhibits a distinctly Gaussian shape, in contrast to the histogram of $f_\pi w_0$ shown in Table 8.3. This difference arises from the use of various experimental inputs and radiative corrections, which introduce additional uncertainties. These uncertainties effectively smooth out the statistical and systematic fluctuations, leading to a more Gaussian-like distribution. The estimation beats the precision of the prediction using the Ω baryon mass and all studies of other lattice groups, including the FLAG average, as can be seen in Figure 9.3. The new w_0 value based on the pion decay constant is perfectly compatible with the estimation using the Ω^- baryon mass and the FLAG average, respectively [20, 194].

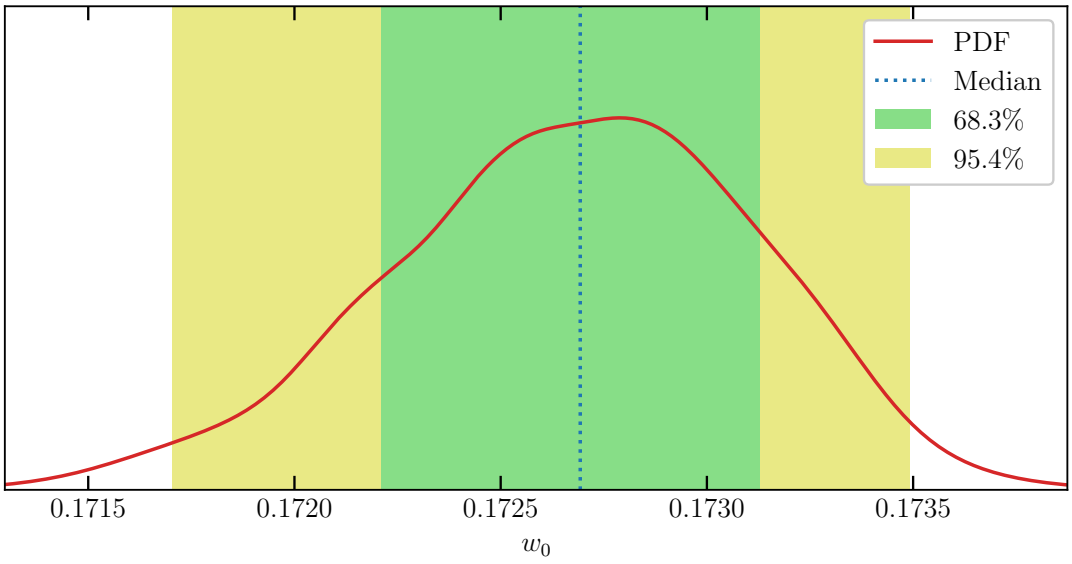

Figure 9.2 Total histogram of our w_0 estimation based on the pion decay constant.

To compute the QED contribution to w_0 in the FLAG scheme we consider the difference

$$w_0^{\text{QED,FLAG}} = w_0 - \frac{[f_\pi w_0]^{\text{FLAG}}}{f_\pi^{\text{FLAG}}} = -0.00026(9)_{\text{stat.}}(1)_{\text{QCD}}(19)_{\text{valence \& exp}}(9)_{\text{sea}}[22]_{\text{tot.}}\,\text{fm} \tag{9.15}$$

which is nearly compatible with zero at our current precision.

9.2 Lattice computation of $\mathcal{F}_K/\mathcal{F}_\pi$ as a test for the CKM-unitarity

In the following section we will discuss the unitarity of the Cabibbo-Kobayashi-Maskawa matrix and its relation to the meson decay constants. The topic is of special interest because state-of-the-art calculations show a $2-3\,\sigma$ discrepancy to experimental results. High precision lattice QCD computations [55, 201, 203, 205–214] can help to further investigate this issue by providing precise values for the mesonic decay constant that — in combination with experimental measurements [43, 140] — put the standard model of particle physics to the test.

9.2.1 The CKM unitarity and its relation to the meson decay constants

With a mass of $M_{\pi^\pm} = 139.57039(18)\,\text{MeV}$ and $M_{\pi^0} = 134.9768(5)\,\text{MeV}$ [43], pions are the lightest hadrons.[1] Therefore it is straightforward to conclude that they are stable under strong interaction. However, a pion can decay via weak processes into leptons, as shown in 9.4. On the other hand, the kaon is the lightest hadron with non-zero strangeness ($M_K = 493.677(16)\,\text{MeV}$ [43]). Since strangeness is a conserved quantity under strong interactions [40], the kaon also only has weak decay channels, but it also has non-leptonic decay products (such as pions). Nevertheless, in this study we only care about the leptonic decay channels, at least for the charged kaon.

In weak interactions, the transformations of the quark-flavors (which are necessary for the vertices at which the $W^\pm$ boson is created) happen with probabilities related to the elements of the Cabibbo-Kobayashi-Maskawa

[1] Note that the $\pi^\pm$ is not allowed to decay into π^0 due to charge conservation.

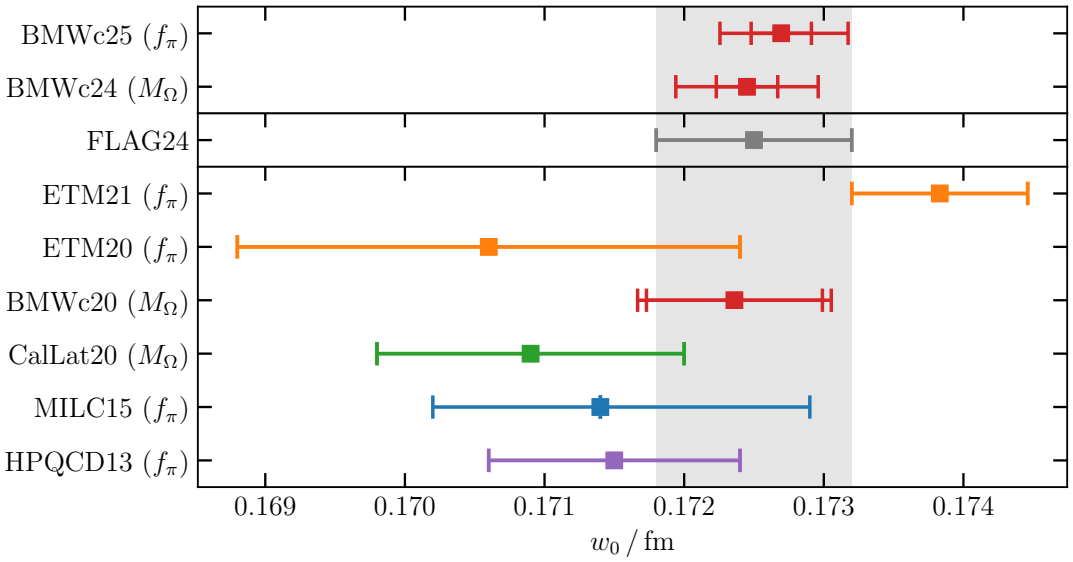

Figure 9.3 Comparison of several estimations of w_0 [19, 20, 201–205] and the average from the FLAG report 2024 [138]. The data are still blinded, so the result from our study is shifted such that it aligns with the FLAG average. However, the relative errors can be compared due to our multiplicative blinding procedure.

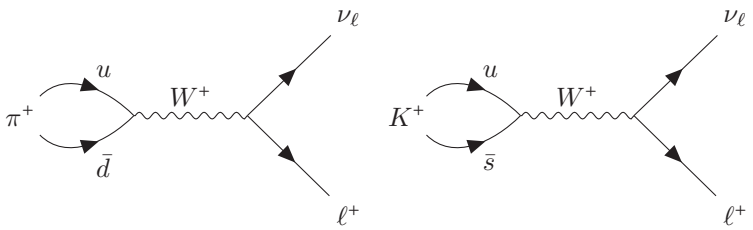

Figure 9.4 The leptonic decay of the positively charged pion π^+ (left) and kaon (right). To get the diagrams for the negatively charged meson all of the particles have to be replaced by their antiparticles. Nearly 100% of all pions decay into muons, because the tauon is heavier than the pion [43] and the e/ν_e final state is suppressed because of helicity conservation [215].

(CKM) matrix [216, 217]:

$$V^{\mathrm{CKM}} = \begin{pmatrix} V_{u\bar{d}} & V_{u\bar{s}} & V_{u\bar{b}} \\ V_{c\bar{d}} & V_{c\bar{s}} & V_{c\bar{b}} \\ V_{t\bar{d}} & V_{t\bar{s}} & V_{t\bar{b}} \end{pmatrix}. \tag{9.16}$$

The unitarity of this matrix is a direct consequence of the fact that each quark of a given up-type flavor can only be transformed into exactly one quark of a given down-type flavor and vice versa.
The CKM matrix has four free real parameters,[2] and is commonly parametrized with the angles $\theta_{12}, \theta_{13}, \theta_{23}$ and the phase δ via

$$V^{\mathrm{CKM}} = \begin{pmatrix} \cos\theta_{12}\cos\theta_{13} & \sin\theta_{12}\cos\theta_{13} & \sin\theta_{13}e^{\mathrm{i}\delta} \\ -\sin\theta_{12}\cos\theta_{23} - \sin\theta_{23}\cos\theta_{12}\sin\theta_{13}e^{\mathrm{i}\delta} & \cos\theta_{12}\cos\theta_{23} - \sin\theta_{23}\sin\theta_{12}\sin\theta_{13}e^{\mathrm{i}\delta} & \sin\theta_{23}\cos\theta_{12} \\ \sin\theta_{12}\sin\theta_{23} - \cos\theta_{23}\cos\theta_{12}\sin\theta_{13}e^{\mathrm{i}\delta} & -\cos\theta_{12}\sin\theta_{23} - \cos\theta_{23}\sin\theta_{12}\sin\theta_{13}e^{\mathrm{i}\delta} & \cos\theta_{23}\cos\theta_{12} \end{pmatrix}. \tag{9.17}$$

Using the parameters

$$\lambda = \sin\theta_{12} \tag{9.18}$$

$$A = \frac{\sin\theta_{23}}{\sin^2\theta_{12}} \tag{9.19}$$

$$\eta = \frac{\sin\theta_{13}}{\sin\theta_{12}\sin\theta_{23}}\sin\delta \tag{9.20}$$

$$\rho = \frac{\sin\theta_{13}}{\sin\theta_{12}\sin\theta_{23}}\cos\delta \tag{9.21}$$

one can introduce the Wolfenstein parametrization of the CKM matrix [218]:

$$V^{\mathrm{CKM}} = \begin{pmatrix} 1 - \frac{\lambda^2}{2} & \lambda & A\lambda^3(\rho - \mathrm{i}\eta) \\ -\lambda & 1 - \frac{\lambda^2}{2} & A\lambda^2 \\ A\lambda^3(1 - \rho - \mathrm{i}\eta) & -A\lambda^2 & 1 \end{pmatrix} + \mathcal{O}(\lambda^4). \tag{9.22}$$

Within this project a simplified view on the unitarity of the CKM matrix is sufficient. However, we only investigate the first row unitarity, i.e.,

$$|V_{u\bar{d}}|^2 + |V_{u\bar{s}}|^2 + |V_{u\bar{b}}|^2 = 1. \tag{9.23}$$

On the other hand, experimental measurements suggest that the value of $|V_{u\bar{b}}|^2$ is much smaller than the precision of current lattice computations [43], therefore the latter equation can be reduced to

$$|V_{u\bar{d}}|^2 + |V_{u\bar{s}}|^2 \approx 1 \tag{9.24}$$

and λ from the Wolfenstein parametrization in Equation (9.18) and (9.22) is the remaining quantity of interest.
Now the question arises how Equation (9.24) is related to the meson decay constants. In order to clarify this

[2] A generic 3×3 complex matrix has 18 real parameters. Here, there are nine constraints from the unitarity. Furthermore, five degrees of freedom are phases that can be absorbed into the quark fields, whereas one overall global phase cannot be absorbed.

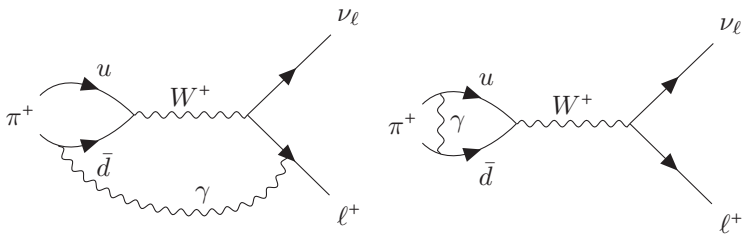

Figure 9.5 Examples for diagrams that include the radiative corrections from Equation (9.25). The diagram on the left describes an additional photon exchange between one of the quarks and the lepton, while on the right diagram an additional photon connects the two quarks of the pion. More diagrams that contribute to radiative corrections for meson decays are shown in [163].

issue we consider the decay width of the processes that are shown in Figure 9.4:

$$\Gamma(\pi^+ \to \ell\bar{\nu}_\ell) = \frac{G_F^2}{8\pi} m_\ell^2 M_\pi \left(1 - \frac{m_\ell^2}{M_\pi^2}\right)^2 \times |V_{u\bar{d}}|^2 \times f_\pi^2 \times (1 + \delta_\pi) \tag{9.25}$$

$$\Gamma(K^+ \to \ell\bar{\nu}_\ell) = \frac{G_F^2}{8\pi} m_\ell^2 M_K \left(1 - \frac{m_\ell^2}{M_K^2}\right)^2 \times |V_{u\bar{s}}|^2 \times f_K^2 \times (1 + \delta_K) \tag{9.26}$$

Here $G_F = 1.1663787(6)\,\mathrm{GeV}^{-2}$ [219] is the Fermi-constant that is related to the coupling constant of the weak interaction g_w via

$$G_F = \frac{\sqrt{2}}{8} \frac{g_w^2}{m_W^2}. \tag{9.27}$$

m_X is the mass of a fundamental particle X and M_Y describes the mass of a hadron Y. f_π and f_K are the decay constants of the respective mesons and the δ's are the radiative corrections that take care of the inclusion of QCD+QED diagrams, some examples are shown in Figure 9.5. For the combined QCD+QED decay constant, the notation $\mathcal{F}_H := f_H\sqrt{1+\delta_H}$ is commonly used. Combing the Equations (9.25) and (9.26) we can immediately observe that the matrix elements of the CKM matrix are related via the formula

$$|V_{ud}| = \frac{\sqrt{M_K}\left(1 - \frac{m_\ell^2}{M_K^2}\right)}{\sqrt{M_\pi}\left(1 - \frac{m_\ell^2}{M_\pi^2}\right)} \frac{f_K}{f_\pi} \sqrt{\frac{1+\delta_K}{1+\delta_\pi}} |V_{us}|. \tag{9.28}$$

From the Wolfenstein parametrization in Equation (9.22) one can get another connection:

$$|V_{ud}| = 1 - \frac{|V_{us}|^2}{2} + \mathcal{O}\left(|V_{ud}|^4\right) \tag{9.29}$$

Using elementary calculus it can be found out that there is a unique positive solution of both of the latter equations. So the question arises where the $2-3\,\sigma$ tension between theory and experiment comes in. The answer is that there are two more experiments that provide constraint on $|V_{ud}|$ respectively $|V_{us}|$ separately. One the one hand, results on the super-allowed β decays [200, 220, 221] give further information on $|V_{ud}|$, whereas on the other hand, semi-leptonic kaon decays provide a value for $|V_{us}|$.

Nuclear β decay is the conversion of a neutron into proton or vice-versa (whatever is energetically favorable) under radiation of an electron(positron) and the corresponding (anti)neutrino. The corresponding Feynman diagrams are shown in Figure 9.6.

A β decay is called *superallowed* if the wave-function of the nucleon is unchanged apart from the fact that the flavor of one quark is changed. While the half-lives of the whole set of β decays span more than 20 orders of magnitude, the small set of 13 superallowed β decays has shown to have a constant intrinsic strength [222].

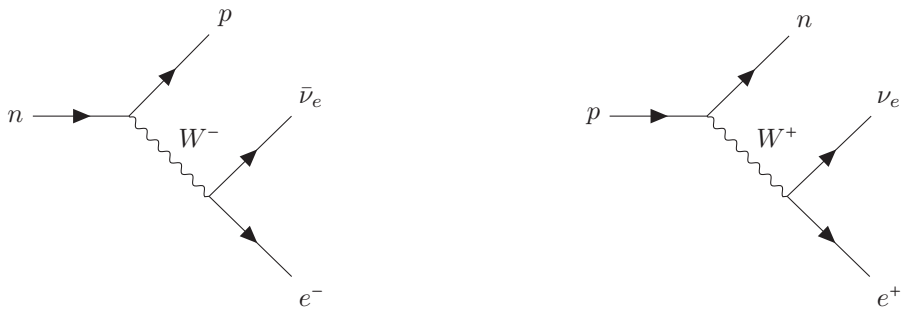

Figure 9.6 *Left-hand side:* Nuclear β decay: A down quark is transformed into an up quark under radiation of a W^- boson. Since the down quark was a parton of a neutron, this neutron is transformed into a proton. The total charge of the nucleus is increased by 1, therefore this nuclear process changed the element. The W^- boson decays into an electron and the corresponding antineutrino. *Right-hand side:* Inverse Nuclear β decay: The charge of the nucleus is decreased by 1 and a positron and the corresponding neutrino are emitted.

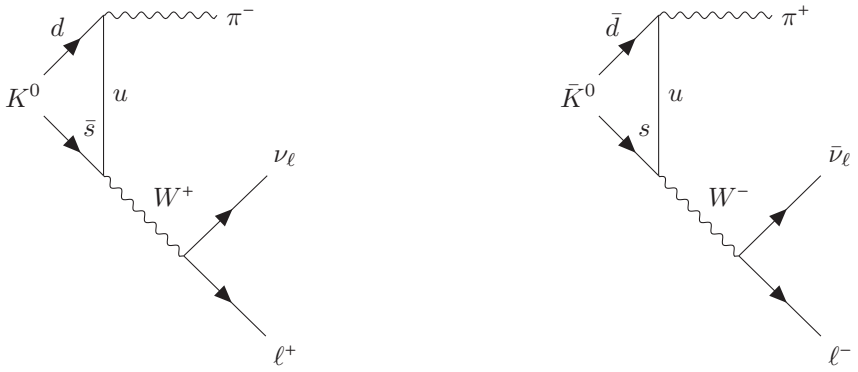

Figure 9.7 *Left-hand side:* Semi-leptonic decay of the K^0. *Right-hand side:* Semi-leptonic decay of the $\bar{K}^0$.

From those one can extract a value for $|V_{ud}|$, Hardy and Towner published in 2020 a value [200] of

$$|V_{ud}| = 0.97373 \pm 0.00031. \tag{9.30}$$

A value for the up-strange quark-mixing element can be received using date from semi-leptonic kaon decays. The neutral kaons K^0 and $\bar{K}^0$, which consist of a down and a strange quark have decay channels, that consist of a lepton-neutrino pair and a pion, as it can be seen in Figure 9.7. From this processes it is possible to give an estimate of [133, 223]

$$|V_{us}| = 0.2232(6). \tag{9.31}$$

An independent way of measuring $|V_{us}|$ is given in [224–228] by considering decays of the τ lepton as the ones that are shown in Figure 9.8. In this case the corresponding CKM matrix element is significantly smaller [43]:

$$|V_{us}| = 0.2207(14). \tag{9.32}$$

In all of these cases $2-3\,\sigma$ discrepancies with the CKM unitarity can be seen. Thus, the task in this part is to use a high-precision lattice estimation of the kaon and pion decay constant ratio. This can be used for further investigations of the CKM unitarity.

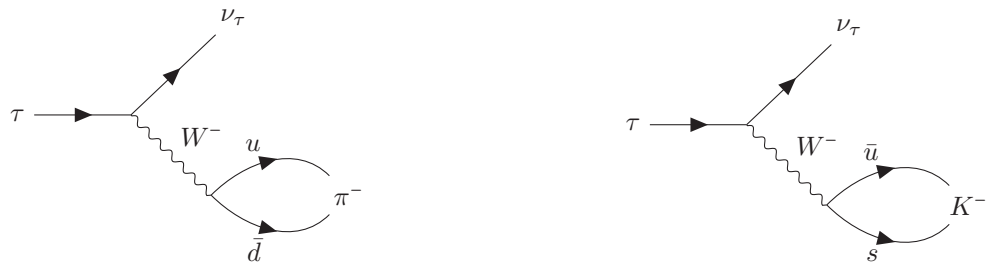

Figure 9.8 Diagram of hadronic τ decays. *Left-hand side:* Strange hadronic τ decay. *Right-hand side:* Non-strange hadronic τ decay.

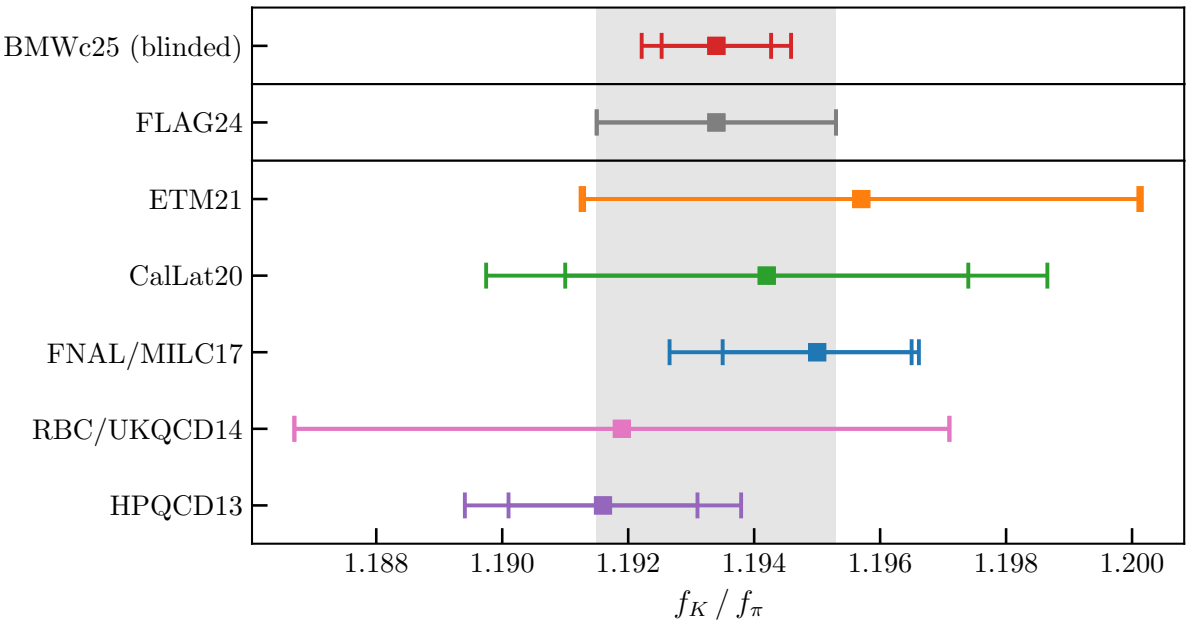

Figure 9.9 Comparison on the results on f_K/f_π. The values include the FLAG average [138], and existing lattice studies [55, 201, 203, 205–209]. For some of the data, the available values do not include strong-isospin breaking corrections. Then, the corrections are taken from the FLAG report [138], which uses the $SU(3)$ χPT formula from [229]. The data are still blinded, so the result from our study is shifted such that it aligns with the FLAG average. However, the relative errors can be compared due to our multiplicative blinding procedure.

9.2.2 Phenomenological consequences of the lattice results

If the isospin symmetric and isospin-breaking contributions to f_K/f_π that are given in Section 8.1 are combined properly one gets the full QCD results of f_K/f_π in the FLAG scheme which is the common scheme to compare the results with those from other groups. In this study we get the result

$$\alpha^K_{\text{blind}} \left[\frac{f_K}{f_\pi}\right]^{\text{FLAG}} = 1.9226(14)(13)[19] \tag{9.33}$$

where the first error is statistical and the second error is systematic. The total error is given in squared brackets. A comparison with the result from other collaborations as well as the averaged results from the 2024 FLAG report is shown in the left column of Figure 9.9. It can be seen that this study provides the most accurate (0.10 %) QCD result of the ratio of the kaon and pion decay constants. To extract information on the CKM unitarity from the ratio of the pseudo-scalar decay constants we need to re-call the pion and kaon

decay widths:

$$\Gamma(\pi^+ \to \ell\bar{\nu}_\ell) = \frac{G_F^2}{8\pi} m_\ell^2 M_\pi \left(1 - \frac{m_\ell^2}{M_\pi^2}\right)^2 \times |V_{u\bar{d}}|^2 \times f_\pi^2 \times (1 + \delta_\pi) \tag{9.34}$$

$$\Gamma(K^+ \to \ell\bar{\nu}_\ell) = \frac{G_F^2}{8\pi} m_\ell^2 M_K \left(1 - \frac{m_\ell^2}{M_K^2}\right)^2 \times |V_{u\bar{s}}|^2 \times f_K^2 \times (1 + \delta_K) \tag{9.35}$$

The ratio of these two equations leads to the expression

$$\left|\frac{V_{ud}}{V_{us}}\right|^2 = \frac{\Gamma(\pi^+ \to \ell\nu_\ell)}{\Gamma(K^+ \to \ell\nu_\ell)} \frac{M_K}{M_\pi} \frac{\left(1 - \frac{m_\ell^2}{M_K^2}\right)^2}{\left(1 - \frac{m_\ell^2}{M_\pi^2}\right)^2} \frac{f_K^2}{f_\pi^2} \frac{1 + \delta_K}{1 + \delta_\pi} \tag{9.36}$$

$$=: C_{\pi,K} \frac{f_K^2}{f_\pi^2} (1 + \delta_{K,\pi}) \tag{9.37}$$

Since we want to use the radiative corrections $\delta_{\pi,K}$ in GRS scheme from RM123 [163] also the decay constant ratio has to be transformed in the preferred scheme. In order to do so, we can take the values from Table 8.1 such that we have a lattice estimate of the decay constant ratio of

$$\left(\alpha^K_{\text{blind}}\right)^2 \left|\frac{V_{ud}}{V_{us}}\right|^2 = \left(\alpha^K_{\text{blind}}\right)^2 \times \left[\frac{\mathcal{F}_K}{\mathcal{F}_\pi}\right] \times C_{\pi,K} \tag{9.38}$$

$$= \left(A + B(X_l^{\text{GRS}} - X_l^{\text{FLAG}}) + C(X_s^{\text{GRS}} - X_s^{\text{FLAG}}) + D\frac{\delta M^2}{2 f_\pi^{\text{GRS}}} + G(B,C)\right)^2 \times (1 + \delta^{\text{valence}}_{K,\pi}) \times C_{\pi,K} \tag{9.39}$$

The sum in the first brackets of Equation (9.39) which is the lattice estimation of $\frac{f_K}{f_\pi}$ in the GRS scheme (including sea quark effects) is computed according to the methods that were introduced in Section 5.4 for estimating the covariance of quantities with systematic and statistical uncertainties. The sea quark effects G are measured for two values of B and C, respectively, so they can be interpolated to their values at the corresponding systematic. $\delta_{\pi,K}$ and $C_{\pi,K}$ also have an uncertainty that is respected by taking their upper and lower one-sigma quantile, respectively.
Since we include a lattice estimation of the sea quark effects we need to purify the radiative corrections that are given in [163] from those contributions:

$$\delta_\pi^{\text{valence}} = 0.0150(18) \tag{9.40}$$

$$\delta_K^{\text{valence}} = 0.0021(8) \tag{9.41}$$

$$\delta_{K,\pi}^{\text{valence}} = \delta R_K^{\text{valence}} - \delta R_\pi^{\text{valence}} = 0.0129(14) \tag{9.42}$$

Thus the theoretical prediction of the full QCD+QED decay constants is given by:

$$\alpha^K_{\text{blind}} \left[\frac{\mathcal{F}_K}{\mathcal{F}_\pi}\right]^{\text{theory}} = 1.9251(15)(27)[31] \tag{9.43}$$

which corresponds to a precision of 0.16% One can check whether the expressions

$$|V_{ud}^{\text{HT}}|^2 \left(1 + \left|\frac{V_{ud}}{V_{us}}\right|^{-2}\right) \quad \text{and} \quad |V_{us}^{\text{FLAG}}|^2 \left(1 + \left|\frac{V_{ud}}{V_{us}}\right|^2\right) \tag{9.44}$$

are compatible with one by using the value of the up-down element from Hardy and Towner [200] and the FLAG value for the up-strange element [194], respectively. A total comparison of our results, the CKM unitarity and the results from the FLAG and Hardy and Towner is shown in Figure 9.10. Since the lattice

estimations in this work are not unblinded yet, the results are set to the PDG values using the precision of our result.

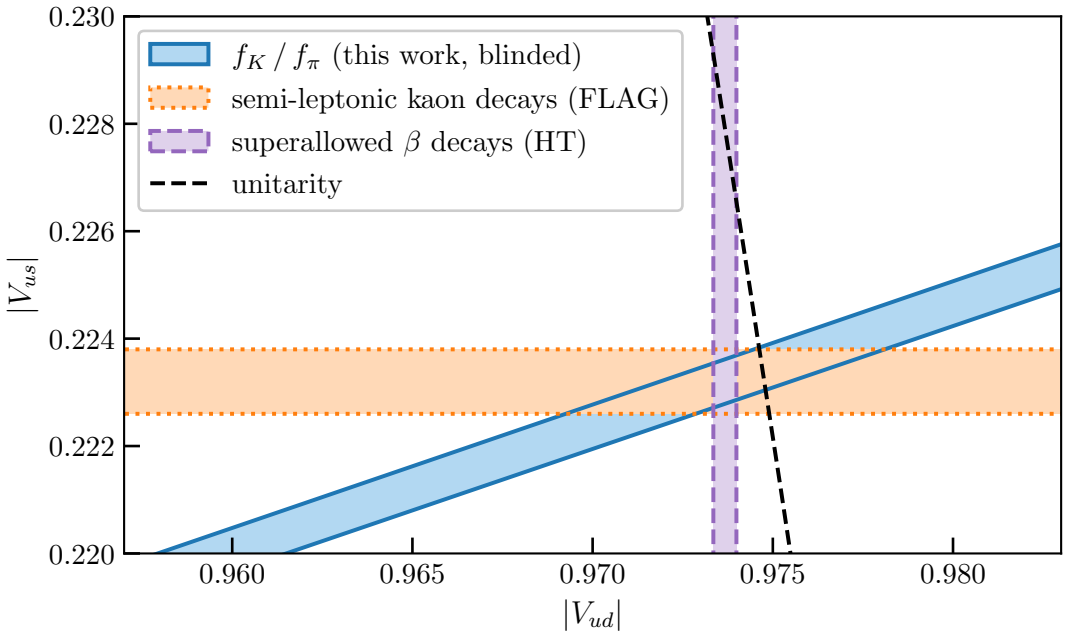

Figure 9.10 CKM constraints for the pseudo-scalar decay constants. The results from our work [26] are given by the blue band, the super-allowed β decay results [200] are marks by the purple band, the semi-leptonic kaon decays [138] are given by the yellow band and the dashed line corresponds to the CKM unitarity using the assumption $|V_{ub}| = 0$ which compatible with our reached precision.

With a relative precision of 2 permille for V_{us}/V_{ud}, my result surpasses the precision of the PDG value [43] for V_{us}, which stands at 3 permille. This is particularly notable given that the V_{ud} input from Hardy and Towner is already determined with very high precision [200].

9.3 Discrepancies in scale setting

As shown in Figure 9.11, there are significant discrepancies among different lattice determinations of the gradient-flow-based scale $\sqrt{t_0}$, which are not observed for the w_0 scale (see Figure 9.3). These various determinations of $\sqrt{t_0}$ employ different discretization schemes and physical input parameters. This raises the question: what is the origin of these discrepancies? Using our data, we are also able to compute this scale and contribute to the discussion.
Using the pion decay rate in the FLAG scheme ($f_\pi^{\text{FLAG}} = 130.5\,\text{MeV}$ [138]), we can give a value of

$$\alpha^{t_0}_{\text{blind}}\sqrt{t_0^{\text{QCD, FLAG}}} = 0.1791(3)(^{+3}_{-2})[^{+4}_{-4}]\,\text{fm}, \tag{9.45}$$

which has a higher precision than most of the existing lattice studies as can be seen in the right panel of Figure 9.11. However, the QED contributions are missing, but in the previous section we could observe that $w_0^{\text{QCD, FLAG}} \sim 0$ at our current level of precision. Therefore, no large differences are expected, even though this assumption still has to be proven.

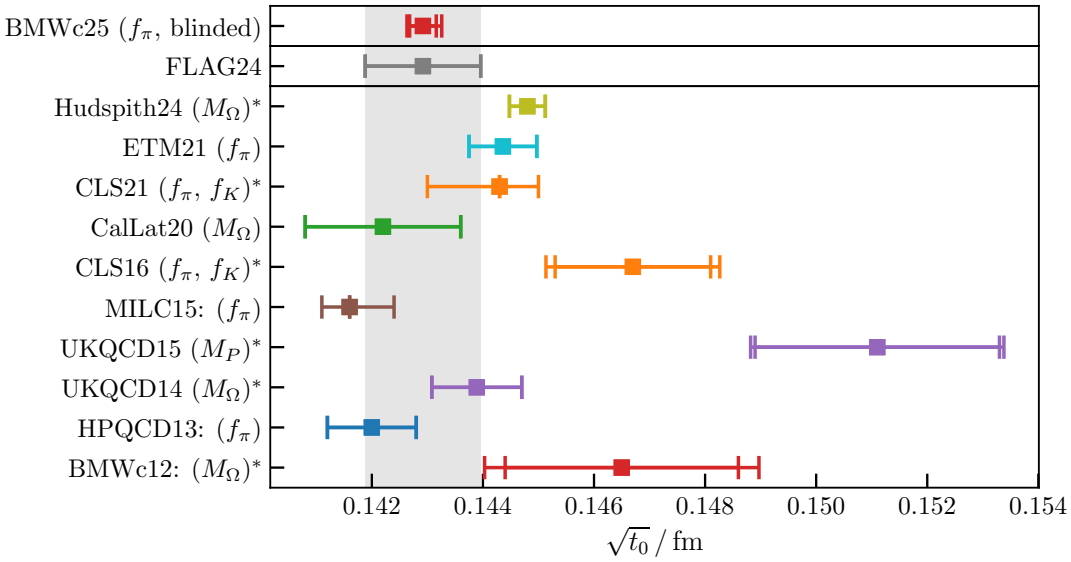

Figure 9.11 Comparison of several estimations of $\sqrt{t_0}$ [139, 201–203, 207, 230–233] and the average from the FLAG report 2024 [138]. Estimations based on simulations using $N_f = 2 + 1$ instead of $N_f = 2 + 1 + 1$ are marked with *. The data are still blinded, so the result from our study is shifted such that it aligns with the FLAG average. However, the relative errors can be compared due to our multiplicative blinding procedure.

10 Exploratory techniques

Most of the works contributing to the muon $g-2$ puzzle only give results for certain windows. It was shown that a large amount of the uncertainties are related to the bad signal-to-noise ratio of the vector correlator at large time distances. While in the fist high-precision estimation of $a_\mu^{\text{LO-HVP}}$ [19] the bounding method was used (which uses estimates for upper and lower bound the vector propagator in the critical regime), the idea came up to reconstruct the long-distance behavior by a spectral decomposition of the correlation function at shorter distances [128, 179, 180, 234]. Nevertheless, the by far best reduction of statistical uncertainties in the long-distance regime could be made by including the data-driven approach for only a small part the long-distance window while using the lattice simulations for the bulk of $a_\mu^{\text{LO-HVP}}$. This approach was first published by the BMW collaboration in 2024 [20]. Before it could shown that the discrepancies of data-driven and lattice approach arise from the shorter distances [127]. Even though we have a very precise methods for the tail distributions by now, it is still interesting to reconstruct the vector propagator for large distances to have an independent check of the data-driven approach.

Since there is a strong decay of the vector meson (ρ) into two pions, the vector correlator has contributions of the form $\exp(-E_{2\pi}t)$[1]. If there the are two-pion states with an energy below the mass of the ρ-meson (which is actually the case), the long-distance regime is dominated by the two-pion states. So we plan to extract the two-pion contributions from the vector correlator using a GEVP (see Section 5.5) that includes the vector meson and two-pion states at short distances. The extracted parameters can then be used to reconstruct the correlator at long distances.
This chapter is divided into the following sections. First, I present my mathematical consideration to construct two-pion states with the same quantum numbers as the vector meson using staggered fermions. Next, I will present the ideas of the implementation. In particular I will construct a method for an efficient computation of connected two-pion diagrams. The content of the following section has been presented on the LATICE2023 and LATTICE2024 conferences and published in the corresponding Proceedings of Science (PoS) [119, 120].

10.1 Two pion contribution to vector mesons

The staggered symmetry group on a fixed time slice is given by

$$\mathbb{Z}_N^3 \rtimes \left[\Gamma^{4,1} \rtimes W_3\right], \tag{10.1}$$

with $\rtimes$ denoting the semi-direct product. The first factor describes the translations on the three dimensional torus, the second one the charge conjugation and taste transformations and the last factor the rotations and inversions of three dimensional cube. More details on the symmetry group of the staggered action is given in Section 3.2.2. In this study a vector meson at rest, trivial in taste space, is considered. Therefore, the representation of the vector state is given by

$$C \otimes V, \tag{10.2}$$

where C is the non-trivial ($\mathbb{Z}_2$) representation of the charge conjugation[2] and V is the vector representation of the Würfel group, i.e., the defining representation of the orthogonal group $O(3)$ restricted on W_3.
The pion states are somewhat more involved since they are not trivial in position and taste. Indeed, the

[1] $E_{2\pi}$ denotes the energy of a two-pion system, thus, $E_{2\pi} \geq 2M_\pi$.
[2] Later we will include $\pi\pi$ states with negative charge conjugacy ($I = 1$ combination). Therefore, we can ignore the charge conjugation issues in the mathematical derivation.

representation of resting Goldstone-pions is trivial. However, when considering two-pion states taste momentum structure will be more involved. Basis vectors of the pion representation are given by

$$\left|\vec{p},\vec{\xi},\xi_4\right\rangle_{\pi^\pm}, \tag{10.3}$$

where the 4th component of the taste is separated from the others, because this component is not affected by the spatial rotations. These states transform under the generators of the staggered symmetry group in the following way

$$S_i\left|\vec{p},\vec{\xi},\xi_4\right\rangle_{\pi^\pm} = e^{-ip_i}\left|\vec{p},\vec{\xi},\xi_4\right\rangle_{\pi^\pm} \tag{10.4}$$

$$\Xi_\mu\left|\vec{p},\vec{\xi},\xi_4\right\rangle_{\pi^\pm} = (-)^{\xi_\mu}\left|\vec{p},\vec{\xi},\xi_4\right\rangle_{\pi} \tag{10.5}$$

$$R\left|\vec{p},\vec{\xi},\xi_4\right\rangle_{\pi^\pm} = \det(R)\left|R\vec{p},R\vec{\xi},\xi_4\right\rangle_{\pi^\pm} \tag{10.6}$$

$$C\left|\vec{p},\vec{\xi},\xi_4\right\rangle_{\pi^\pm} = \left|\vec{p},\vec{\xi},\xi_4\right\rangle_{\pi^\mp}. \tag{10.7}$$

This structure can be derived using the little group procedure mentioned in the Appendix 12.3.
A two-pion state with $I = 1$ is given (up to normalization) by the wedge product $a \wedge b = \frac{1}{\sqrt{2}}(a \otimes b - b \otimes a)$ of two single-pion states with charge + resp. −. So the group representation is generated by

$$S_i\left(\left|\vec{p}^a,\vec{\xi}^a,\xi_4^a\right\rangle_{\pi^+} \wedge \left|\vec{p}^b,\vec{\xi}^b,\xi_4^b\right\rangle_{\pi^-}\right) = e^{-i(p_i^a+p_i^b)}\left(\left|\vec{p}^a,\vec{\xi}^a,\xi_4^a\right\rangle_{\pi^+} \wedge \left|\vec{p}^b,\vec{\xi}^b,\xi_4^b\right\rangle_{\pi^-}\right) \tag{10.8}$$

$$\Xi_\mu\left(\left|\vec{p}^a,\vec{\xi}^a,\xi_4^a\right\rangle_{\pi^+} \wedge \left|\vec{p}^b,\vec{\xi}^b,\xi_4^b\right\rangle_{\pi^-}\right) = (-)^{\xi_\mu^a+\xi_\mu^b}\left(\left|\vec{p}^a,\vec{\xi}^a,\xi_4^a\right\rangle_{\pi^+} \wedge \left|\vec{p}^b,\vec{\xi}^b,\xi_4^b\right\rangle_{\pi^-}\right) \tag{10.9}$$

$$R\left(\left|\vec{p}^a,\vec{\xi}^a,\xi_4^a\right\rangle_{\pi^+} \wedge \left|\vec{p}^b,\vec{\xi}^b,\xi_4^b\right\rangle_{\pi^-}\right) = \left(\left|R\vec{p}^a,R\vec{\xi}^a,\xi_4^a\right\rangle_{\pi^+} \wedge \left|R\vec{p}^b,R\vec{\xi}^b,\xi_4^b\right\rangle_{\pi^-}\right) \tag{10.10}$$

$$C\left(\left|\vec{p}^a,\vec{\xi}^a,\xi_4^a\right\rangle_{\pi^+} \wedge \left|\vec{p}^b,\vec{\xi}^b,\xi_4^b\right\rangle_{\pi^-}\right) = -\left(\left|\vec{p}^a,\vec{\xi}^a,\xi_4^a\right\rangle_{\pi^+} \wedge \left|\vec{p}^b,\vec{\xi}^b,\xi_4^b\right\rangle_{\pi^-}\right). \tag{10.11}$$

Here, it is used that $\det(R)^2 = 1$ for all elements of W_3. For simplicity we will denote these states as

$$\left|\vec{p}^a,\vec{\xi}^a,\xi_4^a\right\rangle_{\pi^+} \wedge \left|\vec{p}^b,\vec{\xi}^b,\xi_4^b\right\rangle_{\pi^-} =: \left|\vec{p}^a,\vec{\xi}^a,\xi_4^a;\vec{p}^b,\vec{\xi}^b,\xi_4^b\right\rangle. \tag{10.12}$$

Of course, not all two-pion states have the same overlap to all vector meson states. Quantum numbers have to be conserved as well as some of the states appear with a different multiplicity. Mathematically spoken, it behaves the following way: The vector meson representation of the Würfel group is irreducible while the two-pion representations are reducible. Therefore, the two-pion states can be decomposed into irreducible representations, from which we expect some to be the vector meson irrep. So we can construct vector-meson like states from the two-pion states with the same quantum numbers according to

$$\left|\vec{q}=0,\zeta_\mu=0;s,m,\alpha\right\rangle = \sum_{(\vec{p}^a,\xi_\mu^a,\vec{p}^b,\xi_\mu^b)\in s}\left|\vec{p}^a,\vec{\xi}^a,\xi_4^a;\vec{p}^b,\vec{\xi}^b,\xi_4^b\right\rangle\left\langle\vec{p}^a,\vec{\xi}^a,\xi_4^a;\vec{p}^b,\vec{\xi}^b,\xi_4^b\middle|\vec{q}=0,\zeta_\mu=0;s,m,\alpha\right\rangle, \tag{10.13}$$

where $\vec{q}$ denotes the momentum and ζ_μ the taste of the vector meson, s labels the orbit O_s of the two-pion states under W_3 rotations and spatial inversions, $m \in (1,...,a_s)$ labels the multiplicities with which the corresponding orbit occurs, and $\alpha = x,y,z$ represents the orientation of the reconstructed vector meson. One should note that the vector-like states have a rotational symmetry and therefore, the final states only depend on the absolute value of the momentum and taste vectors (this is why they are classified into orbits) and on the 4^{th} component of the taste. Of course, the rotations affects the direction of the vector state but this is considered in further calculations.
The derivation is similar to Wigner's little group procedure mentioned in Section 12.3 and in [34].
So one has to figure out the multiplicities a_s as well as the Clebsch-Gordan coefficients which are given defined as the scalar product from Equation (10.13). Computing the multiplicities is straightforward using basic essences of finite group theory. The character of a representation is given by the trace of a corresponding

group element, which means in the case of a two-pion state

$$\chi^{2\pi}(\vec{S}, R, \Xi_\mu) = \sum_{\vec{p}^a, \vec{p}^b, \xi^a_\mu, \xi^b_\mu} \left\langle \vec{p}^a, \vec{\xi}^a, \xi^a_4; \vec{p}^b, \vec{\xi}^b, \xi^b_4 \middle| R\vec{p}^a, \vec{R}\xi^a, \xi^a_4; R\vec{p}^b, R\vec{\xi}^b, \xi^b_4 \right\rangle e^{-i\vec{S}\cdot R(\vec{p}^a+\vec{p}^b) - i\pi\vec{\Xi}\cdot R(\vec{\xi}^a+\vec{\xi}^b) - i\pi\Xi_4(\xi^a_4+\xi^b_4)} \tag{10.14}$$

$$\tag{10.15}$$

and in the case of the vector meson

$$\chi^\rho(R) = \mathrm{Tr}(R). \tag{10.16}$$

Then, the multiplicity of a given orbit is given by

$$a_s = \frac{1}{2^4 \cdot 48 \cdot L^3} \sum_{nR\Xi} \chi^\rho(R)^* \times \chi^{2\pi}(n, R, \Xi) \tag{10.17}$$

$$= \frac{1}{48} \sum_R \chi_\rho(R)^* \times \sum_{\vec{p}^b} \sum_{\vec{p}^a = R\vec{p}^a} \delta(\vec{p}^a + \vec{p}^b) \times \sum_{\vec{\xi}^b} \sum_{\vec{\xi}^a = R\vec{\xi}^a} \delta(\xi^a_{1,2,3,4} - \xi^b_{1,2,3,4}), \tag{10.18}$$

which can be computed very easily using a small script. Please note that the resulting formula is independent of the lattice volume as long as the cubic symmetry is valid.
When computing this coefficients one will notice that the only two-pion states that have overlap to the resting taste-singlet vector meson are those that have total momentum 0 and constitute of two pions that have the same taste. Therefore, the multiplicities (and the CG-coefficients) can be labeled by a single momentum (which we call $\vec{p}$) and a single taste (which we call ξ)[3]. Independent of the choice of ξ_4 we get the coefficients shown in table 10.1. The multiplicities as well as the Clebsch-Gordan coefficient only depend on the orbit of the pion state under the action of the Würfel group. The orbits can be labeled by the absolute value of taste and momentum and from this point we will denote the two-pion states that have total momentum zero and that are taste-singlets in the bra-ket notation as

$$\left|\vec{p}, \vec{\xi}, \xi_4; -\vec{p}, \vec{\xi}, \xi_4\right\rangle =: \left|\vec{p}, \vec{\xi}, \xi_4; I = 1\right\rangle. \tag{10.19}$$

Next one needs to compute the Clebsch-Gordan coefficients, that are given by the scalar product in Equation (10.13):

$$C^{s,m,\alpha}_{\vec{p},\vec{\xi},\xi_4;R} = \left\langle R\vec{p}, R\vec{\xi}, \xi_4; I = 1 \middle| \vec{q} = \vec{0}, \zeta_\mu = 0; s, m, \alpha \right\rangle. \tag{10.20}$$

The Clebsch-Gordon coefficients do not depend on ξ_4 and can of course be given in terms of momenta and tastes from the corresponding rotational orbit:

$$C^{s,m,\alpha}_{\vec{p},\vec{\xi}} = \left\langle \vec{p}, \vec{\xi}, \xi_4, I = 1 \middle| \vec{q} = \vec{0}, \zeta_\mu = 0; s, m, \alpha \right\rangle. \tag{10.21}$$

Since the symmetry group that is considered here is a finite group, we can use brute-force techniques [235] in order to compute the CG-coefficients. The application of this method for the two-pion-vector-meson overlap is explained very briefly in the following paragraph:
Let $T(R)$ be the vector representation of a Würfel group element R. In this case, all of those 48 matrices are real, orthogonal and three dimensional. For a given taste and momentum orbit O and Rotation $R \in W_3$ we

[3] Of course, $\vec{p}$ can be replaced by $-\vec{p}$. This results in an interchange of the two pions and produces only a global sign which is not relevant in the generalized eigenvalue problem.

define $D^O(R)$ as a matrix of dimension $|O|$ fulfilling the following condition:

$$D^O(R)_{\vec{p}^a,\xi^a;\vec{p}^b,\xi^b} = \delta_{\vec{p}^a,R\vec{p}^b}\delta_{\xi^a,R\xi^b} \quad \forall(\vec{p}^a,\xi^a),\,(\vec{p}^b,\xi^b) \in O \tag{10.22}$$

One has to note that for the taste one does not need to distinguish between positive and negative number, i.e., the rotations R act on the taste vector as elements of $O(\mathbb{Z}_2^3)$. For example a rotation be π around the z-axis leaves the unit vector in z-unit vector invariant:

$$\begin{pmatrix} 1 & 0 & 0 \\ 0 & -1 & 0 \\ 0 & 0 & -1 \end{pmatrix}\begin{pmatrix} 0 \\ 0 \\ 1 \end{pmatrix} \equiv \begin{pmatrix} 0 \\ 0 \\ 1 \end{pmatrix} \mod 2. \tag{10.23}$$

One might ask why the representation in Equation (10.22) has no dependence on the shift or taste operation. This is because in this special case of two pion states the phases (signs) for shift (taste) operation cancel exactly. E.g. while the first pion gives a phase of $e^{i\vec{p}^a\cdot\vec{s}}$, the second one gives a phase of $e^{i\vec{p}^b\cdot\vec{s}} = e^{-i\vec{p}^a\cdot\vec{s}}$. Therefore, the whole computation becomes independent of the lattice size which reduces the computational effort by far. The whole computation can be done within a few seconds on a usual laptop PC.
We can compute the coefficients by normalizing the columns of

$$\sum_R D^O(R)\cdot A\cdot T(R)\,, \tag{10.24}$$

where A is a matrix with general coefficients and the size of A is chosen such that the multiplications are well-defined. Most of the general entries of A will cancel after this procedure but the remaining ones will span a vector space whose dimension is the multiplicity we computed before[4]. Choosing a certain basis here will give the coefficients for the different copies of the vector space. The final matrix will have three columns each representing one component of the vector current. The entries in each of the rows will denote the Clebsch-Gordan coefficient of the corresponding state. For example let us consider the $|\vec{p}| = 1$, $|\vec{\xi}| = 3$ and $\xi_4 = 1$ orbit with the ordered basis

$$\left|\vec{p} = \vec{e}_x, \vec{\xi} = \vec{e}_x + \vec{e}_y + \vec{e}_z, \xi_4 = 1\right\rangle, \left|\vec{p} = -\vec{e}_x, \vec{\xi} = \vec{e}_x + \vec{e}_y + \vec{e}_z, \xi_4 = 1\right\rangle, \tag{10.25}$$

$$\left|\vec{p} = \vec{e}_y, \vec{\xi} = \vec{e}_x + \vec{e}_y + \vec{e}_z, \xi_4 = 1\right\rangle, \left|\vec{p} = -\vec{e}_y, \vec{\xi} = \vec{e}_x + \vec{e}_y + \vec{e}_z, \xi_4 = 1\right\rangle, \tag{10.26}$$

$$\left|\vec{p} = \vec{e}_z, \vec{\xi} = \vec{e}_x + \vec{e}_y + \vec{e}_z, \xi_4 = 1\right\rangle, \left|\vec{p} = -\vec{e}_z, \vec{\xi} = \vec{e}_x + \vec{e}_y + \vec{e}_z, \xi_4 = 1\right\rangle. \tag{10.27}$$

The resulting matrix (after normalizing the columns) of Equation (10.24) will be

$$\frac{1}{\sqrt{2}}\begin{pmatrix} 1 & 0 & 0 \\ -1 & 0 & 0 \\ 0 & 1 & 0 \\ 0 & -1 & 0 \\ 0 & 0 & 1 \\ 0 & 0 & -1 \end{pmatrix}, \tag{10.28}$$

which means that the ith component of the vector overlap with this orbit is given by

$$\frac{1}{2}\left(\left|\vec{p} = \vec{e}_i, \vec{\xi} = \vec{e}_x + \vec{e}_y + \vec{e}_z, \xi_4 = 1\right\rangle - \left|\vec{p} = -\vec{e}_i, \vec{\xi} = \vec{e}_x + \vec{e}_y + \vec{e}_z, \xi_4 = 1\right\rangle\right). \tag{10.29}$$

For states with a multiplicity larger than one (e.g. the same pion states with $|\vec{\xi}| = 2$), one can construct more

[4] In principle we do not need to compute the multiplicities before, but it is very straightforward and some kind of crosscheck for the computation of the coefficients.

	$\lvert\vec{p}\rvert^2 = 0$	$\lvert\vec{p}\rvert^2 = 1$	$\lvert\vec{p}\rvert^2 = 2$	$\lvert\vec{p}\rvert^2 = 3$	$\lvert\vec{p}\rvert^2 = 4$
$\lvert\vec{\xi}\rvert^2 = 0$	0	1	1	1	1
$\lvert\vec{\xi}\rvert^2 = 1$	0	2	3	2	2
$\lvert\vec{\xi}\rvert^2 = 2$	0	2	3	2	2
$\lvert\vec{\xi}\rvert^2 = 3$	0	1	1	1	1

Table 10.1 Multiplicities of 2π representations in the resting vector meson depending on the absolute momentum and taste. The multiplicities can be computed using the scalar product of characters of the representations of the vector states and the two-pion state, respectively.

	$\vec{\xi}^2 = 0(3)$	$\vec{\xi}^2 = 1(2)$
$\vec{p}^2 = 1$	$C^{1,\alpha}_{\lambda\vec{e}_i,\vec{0}} = \lambda\frac{1}{\sqrt{2}}\delta^{\alpha i}$	$C^{1,\alpha}_{\lambda\vec{e}_i,\vec{f}_j} = \lambda\frac{1}{\sqrt{2}}\delta^{ij}\delta^{\alpha i}$ $C^{2,\alpha}_{\lambda\vec{e}_i,\vec{f}_j} = \frac{\lambda}{2}(1-\delta_{ij})\delta^{\alpha i}$
$\vec{p}^2 = 2$	$C^{1,\alpha}_{\lambda\vec{e}_i+\mu\vec{e}_j,\vec{0}} = \frac{\lambda}{2\sqrt{2}}\delta^{\alpha i}$	$C^{1,\alpha}_{\lambda\vec{e}_i+\mu\vec{e}_j,\vec{f}_k} = \frac{\lambda}{2\sqrt{2}}\lvert\epsilon^{ijk}\rvert\delta^{\alpha i}$ $C^{2,\alpha}_{\lambda\vec{e}_i+\mu\vec{e}_j,\vec{f}_k} = \frac{\lambda}{2\sqrt{2}}\delta^{ki}\delta^{\alpha i}$ $C^{3,\alpha}_{\lambda\vec{e}_i+\mu\vec{e}_j,\vec{f}_k} = \frac{\lambda}{2\sqrt{2}}\delta^{kj}\delta^{\alpha i}$
$\vec{p}^2 = 3$	$C^{1,\alpha}_{\lambda\vec{e}_i+\mu\vec{e}_j+\nu\vec{e}_k,\vec{0}} = \frac{\lambda}{2\sqrt{2}}\delta^{\alpha i}$	$C^{1,\alpha}_{\lambda\vec{e}_i+\mu\vec{e}_j+\nu\vec{e}_k,\vec{f}_l} = \frac{\lambda}{2\sqrt{2}}\delta^{il}\delta^{\alpha i}$ $C^{2,\alpha}_{\lambda\vec{e}_i+\mu\vec{e}_j+\nu\vec{e}_k,\vec{f}_l} = \frac{\lambda}{4}\lvert\epsilon^{jkl}\rvert\delta^{\alpha i}$
$\vec{p}^2 = 4$	$C^{1,\alpha}_{2\lambda\vec{e}_i,\vec{0}} = \lambda\frac{1}{\sqrt{2}}\delta^{\alpha i}$	$C^{1,\alpha}_{2\lambda\vec{e}_i,\vec{f}_j} = \lambda\frac{1}{\sqrt{2}}\delta^{ij}\delta^{\alpha i}$ $C^{2,\alpha}_{2\lambda\vec{e}_i,\vec{f}_j} = \frac{\lambda}{2}(1-\delta_{ij})\delta^{\alpha i}$

Table 10.2 The Clebsch-Gordan coefficients needed for constructing the vector meson out of two-pion states.

independent linear combinations of the overlapping states.
Next we will present the CG coefficients for the taste and momentum orbits up to $\vec{p}^2 = 4$. Due to symmetries, there is no distinction between $\vec{p}^2 = 1$ and $\vec{p}^2 = 4$. The unit vectors in momentum space are denoted with $\vec{e}_i$, while f_i represents unit vectors in taste space, whenever $\vec{p}^2 = 1$ or $\vec{\xi}^2 = 1$. If the orbits are of the type $\vec{\xi}^2 = 2$, f_i denotes a vector with a zero in the ith component and a one in the other ones. $\vec{0}$ denotes the zero vector in the case $\vec{\xi}^2 = 0$ and $(1,1,1)^T$ when $\vec{\xi}^2 = 3$. Here, λ, μ, and ν refer to 1 and -1, respectively. The Clebsch-Gordan coefficients are shown in Table 10.2.

10.2 Implementation

The coordinate-space correlation function of the π^+ operator is defined as

$$C_{\pi^+}(x,y) = [u(x)O(x)\bar{d}(x)][d(y)O^\dagger(y)\bar{u}(y)], \tag{10.30}$$

whereas the π^- correlation function is

$$C_{\pi^-}(x,y) = [\bar{u}(x)O(x)d(x)][\bar{d}(y)O^\dagger(y)u(y)]. \tag{10.31}$$

Here, we define $O(x) = (\gamma_5 \otimes \Xi)\exp(-\mathrm{i}\vec{p}\cdot\vec{x})$ in the spin-taste representation with a certain taste Ξ, the momentum is given by $\vec{p} = \frac{2\pi}{L}\vec{n}$ with L being the spatial lattice extend and $\vec{n} \in \mathbb{N}^3$. The definition of the spin-taste operators for staggered fermions is given in Section 3.2. From now on I will drop the coordinate of the operator O since it is given implicitly by the neighboring arguments.
To construct two-pion states we consider a combination of π^+ and π^- with negative charge conjugation

quantum number given by:

$$\frac{\pi^+\pi^- - \pi^-\pi^+}{2} \tag{10.32}$$

This is done in order to match the strong isospin and charge conjugation quantum number of the vector meson.
Therefore, the correlation function of the antisymmetrized $\pi^+\pi^-$-state has to be considered:

$$C_{\pi^+\pi^-}(x,y,z,w) = [u(x)O\bar{d}(x)][d(y)P\bar{u}(y)][d(z)O^\dagger\bar{u}(z)][u(w)P^\dagger\bar{d}(w)]$$

From this we get four different contractions:

$$\langle C_{\pi^+\pi^-}(x,y,z,w)\rangle = \underbrace{\mathrm{Tr}\left[M_u^{-1}(y,x)OM_d^{-1}(x,y)P\right]\mathrm{Tr}\left[M_d^{-1}(w,z)O^\dagger M_u^{-1}(z,w)P^\dagger\right]}_{\text{disconnected, “t-channel”}} \tag{10.33}$$

$$-\underbrace{\mathrm{Tr}\left[M_u^{-1}(z,x)OM_d^{-1}(x,y)PM_d^{-1}(w,z)O^\dagger M_u^{-1}(y,w)P^\dagger\right]}_{\text{connected}} \tag{10.34}$$

$$-\underbrace{\mathrm{Tr}\left[M_u^{-1}(y,x)OM_d^{-1}(x,z)PM_d^{-1}(w,y)O^\dagger M_u^{-1}(z,w)P^\dagger\right]}_{\text{connected}} \tag{10.35}$$

$$+\underbrace{\mathrm{Tr}\left[M_u^{-1}(z,x)OM_d^{-1}(x,z)P\right]\mathrm{Tr}\left[M_d^{-1}(w,y)O^\dagger M_u^{-1}(y,w)P^\dagger\right]}_{\text{disconnected, “s-channel”}} \tag{10.36}$$

Here, $\langle ...\rangle$ denotes the expectation value with respect to the fermion path-integral at a fixed gauge configuration. The trace is taken with respect to the color components. As mentioned before, it is necessary to antisymmetrize the ingoing as well as the outgoing pions. So we are left with

$$\frac{1}{4}\left(C_{\pi^+\pi^-}(x,y,z,w) - C_{\pi^+\pi^-}(y,x,z,w) - C_{\pi^+\pi^-}(x,y,w,z) - C_{\pi^+\pi^-}(y,x,w,z)\right). \tag{10.37}$$

The first disconnected term (Equation (10.33)) will be zero due to its symmetric structure in combination with the antisymmetrization of the two-pion correlator. Therefore, no implementation for this term is needed and the term in Equation (10.36) will be called *disconnected* from now on. Additionally, one will see that Equation (10.34) and Equation (10.35) are indistinguishable after the antisymmetrization. Therefore, we will only consider one of those and call it the *connected* diagram. One has to note that this connected diagram then gets a prefactor of −2. Within the analysis one should ensure that a proper antisymmetrization with respect to the ingoing and outgoing pions is done.
Since the pions need to have back-to-back momentum one has to add certain phase factors before summing up the spatial components. We consider the center-of-mass frame and therefore, the ingoing and the outgoing momenta have to sum up to zero. The momentum of each ingoing pion is $\vec{p}$ (resp. $-\vec{p}$) and the momentum for the outgoing pions is $\vec{q}$ (resp. $-\vec{q}$).
Of course, the two-pion states are not the only states needed in the GEVP for the reconstructions of the vector meson. One also has to implement the vector meson (ρ-meson) correlation function it self to resolve all energy eigenstates. This correlation function is given by

$$C_\rho(x,z) = \frac{1}{2}\left([u(x)O\bar{u}(x)] - [d(x)O^\dagger\bar{d}(x)]\right)\left([\bar{u}(z)Ou(z)] - [\bar{d}(z)O^\dagger d(z)]\right), \tag{10.38}$$

where $O = \gamma_i \otimes \mathbb{1}$ in the spin-taste representation, which corresponds to a taste-singlet vector meson. Finally, one has only two contributing contractions which corresponds to one contributing contraction in the isospin-

symmetric limit, which is used for the implementation:

$$\mathrm{Tr}\left[M_{u/d}^{-1}(x,z)OM_{u/d}^{-1}(z,x)O^{\dagger}\right] \tag{10.39}$$

The GEVP also requires terms that mix the vector and the two-pion state of which the correlation functions are given by:

$$C_{\rho\pi\pi}(x,z,w) = \frac{1}{2}\left([u(x)O\bar{u}(x)] - [d(x)O^{\dagger}\bar{d}(x)]\right)[d(z)P^{\dagger}\bar{u}(z)][u(w)P^{\dagger}\bar{d}(w)]. \tag{10.40}$$

In comparison to the pure pion or vector states, this three-point correlation functions are not real but complex valued. In addition one can prove the identity

$$C_{\rho\pi\pi}(x,w,z) = C_{\rho\pi\pi}(x,z,w)^{*}, \tag{10.41}$$

which, combined with the antisymmetrization in the pions, leads to the following expression that has to be implemented:

$$\mathrm{Im}\,\mathrm{Tr}\left[M_{u/d}^{-1}(w,z)OM_{u/d}^{-1}(x,w)P^{\dagger}M_{d/u}^{-1}(z,w)P\right]. \tag{10.42}$$

For the implementation, we use certain noise sources $\xi_{e/o,t_0}$ that fulfill the following properties:

$$\xi_{e,t_0}^{T}\xi_{e,t_1} = \frac{N_c L^3}{2}\delta_{t_0,t_1}, \tag{10.43}$$

$$\xi_{e,t_0}^{T}\xi_{e,t_1} = 0, \tag{10.44}$$

$$\xi_{e,t_0}^{T}\xi_{e,t_1} = 0, \tag{10.45}$$

$$\xi_{e,t_0}^{T}\xi_{e,t_1} = \frac{N_c L^3}{2}\delta_{t_0,t_1}. \tag{10.46}$$

In this case, they are represented by wall sources in the following way:

$$\begin{aligned}\xi_{e,t_0}(\vec{x},t,c) &= \begin{cases} 0 & \text{if } |x|_1 \% 2 = 1 \\ (-1)^{r(\vec{x},c)}\delta_{t_0,t} & \text{else} \end{cases}, \\ \xi_{o,t_0}(\vec{x},t,c) &= \begin{cases} 0 & \text{if } |x|_1 \% 2 = 0 \\ (-1)^{r(\vec{x},c)}\delta_{t_0,t} & \text{else} \end{cases}. \end{aligned} \tag{10.47}$$

Here, $r(\vec{x},c)$ is a randomly chosen integer for each spatial lattice site and each color index.
For certain cases (vector mesons) we need point sources instead of the aforementioned wall sources. Those can be written as

$$\xi_{e/o,t_0}(\vec{x},t,c) = \sqrt{\frac{N_c L^3}{2}}\delta(\vec{y}-\vec{x})\delta_{t_0,t}\delta_{d,c} \tag{10.48}$$

Here $\vec{y}$ is a randomly chosen spatial lattice site (that is even (e) or odd(o)) and d is a random color index.

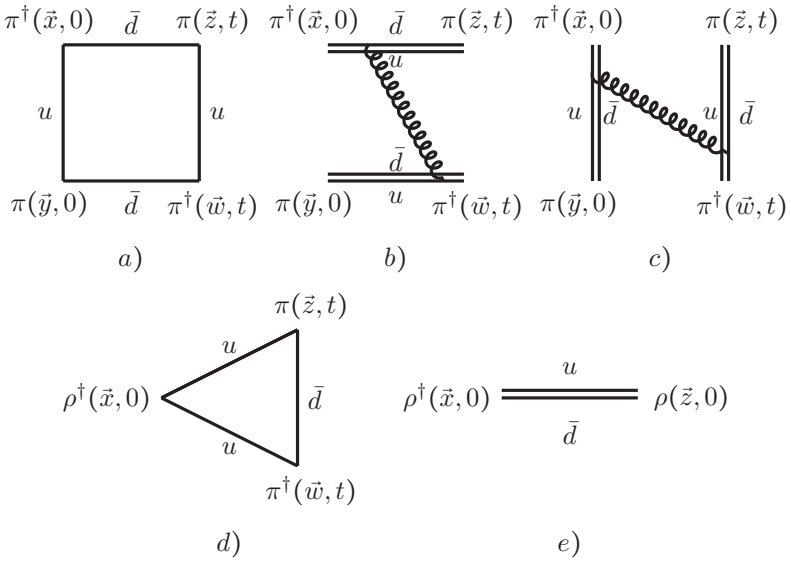

Figure 10.1 The diagrams corresponding to the GEVP including vector-meson-type states. The first one (conn., *a*)) includes interchange of quarks in the two pion states, the second one (free, *b*)) describes two pions propagating independently and the third one (disc., *c*)) is identical to zero due to the isospin combination of the pions. The decay of the vector mesons into two pions is described by the triangle (*d*)) and the remaining diagram (*e*)) is the vector meson correlation function [119]

10.2.1 Vector meson correlator

The computation of the vector meson correlation function is done by implementing the scalar product

$$C_\rho(t_0,t) = \frac{1}{N_\xi}\sum_\xi \sum_{t_1,t_2} \left\langle \xi_{t_0} M^{-1}_{t_0,t_1} B\,(P_t)_{t_1,t_2} \middle| M^{-1}_{t_2,t_0} A \xi_{t_0} \right\rangle, \tag{10.49}$$

where A/B denote components of the taste-singlet vector meson operator (in this case we have $A = B$) and P_t is a projection on a fixed time slice t that is given by

$$(P(t))_{t_1,t_2} = \delta_{t,t_1}\delta_{t,t_2}. \tag{10.50}$$

From now on, this projection is included implicitly. The expectation value is computed by the mean values with different random sources ξ that are only non-zero at a randomly chosen time slice t_0 according to Equation (10.47) and (10.48). The number of inversion, which is the most costly factor of such a computation for the vector meson correlator is given by

$$N_\xi(1 + N_O) = N_\xi(1 + 3) = 4N_\xi \tag{10.51}$$

where N_ξ gives the number of random sources ξ and N_O is the number of vector meson operators (smeared and unsmeared, three components). Unfortunately, this expression converges only very slowly towards the exact result when increasing N_ξ. Therefore, for our usual values of N_ξ the vector meson correlator is dominated by noise. In order to get rid of the problem, we include *low-mode averaging* (LMA). The idea behind LMA is that we expect the correlator mainly to depend on the eigenvalues of M with small absolute value. From the preconditioning, we already know the lowest eigenvalues λ_i and the corresponding eigenvectors v_i so we can

compute the most contributing part exactly:

$$C_{\rho}^{LMA}(t_0,t) = \sum_{ij}^{N_{\text{eig}}} \frac{1}{\lambda_i \lambda_j} \langle v_i O_A | P_{t_0} | v_j \rangle \langle v_j O_B | P_t | v_i \rangle . \tag{10.52}$$

The eigen-part of the inversion is defined as

$$M_e^{-1} = \sum_{i}^{N_{\text{eig}}} \frac{1}{\lambda_i} |v_i\rangle\langle v_i| \tag{10.53}$$

and is of course, not the true inversion of the staggered matrix. There is a rest-part we define as

$$M_r^{-1} = M^{-1} - M_e^{-1}.$$

Due to the fact that the correlator in Equation (10.49) includes two inversions of the staggered matrix, we have eigen-eigen (ee), rest-rest (rr) and eigen-rest and rest-eigen (er) contributions in the vector meson correlator. If the number of pre-calculated eigenvectors gets to a suitable extend, the eigen-eigen part is the dominant one. This part then will be replaced by the low-mode averaging expression to receive a strong improvement of the signal-to-noise ratio especially for larger Euclidean time distances. The eigen-eigen part of Equation (10.49) can be used to cross-check the low-mode-averaging.

10.2.2 Free pion diagram

The free pion diagram has to advantage that it can be computed by multiplying two one-pion correlation functions. The computation looks similar as the vector meson in the previous subsection, but the operator has to be replaced by the corresponding pion-operator with proper taste quantum numbers. Due to the fact that the pion signal is very clean (since we deal with π^+/π^-) low-mode averaging is not necessary. In addition we do not need to smear the operators and, therefore, we can use a wall-source instead of a point source. The main problem in the implementation of this diagram is that we might have time-non-local operators. In the lattice simulation, an operator includes shift by $(s_\mu + t_\mu) \mod 2$ in the μ direction. Whenever μ is spatial this is no problem, because the shift in symmetrized in forward and backward direction. But since we measure correlation functions at a given time slice, we cannot do this in time direction. The application of a time-non-local operator would shift the time slice at which the operator is measured from t to $t-1$. Therefore, we also include sources at t_0+1 and average over different correlation functions in the following way, where O^l denotes a local and O^n a time-non-local operator. We start explaining the case in which A is a local operator and B can be either local or non-local. The first case is well-known:

$$C_{B^l A^l}(t_0,t) \coloneqq \langle \xi_{t_0} M^{-1}_{t_0,t} B^l | M^{-1}_{t,t_0} A^l \xi_{t_0} \rangle, \tag{10.54}$$

$$C_{B^n A^l}(t_0,t) \coloneqq \frac{1}{2}\left(\langle \xi_{t_0} M^{-1}_{t_0,t} B^n | M^{-1}_{t,t_0} A^l \xi_{t_0} \rangle + \langle \xi_{t_0} M^{-1}_{t_0,t} | \left(B^n\right)^\dagger M^{-1}_{t,t0} A^l \xi_{t_0} \rangle \right). \tag{10.55}$$

At the vertical line we compute the scalar-product which includes a projection on time slice t, but the difference of t and t_0 differs by one between the two terms in $C_{B^n A^l}$. To include non-local operators for A, we compute

$$C_{B^l A^n}(t_0,t) \coloneqq \frac{1}{2}\left(\langle \xi_{t_0} M^{-1}_{t_0,t} B^l | M^{-1}_{t,t_0} A^l \xi_{t_0} \rangle + \langle \xi_{t_0+1} \left(A^n\right)^\dagger M^{-1}_{t_0,t} B^l | M^{-1}_{t,t_0+1} \xi_{t_0+1} \rangle \right)$$

Combining the two methods for computing non-local A resp. B one yields the expression for both to be non-local:

$$C_{B^n A^n}(t_0,t) \coloneqq \frac{1}{4}\Big(\langle \xi_{t_0} M^{-1}_{t_0,t} B^l | M^{-1}_{t,t_0} A^l \xi_{t_0}\rangle + \langle \xi_{t_0+1} (A^n)^\dagger M^{-1}_{t_0+1,t} B^l | M^{-1}_{t,t_0+1} \xi_{t_0+1}\rangle$$
$$+\langle \xi_{t_0} M^{-1}_{t_0,t} B^n | M^{-1}_{t,t_0} A^l \xi_{t_0}\rangle + \langle \xi_{t_0} M^{-1}_{t_0,t} | (B^n)^\dagger M^{-1}_{t,t_0} A^l \xi_{t_0}\rangle + \langle \xi_{t_0+1} M^{-1}_{t_0+1,t} B^l | M^{-1}_{t,t_0+1} A^l \xi_{t_0+1}\rangle\Big). \tag{10.56}$$

The free part will be the dominating contribution to the two-pion interaction especially for small time separations. Nevertheless for larger separations, the connected part may play a more significant role.

10.2.3 Interaction diagram

For the implementation of the interaction diagram between the ρ-meson and the two-pion state, there are two possible ways of implementation. Let A be the operator describing one of the corresponding pions. It has to be mentioned that both A operators will have opposite momentum, so one has to take care of this issue when implementing the diagrams. The ρ operator will be denoted by B. The first method is the implementation of the decay:

$$C_{\rho AA}(t_0,t) = \langle \xi_{t_0} M^{-1}_{t_0,t} A M^{-1}_{t,t} A | M^{-1}_{t_0,t_0} \rho \xi_{t_0}\rangle \tag{10.57}$$

Here, a problem appears that also arises in the next section that discusses the connected pion diagram. The red inversion has to be perform on each time-slice which will increases the computational time drastically. Luckily, one can compute the diagram in the opposite direction:

$$C_{AA\rho} = \langle \xi_{t_0} M^{-1}_{t_0,t} B | M^{-1}_{t,t_0} A M^{-1}_{t_0,t_0} A \xi_{t_0}\rangle. \tag{10.58}$$

This way, the dominant part of computational costs comes from the right-hand-side of the scalar product where it is proportional to the number of operators included but not to the number of time-slices.

10.2.4 Connected pion diagram

The connected part of the diagram is by far the most expensive part of the computation and requires the most elaborated strategy for a efficient computation. The main issue for the high costs can be seen from a naive implementation for local operators:

$$C^{\text{conn.}}_{BBAA}(t_0,t) = \langle \xi_{t_0} M^{-1}_{t_0,t} B M^{-1}_{t,t} B | M^{-1}_{t,t_0} A M^{-1}_{t_0,t_0} A \xi_{t_0}\rangle. \tag{10.59}$$

The red inversion has to be performed on every timeslice, so that there occurs an overall number of inversions proportional to [120]

$$T/a \times \#O \times \#N_\xi \tag{10.60}$$

. This is no problem on small volumes but since the cost of a single inversion scales roughly with $V = L^3 \times T$, the additional time scaling becomes a problem at larger volumes. An approach to save computational time for the connected diagrams was presented by me at the LATTICE2024 conference. The key ingredient is the low-mode averaging that was also used in Section 10.2.1. Therefore, the red inversion in replaced by the sum

of the eigen-part $M_e^{-1} = \sum_i^{N_{\text{eig}}} \frac{1}{\lambda_i} |v_i\rangle \langle v_i|$ and $M_r^{-1} = M^{-1} - M_e^{-1}$:

$$C_{BBAA}^{\text{conn.}} = \langle \xi_{t_0} M_{t_0,t}^{-1} B \sum_i^{N_{\text{eig}}} \frac{1}{\lambda_i} |v_i\rangle \langle v_i| B | M_{t,t_0}^{-1} A M_{t_0,t_0}^{-1} A \xi_{t_0} \rangle \tag{10.61}$$

$$+ \langle \xi_{t_0} M_{t_0,t}^{-1} B \left(M_r^{-1}\right)_{t,t} B | M_{t,t_0}^{-1} A M_{t_0,t_0}^{-1} A \xi_{t_0} \rangle. \tag{10.62}$$

Of course the rest part also requires inversions at each time slice. Therefore, an approximation of the identity $\mathbb{1} \approx \sum_\sigma |\sigma\rangle \langle\sigma|$ is included, where the vectors $|\sigma\rangle$ are normalized stochastic sources. The number of stochastic

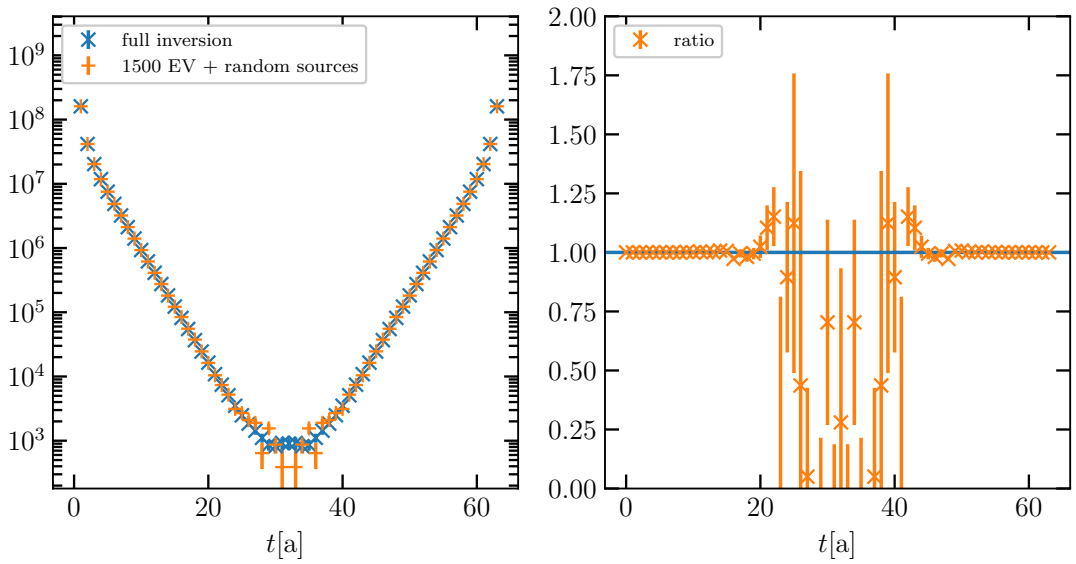

Figure 10.2 Comparison of exact and estimated two-pion propagator on the ensemble with $\beta = 3.7000$, $L/a = 48$ and $T/a = 64$. Left panel: Correlation function of the two-pion propagator with both pions having Goldstone and two units of momentum (in opposite directions). The blue data are measured exactly using the full inversion whereas the orange are exact on the lowest 1500 eigenvalues with the rest part being estimated using 24 random sources. Right panel: Ratio of the propagators from the two different methods. For a better visibility the optimal ratio is marked by a blue line. Previously published in [120].

sources N_σ has to be fine-tuned, not least because we are interested in saving computational resources. Of course, we also need a sufficient large amount of random sources such that we can reach the desired accuracy. It could be shown that choosing $N_\sigma \sim L/(2a)$ is an appropriate first choice.

The quality of the result and the savings of computational time are the two things that need further investigations. In order to do this we employ representative configurations out of the repository for the $g-2$ project, a list of the ensembles can be found in Table 6.1 and Table 6.2. Finally, it was made the decision to explore the coarsest ensembles available ($\beta = 3.7000$). This has the advantage that we can save computational resources even if we do simulations at our usual volume of $(6^3 \times 9)\,\text{fm}^4$. Additionally, we have access to different volumes at this β and therefore are able to investigate the volume scaling of the computing time.

When comparing the quality of the exact method and the approximation with low-mode-averaging and random sources it could be seen, that the quality of the second method strongly depends on the operator. For the Goldstone taste in combination with zero-momentum it is fairly easy to get a good quality even with a really small choice for N_σ. This is related to the fact that in this case the two-pion propagator is dominated by the low-modes. However, $p = 0$ does not have an overlap to the vector states because it has no particular direction. Thus, one cannot use this method in the way it works best.

Unfortunately, the quality gets worse and worse the higher the momentum and the more non-local the taste. This is due to the fact that in these cases the contribution of higher modes starts to dominate the overall

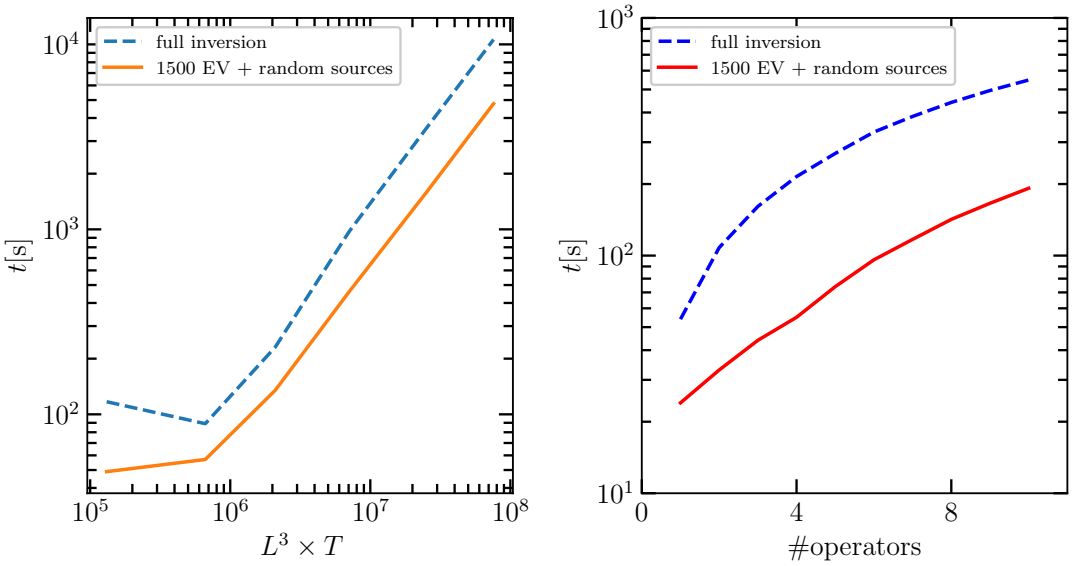

Figure 10.3 Comparison of the computational time for measuring all observables on a single configuration using the full inversion and the low-mode-averaging, respectively. Left panel: Computational time depending on the volume. Right panel: Computational time depending on the number of operators. Previously published in [120].

result. Increasing the number of eigenvalues and the number of random sources are possible solutions, but of course they come along with more computational effort. As a representative example I show a comparison of the quality of the Goldstone taste with the momentum being $\frac{4\pi}{L}$, i.e., two times the smallest possible momentum. It is shown in Figure 10.2. The propagators in the right panel look very similar apart from the noisy region around $T/2$. The comparison in the right panel is much more useful in this case. Here, the ratio of exact and low-mode-averaged is given. It is evident that the deviation starts to be significant around $18a \approx 2.3\,\text{fm}$. However, this is not a big deal since we want to use early windows to extract the mass plateaus and matrix elements. Thus larger noise at later windows does not provide any problems.

Apart from the fact that the new method seems to be sufficiently precise, the question remains whether we can save computational time. In order to clarify this, two tests were performed whose results are given in Figure 10.3. The first measures the simulation time as a function of the volume. In both cases, a behavior of polynomial order can be observed with the low-mode-averaging method scaling slightly better. The other test is performed with respect to the number of operators included. Here, it can be seen that both methods also scale similarly, with the low-mode-averaged method being superior by a global factor of three. All these tests are performed with the number of eigenvalues and N_σ being tuned so that both methods give a similar precision on the result.

10.3 Decomposition of the vector-like states and reconstruction of the vector propagator

In this section, a few results on the tail reconstruction of the vector meson propagator are discussed. We use 48 configurations of the $\beta = 3.7000$ ensemble with a physical extension of $(6^3 \times 9)\,\text{fm}^4$. The lattice spacing is (depending on the scheme) slightly larger than 0.13 fm and we use $2+1+1$ quarks that are close to the (isospin-symmetric) physical point. The configurations are generated with the `4stout` action [19, 20, 26, 50, 101].

On this configuration, the two-pion propagators (connected and disconnected), the vector correlator and the interaction propagator are measured. Of course, not all possible two-pion states are included in this study,

but only those with an energy smaller than the mass of the vector meson m_ρ. This is the case for Goldstone pions with up to three units of momentum, for axial-taste pions with up to two units of momentum, and for tensor-taste pions with one unit of momentum. For nearly all of the relevant combinations, 120 random sources are used. However, since the connected diagram is the most expensive and, additionally, very small compared to the disconnected one, only 30 random sources are used.

To resolve the energy states that contribute to the vector-meson propagator, a generalized eigenvalue problem is constructed. To deal with the noise related to higher excitation of the vector meson ($E > m_\rho$), we use the pencil-of-functions method [129, 236]. This means that time-shifted ρ-propagators are also included in the GEVP. This method is also applied in Chapter 6. As it can be seen in Table 10.2 there are now ten different two-pion combinations with an energy lower than that of the ρ-meson. Together with tree different time-shifts of the vector propagator from the pencil-of-functions method the overall correlation matrix is given by

$$\mathbf{C}(t) = \begin{pmatrix} C_{\rho\rho}(t-4) & C_{\rho\rho}(t-3) & C_{\rho\rho}(t-2) & C_{\rho(\pi\pi)^1}(t-2) & C_{\rho(\pi\pi)^2}(t-2) & \dots \\ C_{\rho\rho}(t-3) & C_{\rho\rho}(t-2) & C_{\rho\rho}(t-1) & C_{\rho(\pi\pi)^1}(t-1) & C_{\rho(\pi\pi)^2}(t-1) & \dots \\ C_{\rho\rho}(t-2) & C_{\rho\rho}(t-1) & C_{\rho\rho}(t) & C_{\rho(\pi\pi)^1}(t) & C_{\rho(\pi\pi)^2}(t) & \dots \\ C_{(\pi\pi)^1\rho}(t-2) & C_{(\pi\pi)^1\rho}(t-1) & C_{(\pi\pi)^1\rho}(t) & C_{(\pi\pi)^1(\pi\pi)^1}(t) & C_{(\pi\pi)^1(\pi\pi)^2}(t) & \dots \\ C_{(\pi\pi)^2\rho}(t-2) & C_{(\pi\pi)^2\rho}(t-1) & C_{(\pi\pi)^2\rho}(t) & C_{(\pi\pi)^2(\pi\pi)^1}(t) & C_{(\pi\pi)^2(\pi\pi)^2}(t) & \dots \\ \dots & \dots & \dots & \dots & \dots & \dots \end{pmatrix}. \tag{10.63}$$

Here, we denote the two-pion states that have the same quantum numbers as the ρ-meson by $(\pi\pi)^i$, where we used $1 \leq i \leq 10$ to label the states whose total energy is bound by 770 MeV.
We solve the GEVP

$$\mathbf{C}(t) \cdot V(t, t_0) = \lambda(t, t_0)\mathbf{C}(t) \cdot V(t, t_0), \tag{10.64}$$

where we choose $t_0 = 5$ and $t = 6$. The correlators are reconstructed by

$$\tilde{\lambda}_i(t) = V_i^\dagger \cdot \mathbf{C}(t) \cdot V_i. \tag{10.65}$$

They are shown in Figure 10.4. It is evident that there are two states that are very noisy, namely the green and the orange one. They are related to the higher excitations that appear in the ρ-propagator and are filtered out using the pencil of functions. Those two states are not considered in the reconstruction. However, this is not necessary because higher-energy states dominate the short-distance contributions and are suppressed exponentially in the long range. To get the energy states that contribute to the long distance contributions, we compute the corresponding effective masses using the local mass extraction formula

$$M^{\text{eff, loc}}(t) = \frac{1}{\Delta} \cosh^{-1} \frac{G(t+\Delta) + G(t-\Delta)}{2G(t)}, \tag{10.66}$$

where Δ is chosen to be $2a$. The corresponding effective masses are shown in Figure 10.5. Here, also the effective masses from the higher states (orange and green) are shown and it can be seen that they do not form a proper plateau at this level of precision. However, it is very likely that these states indeed correspond to higher energies, since most of the orange and green points are above the threshold of $am_\rho \approx 0.5$. To reconstruct the matrix elements that are needed to reconstruct the vector meson correlation function, we use the expression

$$a_i^{\text{eff.}} = \frac{(V_i \cdot \mathbf{C}(t) \cdot e_\rho)^2}{\tilde{\lambda}_i(t)} \times \exp\left(m^{\text{eff}}(t) \times t\right), \tag{10.67}$$

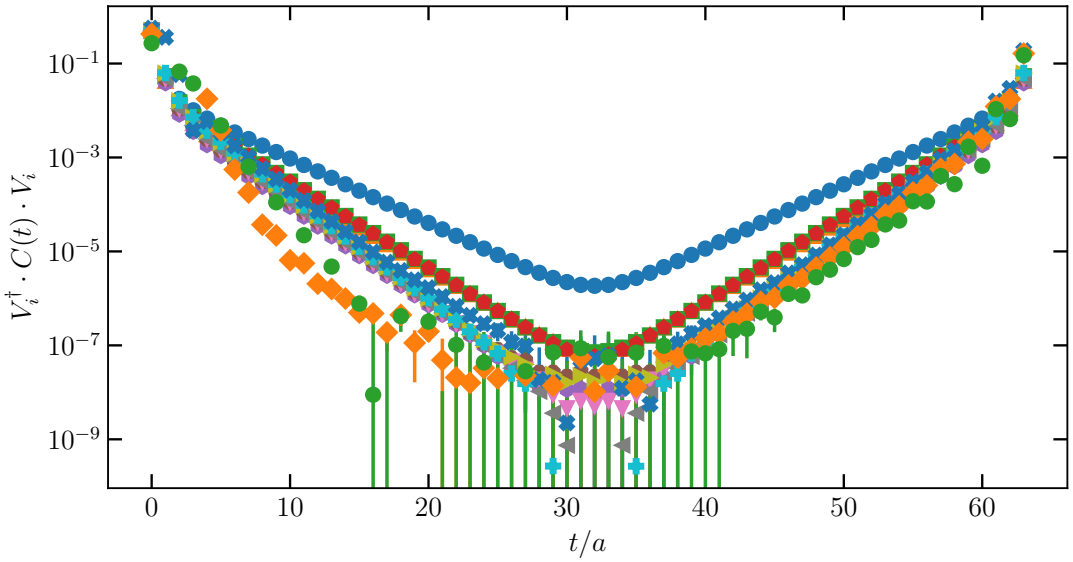

Figure 10.4 Eigenvalues of the vector GEVP. Previously published in [120].

where e_ρ is the unit vector that picks out the unshifted ρ-components of the of the correlation matrix $\mathbf{C}(t)$. The corresponding effective matrix elements can be seen in Figure 10.6. Again, the green and the orange do not build a plateau; however, they are not considered in the reconstruction. Furthermore, apart from the blue state, all matrix elements have a very large relative error. Additionally, the blue state dominates the overall result by far. This suggests that there appeared some problems in the generalized eigenvalue problem. However, we want to use the data to reconstruct the first moment $\sum_t \frac{t^4}{24}\rho(t)$. The integrand of the first moment can be seen in Figure 10.7, where the reconstruction is compared to the result of the direct simulation of the vector propagator. The two data sets are not compatible in the short-distance window, however, this is due to the fact that we did not include the (very noisy) higher excitations. Nevertheless, in the longer distances, the two methods are compatible with the reconstruction being much more precise.

10.4 Summary and comment on the further progress

In this work, a mathematical framework to to construct the two-pion states with the same quantum numbers as the taste-singlet vector meson at rest was derived. In principle, this framework can also be used for other tastes and momenta of the vector meson. The diagrams corresponding to this project (vector-meson, two-pion (connected and disconnected) and interaction) were implemented in the software framework *dynqcd*. For the connected two-pion contributions, a method for more efficient computations was designed. Some tests were performed to compare this method to the direct computation of the connected diagram and it was found out that the new method is superior. Finally, all this methods were combined to reconstruct the vector meson on our coarsest ensemble with a size of $(6^3 \times 9)\,\mathrm{fm}^4$, a lattice spacing of $a \approx 0.134\,\mathrm{fm}$ and physical quark masses. A precise computation of the tail of the vector-meson propagator is a very challenging task. Especially if staggered fermions are used, a lot of problems can occur. Staggered fermions have, in contrast to e.g. Wilson fermions, a taste structure. Thus, a large variety of states is present at finite lattice spacing, which have to be included in the generalized eigenvalue problem. For example, in this study ten two-pion states are used in the GEVP, without the taste structure it would have been three. Apart from the large number of contributing states, the taste structure provides more problems: The non-local tastes lead to an increment of the noise of the corresponding correlators, which makes it harder to resolve the energy states properly. As discussed in Section 10.2, the large number of operators require additional methods like low-mode averaging. It was also

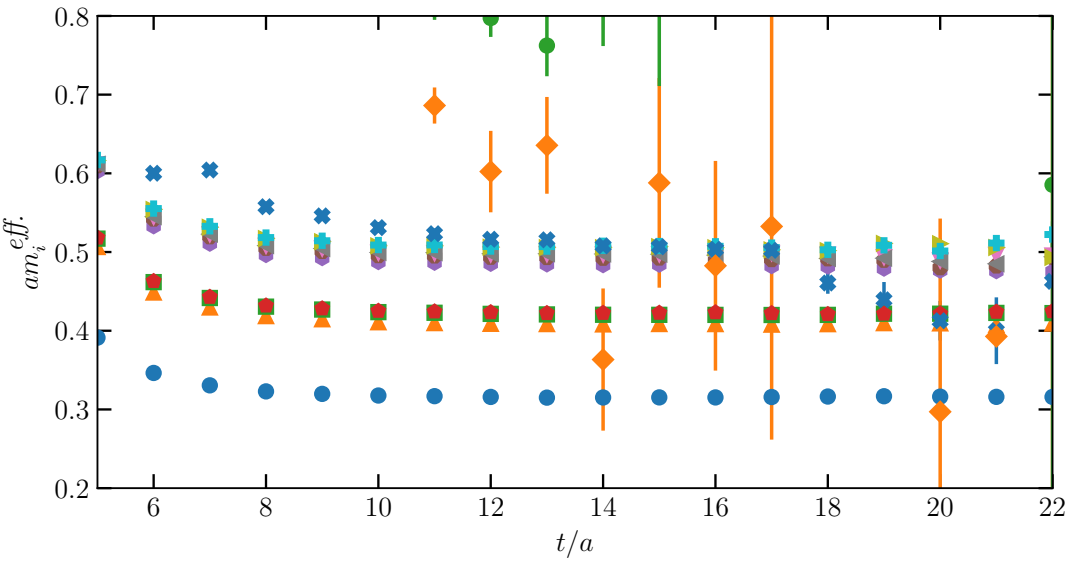

Figure 10.5 Effective masses of the vector GEVP. Previously published in [120].

shown that this method suffer from non-locality of the tastes.

In addition to the large number of problems with the taste structure, solving the GEVP does not seem to work optimally in this case. The overlap of the ρ and the two-pion state is likely too small. This issue could be resolved by adding a few steps of (for example) Wuppertal smearing [107] as it is done in our Ω-study in Chapter 6.

However, there are already working studies on the reconstruction of the tail of the vector meson for Domain-wall fermions [179], Wilson fermions [180] and also staggered fermions [128, 237]. However, in the staggered study of the MILC collaboration only a coarse lattice ($a \approx 0.15\,\mathrm{fm}$) is used with a physical extension of less than 5 fm. This leads to the fact that only three different two-pion states are included: Goldstone taste with one or two units of momentum and the axial taste with one unit of momentum. In combination with an appropriate smearing of the vector correlator they are able to give a proper reconstruction of the long-distance regime. Other discretization schemes of fermions, on the other hand, already provide a continuum extrapolation of the long-distance reconstruction [179, 180].

In summary it can be said that the reconstruction of the tail of the vector correlator using staggered fermions is hard task and there is still a lot of work to do. For other discretizations this task is easier already applied to $g-2$. Luckily, there are also methods like data-driven approaches, that allow us to compute the long-distance contributions to $g-2$ with a high-precision [20, 127].

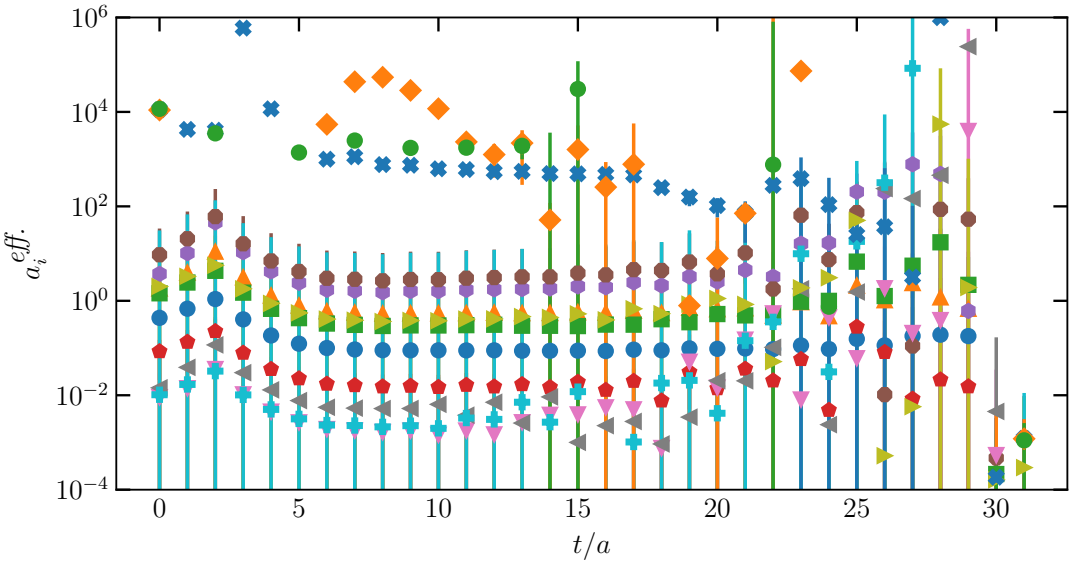

Figure 10.6 Matrix elements of the GEVP. Previously published in [120].

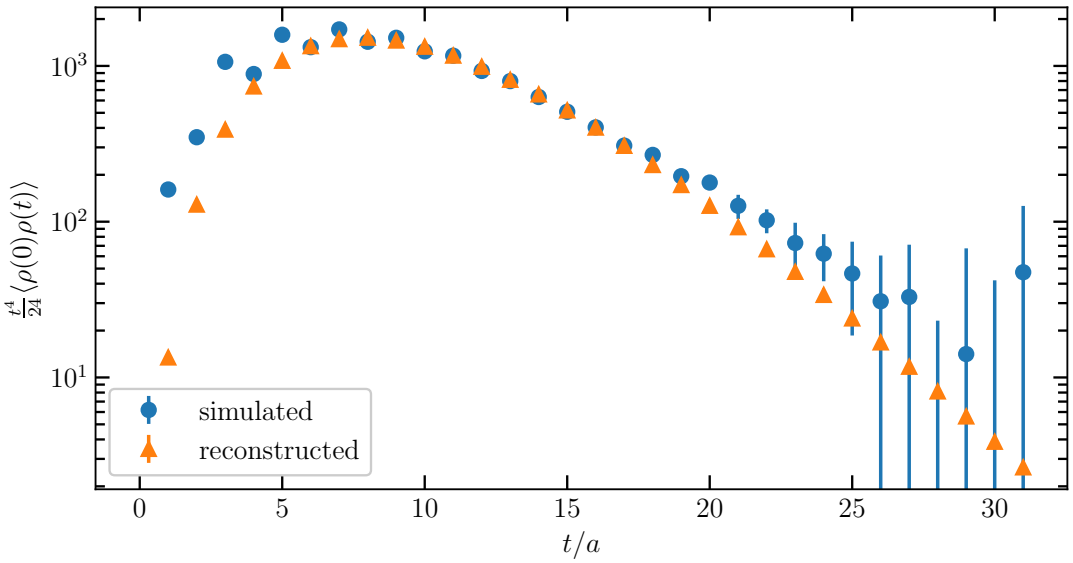

Figure 10.7 Reconstruction of the integrand of the first moment. Previously published in [120].

11 Conclusion and Outlook

This thesis presented several contributions to the field of lattice quantum chromodynamics, with a focus on high-precision determinations relevant for tests of the Standard Model.

The **first part** (Chapters 2–5) laid the theoretical groundwork for lattice field theory and provided a systematic introduction to path integral quantization, fermion discretization and the corresponding symmetry properties and the essential tools for data analysis in lattice simulations.

The **second part** of this thesis presents research I carried out in cooperation with the Budapest-Marseille-Wuppertal collaboration.

Two methods were employed to estimate the reference scales w_0 and t_0: one based on the Ω^- baryon mass, and another using the pion decay constant. Both approaches led to estimates with unprecedented precision. Both methods of estimating w_0 are now used in the most accurate lattice prediction of the hadronic vacuum polarization contribution to the muon anomaly [20].

Furthermore, techniques were explored to investigate the long-distance contributions to the muon $g-2$. Two-pion states with the same quantum numbers as the vector meson were constructed, and a mathematical framework was developed to resolve the mixing between two-pion and vector meson states using a generalized eigenvalue problem. Particular emphasis was placed on the implementation of the contributing diagrams, and a computational strategy was devised to reduce the cost of evaluating the computationally expensive connected diagrams. It was demonstrated that this approach significantly lowers runtime without compromising the quality of the resulting signal.

These techniques were implemented and tested on a large-volume ensemble ($6, \mathrm{fm}^3 \times 9, \mathrm{fm}$, $a \approx 0.13, \mathrm{fm}$). While first results on the reconstruction were obtained, this topic remains rich in open questions and challenges. At the end of this chapter, I provide a brief overview of the current status of the tail reconstruction and discuss several potential strategies to address the remaining issues.

Additionally, a high-precision lattice determination of the pseudo-scalar decay constant ratio was performed. This study included all relevant effects such as finite-volume corrections, strong isospin breaking and a careful treatment of sea and valence quark contributions. A noteworthy feature of this work was the inclusion of a novel fine lattice ensemble with $a = 0.034\,\mathrm{fm}$, which allowed for an unprecedented level of precision. The resulting estimate of f_K/f_π directly translates into a highly accurate determination of the relevant CKM matrix elements, and provides a stringent test of CKM unitarity within the Standard Model.

Outlook

The results of this thesis contribute to ongoing efforts to reduce the theoretical uncertainties in key observables of the Standard Model. In particular, the reconstruction of the long-distance tail of the vector correlator represents a step forward in lattice determinations of the hadronic vacuum polarization contribution to the muon anomalous magnetic moment. By implementing a method based on a generalized eigenvalue problem and applying it on a large-volume ensemble, this work demonstrated that improved control over the low-energy region is possible. However, in case of staggered fermions there is still a lot of open work as discussed in Section 10.4.

Further progress will require complementary approaches. Data-driven methods remain essential for validating lattice results in the region where the signal is suppressed but still relevant [20, 127]. Moreover, cross-checks using different fermion discretizations are crucial to ensure that systematic effects are under control. These aspects were already discussed in Section 10.4, and future work will need to build upon both the algorithmic and conceptual developments presented here.

An important element of this thesis is the inclusion of a new, exceptionally fine lattice ensemble with a

spacing of approximately 0.038 fm. While it played a central role in the precise determination of f_K/f_π, its usefulness goes far beyond that single application. The ensemble offers an opportunity to perform lattice simulations with significantly reduced discretization errors, which will benefit a broad class of observables ranging from hadron spectroscopy to weak matrix elements.

Finally, the determination of the reference scales w_0 and t_0 with previously unmatched precision has immediate practical value. These scales serve as key ingredients in setting the overall scale for many lattice calculations and have already been adopted in recent state-of-the-art determinations of a_μ^{HVP}. Reliable scale setting is a prerequisite for meaningful comparisons between theory and experiment, and the methods developed here will support future precision studies across a wide range of applications.

Part III

Appendices

12 Supplementary Material

12.1 Projective representations

Let G be a group, and $c : G \times G \to \mathbb{C}$ a function that fulfills the following conditions (for arbitrary $x, y, z \in G$):

- $|c(x, y)| = 1$
- $c(1_G, x) = c(x, 1_G) = 1$
- $c(x, y)^{-1} = c(y, x)^*$
- $c(x, y)c(xy, z) = c(x, yz)c(y, z)$

Then c is called a *standard factor system* or a *co-cycle* of G.
A projective representation of dimension n of G is given by a n dimensional vector space V and a mapping $\rho : G \to GL(V)$, that fulfills the condition

$$\rho(x) \cdot \rho(y) = c(x, y)\rho(xy) \quad \forall x, y, \in G. \tag{12.1}$$

If $c(x, y) = 1$ for all x, y in G then this projective representation is called a *true representation* or simply a *representation* [238]. The matrix representation of ρ is often written as d^ρ. A subspace $U \subset V$ is called an invariant subspace of ρ, if $\rho(U) \subset U$. If V and $\{0\}$ are the only possible choices for U, then ρ is called an irreducible representation or an *irrep* [239].
A representation is called *faithful* if it is injective.

12.2 Central Group Extensions

It is possible to write a group G as a direct product of a normal subgroup N and the quotient group G/N as

$$G = N \times G/N. \tag{12.2}$$

A group extension proceeds the other way around, a group G is constructed out of two groups N and Q, where N is a normal subgroup of G and $Q \sim G/N$. One often calls G a group extension of N by Q. If N is in the center of G, i.e., each element of N commutes with every element of G, the group extension is called a central extension.
In this thesis mainly irreducible matrix groups are considered. The center of those groups is always proportional to the identity. For example every central extension of $SU(N)$ is a subgroup of $U(n) = \mathbb{C} \rtimes SU(n)$.

12.3 Generelization of Wigner's Little Group Procedure

In this section the method to compute irreps of semi-direct products is given, i.e., the way to construct the irreps of $G = N \rtimes H$ out of the irreps of N and H. This method consists of four steps which will be explained in detail:

1. At first one has to decompose the representations of N into H-orbits. In order to do this one defines the following equivalence relation:

$$\gamma \sim \gamma' \iff \exists h \in H \text{ and } U \in SU(V) : d^\gamma(hnh^{-1}) = U d^{\gamma'}(n) U^\dagger. \tag{12.3}$$

This means that two irreps of N are in the same orbits iff they can be transformed into each other by conjugation with h up to equivalence. If N is an abelian group, all of its irreps are one dimensional and the transformation U can be left out.

2. Next one has to select a representative γ for each orbit and define its little group $H(\gamma)$ in the following way:

$$H(\gamma) = \{h \in H : d^{\gamma}(hnh^{-1}) = U d^{\gamma}(n) U^{\dagger} \text{ for some } U \in SU(V)\}. \tag{12.4}$$

Again, if N is an abelian group the unitary transformation can be left out. The stability group of γ is then given by

$$L(\gamma) = N \rtimes H(\gamma) \subset G. \tag{12.5}$$

3. The next task is to find the *allowable* irreps of $L(\gamma)$. If N is an abelian group it is rather simple: The irreps are given by $d^{\gamma} \otimes d^{\delta}$, where δ is an irrep of $H(\gamma)$. For the non-abelian case we have

$$d^{(\gamma)}(hnh^{-1}) = U(h) d^{(\gamma)}(n) U^{-1}(h). \tag{12.6}$$

By Schur's Lemma, $U(h)$ is unique up to a phase, and therefore these transformations generate a projective representation of H. If the phases can be chosen such that the $U(h)$ give a true representation, then the irreps are given by

$$(0,h) \cdot (n,1) = (hnh^{-1}, h) \mapsto U(h) \cdot d^{\gamma}(n) \otimes d^{\delta}(h). \tag{12.7}$$

If the unitary matrices cannot be chosen in this way, one uses projective representations of $H(\gamma)$ such that they cancel. In order to do this one considers the central extension $\tilde{H}(\gamma)$ of $H(\gamma)$ and takes its faithful representations $\tilde{\delta}$ instead of δ [59, 238, 240].

12.4 Grassmann algebra

While scalar fields can be described by complex numbers and vector fields are usually described by real four-component vectors, fermions have to be described by a type of numbers that anticommute in order to satisfy the spin-statistics theorem. The type of numbers needed in this case is called the Grassmann algebra. Its construction is explained in the following section.
The first ingredient is a vector space V whose dimension N corresponds to two times the number of degrees of freedoms of the fermion field. In the context of staggered fermions in lattice gauge theory we have $\dim(V) = 2N_c \times L^3 \times T$, in a continuous theory this vector space has infinite dimension. Next a basis $\{\eta_i\}_{1 \le i \le N} \subset V$ is chosen, which is used to construct a basis of the exterior product of V with itself $V_2 \coloneqq V \wedge V$

$$\{\eta_i \wedge \eta_j\}_{1 \le i \le j \le N} \subset V_2 \quad (\eta_j \wedge \eta_i = -\eta_i \wedge \eta_j), \tag{12.8}$$

as well as the basis n-fold exterior product V_n

$$\{\eta_{i_1} \wedge \eta_{i_2} \wedge \ldots \wedge \eta_{i_n}\}_{1 \le i_1 \le i_2 \le \ldots \le i_n} \subset V_n. \tag{12.9}$$

The Grassmann algebra over V is thus defined as

$$\Lambda(V) = V_0 \oplus V_1 \oplus \ldots \oplus V_N, \tag{12.10}$$

where V_0 is defined to be the field of complex or real numbers and $V_1 \coloneqq V$. The wedge product symbol is often omitted, so one writes vw instead of $v \wedge w$. The Grassmann algebra is an anticommutative algebra with unity of dimension 2^{2N}, where usually half of its generators are labeled by $(\eta_i)_i$ and half by $(\eta_i^\dagger)_i$. The dagger does not mean that the second set is the adjoint of the first set, but it plays a similar role as the complex conjugate in the case of pseudo-fermions.
Due to the fact that the square of an element of the Grassmann algebra is zero, it can be concluded that each Taylor expansion only has a finite number of terms. In other words, every analytical function on the Grassmann algebra is a polynomial. Integration and differentiation on $\Lambda(V)$ are defined via

$$\int \mathrm{d}\eta_i \, \eta_j = \delta_{ij}, \tag{12.11}$$

$$\frac{\partial}{\partial \eta_i} \eta_j = \delta_{ij}. \tag{12.12}$$

The most important integral in the context of Grassmann numbers, the Gaussian integral on $\Lambda(V)$, is

$$\int \prod_{i=1}^{N} \left[\mathrm{d}\eta_i^\dagger \mathrm{d}\eta_i\right] \exp\left(-\sum_{kl} \eta_k^\dagger M^{kl} \eta_l\right) = \det(M), \tag{12.13}$$

whenever it is a normal matrix, i.e., it commutes with its adjoint and therefore is diagonalizable. This can be derived using the one dimensional integral

$$\int \mathrm{d}\eta^\dagger \mathrm{d}\eta \, \exp\left(-\lambda \eta^\dagger \eta\right) = \int \mathrm{d}\eta^\dagger \mathrm{d}\eta \, \left(1 - \lambda \eta^\dagger \eta\right) = \lambda \tag{12.14}$$

and a suitable coordinate transformation for the Grassmann algebra.

Bibliography

[1] Albrecht Fölsing. *Albert Einstein: Eine Biographie*. Suhrkamp-Taschenbuch 3087. Letter from August 10, 1954 to Michele Besso, cited on p. 824. Frankfurt am Main: Suhrkamp, 1999. ISBN: 3-518-39587-4.

[2] Pierre Cladé et al. "Determination of the Fine Structure Constant Based on Bloch Oscillations of Ultracold Atoms in a Vertical Optical Lattice". In: *Phys. Rev. Lett.* 96 (3 2006), p. 033001. DOI: 10.1103/PhysRevLett.96.033001. URL: https://link.aps.org/doi/10.1103/PhysRevLett.96.033001.

[3] X. Fan et al. "Measurement of the Electron Magnetic Moment". In: *Phys. Rev. Lett.* 130 (7 2023), p. 071801. DOI: 10.1103/PhysRevLett.130.071801. URL: https://link.aps.org/doi/10.1103/PhysRevLett.130.071801.

[4] T. Albahri et al. "Beam dynamics corrections to the Run-1 measurement of the muon anomalous magnetic moment at Fermilab". In: *Phys. Rev. Accel. Beams* 24 (4 2021), p. 044002. DOI: 10.1103/PhysRevAccelBeams.24.044002. URL: https://link.aps.org/doi/10.1103/PhysRevAccelBeams.24.044002.

[5] T. Albahri et al. "Magnetic-field measurement and analysis for the Muon $g-2$ Experiment at Fermilab". In: *Phys. Rev. A* 103 (4 2021), p. 042208. DOI: 10.1103/PhysRevA.103.042208. URL: https://link.aps.org/doi/10.1103/PhysRevA.103.042208.

[6] T. Albahri et al. "Measurement of the anomalous precession frequency of the muon in the Fermilab Muon $g-2$ Experiment". In: *Phys. Rev. D* 103 (7 2021), p. 072002. DOI: 10.1103/PhysRevD.103.072002. URL: https://link.aps.org/doi/10.1103/PhysRevD.103.072002.

[7] B. Abi et al. "Measurement of the Positive Muon Anomalous Magnetic Moment to 0.46 ppm". In: *Phys. Rev. Lett.* 126 (14 2021), p. 141801. DOI: 10.1103/PhysRevLett.126.141801. URL: https://link.aps.org/doi/10.1103/PhysRevLett.126.141801.

[8] D. P. Aguillard et al. "Measurement of the Positive Muon Anomalous Magnetic Moment to 0.20ăppm". In: *Physical Review Letters* 131.16 (2023). ISSN: 1079-7114. DOI: 10.1103/physrevlett.131.161802. URL: http://dx.doi.org/10.1103/PhysRevLett.131.161802.

[9] D. P. Aguillard et al. "Detailed report on the measurement of the positive muon anomalous magnetic moment to 0.20 ppm". In: *Phys. Rev. D* 110 (3 2024), p. 032009. DOI: 10.1103/PhysRevD.110.032009. URL: https://link.aps.org/doi/10.1103/PhysRevD.110.032009.

[10] Robert Oerter and B. Holstein. "The Theory of Almost Everything: The Standard Model, the Unsung Triumph of Modern Physics". In: *Physics Today - PHYS TODAY* 59 (July 2006). DOI: 10.1063/1.2337829.

[11] H. Harari. "A new quark model for hadrons". In: *Physics Letters B* 57.3 (1975), pp. 265–269. ISSN: 0370-2693. DOI: https://doi.org/10.1016/0370-2693(75)90072-6. URL: https://www.sciencedirect.com/science/article/pii/0370269375900726.

[12] F. Abe et al. "Observation of Top Quark Production in pp Collisions with the Collider Detector at Fermilab". In: *Physical Review Letters* 74.14 (1995), pp. 2626–2631. ISSN: 1079-7114. DOI: 10.1103/physrevlett.74.2626. URL: http://dx.doi.org/10.1103/PhysRevLett.74.2626.

[13] K. Kodama et al. "Observation of tau neutrino interactions". In: *Physics Letters B* 504.3 (2001), pp. 218–224. ISSN: 0370-2693. DOI: https://doi.org/10.1016/S0370-2693(01)00307-0. URL: https://www.sciencedirect.com/science/article/pii/S0370269301003070.

[14] G. Aad et al. "Combined search for the Standard Model Higgs boson using up to 4.9fb^{-1} of pp collision data at s = 7,TeV with the ATLAS detector at the LHC". In: *Physics Letters B* 710.1 (2012), pp. 49–66. ISSN: 0370-2693. DOI: 10.1016/j.physletb.2012.02.044. URL: http://dx.doi.org/10.1016/j.physletb.2012.02.044.

[15] Lev Davidovich Landau, A. A. Abrikosov, and I. M. Khalatnikov. "The Removal of Infinities in Quantum Electrodynamics". In: *Dokl. Akad. Nauk SSSR* 95 (1954). Ed. by D. ter Haar. DOI: 10.1016/b978-0-08-010586-4.50083-3.

[16] Michael E. Peskin and Daniel V. Schröder. *An Introduction to Quantum Field Theory*. Westview Press, 1995.

[17] Kenneth G. Wilson. "Confinement of quarks". In: *Phys. Rev. D* 10 (8 1974), pp. 2445–2459. DOI: 10.1103/PhysRevD.10.2445. URL: https://link.aps.org/doi/10.1103/PhysRevD.10.2445.

[18] Michael Creutz. "Confinement and the Critical Dimensionality of Space-Time". In: *Phys. Rev. Lett.* 43 (8 1979), pp. 553–556. DOI: 10.1103/PhysRevLett.43.553. URL: https://link.aps.org/doi/10.1103/PhysRevLett.43.553.

[19] Sz. Borsanyi et al. "Leading hadronic contribution to the muon magnetic moment from lattice QCD". In: *Nature* 593.7857 (2021), pp. 51–55. DOI: 10.1038/s41586-021-03418-1. URL: https://doi.org/10.1038%2Fs41586-021-03418-1.

[20] A. Boccaletti et al. "High precision calculation of the hadronic vacuum polarisation contribution to the muon anomaly". In: (2024). arXiv: 2407.10913 [hep-lat].

[21] M. A. Clark et al. "Solving Lattice QCD systems of equations using mixed precision solvers on GPUs". In: *Comput. Phys. Commun.* 181 (2010), pp. 1517–1528. DOI: 10.1016/j.cpc.2010.05.002. arXiv: 0911.3191 [hep-lat].

[22] Gyozo I. Egri et al. "Lattice QCD as a video game". In: *Comput. Phys. Commun.* 177 (2007), pp. 631–639. DOI: 10.1016/j.cpc.2007.06.005. arXiv: hep-lat/0611022.

[23] Piyush Kumar et al. "Portable Lattice QCD implementation based on OpenCL". In: *PoS* LATTICE2024 (2025), p. 438. DOI: 10.22323/1.466.0438. arXiv: 2502.03249 [hep-lat].

[24] Luca Chirminisi. "Gauge fixing in lattice models using quantum annealing". BA thesis. University of Wuppertal, 2025.

[25] M. S. Albergo, G. Kanwar, and P. E. Shanahan. "Flow-based generative models for Markov chain Monte Carlo in lattice field theory". In: *Phys. Rev. D* 100.3 (2019), p. 034515. DOI: 10.1103/PhysRevD.100.034515. arXiv: 1904.12072 [hep-lat].

[26] Frech et al. "Determination of f_K/f_π from 2+1+1 flavor 4-stout staggered lattices". to be published.

[27] Andreas Klümper. *Fortgeschrittene Quantenmechanik*. Lecture series at University of Wuppertal. 2023. URL: http://wptl26.physik.uni-wuppertal.de/~kluemper/FQM_2223/FQM_Skript.pdf.

[28] Christian Hölbling. *QFT*. Lecture series at University of Wuppertal. 2019. URL: http://particle.uni-wuppertal.de/hch/qft_19.pdf.

[29] Andreas Risch. *Einführung in die Quantenfeldtheorie*. Lecture series at University of Wuppertal. 2024.

[30] Reinhard Hentschke and Christian Hölbling. *A Short Course in General Relativity and Cosmology*. Undergraduate Lecture Notes in Physics. Springer, 2020. DOI: 10.1007/978-3-030-46384-7.

[31] Reinhard Hentschke. *Klassische Elektrodynamik*. Lecture series at University of Wuppertal. 2017. URL: https://constanze.materials.uni-wuppertal.de/fileadmin/physik/theochemphysik/Skripten/Elektrodynamik.pdf.

[32] Lev D. Landau and Evgenij M. Lifschitz. *Lehrbuch der theoretischen Physik: Bd. 7: Elastizitätstheorie; 7., unveränd. Aufl.* Berlin: Akademie-Verl., 1991, 223 Seiten. ISBN: 3055005805.

[33] Matthew D. Schwartz. *Quantum Field Theory and the Standard Model*. Cambridge University Press, 2013.

[34] Steven Weinberg. *Quantum Theory of fields*. Cambridge University Press, 1995.

[35] Christof Gattringer and Christian B. Lang. *Quantum Chromodynamics on the Lattice*. Springer Heidelberg Dordrecht London New York, 2010.

[36] Andreas Klümper. *Quantenmechanik*. Lecture series at University of Wuppertal. 2024. URL: http://wptl26.physik.uni-wuppertal.de/~kluemper/QM_2324/QM.pdf.

[37] Lukas Varnhorst. *Ausgewählte Kapitel der Gittereichtheorie*. Lecture series at University of Wuppertal. 2020.

[38] S. Scherer. *Introduction to Chiral Perturbation Theory*. 2002. arXiv: hep-ph/0210398 [hep-ph]. URL: https://arxiv.org/abs/hep-ph/0210398.

[39] David Griffiths. *Introduction to elementary particles*. WILEY-VCH, 2008.

[40] F. Halzen and A.D. Martin. *Quarks and Leptones: An Introductory Course in Modern Particle Physics*. Wiley, 1984. ISBN: 9780471887416. URL: https://books.google.de/books?id=zwDvAAAAMAAJ.

[41] Steven Weinberg. *Quantum Theory of fields II*. Cambridge University Press, 2005.

[42] S. Bethke. "Experimental tests of asymptotic freedom". In: *Progress in Particle and Nuclear Physics* 58.2 (2007), pp. 351–386. ISSN: 0146-6410. DOI: https://doi.org/10.1016/j.ppnp.2006.06.001. URL: https://www.sciencedirect.com/science/article/pii/S0146641006000615.

[43] S. Navas et al. "Review of particle physics". In: *Phys. Rev. D* 110.3 (2024), p. 030001. DOI: 10.1103/PhysRevD.110.030001.

[44] Siegfried Bethke. "World Summary of α_s (2012)". In: *Nucl. Phys. B Proc. Suppl.* 234 (2013). Ed. by Stephan Narison, pp. 229–234. DOI: 10.1016/j.nuclphysbps.2012.12.020. arXiv: 1210.0325 [hep-ex].

[45] David J. Gross and Frank Wilczek. "Ultraviolet Behavior of Non-Abelian Gauge Theories". In: *Phys. Rev. Lett.* 30 (26 1973), pp. 1343–1346. DOI: 10.1103/PhysRevLett.30.1343. URL: https://link.aps.org/doi/10.1103/PhysRevLett.30.1343.

[46] H. David Politzer. "Reliable Perturbative Results for Strong Interactions?" In: *Phys. Rev. Lett.* 30 (26 1973), pp. 1346–1349. DOI: 10.1103/PhysRevLett.30.1346. URL: https://link.aps.org/doi/10.1103/PhysRevLett.30.1346.

[47] G. C. Wick. "Properties of Bethe-Salpeter Wave Functions". In: *Phys. Rev.* 96 (4 1954), pp. 1124–1134. DOI: 10.1103/PhysRev.96.1124. URL: https://link.aps.org/doi/10.1103/PhysRev.96.1124.

[48] Timo Eichhorn. "Slowing down critical slowing down". MA thesis. University of Wuppertal, 2024.

[49] K. Symanzik. "Continuum limit and improved action in lattice theories: (I). Principles and phi4 theory". In: *Nuclear Physics B* 226.1 (1983), pp. 187–204. ISSN: 0550-3213. DOI: https://doi.org/10.1016/0550-3213(83)90468-6. URL: https://www.sciencedirect.com/science/article/pii/0550321383904686.

[50] M. Luscher and P. Weisz. "On-Shell Improved Lattice Gauge Theories". In: *Commun. Math. Phys.* 97 (1985). [Erratum: Commun.Math.Phys. 98, 433 (1985)], p. 59. DOI: 10.1007/BF01206178.

[51] Tetsuya Takaishi. "Heavy quark potential and effective actions on blocked configurations". In: *Phys. Rev. D* 54 (1996), pp. 1050–1053. DOI: 10.1103/PhysRevD.54.1050.

[52] Y. Iwasaki. "Renormalization Group Analysis of Lattice Theories and Improved Lattice Action. II. Four-dimensional non-Abelian SU(N) gauge model". In: (Dec. 1983). arXiv: 1111.7054 [hep-lat].

[53] John Kogut and Leonard Susskind. "Hamiltonian formulation of Wilson's lattice gauge theories". In: *Phys. Rev. D* 11 (2 1975), pp. 395–408. DOI: 10.1103/PhysRevD.11.395. URL: https://link.aps.org/doi/10.1103/PhysRevD.11.395.

[54] Christian Zielinski. "Theoretical and Computational Aspects of New Lattice Fermion Formulations". PhD thesis. Nanyang Technol. U., 2016. arXiv: 1703.06364 [hep-lat].

[55] E. Follana et al. "High Precision determination of the π, K, D and $D(s)$ decay constants from lattice QCD". In: *Phys. Rev. Lett.* 100 (2008), p. 062002. DOI: 10.1103/PhysRevLett.100.062002. arXiv: 0706.1726 [hep-lat].

[56] M. Baake, B. Gemünden, and R. Oedingen. "Erratum: Structure and representations of the symmetry group of the fourdimensional cube [J. Math. Phys. 23, 944 (1982)]". In: *Journal of Mathematical Physics* 23.12 (1982), pp. 2595–2595. DOI: 10.1063/1.525334. eprint: https://doi.org/10.1063/1.525334. URL: https://doi.org/10.1063/1.525334.

[57] Jeffrey E. Mandula, George Zweig, and Jan Govaerts. "Representations of the rotation reflection symmetry group of the four-dimensional cubic lattice". In: *Nuclear Physics B* 228.1 (1983), pp. 91–108. ISSN: 0550-3213. DOI: https://doi.org/10.1016/0550-3213(83)90399-1. URL: https://www.sciencedirect.com/science/article/pii/0550321383903991.

[58] Simon Mages et al. "Lattice QCD on nonorientable manifolds". In: *Phys. Rev. D* 95 (2017), p. 094512. DOI: 10.1103/PhysRevD.95.094512. arXiv: 1512.06804 [hep-lat].

[59] G.W. Kilcup and Stephen R. Sharpe. "A tool kit for staggered fermions". In: *Nuclear Physics B* 283 (1987), pp. 493–550. ISSN: 0550-3213. DOI: https://doi.org/10.1016/0550-3213(87)90285-9. URL: https://www.sciencedirect.com/science/article/pii/0550321387902859.

[60] E. Follana et al. "Highly improved staggered quarks on the lattice, with applications to charm physics". In: *Phys. Rev. D* 75 (2007), p. 054502. DOI: 10.1103/PhysRevD.75.054502. arXiv: hep-lat/0610092.

[61] Lukas Varnhorst. *Ausgewählte Kapitel der Gittereichtheorie 2*. Lecture series at University of Wuppertal. 2023.

[62] Maarten Golterman. "Staggered fermions". In: (2024). arXiv: 2406.02906 [hep-lat].

[63] T. Banks et al. "Strong-coupling calculations of the hadron spectrum of quantum chromodynamics". In: *Phys. Rev. D* 15 (4 1977), pp. 1111–1127. DOI: 10.1103/PhysRevD.15.1111. URL: https://link.aps.org/doi/10.1103/PhysRevD.15.1111.

[64] Leonard Susskind. "Lattice fermions". In: *Phys. Rev. D* 16 (10 1977), pp. 3031–3039. DOI: 10.1103/PhysRevD.16.3031. URL: https://link.aps.org/doi/10.1103/PhysRevD.16.3031.

[65] Maarten F. L. Golterman. "Staggered mesons". In: *Nucl. Phys. B* 273 (1986), pp. 663–676. DOI: 10.1016/0550-3213(86)90383-4.

[66] Russel E. Caflisch. "Monte Carlo and quasi-Monte Carlo methods". In: *Acta Numerica* 7 (1998), pp. 1–49. DOI: 10.1017/S0962492900002804.

[67] Francesco Knechtli and Ulli Wolff. "Dynamical fermions as a global correction". In: *Nucl. Phys. B* 663 (2003), pp. 3–32. DOI: 10.1016/S0550-3213(03)00369-9. arXiv: hep-lat/0303001.

[68] Michael Creutz. "Monte Carlo study of quantized SU(2) gauge theory". In: *Phys. Rev. D* 21 (8 1980), pp. 2308–2315. DOI: 10.1103/PhysRevD.21.2308. URL: https://link.aps.org/doi/10.1103/PhysRevD.21.2308.

[69] K. Fabricius and O. Haan. "Heat bath method for the twisted Eguchi-Kawai model". In: *Physics Letters B* 143.4 (1984), pp. 459–462. ISSN: 0370-2693. DOI: https://doi.org/10.1016/0370-2693(84)91502-8. URL: https://www.sciencedirect.com/science/article/pii/0370269384915028.

[70] A.D. Kennedy and B.J. Pendleton. "Improved heatbath method for Monte Carlo calculations in lattice gauge theories". In: *Physics Letters B* 156.5 (1985), pp. 393–399. ISSN: 0370-2693. DOI: https://doi.org/10.1016/0370-2693(85)91632-6. URL: https://www.sciencedirect.com/science/article/pii/0370269385916326.

[71] Stephen L. Adler. "Over-relaxation method for the Monte Carlo evaluation of the partition function for multiquadratic actions". In: *Phys. Rev. D* 23 (12 1981), pp. 2901–2904. DOI: 10.1103/PhysRevD.23.2901. URL: https://link.aps.org/doi/10.1103/PhysRevD.23.2901.

[72] Simon Duane et al. "Hybrid Monte Carlo". In: *Physics Letters B* 195.2 (1987), pp. 216–222. ISSN: 0370-2693. DOI: https://doi.org/10.1016/0370-2693(87)91197-X. URL: https://www.sciencedirect.com/science/article/pii/037026938791197X.

[73] Frank R. Brown and Thomas J. Woch. "Overrelaxed heat-bath and Metropolis algorithms for accelerating pure gauge Monte Carlo calculations". In: *Phys. Rev. Lett.* 58 (23 1987), pp. 2394–2396. DOI: 10.1103/PhysRevLett.58.2394. URL: https://link.aps.org/doi/10.1103/PhysRevLett.58.2394.

[74] Stephan Durr. "Physics of η' with rooted staggered quarks". In: *Phys. Rev. D* 85 (2012), p. 114503. DOI: 10.1103/PhysRevD.85.114503. arXiv: 1203.2560 [hep-lat].

[75] Timo Eichhorn and Christian Hoelbling. "Comparison of topology changing update algorithms". In: *PoS* LATTICE2021 (2022), p. 573. DOI: 10.22323/1.396.0573. arXiv: 2112.05188 [hep-lat].

[76] Timo Eichhorn et al. "Topology changing update algorithms for SU(3) gauge theory". In: *PoS* LATTICE2022 (2023), p. 009. DOI: 10.22323/1.430.0009. arXiv: 2210.11453 [hep-lat].

[77] Timo Eichhorn et al. "Parallel Tempered Metadynamics: Overcoming potential barriers without surfing or tunneling". In: (July 2023). arXiv: 2307.04742 [hep-lat].

[78] Philip Rouenhoff et al. "Metadynamics Surfing on Topology Barriers in the Schwinger Model". In: *PoS* LATTICE2022 (2022), p. 253. DOI: 10.22323/1.430.0253. arXiv: 2212.11665 [hep-lat].

[79] A. Laio, G. Martinelli, and F. Sanfilippo. "Metadynamics surfing on topology barriers: the CP^{N-1} case". In: *Journal of High Energy Physics* 2016.7 (2016). ISSN: 1029-8479. DOI: 10.1007/jhep07(2016)089. URL: http://dx.doi.org/10.1007/JHEP07(2016)089.

[80] Timo Eichhorn et al. "Parallel Tempered Metadynamics". In: *41st International Symposium on Lattice Field Theory*. Mar. 2025. DOI: 10.22323/1.466.0061. arXiv: 2503.09747 [hep-lat].

[81] Zoltan Fodor, Sandor D. Katz, and Christian Schmidt. "The Density of states method at non-zero chemical potential". In: *JHEP* 03 (2007), p. 121. DOI: 10.1088/1126-6708/2007/03/121. arXiv: hep-lat/0701022.

[82] Christof Gattringer, Michael Mandl, and Pascal Törek. "New density of states approaches to finite density lattice QCD". In: *Physical Review D* 100.11 (2019). ISSN: 2470-0029. DOI: 10.1103/physrevd.100.114517. URL: http://dx.doi.org/10.1103/PhysRevD.100.114517.

[83] N. Metropolis et al. "Equation of state calculations by fast computing machines". In: *J. Chem. Phys.* 21 (1953), pp. 1087–1092. DOI: 10.1063/1.1699114.

[84] S. Duane et al. "Hybrid Monte Carlo". In: *Phys. Lett. B* 195 (1987), pp. 216–222. DOI: 10.1016/0370-2693(87)91197-X.

[85] A. D. Kennedy. "Algorithms for dynamical fermions". In: (July 2006). arXiv: hep-lat/0607038.

[86] I. P. Omelyan, I. M. Mryglod, and R. Folk. "Symplectic analytically integrable decomposition algorithms: classification, derivation, and application to molecular dynamics, quantum and celestial mechanics simulations". In: *Comput. Phys. Commun.* 151.3 (2003), pp. 272–314. DOI: 10.1016/S0010-4655(02)00754-3.

[87] M. R. Hestenes and E. Stiefel. "Methods of conjugate gradients for solving linear systems". In: *Journal of research of the National Bureau of Standards* 49 (1952), pp. 409–436.

[88] E. Marinari, G. Parisi, and C. Rebbi. "Monte Carlo Simulation of the Massive Schwinger Model". In: *Nucl. Phys. B* 190 (1981). Ed. by J. Julve and M. Ramón-Medrano, p. 734. DOI: 10.1016/0550-3213(81)90048-1.

[89] Michael Creutz. "Comments on staggered fermions: Panel discussion". In: *PoS* CONFINEMENT8 (2008), p. 016. DOI: 10.22323/1.077.0016. arXiv: 0810.4526 [hep-lat].

[90] Stephen R. Sharpe. *Rooted staggered fermions: good, bad or ugly?* 2006. arXiv: hep-lat/0610094 [hep-lat]. URL: https://arxiv.org/abs/hep-lat/0610094.

[91] Andreas Frommer et al. "Many masses on the stroke: economic computation of quark propagators". In: *International Journal of Modern Physics C* 06.05 (1995), pp. 627–638. ISSN: 1793-6586. DOI: 10.1142/s0129183195000538. URL: http://dx.doi.org/10.1142/S0129183195000538.

[92] M. A. Clark. *The Rational Hybrid Monte Carlo Algorithm.* 2006. arXiv: hep-lat/0610048 [hep-lat]. URL: https://arxiv.org/abs/hep-lat/0610048.

[93] Martin Luscher. "Trivializing maps, the Wilson flow and the HMC algorithm". In: *Commun. Math. Phys.* 293 (2010), pp. 899–919. DOI: 10.1007/s00220-009-0953-7. arXiv: 0907.5491 [hep-lat].

[94] Martin Lüscher. "Properties and uses of the Wilson flow in lattice QCD". In: *JHEP* 08 (2010). [Erratum: JHEP 03, 092 (2014)], p. 071. DOI: 10.1007/JHEP08(2010)071. arXiv: 1006.4518 [hep-lat].

[95] Stefan Sint and Alberto Ramos. "On O(a^2) effects in gradient flow observables". In: *PoS* LATTICE2014 (2015), p. 329. DOI: 10.22323/1.214.0329. arXiv: 1411.6706 [hep-lat].

[96] A. Ramos and S. Sint. "Symanzik improvement of the gradient flow in lattice gauge theories". In: *Eur. Phys. J. C* 76.1 (2016), p. 15. DOI: 10.1140/epjc/s10052-015-3831-9. arXiv: 1508.05552 [hep-lat].

[97] Timo Eichhorn and Fabian Frech. *Autocorrelation in SU(3) gauge theories.* Project practical. 2021.

[98] M. Albanese et al. "Glueball masses and string tension in lattice QCD". In: *Physics Letters B* 192.1 (1987), pp. 163–169. ISSN: 0370-2693. DOI: https://doi.org/10.1016/0370-2693(87)91160-9. URL: https://www.sciencedirect.com/science/article/pii/0370269387911609.

[99] Anna Hasenfratz and Francesco Knechtli. "Flavor symmetry and the static potential with hypercubic blocking". In: *Phys. Rev. D* 64 (3 2001), p. 034504. DOI: 10.1103/PhysRevD.64.034504. URL: https://link.aps.org/doi/10.1103/PhysRevD.64.034504.

[100] Stefano Capitani, Stephan Dürr, and Christian Hoelbling. "Rationale for UV-filtered clover fermions". In: *Journal of High Energy Physics* 2006.11 (2006), p. 028. DOI: 10.1088/1126-6708/2006/11/028. URL: https://dx.doi.org/10.1088/1126-6708/2006/11/028.

[101] Colin Morningstar and Mike Peardon. "Analytic smearing of link variables in lattice QCD". In: *Physical Review D* 69.5 (2004). DOI: 10.1103/physrevd.69.054501. URL: https://doi.org/10.1103%2Fphysrevd.69.054501.

[102] J. B. Zhang et al. "Stout-link smearing in lattice fermion actions". In: *Phys. Rev. D* 80 (2009), p. 074503. DOI: 10.1103/PhysRevD.80.074503. arXiv: 0908.3726 [hep-lat].

[103] Masato Nagatsuka, Keita Sakai, and Shoichi Sasaki. "Equivalence between the Wilson flow and stout-link smearing". In: *Phys. Rev. D* 108.9 (2023), p. 094506. DOI: 10.1103/PhysRevD.108.094506. arXiv: 2303.09938 [hep-lat].

[104] Maximilian Ammer and Stephan Durr. "Stout smearing and Wilson flow in lattice perturbation theory". In: *Phys. Rev. D* 110.5 (2024), p. 054504. DOI: 10.1103/PhysRevD.110.054504. arXiv: 2406.03493 [hep-lat].

[105] Sz. Borsanyi et al. "Ab initio calculation of the neutron-proton mass difference". In: *Science* 347 (2015), pp. 1452–1455. DOI: 10.1126/science.1257050. arXiv: 1406.4088 [hep-lat].

[106] Philip Rouenhoff and Stephan Durr. "Topology in 2D non-Abelian Lattice Gauge Theories". In: *PoS* LATTICE2024 (2025), p. 461. DOI: 10.22323/1.466.0461. arXiv: 2411.11593 [hep-lat].

[107] S. Gusken et al. "Nonsinglet Axial Vector Couplings of the Baryon Octet in Lattice QCD". In: *Phys. Lett. B* 227 (1989), pp. 266–269. DOI: 10.1016/S0370-2693(89)80034-6.

[108] Stefan Schaefer, Rainer Sommer, and Francesco Virotta. "Critical slowing down and error analysis in lattice QCD simulations". In: *Nuclear Physics B* 845.1 (2011), pp. 93–119. ISSN: 0550-3213. DOI: 10.1016/j.nuclphysb.2010.11.020. URL: http://dx.doi.org/10.1016/j.nuclphysb.2010.11.020.

[109] Ulli Wolff. "Monte Carlo errors with less errors". In: *Comput. Phys. Commun.* 156 (2004). [Erratum: Comput.Phys.Commun. 176, 383 (2007)], pp. 143–153. DOI: 10.1016/S0010-4655(03)00467-3. arXiv: hep-lat/0306017.

[110] Fabian Joswig et al. "pyerrors: A python framework for error analysis of Monte Carlo data". In: *Comput. Phys. Commun.* 288 (2023), p. 108750. DOI: 10.1016/j.cpc.2023.108750. arXiv: 2209.14371 [hep-lat].

[111] Stefan Schaefer, Rainer Sommer, and Francesco Virotta. *Investigating the critical slowing down of QCD simulations*. 2009. arXiv: 0910.1465 [hep-lat].

[112] Joan Fisher Box. "R. A. Fisher and the Design of Experiments, 1922-1926". In: *The American Statistician* 34.1 (1980), pp. 1–7. ISSN: 00031305. URL: http://www.jstor.org/stable/2682986 (visited on 04/22/2024).

[113] Stephan Durr and Gianluca Fuwa. "The topological susceptibility and excess kurtosis in SU(3) Yang-Mills theory". In: (2025). arXiv: 2501.08217 [hep-lat].

[114] Alberto Ramos. "Automatic differentiation for error analysis of Monte Carlo data". In: *Comput. Phys. Commun.* 238 (2019), pp. 19–35. DOI: 10.1016/j.cpc.2018.12.020. arXiv: 1809.01289 [hep-lat].

[115] Alberto Ramos. "Automatic differentiation for error analysis". In: *PoS* TOOLS2020 (2021), p. 045. DOI: 10.22323/1.392.0045. arXiv: 2012.11183 [hep-lat].

[116] C. Michael. "Fitting correlated data". In: *Physical Review D* 49.5 (1994), pp. 2616–2619. ISSN: 0556-2821. DOI: 10.1103/physrevd.49.2616. URL: http://dx.doi.org/10.1103/PhysRevD.49.2616.

[117] M. H. Qeenouille. "Notes on bias in estimation". In: *Biometrika* 43.3-4 (1956), pp. 353–360. ISSN: 0006-3444. DOI: 10.1093/biomet/43.3-4.353. eprint: https://academic.oup.com/biomet/article-pdf/43/3-4/353/987603/43-3-4-353.pdf. URL: https://doi.org/10.1093/biomet/43.3-4.353.

[118] J.W. Tukey. "Bias and Confidence in Not-Quite Large Sample". In: *Annals of Mathematical Statistics* 29 (1958), p. 614.

[119] Fabian J. Frech et al. "The mixing of two-pion and vector-meson states using staggered fermions". In: (Dec. 2023). arXiv: 2401.00514 [hep-lat].

[120] Fabian J. Frech, Finn M. Stokes, and Kalman K. Szabo. "Reconstruction of the vector meson propagator using a generalized eigenvalue problem". In: (Jan. 2025). arXiv: 2501.19186 [hep-lat].

[121] Mattia Bruno and Rainer Sommer. "On fits to correlated and auto-correlated data". In: *Computer Physics Communications* 285 (2023), p. 108643. ISSN: 0010-4655. DOI: 10.1016/j.cpc.2022.108643. URL: http://dx.doi.org/10.1016/j.cpc.2022.108643.

[122] Brian Colquhoun et al. "Form factors of $B \to \pi\ell\nu$ and a determination of $|V_{ub}|$ with Möbius domain-wall fermions". In: *Phys. Rev. D* 106 (5 2022), p. 054502. DOI: 10.1103/PhysRevD.106.054502. URL: https://link.aps.org/doi/10.1103/PhysRevD.106.054502.

[123] R. J. Dowdall et al. "Neutral B-meson mixing from full lattice QCD at the physical point". In: *Phys. Rev. D* 100 (9 2019), p. 094508. DOI: 10.1103/PhysRevD.100.094508. URL: https://link.aps.org/doi/10.1103/PhysRevD.100.094508.

[124] R. A. Fisher. "Statistical Methods for Research Workers". In: *Breakthroughs in Statistics: Methodology and Distribution*. Ed. by Samuel Kotz and Norman L. Johnson. New York, NY: Springer New York, 1992, pp. 66–70. ISBN: 978-1-4612-4380-9. DOI: 10.1007/978-1-4612-4380-9_6. URL: https://doi.org/10.1007/978-1-4612-4380-9_6.

[125] Ronald L. Wasserstein and Nicole A. Lazar. "The ASA Statement on p-Values: Context, Process, and Purpose". In: *The American Statistician* 70.2 (2016), pp. 129–133. DOI: 10.1080/00031305.2016.1154108. eprint: https://doi.org/10.1080/00031305.2016.1154108. URL: https://doi.org/10.1080/00031305.2016.1154108.

[126] H. Akaike. "A new look at the statistical model identification". In: *IEEE Trans. Automatic Control* 19.6 (1974), pp. 716–723. DOI: 10.1109/TAC.1974.1100705.

[127] Michel Davier et al. "Hadronic vacuum polarization: Comparing lattice QCD and data-driven results in systematically improvable ways". In: *Phys. Rev. D* 109.7 (2024), p. 076019. DOI: 10.1103/PhysRevD.109.076019. arXiv: 2308.04221 [hep-ph].

[128] Shaun Lahert. "The light-quark connected contribution to the muons anomalous magnetic moment". PhD thesis. Illinois U., Urbana (main), Illinois U., Urbana, 2023.

[129] Carleton DeTar and Song-Haeng Lee. "Variational method with staggered fermions". In: *Physical Review D* 91.3 (2015). ISSN: 1550-2368. DOI: 10.1103/physrevd.91.034504. URL: http://dx.doi.org/10.1103/PhysRevD.91.034504.

[130] C. Aubin et al. "A new approach for Delta form factors". In: *AIP Conference Proceedings*. AIP, 2011, pp. 621–624. DOI: 10.1063/1.3647217. URL: http://dx.doi.org/10.1063/1.3647217.

[131] Lukas Varnhorst. "Aspects of quark mass dependence in lattice QCD". PhD thesis. Wuppertal U., 2020. DOI: 10.25926/vrwh-6t66.

[132] Andreas Risch. "Checks on QED and strong-isospin breaking corrections to the HVP contribution in the standard model prediction of the muon $g-2$". In: *PoS* LATTICE2024 (2025), p. 271.

[133] Y. Aoki et al. "FLAG Review 2021". In: *Eur. Phys. J. C* 82.10 (2022), p. 869. DOI: 10.1140/epjc/s10052-022-10536-1. arXiv: 2111.09849 [hep-lat].

[134] C. McNeile et al. "High-Precision c and b Masses, and QCD Coupling from Current-Current Correlators in Lattice and Continuum QCD". In: *Phys. Rev. D* 82 (2010), p. 034512. DOI: 10.1103/PhysRevD.82.034512. arXiv: 1004.4285 [hep-lat].

[135] Sz. Borsanyi et al. "Calculation of the axion mass based on high-temperature lattice quantum chromodynamics". In: *Nature* 539.7627 (2016), pp. 69–71. DOI: 10.1038/nature20115. arXiv: 1606.07494 [hep-lat].

[136] A. Bazavov et al. "Topological susceptibility with the asqtad action". In: *Phys. Rev. D* 81 (2010), p. 114501. DOI: 10.1103/PhysRevD.81.114501. arXiv: 1003.5695 [hep-lat].

[137] N. Ishizuka et al. “Operator dependence of hadron masses for Kogut-Susskind quarks on the lattice”. In: *Nucl. Phys. B* 411 (1994), pp. 875–902. DOI: 10.1016/0550-3213(94)90475-8.

[138] Y. Aoki et al. “FLAG Review 2024”. In: (2024). arXiv: 2411.04268 [hep-lat].

[139] Szabolcs Borsányi et al. “High-precision scale setting in lattice QCD”. In: *JHEP* 09 (2012), p. 010. DOI: 10.1007/JHEP09(2012)010. arXiv: 1203.4469 [hep-lat].

[140] R. L. Workman et al. “Review of Particle Physics”. In: *PTEP* 2022 (2022), p. 083C01. DOI: 10.1093/ptep/ptac097.

[141] William Detmold and Michael G. Endres. “Signal/noise enhancement strategies for stochastically estimated correlation functions”. In: *Physical Review D* 90.3 (2014). ISSN: 1550-2368. DOI: 10.1103/physrevd.90.034503. URL: http://dx.doi.org/10.1103/PhysRevD.90.034503.

[142] Konstantin Ottnad. “Excited states in nucleon structure calculations”. In: *The European Physical Journal A* 57 (Feb. 2021). DOI: 10.1140/epja/s10050-021-00355-5.

[143] Maximilian Ammer and Stephan Durr. “Details of a staggered fermion data analysis”. In: *PoS* LATTICE2019 (2020), p. 048. DOI: 10.22323/1.363.0048. arXiv: 1910.11046 [hep-lat].

[144] G. D’Agostini. “On the use of the covariance matrix to fit correlated data”. In: *Nucl. Instrum. Meth. A* 346 (1994), pp. 306–311. DOI: 10.1016/0168-9002(94)90719-6.

[145] Finn Stokes. *Correlation of d’Agonstini effect and condition number of the covarinace matrix*. Presented at an internal meeting. Unpublished presentation. 2022.

[146] Nickolay Smirnov. “Table for estimating the goodness of fit of empirical distributions”. In: *The annals of mathematical statistics* 19.2 (1948), pp. 279–281.

[147] Andrey Kolmogorov and Nikolaj Smirnow. “Sulla determinazione empírica di uma legge di distribuzione”. In: 1933. URL: https://api.semanticscholar.org/CorpusID:222427298.

[148] J. Gasser and H. Leutwyler. “Light Quarks at Low Temperatures”. In: *Phys. Lett. B* 184 (1987), pp. 83–88. DOI: 10.1016/0370-2693(87)90492-8.

[149] Gilberto Colangelo, Stephan Durr, and Christoph Haefeli. “Finite volume effects for meson masses and decay constants”. In: *Nucl. Phys. B* 721 (2005), pp. 136–174. DOI: 10.1016/j.nuclphysb.2005.05.015. arXiv: hep-lat/0503014.

[150] Johan Bijnens and Thomas Rössler. “Finite Volume at Two-loops in Chiral Perturbation Theory”. In: *JHEP* 01 (2015), p. 034. DOI: 10.1007/JHEP01(2015)034. arXiv: 1411.6384 [hep-lat].

[151] Johan Bijnens. “CHIRON: a package for ChPT numerical results at two loops”. In: *Eur. Phys. J. C* 75.1 (2015), p. 27. DOI: 10.1140/epjc/s10052-014-3249-9. arXiv: 1412.0887 [hep-ph].

[152] Sz. Borsanyi et al. “High precision scale setting on the lattice”. In: *PoS* LATTICE2021 (2022), p. 371. DOI: 10.22323/1.396.0371.

[153] C. Aubin and C. Bernard. “Pion and kaon masses in staggered chiral perturbation theory”. In: *Phys. Rev. D* 68 (2003), p. 034014. DOI: 10.1103/PhysRevD.68.034014. arXiv: hep-lat/0304014.

[154] C. Aubin and C. Bernard. “Pseudoscalar decay constants in staggered chiral perturbation theory”. In: *Phys. Rev. D* 68 (2003), p. 074011. DOI: 10.1103/PhysRevD.68.074011. arXiv: hep-lat/0306026.

[155] Jon A. Bailey, Hyung-Jin Kim, and Weonjong Lee. “Taste non-Goldstone, flavor-charged pseudo-Goldstone boson masses in staggered chiral perturbation theory”. In: *Phys. Rev. D* 85 (2012), p. 094503. DOI: 10.1103/PhysRevD.85.094503. arXiv: 1112.2108 [hep-lat].

[156] Jon A. Bailey, Weonjong Lee, and Boram Yoon. “Taste non-Goldstone, flavor-charged pseudo-Goldstone boson decay constants in staggered chiral perturbation theory”. In: *Phys. Rev. D* 87.5 (2013), p. 054508. DOI: 10.1103/PhysRevD.87.054508. arXiv: 1212.5369 [hep-lat].

[157] A. Bazavov et al. "$|V_{us}|$ from $K_{\ell 3}$ decay and four-flavor lattice QCD". In: *Phys. Rev. D* 99.11 (2019), p. 114509. DOI: 10.1103/PhysRevD.99.114509. arXiv: 1809.02827 [hep-lat].

[158] Maarten F. L. Golterman and Jan Smit. "Lattice Baryons With Staggered Fermions". In: *Nucl. Phys. B* 255 (1985), pp. 328–340. DOI: 10.1016/0550-3213(85)90138-5.

[159] Jon A. Bailey. "Staggered baryon operators with flavor SU(3) quantum numbers". In: *Phys. Rev. D* 75 (2007), p. 114505. DOI: 10.1103/PhysRevD.75.114505. arXiv: hep-lat/0611023.

[160] Carleton DeTar and Song-Haeng Lee. "Variational method with staggered fermions". In: *Phys. Rev. D* 91.3 (2015), p. 034504. DOI: 10.1103/PhysRevD.91.034504. arXiv: 1411.4676 [hep-lat].

[161] J. Yelton et al. "Observation of an Excited Omega Baryon". In: *Physical Review Letters* 121.5 (2018). ISSN: 1079-7114. DOI: 10.1103/physrevlett.121.052003. URL: http://dx.doi.org/10.1103/PhysRevLett.121.052003.

[162] C. M. Bouchard et al. "$B \to K\ell\nu$ form factors from lattice QCD". In: *Physical Review D* 90.5 (2014). ISSN: 1550-2368. DOI: 10.1103/physrevd.90.054506. URL: http://dx.doi.org/10.1103/PhysRevD.90.054506.

[163] M. Di Carlo et al. "Light-meson leptonic decay rates in lattice QCD+QED". In: *Phys. Rev. D* 100.3 (2019), p. 034514. DOI: 10.1103/PhysRevD.100.034514. arXiv: 1904.08731 [hep-lat].

[164] Szabocls Borsanyi et al. "Full result for the QCD equation of state with 2+1 flavors". In: *Phys. Lett. B* 730 (2014), pp. 99–104. DOI: 10.1016/j.physletb.2014.01.007. arXiv: 1309.5258 [hep-lat].

[165] J. Gasser, A. Rusetsky, and I. Scimemi. "Electromagnetic corrections in hadronic processes". In: *Eur. Phys. J. C* 32 (2003), pp. 97–114. DOI: 10.1140/epjc/s2003-01383-1. arXiv: hep-ph/0305260.

[166] K. Symanzik. "Some topics in quantum field theory". In: *Mathematical Problems in Theoretical Physics*. Ed. by R. Schrader, R. Seiler, and D. A. Uhlenbrock. Berlin, Heidelberg: Springer Berlin Heidelberg, 1982, pp. 47–58. ISBN: 978-3-540-38982-8.

[167] Andreas S. Kronfeld. "Uses of effective field theory in lattice QCD". In: *At the Frontier of Particle Physics*, pp. 2412–2477. DOI: 10.1142/9789812777270_0004. eprint: https://www.worldscientific.com/doi/pdf/10.1142/9789812777270_0004. URL: https://www.worldscientific.com/doi/abs/10.1142/9789812777270_0004.

[168] T. Aoyama et al. "The anomalous magnetic moment of the muon in the Standard Model". In: *Physics Reports* 887 (2020), pp. 1–166. ISSN: 0370-1573. DOI: 10.1016/j.physrep.2020.07.006. URL: http://dx.doi.org/10.1016/j.physrep.2020.07.006.

[169] Zoltan Fodor et al. "Hadronic light-by-light scattering contribution to the anomalous magnetic moment of the muon at the physical pion mass". In: (2024). arXiv: 2411.11719 [hep-lat].

[170] Christian Zimmermann and Antoine Gérardin. "The hadronic light-by-light contribution to the muon $g-2$ using staggered fermions at the physical point". In: *PoS* LATTICE2024 (2025), p. 244. DOI: 10.22323/1.466.0244. arXiv: 2410.17092 [hep-lat].

[171] Christian Zimmermann and Antoine Gérardin. "Investigation of the hadronic light-by-light contribution to the muon $g-2$ using staggered fermions". In: *PoS* LATTICE2023 (2024), p. 247. DOI: 10.22323/1.453.0247. arXiv: 2311.10628 [hep-lat].

[172] Antoine Gérardin et al. "Lattice calculation of the π^0, η and η' transition form factors and the hadronic light-by-light contribution to the muon $g-2$". In: (2023). arXiv: 2305.04570 [hep-lat].

[173] Willem E. A. Verplanke et al. "Pseudoscalar transition form factors and the hadronic light-by-light contribution to the muon g-2". In: *PoS* LATTICE2022 (2023), p. 332. DOI: 10.22323/1.430.0332. arXiv: 2211.04159 [hep-lat].

[174] Willem E. A. Verplanke et al. "Pseudoscalar transition form factors and the hadronic light-by-light contribution to the muon g-2". In: *PoS* LATTICE2021 (2022), p. 592. DOI: 10.22323/1.396.0592. arXiv: 2112.08101 [hep-lat].

[175] G. W. Bennett et al. "Measurement of the Negative Muon Anomalous Magnetic Moment to 0.7 ppm". In: *Physical Review Letters* 92.16 (2004). ISSN: 1079-7114. DOI: 10.1103/physrevlett.92.161802. URL: http://dx.doi.org/10.1103/PhysRevLett.92.161802.

[176] G. W. Bennett et al. "Final Report of the E821 Muon Anomalous Magnetic Moment Measurement at BNL". In: *Phys. Rev. D* 73 (2006), p. 072003. DOI: 10.1103/PhysRevD.73.072003. arXiv: hep-ex/0602035 [hep-ex].

[177] D. P. Aguillard et al. "Measurement of the Positive Muon Anomalous Magnetic Moment to 127 ppb". In: (June 2025). arXiv: 2506.03069 [hep-ex].

[178] R. Aliberti et al. "The anomalous magnetic moment of the muon in the Standard Model: an update". In: (May 2025). arXiv: 2505.21476 [hep-ph].

[179] T. Blum et al. "The long-distance window of the hadronic vacuum polarization for the muon $g-2$". In: (Oct. 2024). arXiv: 2410.20590 [hep-lat].

[180] Dalibor Djukanovic et al. "The hadronic vacuum polarization contribution to the muon $g-2$ at long distances". In: (Nov. 2024). arXiv: 2411.07969 [hep-lat].

[181] Michel Davier et al. "Tensions in $e^+e^- \to \pi^+\pi^-(\gamma)$ measurements: the new landscape of data-driven hadronic vacuum polarization predictions for the muon $g-2$". In: *Eur. Phys. J. C* 84.7 (2024), p. 721. DOI: 10.1140/epjc/s10052-024-12964-7. arXiv: 2312.02053 [hep-ph].

[182] F. V. Ignatov et al. "Measurement of the e+e-→π+π- cross section from threshold to 1.2 GeV with the CMD-3 detector". In: *Phys. Rev. D* 109.11 (2024), p. 112002. DOI: 10.1103/PhysRevD.109.112002. arXiv: 2302.08834 [hep-ex].

[183] Bernard Aubert et al. "Precise measurement of the e+ e- —> pi+ pi- (gamma) cross section with the Initial State Radiation method at BABAR". In: *Phys. Rev. Lett.* 103 (2009), p. 231801. DOI: 10.1103/PhysRevLett.103.231801. arXiv: 0908.3589 [hep-ex].

[184] J. P. Lees et al. "Precise Measurement of the $e^+e^- \to \pi^+\pi^-(\gamma)$ Cross Section with the Initial-State Radiation Method at BABAR". In: *Phys. Rev. D* 86 (2012), p. 032013. DOI: 10.1103/PhysRevD.86.032013. arXiv: 1205.2228 [hep-ex].

[185] F. Ambrosino et al. "Measurement of $\sigma(e^+e^- \to \pi^+\pi^-\gamma(\gamma)$ and the dipion contribution to the muon anomaly with the KLOE detector". In: *Phys. Lett. B* 670 (2009), pp. 285–291. DOI: 10.1016/j.physletb.2008.10.060. arXiv: 0809.3950 [hep-ex].

[186] F. Ambrosino et al. "Measurement of $\sigma(e^+e^- \to \pi^+\pi^-)$ from threshold to 0.85 GeV^2 using Initial State Radiation with the KLOE detector". In: *Phys. Lett. B* 700 (2011), pp. 102–110. DOI: 10.1016/j.physletb.2011.04.055. arXiv: 1006.5313 [hep-ex].

[187] D. Babusci et al. "Precision measurement of $\sigma(e^+e^- \to \pi^+\pi^-\gamma)/\sigma(e^+e^- \to \mu^+\mu^-\gamma)$ and determination of the $\pi^+\pi^-$ contribution to the muon anomaly with the KLOE detector". In: *Phys. Lett. B* 720 (2013), pp. 336–343. DOI: 10.1016/j.physletb.2013.02.029. arXiv: 1212.4524 [hep-ex].

[188] A. Anastasi et al. "Combination of KLOE $\sigma\big(e^+e^- \to \pi^+\pi^-\gamma(\gamma)\big)$ measurements and determination of $a_\mu^{\pi^+\pi^-}$ in the energy range $0.10 < s < 0.95$ GeV^2". In: *JHEP* 03 (2018), p. 173. DOI: 10.1007/JHEP03(2018)173. arXiv: 1711.03085 [hep-ex].

[189] M. Davier et al. "The Discrepancy Between tau and e+e- Spectral Functions Revisited and the Consequences for the Muon Magnetic Anomaly". In: *Eur. Phys. J. C* 66 (2010), pp. 127–136. DOI: 10.1140/epjc/s10052-009-1219-4. arXiv: 0906.5443 [hep-ph].

[190] Michel Davier et al. "Update of the ALEPH non-strange spectral functions from hadronic τ decays". In: *Eur. Phys. J. C* 74.3 (2014), p. 2803. DOI: 10.1140/epjc/s10052-014-2803-9. arXiv: 1312.1501 [hep-ex].

[191] T. Blum et al. "Calculation of the Hadronic Vacuum Polarization Contribution to the Muon Anomalous Magnetic Moment". In: *Physical Review Letters* 121.2 (2018). ISSN: 1079-7114. DOI: 10.1103/physrevlett.121.022003. URL: http://dx.doi.org/10.1103/PhysRevLett.121.022003.

[192] B. Abi et al. "Measurement of the Positive Muon Anomalous Magnetic Moment to 0.46ăppm". In: *Physical Review Letters* 126.14 (2021). ISSN: 1079-7114. DOI: 10.1103/physrevlett.126.141801. URL: http://dx.doi.org/10.1103/PhysRevLett.126.141801.

[193] Alexei Bazavov et al. "Hadronic vacuum polarization for the muon $g-2$ from lattice QCD: Long-distance and full light-quark connected contribution". In: (2024). arXiv: 2412.18491 [hep-lat].

[194] Alexei Bazavov et al. "Hadronic vacuum polarization for the muon $g-2$ from lattice QCD: Complete short and intermediate windows". In: (Nov. 2024). arXiv: 2411.09656 [hep-lat].

[195] Alexei Bazavov et al. "Light-quark connected intermediate-window contributions to the muon $g-2$ hadronic vacuum polarization from lattice QCD". In: *Phys. Rev. D* 107.11 (2023), p. 114514. DOI: 10.1103/PhysRevD.107.114514. arXiv: 2301.08274 [hep-lat].

[196] C. T. H. Davies et al. "Windows on the hadronic vacuum polarization contribution to the muon anomalous magnetic moment". In: *Phys. Rev. D* 106.7 (2022), p. 074509. DOI: 10.1103/PhysRevD.106.074509. arXiv: 2207.04765 [hep-lat].

[197] G. Colangelo et al. "Prospects for precise predictions of a_μ in the Standard Model". In: (Mar. 2022). arXiv: 2203.15810 [hep-ph].

[198] Sebastian Spiegel and Christoph Lehner. "A high-precision continuum limit study of the HVP short-distance window". In: (Oct. 2024). arXiv: 2410.17053 [hep-lat].

[199] Simon Kuberski et al. "Hadronic vacuum polarization in the muon $g-2$: the short-distance contribution from lattice QCD". In: *JHEP* 03 (2024), p. 172. DOI: 10.1007/JHEP03(2024)172. arXiv: 2401.11895 [hep-lat].

[200] J. C. Hardy and I. S. Towner. "Superallowed $0^+ \to 0^+$ nuclear β decays: 2020 critical survey, with implications for V_{ud} and CKM unitarity". In: *Phys. Rev. C* 102.4 (2020), p. 045501. DOI: 10.1103/PhysRevC.102.045501.

[201] Nolan Miller et al. "F_K/F_π from Möbius Domain-Wall fermions solved on gradient-flowed HISQ ensembles". In: *Phys. Rev. D* 102.3 (2020), p. 034507. DOI: 10.1103/PhysRevD.102.034507. arXiv: 2005.04795 [hep-lat].

[202] A. Bazavov et al. "Gradient flow and scale setting on MILC HISQ ensembles". In: *Phys. Rev. D* 93.9 (2016), p. 094510. DOI: 10.1103/PhysRevD.93.094510. arXiv: 1503.02769 [hep-lat].

[203] R. J. Dowdall et al. "V_{us} from π and K decay constants in full lattice QCD with physical u, d, s and c quarks". In: *Phys. Rev. D* 88 (2013), p. 074504. DOI: 10.1103/PhysRevD.88.074504. arXiv: 1303.1670 [hep-lat].

[204] Georg Bergner et al. "Quark masses and decay constants in $N_f = 2+1+1$ isoQCD with Wilson clover twisted mass fermions". In: *PoS* LATTICE2019 (2020), p. 181. DOI: 10.22323/1.363.0181. arXiv: 2001.09116 [hep-lat].

[205] C. Alexandrou et al. "Ratio of kaon and pion leptonic decay constants with $N_f = 2+1+1$ Wilson-clover twisted-mass fermions". In: *Phys. Rev. D* 104.7 (2021), p. 074520. DOI: 10.1103/PhysRevD.104.074520. arXiv: 2104.06747 [hep-lat].

[206] A. Bazavov et al. "B- and D-meson leptonic decay constants from four-flavor lattice QCD". In: *Phys. Rev. D* 98.7 (2018), p. 074512. DOI: 10.1103/PhysRevD.98.074512. arXiv: 1712.09262 [hep-lat].

[207] T. Blum et al. "Domain wall QCD with physical quark masses". In: *Phys. Rev. D* 93.7 (2016), p. 074505. DOI: 10.1103/PhysRevD.93.074505. arXiv: 1411.7017 [hep-lat].

[208] A. Bazavov et al. "MILC results for light pseudoscalars". In: *PoS* CD09 (2009), p. 007. DOI: 10.22323/1.086.0007. arXiv: 0910.2966 [hep-ph].

[209] Christopher Aubin, Jack Laiho, and Ruth S. Van de Water. "Light Pseudoscalar Meson Masses and Decay Constants from Mixed Action Lattice QCD". In: *PoS* LATTICE2008 (2008). Ed. by Christopher Aubin et al., p. 105. DOI: 10.22323/1.066.0105. arXiv: 0810.4328 [hep-lat].

[210] Peter Boyle et al. "Isospin-breaking corrections to light-meson leptonic decays from lattice simulations at physical quark masses". In: (2022). arXiv: 2211.12865 [hep-lat].

[211] Finn M. Stokes. "f_K and f_π from staggered QCD". In: *Talk at LATTICE2022 Conference*. Bonn Germany, 2022. URL: https://indico.hiskp.uni-bonn.de/event/40/contributions/828/.

[212] A. Ramos. "F_K/F_π in full QCD". In: *PoS* LAT2009 (2009). Ed. by Chuan Liu and Yu Zhu, p. 259. DOI: 10.22323/1.091.0259. arXiv: 1002.1665 [hep-lat].

[213] A. Ramos et al. "Decay constants and sigma terms from the lattice". In: *PoS* ICHEP2010 (2010). Ed. by Bernard Pire et al., p. 376. DOI: 10.22323/1.120.0376.

[214] A. Ramos et al. "F_K/F_π from the Budapest-Marseille-Wuppertal Collaboration". In: *6th International Workshop on the CKM Unitarity Triangle*. 2011. arXiv: 1101.3968 [hep-lat].

[215] "The Helicity Formalism". In: *Angular Momentum Techniques in Quantum Mechanics*. Dordrecht: Springer Netherlands, 2002, pp. 165–198. ISBN: 978-0-306-47123-0. DOI: 10.1007/0-306-47123-X_13. URL: https://doi.org/10.1007/0-306-47123-X_13.

[216] Makoto Kobayashi and Toshihide Maskawa. "CP-Violation in the Renormalizable Theory of Weak Interaction". In: *Progress of Theoretical Physics* 49.2 (Feb. 1973), pp. 652–657. ISSN: 0033-068X. DOI: 10.1143/PTP.49.652. eprint: https://academic.oup.com/ptp/article-pdf/49/2/652/5257692/49-2-652.pdf. URL: https://doi.org/10.1143/PTP.49.652.

[217] Nicola Cabibbo. "Unitary Symmetry and Leptonic Decays". In: *Phys. Rev. Lett.* 10 (12 1963), pp. 531–533. DOI: 10.1103/PhysRevLett.10.531. URL: https://link.aps.org/doi/10.1103/PhysRevLett.10.531.

[218] J. Beringer et al. "Review of Particle Physics (RPP)". In: *Phys. Rev. D* 86 (2012), p. 010001. DOI: 10.1103/PhysRevD.86.010001.

[219] National Institute of Science and Technology. https://physics.nist.gov/cgi-bin/cuu/Value?gf. Accessed: 5 February 2025. 2025.

[220] K. G. Leach et al. "Searching for 0^+ states in ^{50}Cr: Implications for the superallowed β decay of ^{50}Mn". In: *Phys. Rev. C* 94 (1 2016), p. 011304. DOI: 10.1103/PhysRevC.94.011304. URL: https://link.aps.org/doi/10.1103/PhysRevC.94.011304.

[221] G.F. Grinyer, C.E. Svensson, and B.A. Brown. "Extraction of V_{ud} from superallowed Fermi beta decay by the Wilkinson techniques". In: *Nuclear Instruments and Methods in Physics Research Section A: Accelerators, Spectrometers, Detectors and Associated Equipment* 622.1 (2010), pp. 236–245. ISSN: 0168-9002. DOI: https://doi.org/10.1016/j.nima.2010.06.265. URL: https://www.sciencedirect.com/science/article/pii/S0168900210014555.

[222] University of Guelph. https://www.physics.uoguelph.ca. Accessed: 6 February 2025. 2025.

[223] Particle Data Group and P A et al. Zyla. "Review of Particle Physics". In: *Progress of Theoretical and Experimental Physics* 2020.8 (2020), p. 083C01. ISSN: 2050-3911. DOI: 10.1093/ptep/ptaa104. eprint: https://academic.oup.com/ptep/article-pdf/2020/8/083C01/34673722/ptaa104.pdf. URL: https://doi.org/10.1093/ptep/ptaa104.

[224] J. C. Hardy and I. S. Towner. "Superallowed $0^+ \to 0^+$ nuclear β decays: 2020 critical survey, with implications for V_{ud} and CKM unitarity". In: *Phys. Rev. C* 102 (4 2020), p. 045501. DOI: 10.1103/PhysRevC.102.045501. URL: https://link.aps.org/doi/10.1103/PhysRevC.102.045501.

[225] Elvira Gámiz et al. "Determination of m_s and $|V_{us}|$ from hadronic tau decays". In: *Journal of High Energy Physics* 2003.01 (2003), pp. 060–060. ISSN: 1029-8479. DOI: 10.1088/1126-6708/2003/01/060. URL: http://dx.doi.org/10.1088/1126-6708/2003/01/060.

[226] Elvira Gámiz et al. "V_{us} and m_s from hadronic tau decays". In: *Physical Review Letters* 94.1 (2005). ISSN: 1079-7114. DOI: 10.1103/physrevlett.94.011803. URL: http://dx.doi.org/10.1103/PhysRevLett.94.011803.

[227] K. Maltman. "A mixed tau-electroproduction sum rule for V_{us}". In: *Physics Letters B* 672.3 (2009), pp. 257–263. ISSN: 0370-2693. DOI: https://doi.org/10.1016/j.physletb.2009.01.036. URL: https://www.sciencedirect.com/science/article/pii/S0370269309000835.

[228] Y. Amhis et al. "Averages of b-hadron, c-hadron, and τ-lepton properties as of 2018: Heavy Flavor Averaging Group (HFLAV)". In: *The European Physical Journal C* 81.3 (2021). ISSN: 1434-6052. DOI: 10.1140/epjc/s10052-020-8156-7. URL: http://dx.doi.org/10.1140/epjc/s10052-020-8156-7.

[229] Vincenzo Cirigliano and Helmut Neufeld. "A note on isospin violation in Pl2(gamma) decays". In: *Phys. Lett. B* 700 (2011), pp. 7–10. DOI: 10.1016/j.physletb.2011.04.038. arXiv: 1102.0563 [hep-ph].

[230] Renwick J. Hudspith, Matthias F. M. Lutz, and Daniel Mohler. "Precise Omega baryons from lattice QCD". In: (Apr. 2024). arXiv: 2404.02769 [hep-lat].

[231] Ben Strassberger et al. "Scale setting for CLS 2+1 simulations". In: *PoS* LATTICE2021 (2022), p. 135. DOI: 10.22323/1.396.0135. arXiv: 2112.06696 [hep-lat].

[232] V. G. Bornyakov et al. "Wilson flow and scale setting from lattice QCD". In: (Aug. 2015). arXiv: 1508.05916 [hep-lat].

[233] Mattia Bruno, Tomasz Korzec, and Stefan Schaefer. "Setting the scale for the CLS $2 + 1$ flavor ensembles". In: *Phys. Rev. D* 95.7 (2017), p. 074504. DOI: 10.1103/PhysRevD.95.074504. arXiv: 1608.08900 [hep-lat].

[234] Shaun Lahert et al. "Hadronic vacuum polarization of the muon on $2 + 1 + 1$-flavor HISQ ensembles: an update." In: *PoS* LATTICE2021 (2022), p. 526. DOI: 10.22323/1.396.0526. arXiv: 2112.11647 [hep-lat].

[235] Jeffrey E. Mandula, George Zweig, and Jan Govaerts. "A general method for obtaining ClebschGordan coefficients of finite groups. I. Its application to point and space group". In: *Journal of Mathematical physics* 15.10 (1974). DOI: https://doi.org/10.1063/1.1666528.

[236] T.K. Sarkar and O. Pereira. "Using the matrix pencil method to estimate the parameters of a sum of complex exponentials". In: *IEEE Antennas and Propagation Magazine* 37.1 (1995), pp. 48–55. DOI: 10.1109/74.370583.

[237] Shaun Lahert et al. "The two-pion contribution to the hadronic vacuum polarization with staggered quarks". In: (Sept. 2024). arXiv: 2409.00756 [hep-lat].

[238] R. Dirl. "Induced projective representations". In: *Journal of Mathematical Physics* 18.10 (Aug. 2008), pp. 2065–2080. ISSN: 0022-2488. DOI: 10.1063/1.523181. eprint: https://pubs.aip.org/aip/jmp/article-pdf/18/10/2065/11310383/2065_1_online.pdf. URL: https://doi.org/10.1063/1.523181.

[239] Stefan Scherer. *Symmetrien und Gruppen in der Teilchenphysik*. Berlin, Heidelberg: Springer Spektrum, 2015. ISBN: 978-3-662-47733-5. DOI: 10.1007/978-3-662-47734-2.

[240] Laurens Janssen and Michael Boon. *Theory of Finite Groups. Applications in physics*. Amsterdam, NL: North-Holland Publishing Company, 1967.